WAVES SERIES

METAMATERIALS APPLIED TO WAVES SET

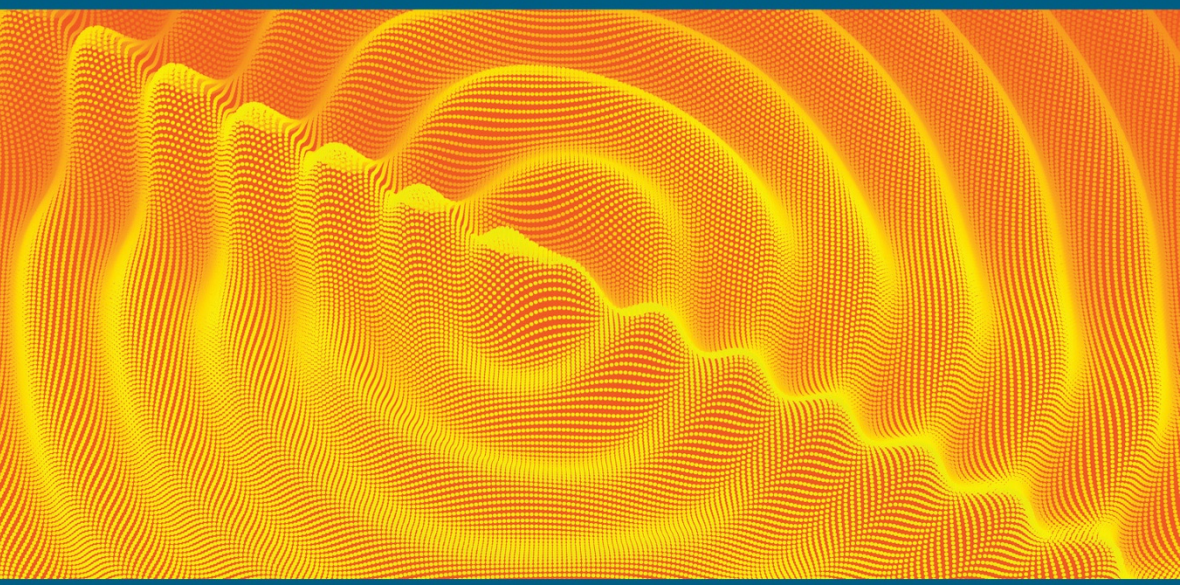

Volume 1

Fundamentals and Applications of Acoustic Metamaterials

From Seismic to Radio Frequency

Edited by
Vicente Romero-García
Anne-Christine Hladky-Hennion

ISTE

WILEY

Fundamentals and Applications of Acoustic Metamaterials

Metamaterials Applied to Waves Set

coordinated by
Frédérique de Fornel and Sébastien Guenneau

Volume 1

Fundamentals and Applications of Acoustic Metamaterials

From Seismic to Radio Frequency

Edited by

Vicente Romero-García
Anne-Christine Hladky-Hennion

ISTE

WILEY

First published 2019 in Great Britain and the United States by ISTE Ltd and John Wiley & Sons, Inc.

ISTE Ltd
27-37 St George's Road
London SW19 4EU
UK

www.iste.co.uk

John Wiley & Sons, Inc.
111 River Street
Hoboken, NJ 07030
USA

www.wiley.com

Library of Congress Control Number: 2019938254

British Library Cataloguing-in-Publication Data
A CIP record for this book is available from the British Library
ISBN 978-1-78630-336-3

Contents

Preface

During recent decades, metamaterials have revolutionized the way waves are controlled in the broad field of wave physics due to the extraordinary physical properties they present. Their locally resonant structure, introducing deep subwavelength band gaps, regions of frequencies where propagation is forbidden, among other properties, have motivated a plethora of applications not available up to now and creating an inflection point in the material science conception. In particular, acoustic metamaterials have shown extraordinary functionalities giving rise to breakthroughs. In many cases, they are able to replace traditional treatments in practical situations due to the better performances in targeted and tunable frequency ranges with strongly reduced dimensions. Acoustic and mechanical metamaterials themselves represent a scientific breakthrough with respect to the conventional treatments for noise, vibrations and radiofrequency problems.

Precursors of such metamaterials are the periodic media. Wave propagation in periodic media has been exploited in the field of wave physics revolutionizing the way of controlling waves in several branches of physics and technology. The secret of these materials lies in their structuring, the origin of peculiar effects like negative refraction or the spatial filtering, explaining, for example, the structural color in nature such as butterfly wings have. Today, these materials count as part of the class of photonic crystals for light or phononic crystals for elastic and acoustic waves with particular dispersion relation. It has been shown that periodic distributions of scatterers embedded in a host medium can be used in the design of effective media in the low frequency regime. When the wavelength, λ, is big compared to the separation between the scatterers, a, (long wavelength regime), homogenization theories can be applied and as a result, this periodic medium behaves as an effective homogeneous medium. If the scatterers are resonators, the effective properties can present extraordinary properties around the resonance frequency, and in this case, the

material becomes a metamaterial. However, in the diffraction regime, the periodic structures present bandgaps at wavelengths of the order of the periodicity of the structure. Among other potential applications, in acoustics these systems have motivated tunable frequency filters, beam forming devices, waveguides, wave traps and slow wave systems. In this regime, these materials are strongly anisotropic, presenting an angular dependence of its scattering properties.

During the summer school *Metagenierie 2017*, organized by the GdR (Groupement de recherche) Meta, the principles of acoustic metamaterials and their possible engineer/industrial applications were discussed with main goal of creating a training course with different steps of the learning procedure: global state of the art, principles and fundamentals and applications. This book is devoted to gathering all the discussions and provides a training book with a large overview on the field of acoustic metamaterials through its nine chapters. The book is divided into three parts:

– Part 1: Overview of the Current Research in Acoustic Metamaterials

– Part 2: Principles and Fundamentals of Acoustic Metamaterials

– Part 3: Applications of Acoustic Metamaterials

Part 1, Chapters 1–3, highlights the properties of the locally resonant structures with deep subwavelength bandgaps, and how the viscothermal losses can affect the physical properties. Chapter 1 shows the recent advances in the study of the presence of losses in double-negative metamaterial; Chapter 2 focuses on the use of deep subwavelength bandgaps to attenuate seismic waves; and finally, Chapter 3 shows how we can make use of both viscothermal losses and slow sound phenomena to create perfect absorbers as well as metadiffusers with deep subwavelength structures.

Part 2, Chapters 4–6, provides the principles and fundamentals of the basic theoretical frameworks to deal with metamaterials and periodic structures. Chapter 4 discusses the homogenization theory for 3D structures in the time domain; Chapter 5 shows the fundamentals of the plane wave expansion method to calculate the dispersion relation of periodic media; and finally, Chapter 6 shows a complete introduction to the multiple scattering theory in order to deal with the finite size effects of periodic structures.

Part 3, Chapters 7–9, shows a broad overview of the industrial applications of metamaterials and periodic media. Chapter 7 shows a review of the acoustic metamaterials for the industrial applications of audible sound; Chapter 8 shows also an extensive review of the possible radiofrequency applications of acoustic metamaterials for radiofrequency applications; and finally, Chapter 9 shows the possibilities of acoustic metamaterials for underwater applications.

The editors of this book would like to acknowledge all the speakers and participants of *Metagenierie 2017*, who have highly enriched scientific discussions. In particular, the editors would like to kindly thank all the participants of this book. They made a great effort and we hope the readers can note this by reading the chapters. We hope that this book will be useful for the community of acoustic metamaterials and motivate future development in this field.

Vicente ROMERO-GARCÍA
Anne-Christine HLADKY-HENNION
May 2019

PART 1

Overview of the Current Research in Acoustic Metamaterials

Fundamentals and Applications of Acoustic Metamaterials: From Seismic to Radio Frequency,
First Edition. Edited by Vicente Romero-García and Anne-Christine Hladky-Hennion.

1

Visco-thermal Effects in Acoustic Metamaterials Based on Local Resonances

1.1. Introduction

Acoustic metamaterials are man-made composite structures whose acoustic properties are new in comparison with that of the components used in their construction. Recent review articles have reported the many fascinating devices based on their extraordinary properties [CUM 16, MA 16, HAB 16]. Among them, acoustic cloaking and negative refraction are phenomena that are currently used to develop devices like noise shelters, acoustic imaging with subwavelength resolution, focusing devices and many others. On the one hand, acoustic cloaking is obtained thanks to the possibility of engineering artificial structures behaving like acoustic materials with an effective anisotropic dynamical mass density [CUM 07, TOR 08]. Later, it was demonstrated that cloaking is also possible with structures with an effective anisotropic bulk modulus, having simultaneously an effective isotropic dynamical mass. On the other hand, negative refraction arises because of the possibility of engineering structures whose effective acoustic parameters (i.e. mass density and bulk modulus) are both negative. Metamaterials with double-negative parameters can be obtained by tailoring structures that have both monopole and dipole resonances [LI 04]. In addition, negative refraction has been also demonstrated using space-coiling acoustic metamaterials [KOC 49, LIA 12, XIE 13] and hyperbolic materials [GAR 14].

The effect of losses in acoustic metamaterials has been scarcely tackled though dissipation seems to play a fundamental role in explaining the degradation of the

Chapter written by José SÁNCHEZ-DEHESA and Vicente CUTANDA HENRÍQUEZ.

predicted performance in many manufactured structures. As a typical example, let us mention the case of three-dimensional labyrinthine acoustic metamaterials characterized by Frenzel *et al.* [FRE 13], who found a significant amount of losses that led them to propose these structures for subwavelength broadband all-angle acoustic absorbers. A recent study by Molerón *et al.* [MOL 16] demonstrated that the actual response of these structures with subwavelength slits in air strongly depends on the viscothermal losses. Previously, it was shown that slow sound propagation observed in waveguides with side resonators was produced by viscothermal dissipation [THE 14]. For the case of metamaterials based on local resonances, the authors claimed the expected double-negative behavior in two specifically designed structures was unobservable, due to the strong influence of viscothermal effects [FOK 11, GRA 13].

This chapter is devoted to study the contribution of viscothermal effects in some specific acoustic metamaterials. Particularly, in those whose negative effective parameters are a consequence of embedded resonances in the building units. First, we briefly report the different approaches developed in order to study viscothermal losses in environments where their expected contribution is relevant. The finite element method (FEM) and the boundary element method (BEM) can be used when explaining the properties of artificial structures with corrugated surfaces where viscothermal losses are relevant, like the ones analyzed here. We have selected the BEM as the more adequate to study the metamaterial samples based on local resonances and therefore we explain this method with some detail in section 1.2.1. Then, in section 1.3, the BEM is applied to comprehensively study the case of a single-negative metamaterial. This quasi-two-dimensional metamaterial structure is made of a two-dimensional (2D) waveguide with a square distribution of drilled holes [GRA 12] and effectively behaves as a material with negative bulk modulus as the one introduced by Fang *et al.* [FAN 06]. It will be shown that the viscothermal losses, although relevant, do not destroy the observation of the negative modulus theoretically predicted. However, this is not the conclusion obtained for the case studied in section 1.4, where the quasi-2D metamaterial has cylindrical inclusions with a periodically corrugated surface and was designed to show double-negative behavior. For this double-negative metamaterial, the viscothermal losses play a paramount importance and its contribution completely destroys the expected behavior, giving support to the experimental data [CUT 17b]. Anyway, we have to stress that the effect of viscothermal losses has been studied for two specific cases and cannot be directly extrapolated to all cases. However, the results are indicative of the type of issues that researchers should consider during the process of designing metamaterials based on embedded resonances.

1.2. Viscothermal effects: numerical methods

Viscous and thermal losses of acoustic waves are only relevant in two cases: i) propagation over long distances, such as large rooms and outdoor acoustics; and ii) a very thin boundary layer of fluid over the domain boundaries. We are not concerned here with case i), which can easily be treated by suitably modifying the existing physical descriptions (e.g. with propagation loss constants). In case ii), viscous and thermal boundary layers have similar thicknesses, ranging from a few micrometers at high frequencies to a fraction of a millimeter at lower frequencies, in the audible range. The viscous and thermal boundary layers arise due to i) the difficulty of the fluid particles to slide over the boundary, and ii) the strong heat exchange between fluid and solid boundary, respectively [PIE 81, MOR 68].

Boundary losses due to viscothermal effects can be accounted for as a boundary impedance in large setups such as rooms [CRE 82]. Such approach is, however, limited for small (in relation to the thickness of the boundary layers) or intricate setups. When the boundary layers fill a significant part, or all, of the volume of the domain, losses can be very relevant. This is the case, for example, of microphones, hearing aids and acoustic couplers. In the case of metamaterials, the effect of viscothermal losses can be very relevant even for cases of a relatively large scale, as will be shown later in this chapter.

Viscothermal losses can be represented by analytical models, such as in the classical solution to a narrow cylindrical tube [RAY 94]. Other authors provide similar solutions, also limited to particular geometries [STI 91, BRU 87]. These solutions are often used in the metamaterial literature. However, their geometrical limitations restrict their range of applicability to simplified versions of quarter-wavelength and Helmholtz resonators.

The BEM with viscothermal losses is used in the test cases shown in the following sections of this chapter. This is a numerical method with no limiting hypotheses other than linearity and absence of flow. The viscothermal implementation of the finite element method (FEM) is another numerical implementation with no geometrical restrictions, which was used in [CUT 17a] to validate BEM metamaterial models. The BEM with losses is chosen here because it has been found more computationally manageable for the metamaterial cases studied.

The FEM and BEM with losses are briefly described in the following sections.

1.2.1. *Finite element method with losses*

The FEM implementation with viscous and thermal losses is available in the commercial software COMSOL. It was initially proposed by Malinen *et al.*

[MAL 04], which is achieved by direct discretization of the full linearized Navier–Stokes equations. The equations solved are the momentum, continuity and energy equations,

$$i\omega\rho_0\mathbf{v} = \nabla\cdot\left(-p\mathbf{I} + \mu\left(\nabla\mathbf{v} + \nabla\mathbf{v}^T\right) - \left(\frac{2}{3}\mu - \eta\right)(\nabla\cdot\mathbf{v})\,\mathbf{I}\right) + \mathbf{F} \qquad [1.1]$$

$$i\omega\rho + \rho_0\nabla\cdot\mathbf{v} = 0 \qquad [1.2]$$

$$i\omega\rho_0 C_p T = -\nabla\cdot(-\lambda\nabla T) + i\omega\alpha_0 T_0 p \qquad [1.3]$$

$$\rho = \rho_0\left(\beta_T p - \alpha_0 T\right) \qquad [1.4]$$

The acoustic variables are: particle velocity $\mathbf{v}$, pressure p and temperature T. $\mathbf{F}$ is a volume force acting on the fluid. The parameters of air are expressed as: ρ_0 the static density, T_0 the equilibrium temperature, μ the coefficient of viscosity, η the bulk viscosity, C_p the heat capacity at constant pressure, λ thermal conductivity, α_0 coefficient of thermal expansion and β_T isothermal compressibility.

Equations [1.1]–[1.4] are solved by transforming the equations into weak form, as is usually done in FEM. This results in a system of equations having pressure, particle velocity and temperature as variables. Five degrees of freedom are introduced per node, meaning that the system will be five times larger as compared to the lossless counterpart for the same mesh. In addition, the boundary layers over the boundaries need to be meshed with sufficient detail, further increasing the size of the calculation.

1.2.2. *Boundary element method with losses*

The BEM implementation with losses is based on the Kirchhoff decomposition of the Navier–Stokes equations [PIE 81, BRU 89],

$$(\Delta + k_a^2)p_a = 0 \qquad [1.5]$$

$$(\Delta + k_h^2)p_h = 0 \qquad [1.6]$$

$$(\Delta + k_v^2)\vec{v}_v = \vec{0}\,, \text{ with } \nabla\cdot\vec{v}_v = 0 \qquad [1.7]$$

where harmonic time dependence $e^{i\omega t}$ is omitted. The indexes (*a,h,v*) indicate the so-called acoustic, thermal and viscous *modes*, represented by equations [1.5], [1.6]

and [1.7] respectively. The modes can be treated independently in the acoustic domain and linked through the boundary conditions. The total pressure can be obtained as the sum $p = p_a + p_h$ of the acoustic and thermal components (there is not a viscous pressure), while the particle velocity has contributions from the three *modes* as $\vec{v} = \vec{v}_a + \vec{v}_h + \vec{v}_v$.

$$k_a^2 = \frac{k^2}{1 + ik(\ell_v + [\gamma - 1)\ell_h] - k^2\ell_h(\gamma - 1)(\ell_h - \ell_v)} \quad [1.8]$$

$$k_h^2 = \frac{-ik}{1 - ik(\gamma - 1)(\ell_h - \ell_v)} \quad [1.9]$$

$$k_v^2 = -\frac{i\rho_0 ck}{\mu}, \quad [1.10]$$

The three wavenumbers k_a, k_h and k_v in equations [1.8], [1.9] and [1.10] depend on the lossless wavenumber k and the physical properties of the fluid: ρ_0 is the static density of air, c is the speed of sound, k is the adiabatic wavenumber and γ is the ratio of specific heat at constant pressure and specific heat at constant volume C_p/C_v. The viscous and thermal characteristic lengths are $\ell_v = (\eta + 4/3\mu)/\rho_0 c$ and $\ell_h = \lambda/(\rho_0 c C_p)$, where λ is the thermal conductivity, μ is the coefficient of viscosity and η is the bulk viscosity or second viscosity [BRU 89].

Equation [1.5] is a wave equation, while equations [1.6] and [1.7] are diffusion equations. Equation [1.7] is a vector equation and can be split into its three components, giving a total of five equations with five unknowns: p_a, p_h and the three components of $\vec{v}_v$. The modes in equations [1.5], [1.6] and [1.7] can be linked through the boundary conditions

$$T = T_a + T_h = \tau_a p_a + \tau_h p_h = 0, \quad [1.11]$$

$$\vec{v}_{boundary} = \vec{v}_a + \vec{v}_h + \vec{v}_v = \phi_a \nabla p_a + \phi_h \nabla p_h + \vec{v}_v. \quad [1.12]$$

Equation [1.11] states that the temperature T, with acoustic and thermal components T_a and T_h, remains constant at the boundary, leading to a condition that links the thermal and acoustic pressures p_a and p_h. Equation [1.12] ensures that the total particle velocity, expressed as the sum of acoustic, thermal and viscous contributions, matches the boundary velocity in any direction. The parameters τ_a, τ_h, ϕ_a and ϕ_h depend, like the wavenumbers in equations [1.5], [1.6] and [1.7], on

physical constants and the frequency. The velocity calculation, equation [1.12], is a vector equation, which can be split for convenience into normal and tangential components,

$$\vec{v}_{boundary,n} = \phi_a \frac{\partial p_a}{\partial n} + \phi_h \frac{\partial p_h}{\partial n} + \vec{v}_{v,n}, \qquad [1.13]$$

$$\vec{v}_{boundary,t} = \phi_a \nabla_t p_a + \phi_h \nabla_t p_h + \vec{v}_{v,t}. \qquad [1.14]$$

The BEM implementation with losses starts by discretizing equations [1.5], [1.6] and [1.7] independently. These equations are formally equivalent to the lossless harmonic Helmholtz equation, and therefore the discretization follows the same procedure as in the lossless BEM, i.e. converting the Helmholtz equation into its integral form [WU 00, JUH 93],

$$C(P)p(P) = \int_S \left[\frac{\partial G(Q)}{\partial n} p(Q) - \frac{\partial p(Q)}{\partial n} G(Q) \right] dS + p^I(P), \qquad [1.15]$$

where p is the sound pressure, G is the Green's function, and P and Q are points in the domain and on the surface respectively. $C(P)$ is a geometrical constant and $p^I(P)$ is the incident pressure, if present. The boundary is then divided into surface elements, and equation [1.15] is discretized as

$$\mathbf{A}\mathbf{p} - \mathbf{B}\frac{\partial \mathbf{p}}{\partial n} + \mathbf{p}^I = 0. \qquad [1.16]$$

Given a set of boundary conditions, equation [1.16] can be solved for obtaining the pressure and normal particle velocity at the boundary. The acoustic magnitudes in the domain are subsequently obtained from the surface solution by re-applying the discretized Helmholtz integral equation. By following this procedure, the harmonic equations, equations [1.5], [1.6] and [1.7] of the Kirchhoff decomposition, can be discretized as

$$\mathbf{A}_a\mathbf{p}_a - \mathbf{B}_a\frac{\partial \mathbf{p}_a}{\partial n} + \mathbf{p}^I = 0, \qquad [1.17]$$

$$\mathbf{A}_h\mathbf{p}_h - \mathbf{B}_h\frac{\partial \mathbf{p}_h}{\partial n} = 0, \qquad [1.18]$$

$$\mathbf{A}_v\vec{\mathbf{v}}_v - \mathbf{B}_v\frac{\partial \vec{\mathbf{v}}_v}{\partial n} = \vec{0}\,, \text{ with } \nabla \cdot \vec{\mathbf{v}}_v = 0. \qquad [1.19]$$

The coupling boundary conditions in equations [1.11] and [1.12] and the null divergence of the viscous velocity in equation [1.19] are used in the coupling of equations [1.17], [1.18] and [1.19]. This coupling is better achieved if the velocity

boundary condition is split, as shown in equations [1.13] and [1.14], into components that are locally normal and tangential to the boundary. Coordinate transformations between the node-based local reference system (normal and tangential vectors n, t_1 and t_2) and the global Cartesian reference (x, y, z) are therefore needed. The resulting system of equations for obtaining the acoustic component of the pressure on the boundary is

$$\begin{aligned}
&\Bigg[\phi_a \mathbf{B}_a^{-1}\mathbf{A}_a - \phi_h \mathbf{B}_h^{-1}\mathbf{A}_h \frac{\tau_a}{\tau_h} \\
&+\left[\mathbf{N}_{11} \circ (\mathbf{B}_v^{-1}\mathbf{A}_v)\right]^{-1}\left(\phi_a - \frac{\tau_a}{\tau_h}\phi_h\right)\Bigg(\left[\mathbf{N}_{12} \circ (\mathbf{B}_v^{-1}\mathbf{A}_v)\right]\frac{\partial}{\partial t_1} \\
&+\left[\mathbf{N}_{13} \circ (\mathbf{B}_v^{-1}\mathbf{A}_v)\right]\frac{\partial}{\partial t_2} + \Delta_t\Bigg)\Bigg]\mathbf{p}_a = \\
&\vec{\mathbf{v}}_{boundary,n} + \left[\mathbf{N}_{11} \circ (\mathbf{B}_v^{-1}\mathbf{A}_v)\right]^{-1}\left[\left[\mathbf{N}_{12} \circ (\mathbf{B}_v^{-1}\mathbf{A}_v)\right] + \frac{\partial}{\partial t_1}\right]\vec{\mathbf{v}}_{boundary,t_1} \\
&+\left[\mathbf{N}_{11} \circ (\mathbf{B}_v^{-1}\mathbf{A}_v)\right]^{-1}\left[\left[\mathbf{N}_{13} \circ (\mathbf{B}_v^{-1}\mathbf{A}_v)\right] + \frac{\partial}{\partial t_2}\right]\vec{\mathbf{v}}_{boundary,t_2} - \phi_a \mathbf{B}_a^{-1}\mathbf{p}^I \quad [1.20]
\end{aligned}$$

The "$\circ$" operator in equation [1.20] is the Hadamard matrix product, and the constant matrices $\mathbf{N}_{11}$, $\mathbf{N}_{12}$ and $\mathbf{N}_{13}$ are obtained as

$$\begin{aligned}
\mathbf{N}_{11} &= \mathbf{n}_x\mathbf{n}_x^T + \mathbf{n}_y\mathbf{n}_y^T + \mathbf{n}_z\mathbf{n}_z^T, \\
\mathbf{N}_{12} &= \mathbf{n}_x\mathbf{t}_{1,x}^T + \mathbf{n}_y\mathbf{t}_{1,y}^T + \mathbf{n}_z\mathbf{t}_{1,z}^T, \\
\mathbf{N}_{13} &= \mathbf{n}_x\mathbf{t}_{2,x}^T + \mathbf{n}_y\mathbf{t}_{2,y}^T + \mathbf{n}_z\mathbf{t}_{2,z}^T,
\end{aligned} \quad [1.21]$$

where the right-hand sides contain products of the (x, y, z) components of the node-based normal and tangential vectors n, t_1 and t_2.

Equation [1.20] relates the prescribed normal and tangential velocities on the boundary ($\vec{\mathbf{v}}_{boundary,n}$, $\vec{\mathbf{v}}_{boundary,t_1}$ and $\vec{\mathbf{v}}_{boundary,t_2}$) and the incident pressure $\mathbf{p}^I$ with the boundary pressures associated with the acoustic mode $\mathbf{p}_a$. After solving this system, it is possible to derive the remaining magnitudes on the boundary ($\mathbf{p}_h, \vec{\mathbf{v}}_v$) and on the domain [STI 91, CUT 13].

The implementation is based on the research software OpenBEM, which solves the Helmholtz wave equation using the direct collocation technique [CUT 10]. In BEM, only the domain boundary is meshed, saving degrees of freedom as compared with other numerical methods like the FEM. Three sets of coefficient matrices are used ($\mathbf{A}_a$, $\mathbf{B}_a$, $\mathbf{A}_h$, $\mathbf{B}_h$, $\mathbf{A}_v$, $\mathbf{B}_v$) corresponding to the three modes: acoustic, thermal and

viscous. The thermal and viscous coefficient matrices are, as a result of the evanescent nature of the viscous and thermal effects, sparse matrices. However, the remaining acoustic mode matrix is fully populated, and all of them are frequency dependent. As compared with FEM, the BEM with losses – although still computationally heavy – can be more efficient for intricate geometries that are on the limit of what is achievable, as is the case of the metamaterial examples in this chapter.

New versions of the BEM with losses have been proposed recently that overcome implementation issues arising from the $\frac{\partial}{\partial t_1}$, $\frac{\partial}{\partial t_2}$ and Δ_t operators in equation [1.20] [CUT 18, AND 18]. These operators are the tangential derivatives and the tangential Laplacian respectively.

1.3. Viscothermal effects in metamaterials with negative bulk modulus

The seminal demonstration of a dynamical bulk modulus with negative value was performed by Fang *et al.* [FAN 06], who used a one-dimensional (1D) water channel with an array of Helmholtz resonators.

They found that the measured effective bulk modulus can be fitted to the following frequency-dependent expression:

$$B_{eff}^{-1} = E_o^{-1}\left[1 - \frac{F\omega_0^2}{\omega^2 - \omega_0^2 + i\Gamma\omega}\right], \qquad [1.22]$$

where F is a geometrical factor, ω_0 is the resonant angular frequency of the resonator and Γ is the dissipation loss in the resonating Helmholtz elements. The loss term was determined by a procedure in which the calculated transmission profile was fitted to the transmitted spectral dip, giving a value of $\Gamma = 2\pi \times 400$ Hz. A few years later, an equivalent quasi-two-dimensional structure was studied in airborne sound with similar conclusions [GAR 12]. The structure consisted of a square array of cylindrical boreholes with equal radii (R) and depths (L) drilled in a flat rigid surface. The theoretical profile fitted to the experimental data provided a value for the losses $\Gamma = 2\pi \times 3.4$ Hz. This value is extremely small in comparison with that obtained using an 1D water waveguide with Helmholtz resonators.

To verify such small amount of losses, we have performed numerical simulations using the BEM implementation described above. The boundary mesh is constructed using the Gmsh meshing software [GEU 09]. The quadratic six-node elements are represented in Figure 1.1. The dimensions of the structure correspond to what was studied in [GAR 12]. The distance between vertical holes (lattice constant) is 30 cm. They are drilled in an infinite 2D waveguide, which is assumed to carry an incident plane wave. This condition is reproduced in the finite structure shown in Figure 1.1 by

placing a moving piston on the emitting end. In addition, a boundary impedance of ρc is defined at both emitting and receiving ends.

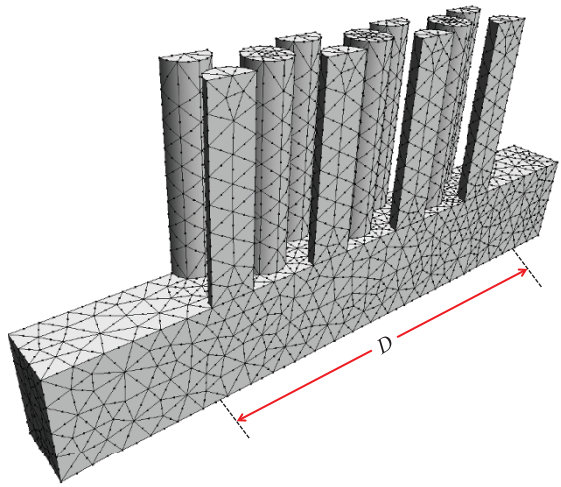

Figure 1.1. *Schematic view of the modeling of an acoustic metamaterial with effective bulk modulus negative. The BEM mesh used consists of 2352 elements and contains 4706 nodes*

Following the experimental setup, reflectance and transmittance are calculated from the acoustic pressures (P_1, P_2, P_3) recorded at three different positions (x_1, x_2, x_3) inside the waveguide; two at the emitting end, in front of the sample, and one at the receiving end, behind the sample. The positions are, respectively, –15.07 cm, –13.9 cm and 15.07 cm, measured from the sample center. The expressions for the reflection and transmission coefficients are:

$$r(\omega) = \frac{P_2 e^{-ik_0 x_1} - P_1 e^{-ik_0 x_2}}{P_1 e^{ik_0 x_2} - P_2 e^{ik_0 x_1}}, \qquad [1.23]$$

$$t(\omega) = \frac{P_3}{P_2} \frac{e^{-ik_0 x_2} - r(\omega) e^{ik_0 x_2}}{e^{-ik_0 x_3}} e^{-ik_0 D}, \qquad [1.24]$$

where k_0 is the wavenumber in air and D is the effective thickness of the metamaterial, which has been determined by considering that the surfaces are located at a half of the distance of the layer separation. From the expressions above, it is possible to obtain the reflectance $R(\omega) = |r(\omega)|^2$ and transmittance $T(\omega) = |t(\omega)|^2$. In addition, the energy balance can be applied to obtain the absorptance $A(\omega) = 1 - T(\omega) - R(\omega)$.

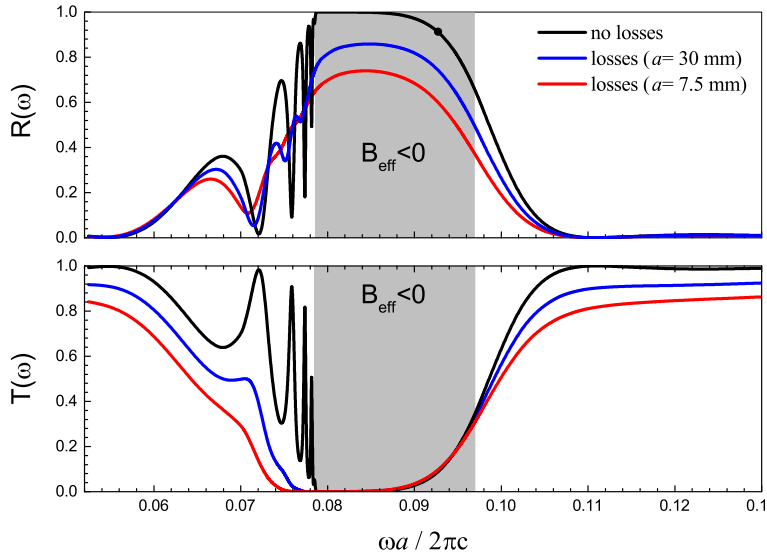

Figure 1.2. *Reflectance $R(\omega)$ and transmittance $T(\omega)$ of the single-negative acoustic metamaterial shown in Figure 1.1. The curves correspond to calculations with no viscothermal losses (black line), and with losses at two different scales: full (blue line) and reduced to one-fourth (red line). The frequencies are given in reduced units to represent all the spectra in a single plot. For a color version of this figure, see www.iste.co.uk/romero/metamaterials.zip*

Figures 1.2 and 1.3 show the reflectance, transmittance and absorptance spectra calculated for the single-negative metamaterial under study. The calculations have been performed with no losses and with viscothermal losses, the latter at two different scales: full and reduced to one-fourth. The reasoning behind the scaling is that viscous and thermal losses do not scale in the same way as the lossless magnitudes. The absorptance for the structure without losses is not shown in Figure 1.3; its value is zero, with the precision of the calculation for all the frequencies, proving that the balance of energy is correct in the calculations. The behavior of the lossless structures does not change with the scale; the results are just shifted in frequency. However, viscous and thermal boundary layers, as mentioned in section 1.2, have thicknesses that vary as $f^{-\frac{1}{2}}$.

Results in Figure 1.2 support the previous simulations, based on the mode-matching technique and the measured data reported in [GAR 12] (see its Figure 1.4). Thus, the calculated spectra with no losses exhibit Fabry–Perot (FP)

peaks (in the transmittance) and troughs (in the reflectance), which are a result of the finite thickness of the metamaterial. Then, a stop band develops in the frequency region (gray strip) where the effective bulk modulus takes negative values and, therefore, the phase velocity is imaginary. When losses are considered, our calculation shows that the FP peaks in the transmittance were strongly reduced and even disappeared when they were experimentally observed. Similar behavior is observed in the reflectance spectra, where the minima defining the FP resonances practically disappear; only the first minimum is kept at both structures. Both the reflectance and transmittance calculated profiles reproduce fairly well the experimental data shown in Figure 4 of [GAR 12], corresponding to the larger dimension. The reason explaining the strong reduction in the transmittance as the frequency is approaching to the bandgap is the corresponding decreasing of the group velocity, which produces an enhancement of the relatively small viscothermal losses.

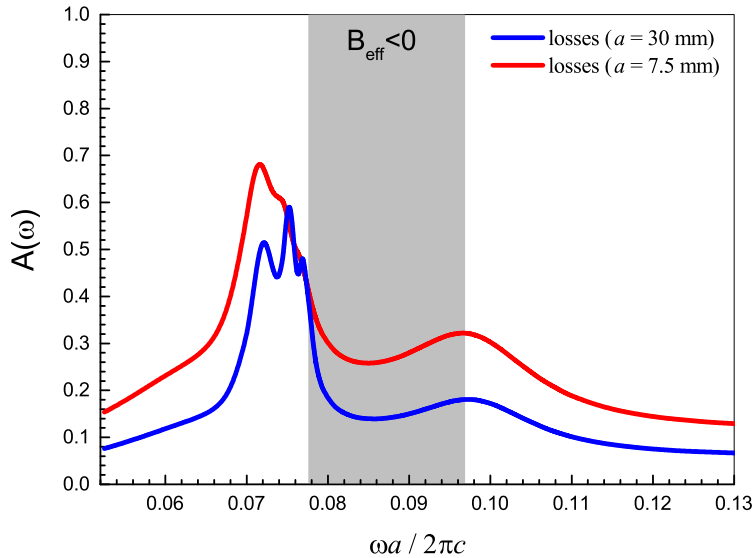

Figure 1.3. *Calculated spectra for the absorptance, $A(\omega)$, of the metamaterial shown in Figure 1.1. Both curves correspond to calculations with viscothermal losses but using structures with two different dimensions. Results obtained with the lattice period $a = 30$ cm (blue line) correspond to the sample studied in [GAR 12], while results obtained with $a = 7.5$ cm (red line) correspond to a scaled-down structure to one-fourth of the original dimensions. Frequencies are given in reduced units to represent both spectra in one plot. For a color version of this figure, see www.iste.co.uk/romero/metamaterials.zip*

It is shown in Figure 1.3 that the absorptance has two maxima: one in the region where the FP resonances are excited and another, located at about 0.096 reduced units, where the imaginary component of the effective modulus has a maximum. Thus, for this single-negative metamaterial, we can conclude that losses due to FP resonances are more efficient in dissipating the incoming energy than that produced by the monopole resonances that provoke the negative bulk modulus. This is not the case for the double-negative structures as explained in section 1.4.

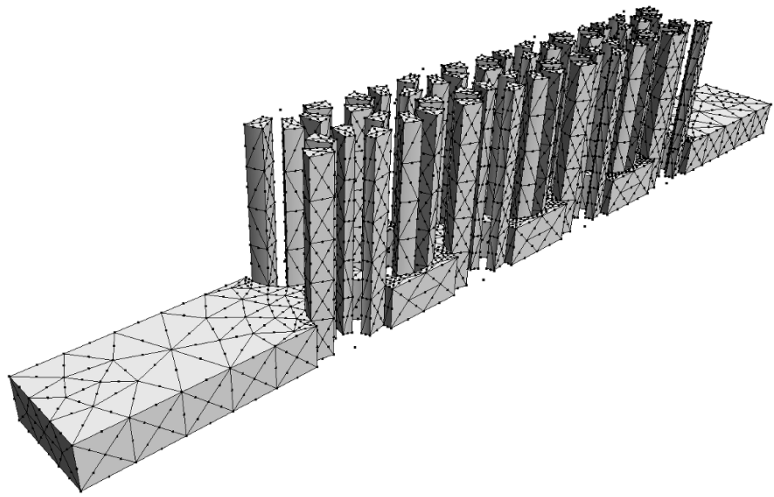

Figure 1.4. *Schematic view of the structure studied in [GRA 13] as an acoustic metamaterial with double-negative parameters. The BEM mesh consists of 4810 elements and contains 9616 nodes*

Regarding the dissipation loss Γ in the resonant elements, we have followed the standard described in previous works [FAN 06, GAR 12]. When no losses are considered, the fitting of B_{eff} obtained from our BEM simulations to the profile in equation [1.22] gives $\Gamma \approx 2\pi \times 0.022$. This value is smaller than confidence bounds and therefore it can be considered zero within the numerical tolerance of the BEM algorithm, as can be expected from the physical description. When losses are considered, $\Gamma \approx 2\pi \times 15.6$, for the full structure, it indicates that our simulation overestimated in about an order of magnitude the experimental data. For the structure scaled down to one-fourth, $\Gamma \approx 2\pi \times 127.3$, about an order of magnitude larger. This last result might lead to the conclusion that losses can be mitigated in metamaterials by using samples with larger dimensions. As we will discuss below, this is not the

case for a certain type of double-negative metamaterials, where an increase in their dimensions does not guarantee a significant decrease in the absorption.

1.4. Viscothermal effects in metamaterials with double-negative parameters

Metamaterials with negative mass density were earlier demonstrated using structures made of metallic spheres embedded in an epoxy matrix [LIU 00]. A few years later, the same group showed that an elastic membrane also provides a dipole resonance, producing a negative effective dynamical mass [YAN 08]. In a further advance, a composite medium consisting of a periodic array of interspaced membranes and side holes was introduced to show that double-negative mediums can be engineered [LEE 10]. In parallel, the demonstration that a 2D array of cylindrical holes behaves like a metamaterial with an effective bulk modulus negative [GAR 12] was soon accompanied by a theoretical proposal in which the negative mass density was simultaneously obtained by adding a specifically designed cylindrical inclusion [GRA 12]. However, its practical implementation was unable to demonstrate the double-negative behavior [GRA 13]. It is shown below that viscothermal losses is the reason justifying the disappearing of the expected property.

The double-negative metamaterial structure was simulated in [GRA 13] using an FEM implementation with linear elements. The BEM boundary mesh used here is shown in Figure 1.4 and it is constructed with quadratic triangular surface elements, which adapt better to the curved features of the structure than their linear versions.

Figure 1.5 shows the transmittance spectra calculated for the two cases of interest, with no losses (black line) and with viscothermal losses (blue line). The experimental data reported in [GRA 13] (symbols) is also depicted for comparison. When no losses are considered, note that the calculated spectrum exhibits FP peaks not only in the regions where the acoustic parameters are positive (i.e. below 2.33 kHz and above 3.7 kHz) but also in the regions where both parameters are negative, corresponding to the narrow frequency band from 2.33 kHz to 2.44 kHz. In both cases, the phase velocities are positive. On the contrary, for the single-negative regions, the transmittance is zero since the waves are evanescent. The FP peaks of the simulation with losses corresponding to the low- and high-frequency passbands are strongly attenuated due to viscothermal dissipation, and the resulting spectrum is in fair agreement with the experimental data. In addition, note that FP peaks corresponding to the double-negative passband completely disappear as a result of the losses. This calculation leads us to conclude that the disappearance of the double-negative band in the experimental spectrum is a consequence of viscothermal losses, which are strongly enhanced by the low group velocity in the band.

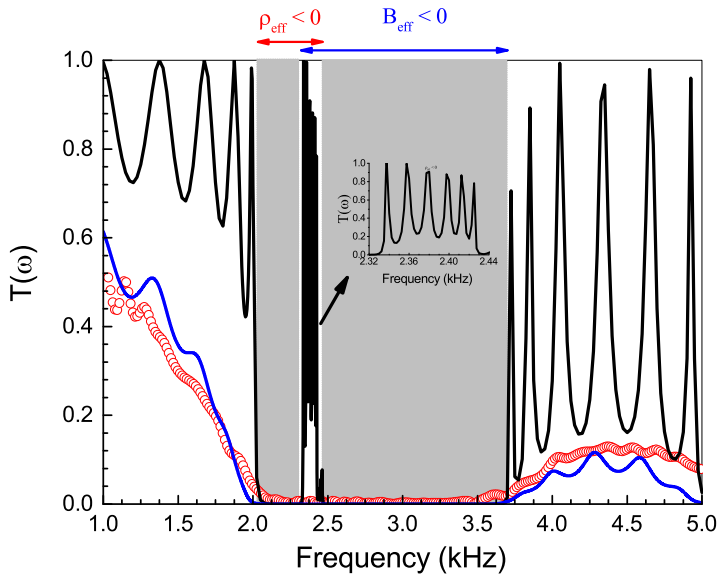

Figure 1.5. *Transmittance spectra (T) obtained for the double-negative metamaterial shown in Figure 1.4. Results corresponding to BEM simulations with no losses (black line) are compared with those including viscothermal losses (blue line). The symbols represent the experimental data. The gray strips indicate frequency regions with the single-negative behavior. The region in between the strips corresponds to the double-negative band, which is shown in the inset. For a color version of this figure, see www.iste.co.uk/romero/metamaterials.zip*

In order to further discuss this effect, Figure 1.6 shows the frequency dependence on the calculated absorptance. It is derived from the corresponding results for the reflectance and the transmittance, which are also displayed in the figure. It is observed that the absorptance has maxima at frequencies corresponding to the FP peaks in the transmittance. Moreover, below the first bandgap, the absorptance increases when approaching to the border of the band. We associate such increasing with the corresponding decreasing of the group velocity, which approaches to zero near the edge of the band. In other words, we should expect an enhancement of viscothermal losses when the propagating wave has a low velocity. This conclusion also applies to the double-negative band, whose dispersion relation is almost flat and, therefore, where the group velocity has extremely low values [CUT 17b]. In fact, the dissipation losses have paramount importance in the double-negative band since they produce a total suppression of the transmitted signal (dashed line in the lower panel). This extraordinary dissipation can be explained in terms of the monopole and dipole

resonances, simultaneously excited at the positions of the metamaterial building units. The excited resonances produce large oscillations of the pressure amplitude in the resonators and at the positions of the scatterers whose boundaries contain sharp corners and kinks. The strong viscothermal losses induced by these types of resonators and scatterers are even enhanced by the extraordinary small group velocity, which completely dissipates the energy of the transmitted wave inside the metamaterial slab.

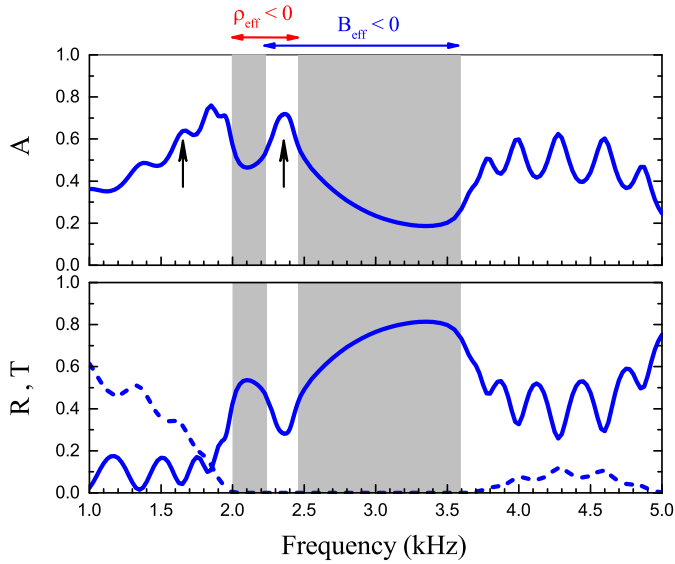

Figure 1.6. *Frequency dependence on the absorptance (A) of the double-negative metamaterial shown in Figure 1.4. Results corresponding to reflectance (R) and the transmittance (T, dashed) are also displayed for comparison. The region between gray strips defines the double-negative band. For a color version of this figure, see www.iste.co.uk/romero/metamaterials.zip*

To obtain a better physical insight of the phenomena discussed above, we have performed series of BEM simulations studying the transmission along the metamaterial slab at several frequencies. Particularly, we have comprehensively analyzed frequencies corresponding to FP resonances where the effects of losses are greatly enhanced. Two representative examples, corresponding to the frequencies indicated by arrows in Figure 1.6, are reported below.

Figures 1.7(a) and 1.7(b) present snapshots of a sound wave with frequency 1675 Hz propagating along the double-negative metamaterial structure shown in Figure 1.4. This frequency corresponds to a FP peak within the first passband; it is

defined by the left arrow in Figure 1.4. The black dots give the pressure values along the 2D waveguide. For a given position x, the dots represent different values of the pressure in the corresponding y-z plane; for example, inside the air cavities of the metamaterial or on the scattering units. The comparison of both plots indicates that the behavior of the propagating wave is basically the same for both cases, the main difference being a moderate reduction of the pressure levels in the structure when viscothermal losses are considered. According to Figure 1.6, about 4% of the impinging energy is reflected and about 34% finally arrives to the end of the metamaterial. Therefore, about 62% is dissipated by the structure due to viscothermal losses.

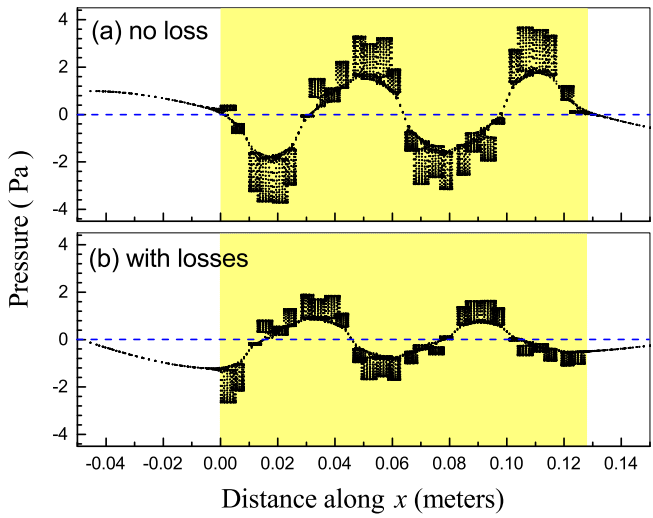

Figure 1.7. *Calculated pressure (in Pa) of a sound wave with frequency 1675 Hz that propagates along the structure shown in Figure 1.4. Results are obtained using a BEM implementation by considering: (a) no losses and (b) with viscothermal losses. The yellow zone defines the limits of the metamaterial slab. The horizontal dashed lines are guides for the eye, indicating the level of zero pressure*

The propagating behavior of a wave with frequency 2380 Hz is shown in Figures 1.8(a) and 1.8(b). This frequency, indicated by the right arrow in Figure 1.4, belongs to the narrow double-negative band. In comparison with the results obtained for the frequency belonging to the double-positive band, two main differences are noticeable. First, in the case of no losses, the pressure values inside the air cavities increase significantly due to the simultaneous excitation of the monopole and dipole resonances. And second, in the case of losses, it is observed that dissipation effects

suppress the traveling wave in just a couple of metamaterial rows. As previously discussed, this dramatic attenuation is a consequence of the viscothermal losses locally produced in the metamaterial units, which are strongly enhanced by the extremely low group velocity of the propagating wave.

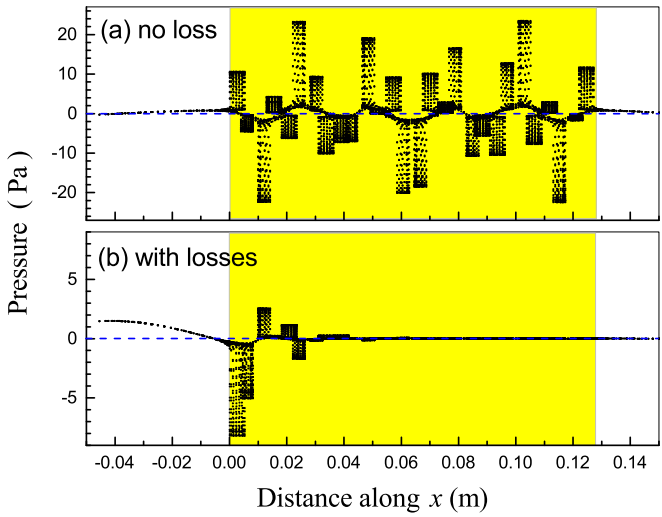

Figure 1.8. *Calculated pressure (in Pa) of a sound wave with frequency 2380 Hz that propagates along the structure shown in Figure 1.4. Results are obtained using a BEM implementation by considering: (a) no losses and (b) with viscothermal losses. Note the different vertical scaling. The yellow zone defines the limits of the metamaterial slab. The horizontal dashed lines are guides for the eye, indicating the level of zero pressure*

A course of action for avoiding the suppression of the transmitted signal for waves belonging to the double-negative band could be increasing the dimensions of the structure by scaling it up. It was previously shown that the single-negative structure studied in section 1.3 exhibited a lower absorptance with increasing dimensions of the sample. In addition, this behavior was practically independent of the frequency. This is particularly true for frequencies in the passbands, where the transmitted signal could be recovered by increasing the scale factor. For the double-negative material, an easy calculation indicates that the viscous boundary layer, δ_v, and the thermal boundary layer, δ_κ, are only 2.3% and 2.7%, respectively, of the minimum separation between building units in the metamaterial slab (1.8 mm). We can further reduce the thickness of the boundary layers in relation to the smallest separation between scatterers by simply applying a scale factor to all the dimensions.

To this end, BEM simulations are conducted for slabs with scale factors from 1 to 20, corresponding to effective lengths of the metamaterial slab from $D = 127.5$ mm to $D = 2.55$ m. In the case of no loss, the calculated profiles of the transmittance spectra are the same at any scale, but are shifted in frequency by the corresponding scale factor. However, when the viscothermal effects are included, the spectra do not scale in the same way due to the frequency dependence on the viscous and thermal boundary layers, which are inversely proportional to $\sqrt{f}$.

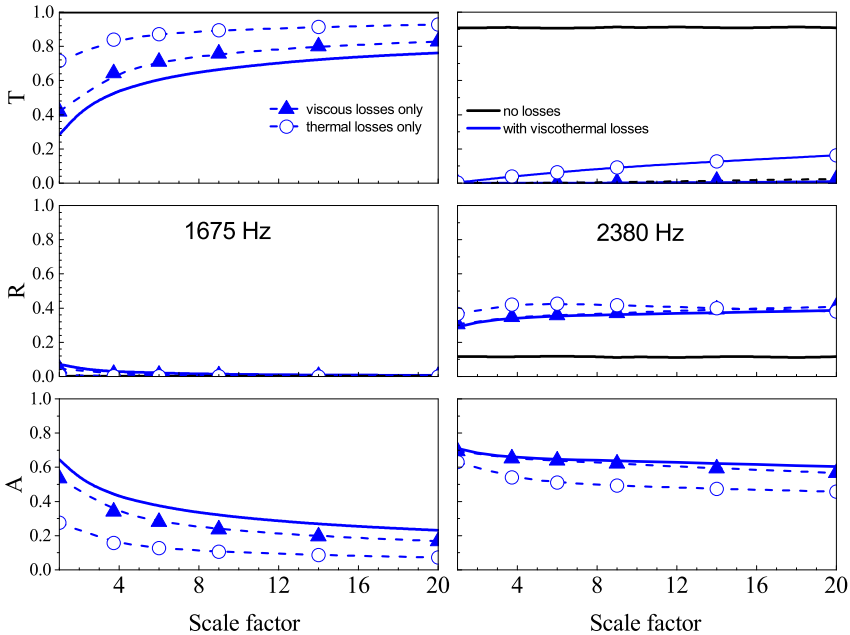

Figure 1.9. *Behavior of the transmittance (T), reflectance (R) and absorptance (A) as a funcion of the scale factor applied to the double-negative metamaterial shown in Figure 1.4. BEM simulations with viscothermal losses (blue lines) are compared with that obtained without losses (black lines). The left panels correspond to the frequency 1675 Hz, inside the first double-positive passband. The right panels corresponds to the frequency 2380 Hz, inside the double-negative band. The symbols define the separated contribution of viscous (circles) and thermal (triangles) losses. For the frequency 1675 Hz, corresponding to a FP peak, the case of no losses gives $T = 1$, $R = 0$ and $A = 0$, which are not shown in the plot*

Figure 1.9 reports the transmittance, reflectance and absorptance as a function of the scale factor applied to the structure shown in Figure 1.4. They are calculated at the two frequencies of interest here, 1675 Hz and 2388 Hz, corresponding to FP peaks inside the double-positive and double-negative passbands, respectively.

This figure also shows the corresponding results when only viscous losses (triangles) or thermal losses (circles) are considered. Two different behaviors are clearly observed. For the FP peak corresponding to 1675 Hz, the scale factor plays a fundamental role in order to reduce the absorptance due to losses; lower dissipation is obtained for larger sample dimensions. Consequently, the transmitted signal is greatly enhanced. It is also observed that viscous losses are the main cause of dissipation taking place in the structure. For the frequency of 2380 Hz, inside the double-negative band, it is shown that the absorption decreases very slowly; in fact, when the dimension increases in a factor of 20, the absorptance only decreases by 9%. The values of the transmittance also indicate that practically a 100% of the energy entering in the metamaterial is dissipated by viscothermal losses.

In summary, we have comprehensively studied the viscothermal effects on two different quasi-2D metamaterial structures. Results have been reported using a BEM numerical implementation of the problem including viscothermal losses, giving results similar to an FEM implementation but with lower computational effort. For the structure showing negative effective modulus [GAR 12], we have demonstrated that the influence of losses is small and is lower than that measured in other structures based on lattices of Helmholtz resonators embedded in water. Although the results are not strictly comparable, the structures analyzed, consisting of monopole resonances in drilled holes, seem to be appropriate to reduce the amount of losses. The single-negative behavior is reproduced even in the presence of losses. For the structure designed to exhibit effective bulk modulus and effective dynamical density both negative [GRA 12, GRA 13], we have shown that the presence of losses makes the observation of the properties associated with the double negativity unfeasible. In addition, we have determined that viscous losses is the main factor explaining the dissipation within this rigid material. Our simulations support the experimental findings, which showed the absence of any of the expected properties [GRA 13]. For this type of designed structures, the viscothermal losses are greatly enhanced due to the large pressure oscillation associated with the excitation of the monopole and dipole resonances, together with the extremely small group velocities of the traveling waves with frequencies within the double-negative band. It is proposed that any artificial structure aimed at having double-negative behavior should be designed taking into account viscothermal losses.

1.5. Acknowledgments

This chapter is based on work from COST Action DENORMS CA15125, supported by COST (European Cooperation in Science and Technology). J.S-D. acknowledge the partial support by the Ministerio de Economía y Competitividad of the Spanish Goverment and the European Union “Fondo Europeo de Desarrollo Regional (FEDER)” through project no. TEC2014-53088-C3-1-R.

1.6. References

[AND 18] ANDERSEN P.R., CUTANDA HENRÍQUEZ V., AAGE N. *et al.*, "A two dimensional acoustic tangential derivative boundary element method including viscous and thermal losses", *Journal of Theoretical and Computational Acoustics*, vol. 26, no. 3, 2018.

[BRU 87] BRUNEAU A.M., BRUNEAU M., HERZOG P. *et al.*, "Boundary layer attenuation of higher order modes in waveguides", *Journal of Sound and Vibration*, vol. 119, no. 1, pp. 15–27, 1987.

[BRU 89] BRUNEAU M., HERZOG P., KERGOMARD J. *et al.*, "General formulation of the dispersion equation in bounded visco-thermal fluid, and application to some simple geometries", *Wave Motion*, vol. 11, no. 5, pp. 441–451, 1989.

[CRE 82] CREMER L., MÜLLER H.A., *Principles and Applications of Room Acoustics* (Vol. 2, Section IV.7.8), Applied Science Publishers, 1982.

[CUM 07] CUMMER S.A., SCHURIG D., "One path to acoustic cloaking", *New Journal of Physics*, vol. 9, p. 45, 2007.

[CUM 16] CUMMER S., CHRISTENSEN J., ALÚ A., "Double-negative acoustic metamaterial based on quasi-two-dimensional fluid-like shells", *Nature Reviews Materials*, vol. 87, no. 4, p. 16001, 2016.

[CUT 10] CUTANDA HENRÍQUEZ V., JUHL P.M., "OpenBEM – An open source boundary element method software in acoustics", *Proceedings of the 39th International Congress on Noise Control Engineering*, Lisbon, Portugal, June 13–16, 2010, International Institute of Noise Control Engineering, Sociedade Portuguesa de Acustica, pp. 5796–5805, 2010.

[CUT 13] CUTANDA HENRÍQUEZ V., JUHL P.M., "Implementation of an acoustic 3D BEM with Visco-thermal losses", *Proceedings of the 42nd International Congress and Exposition on Noise Control Engineering*, Innsbruck, Austria, International Institute of Noise Control Engineering, pp. 1–8, September 15–18, 2013.

[CUT 17a] CUTANDA HENRÍQUEZ V., ANDERSEN P., JENSEN J. *et al.*, "A numerical model of an acoustic metamaterial using boundary element method including viscous and thermal losses", *Journal of Computational Acoustics*, vol. 25, no. 4, p. 1750006, 2017.

[CUT 17b] CUTANDA HENRÍQUEZ V., GARCÍA-CHOCANO V.M., SÁNCHEZ-DEHESA J., "Viscothermal losses in double negative acoustic metamaterials", *Physical Review Applied*, vol. 8, no. 1, p. 014029, 2017.

[CUT 18] CUTANDA HENRÍQUEZ V., ANDERSEN P.R., "A three-dimensional acoustic Boundary Element Method formulation with viscous and thermal losses based on shape function derivatives", *Journal of Theoretical and Computational Acoustics*, vol. 26, no. 3, 2018.

[FAN 06] FANG N., XI Z., XU J. *et al.*, "Ultrasonic metamaterials with negative modulus", *Nature Materials*, vol. 5, pp. 452–456, 2006.

[FOK 11] FOK L., ZHANG X., "Negative acoustic index metamaterial", *Physical Review B*, vol. 83, no. 4, p. 214304, 2011.

[FRE 13] FRENZEL T., BREHM J.D., BUCKMAN T. *et al.*, "Three-dimensional labyrinthine acoustic metamaterials", *Applied Physics Letters*, vol. 103, no. 11, p. 061907, 2013.

[GAR 12] García-Chocano V., Graciá-Salgado R., Torrent D. *et al.*, "Quasi-two-dimensional acoustic metamaterial with negative bulk modulus", *Physical Review B*, vol. 81, no. 18, p. 184102, 2012.

[GAR 14] García-Chocano V., Christensen J., Sánchez-Dehesa J., "Negative refraction and energy funneling by hyperbolic materials: An experimental demonstration in acoustics", *Physical Review Letters*, vol. 112, no. 14, p. 144301, 2014.

[GEU 09] Geuzaine C., Remacle J.-F., "A three-dimensional finite element mesh generator with built-in pre- and post-processing facilities", *International Journal for Numerical Methods in Engineering*, vol. 79, no. 11, pp. 1309–1331, 2009.

[GRA 12] Gracía-Salgado R., Torrent D., Sánchez-Dehesa J., "Double-negative acoustic metamaterial based on quasi-two-dimensional fluid-like shells", *New Journal of Physics*, vol. 14, no. 4, p. 103052, 2012.

[GRA 13] Graciá-Salgado R., García-Chocano V., Torrent D. *et al.*, "Negative mass density and density-near-zero acoustic metamaterial: Design and applications", *Physical Review B*, vol. 88, no. 12, p. 224305, 2013.

[HAB 16] Haberman M., Guild M.D., "Acoustic metamaterials", *Physical Today*, vol. 69, no. 4, pp. 42–44, 2016.

[JUH 93] Juhl P.M., The boundary element method for sound field calculations, PhD thesis, Report No. 55, Technical University of Denmark, Denmark, 1993.

[KOC 49] Kock W.E., Harvey F., "Refractive sound waves", *Journal of the Acoustical Society of America*, vol. 21, no. 5, pp. 471–481, 1949.

[LEE 10] Lee S., Park C., Seo Y. *et al.*, "Composite acoustic medium with simultaneously negative density and modulus", *Physical Review Letters*, vol. 104, no. 5, p. 054301, 2010.

[LI 04] Li J., Chan C.T., "Double negative acoustic metamaterials", *Physical Review E*, vol. 70, no. 4, p. 055602(R), 2004.

[LIA 12] Liang Z., Li J., "Extreme acoustic metamaterial by coiling up space", *Physical Review Letters*, vol. 108, no. 11, p. 114301, 2012.

[LIU 00] Liu Z., Zhang X., Mao Y. *et al.*, "Locally resonant sonic materials", *Science*, vol. 289, no. 4, p. 1734, 2000.

[MA 16] Ma G., Sheng P., "Acoustic metamaterials: From local resonances to broad horizons", *Science Advances*, vol. 2, no. 4, p. e1501595, 2016.

[MAL 04] Malinen M., Lyly M., Rå back P. *et al.*, "A finite element method for the modeling of thermo-viscous effects in acoustics", in Neittaanmki P., Rossi T., Majava K. *et al.* (eds), *Procceding 4th European Congress Computational Methods in Applied Sciences and Engineering*, Jyväskylä, Finland, June 24–28, 2004, University of Jyväskylä, Department of Mathematical Information Technology, 2004.

[MOL 16] Molerón M., Serra-García, Daraio C., "Visco-thermal effects in acoustic metamaterials: From total transmission to total reflection and high absorption", *New Journal of Physics*, vol. 18, p. 033003, 2016.

[MOR 68] Morse P.M., Ingard K.U., *Theoretical Acoustics*, McGraw Hill, Princeton, U.S.A., 1968.

[PIE 81] PIERCE A.D., *Acoustics. An introduction to its physical principles and applications (Ch. 10)*, McGraw Hill, New York, U.S.A., 1981.

[RAY 94] RAYLEIGH J.W.S., *The Theory of Sound*, Dover, U.S.A., 1894.

[STI 91] STINSON M.R., "The propagation of plane sound waves in narrow and wide circular tubes, and generalization to uniform tubes of arbitrary cross-sectional shape", *Journal of the Acoustical Society of America*, vol. 89, no. 2, pp. 550–558, 1991.

[THE 14] THEOCARIS G., RICHOUX O., ROMERO-GARCÍA V. *et al.*, "Limits of slow sound propagation and transparency in lossy, locally resonant periodic structures", *New Journal of Physics*, vol. 16, p. 093017, 2014.

[TOR 08] TORRENT D., SÁNCHEZ-DEHESA J., "Acoustic cloaking in two-dimensions: A feasible approach", *New Journal of Physics*, vol. 10, p. 063015, 2008.

[WU 00] WU T.W., *Boundary Element Acoustics*, WIT Press, 2000.

[XIE 13] XIE Y., POPA B.-I., ZIGONEANU L. *et al.*, "Measurement of a broadband negative index with space-coiling acoustic metamaterials", *Physical Review Letters*, vol. 110, no. 17, p. 175501, 2013.

[YAN 08] YANG Z., MEI M., CHAN C.T. *et al.*, "Membrane-type acoustic acosutic metamaterial with negative dynamic mass", *Physical Review Letters*, vol. 101, no. 4, p. 204301, 2008.

2

Locally Resonant Metamaterials for Plate Waves: the Respective Role of Compressional Versus Flexural Resonances of a Dense Forest of Vertical Rods

Recent experimental and numerical studies have shown that at the geophysics scale, locally resonant metamaterials have potential future applications to seismic engineering. To pursue investigations in geophysics with media that are mostly unknown and heterogeneous, more understanding is needed in terms of the interactions between surface waves with different polarization and the various types of resonance of a unit cell of a metamaterial. Benefiting from an analog experiment at the laboratory scale, this chapter revisits the interactions between plate Lamb waves and a cluster of long vertical rods – with easy-to-identify compressional and flexural resonances – attached to it. Through densely sampled spatial measurements, particular attention is paid to the analysis of the complex wavefield that results from this combination of resonances, on the dominant Lamb wave mode in the plate.

2.1. Introduction

Locally resonant metamaterials derive their effective properties from hybridization between their resonant unit cells and the incoming wave [ACH 13, CHR 12, COW 11, FAN 06, GUE 07, LEM 11, LEM 13, LER 09, LIU 00, PSA 02, RUP 14]. This phenomenon is well understood for waves that propagate in media where the unit cells respect the symmetry of the incident field

Chapter written by Martin LOTT and Philippe ROUX.

Fundamentals and Applications of Acoustic Metamaterials: From Seismic to Radio Frequency,
First Edition. Edited by Vicente Romero-García and Anne-Christine Hladky-Hennion.

[PEN 99, SMI 00]. However, in many systems, such as a set of vertical rods that interact with plate waves, or a pine tree forest that interacts with surface seismic waves, several modes with orthogonal symmetries can coexist at any given frequency, while the resonant unit cells themselves can support different types of resonance [RUP 15, RUP 17].

In this chapter, we revisit metamaterial physics at the mesoscopic scale. At the seismic scale, recent studies have demonstrated that trees can behave as seismic resonators with flexural and compressional resonances, whereby a forest of trees represents a seismic-scale candidate for a locally resonant metamaterial for surface waves [BRÛ 14, COL 14, COL 16a, COL 16b, COL 16c, ROU 18]. Spatial sampling in the METAFORET experimental configuration (for details, see: https://metaforet.osug.fr/) was performed with a dense array of geophones in and around a pine forest with a typical scale of the order of 100 m (Figure 2.1(a)). Mostly surface waves were excited by a vibrometer, with controlled and programmable source signals with horizontal and vertical polarizations that coupled with both flexural and compressional resonances. The goal of the experiment was to establish a link between seismic-relevant scales and microscale and mesoscale studies that pioneered the development of metamaterial physics in optics and acoustics. The main results of the METAFORET experiment were the presence of frequency bandgaps for Rayleigh waves associated with compressional and flexural resonances of the trees, which confirmed the strong influence that a dense collection of trees can have on the propagation of seismic waves [ROU 18].

However, the seismic experiment also indicated the need to better understand the respective roles of these resonances on the wavefield pattern in the context of metamaterial physics. We thus proceed by analogy in the current chapter, going back to the case at the laboratory scale, as a dense set of vertical rods attached to a plate with typical length now of the order of 1 m (Figure 2.1(b)). In the context of a locally resonant metamaterial, the plate-plus-rod system allows the study of the respective roles of flexural and compressional resonances on the hybridization of the plate waves, as these resonances induce a break in the orthogonality between the Lamb wave modes of the free plate.

The chapter is organized as follows. Section 2.2 describes the experimental set-up at the laboratory scale. In section 2.3, the field pattern issued from point-like sources located either inside or outside the metamaterial is analyzed and discussed in the framework of a simplified theoretical approach, where only one type of Lamb waves in the plate and one type of resonance of the rods (i.e. compressional resonance) are considered. The complete wavefield pattern is discussed in section 2.3, and the role of flexural resonances of the rods is magnified through different examples.

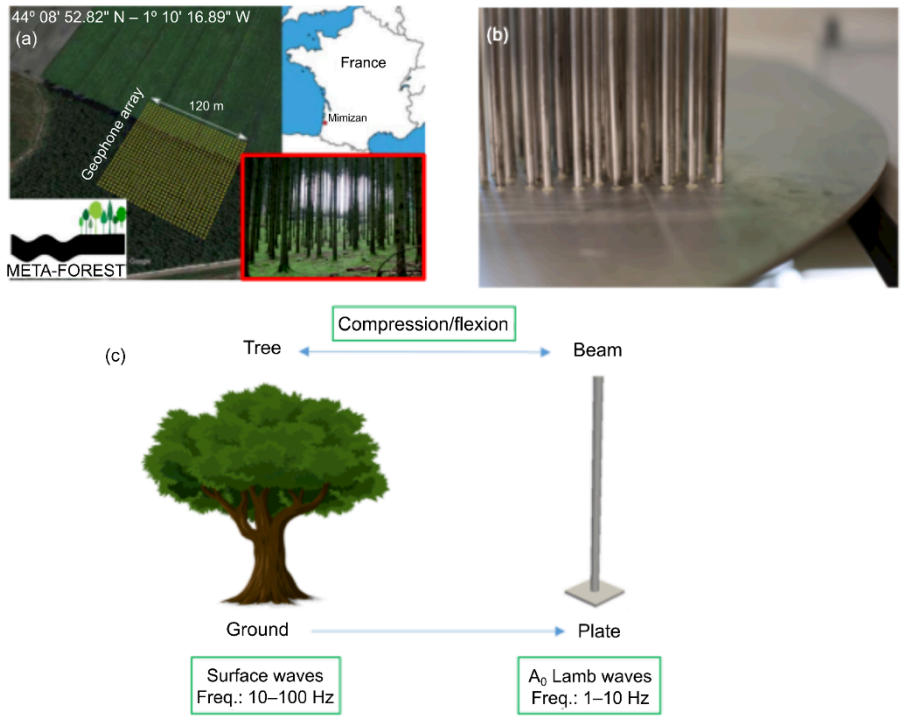

Figure 2.1. *Examples of locally resonant metamaterials at different scales for seismo-elastic waves. (a) Seismic deployment (yellow dot) at the interface between a free field and a dense pine tree forest. (b) Squared area of a random arrangement of vertical metallic rods glued to a thin aluminum plate. (c) Mechanical similitudes of the unit resonant cell for both systems, with their respective frequency bands of interest. For a color version of this figure, see www.iste.co.uk/romero/metamaterials.zip*

2.2. Experimental configuration of the metamaterial at the laboratory scale

Throughout this study, analogy is made between the METAFORET seismic experiment and this laboratory scale experiment, as a "forest" of 61 cm long, 6 mm diameter vertical rods attached to a thin metallic plate (Figure 2.1; for a more general description, see Roux *et al.* [ROU 17]). Unlike the seismic configuration, the rods and plate are made of the same material, which provides perfect coupling for wave propagation. At low frequencies (< 10 kHz), the 6 mm width plate supports two types of waves known as the symmetric and anti-symmetric modes, as S_0 and A_0 [ROY 00]. In practice, the A_0 waves are mostly vertically polarized and can be characterized by out-of-plane (vertical) displacement, while in-plane (horizontal)

displacements in the plate are described by the S_0 waves. A few point-like piezo sources located either inside or outside the metamaterial are attached to one side of the plate, and these mostly excite A_0 Lamb waves. The spatial arrangement of the rods is random, and the average distance d between rods is such that $10 < d/\lambda < 4$, where λ is the A_0 wavelength in the plate over the frequency band of interest.

With this experimental configuration, only the out-of-plane wavefield can be measured on the plate, through a motorized laser vibrometer that covers a large surface inside and outside the metamaterial area, as schematically shown in Figure 2.2. The received signals are highly dispersed because of reverberation at the plate boundaries. Attenuation in the metallic plate is low for the A_0 waves. The billiard-table shape of the plate makes the field spatially random after a few reverberations from the plate boundaries. As will be shown later, these reverberations are of great importance for both array analysis and frequency–time analysis of the received signals in the metamaterial.

This laboratory scale configuration allows us to carefully study the roles of the flexural and compressional resonances inside the forest of rods for the out-of-plane wavefield measured on the plate surface. In the [1 kHz, 10 kHz] frequency bandwidth, the wave propagation in the complex plate-plus-rod system deals with S_0 and A_0 modes in the free plate and two types of resonance – flexural and compressional resonances – that should mostly couple with the S_0 and A_0 waves, respectively.

In parallel with the experimental work, numerical simulations performed with three-dimensional elastic finite-element code in the plate-plus-rod metamaterial confirm that when a vertical force with out-of-plane polarization excites the 6 mm width metallic plate, there is almost no energy in the S_0 mode [COL 14]. This means that to a first approximation, the potential conversion of the excited A_0 waves to S_0 modes upon scattering of the resonating beams can be neglected in this plate-plus-rod configuration.

We expect things to be very different with a thinner (i.e. more flexible) plate, where both in-plane and out-of-plane wavefield components can be excited through bending and flexural moments at the interface between the plate and the rods. In such a case, both flexural and compressional resonances can modify the bandgap structure, which would require the addition of the in-plane component to the theoretical approach, as described by Colquitt *et al*. [COL 17].

In Figure 2.2(i), the spatially averaged Fourier spectra measured both outside and inside the disordered metamaterial reveal two wide bandgaps, which start at 2 kHz and 6 kHz. Rupin *et al*. [RUP 14] showed that the shape and intensity of the bandgaps are independent of the random organization of the rods. As expected, when calculated in the passband, the spectral intensity of the reverberated fields is similar inside and outside the metamaterial.

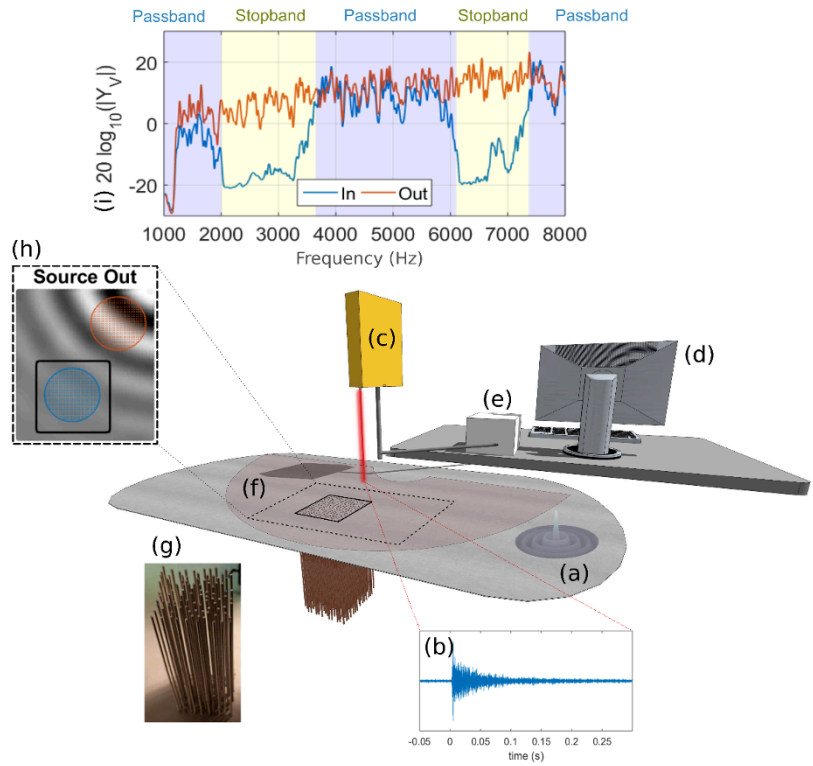

Figure 2.2. *Experimental set-up at the laboratory scale. A piezo-electric point-like source (a) generates A_0 Lamb waves in the aluminum plate. The particle velocity (b) is measured using an out-of-plane laser Doppler velocimeter (c) attached to a PC-controlled (d) motorized robot arm (e). The spatial cover of the robot onto the plate is shown in red (f). The metamaterial (g) is made of 100 vertical rods glued to the opposite side of the plate (black square). The Fourier analysis of the strongly reverberated wavefield (h) measured on the plate surface either inside (in blue) or outside (in red) the forest of rods shows both wide frequency passbands and stopbands where no energy penetrates inside the metamaterial (i). For a color version of this figure, see www.iste.co.uk/romero/metamaterials.zip*

2.3. Interpretation of dispersion curve restricted to the rod compressional resonances

Taking advantage of the spatially uniform two-dimensional sampling of the wavefield in the metamaterial region, the effective properties of the wave propagation of the A_0 Lamb waves inside the metamaterial were described by Rupin *et al.* [RUP 14] in the following way. Considering successive time windows associated

with long-term reverberations, and when filtered in a small bandwidth, the averaged spatial Fourier transforms of the field recorded inside the metamaterial revealed a circle, which confirms the equi-distribution of the wave components for all possible azimuthal directions. At each frequency, the circle radius gives an accurate measure of the effective velocity inside the metamaterial, from which the dispersion curve can be plotted (for more details, see Figure 6.6 in Roux *et al.* [ROU 17]).

In the present study, we proceed differently. We calculate the ensemble-averaged two-point correlation function $C(\omega, \mathrm{d}r)$ at pulsation ω, and for all possible receiving points separated by distance $\mathrm{d}r$ inside the metamaterial. The two-point correlation functions are calculated between points $\overrightarrow{r}$ and $\overrightarrow{r} + \mathrm{d}\overrightarrow{r}$ inside the metamaterial area:

$$C_T(\omega, \mathrm{d}\overrightarrow{r}) = \frac{\langle \Psi_T(\omega, \overrightarrow{r}) \Psi_T^*(\omega, \overrightarrow{r} + \mathrm{d}\overrightarrow{r}) \rangle_{\overrightarrow{r}}}{\langle \mid \Psi_T(\omega, \overrightarrow{r}) \mid^2 \rangle_{\overrightarrow{r}}}, \qquad [2.1]$$

where $\Psi_T(\omega, \overrightarrow{r})$ is the field measured from the laser vibrometer at pulsation ω for a finite-duration recorded window of duration ΔT, starting at time T. We then take advantage of the equi-distribution of the spatial wavefield inside the ergodic cavity-like plate, by averaging the two-point correlation over all azimuth θ:

$$C_T(\omega, \mathrm{d}\overrightarrow{r}) = \langle C_T(\omega, \mathrm{d}\overrightarrow{r}) \rangle_\theta. \qquad [2.2]$$

Finally, we also benefit from the long-term reverberation of the wavefield inside the plate to select as many time windows T as are available, each of which is interpreted as a different source realization for the two-point correlation function:

$$C(\omega, \mathrm{d}\overrightarrow{r}) = \langle C_T(\omega, \mathrm{d}\overrightarrow{r}) \rangle_T. \qquad [2.3]$$

Thus, the ensemble-averaged two-point correlation function results from three different averaging process: (1) from the set of positions (x, y) of all of the receiving points inside the metamaterial from which inter-distances $\mathrm{d}r$ are calculated; (2) from a set of five piezo-sources located outside the metamaterial area; and (3) from the long reverberation time T of the strongly reverberated wavefield inside the cavity. In practice, we choose $\Delta T = 10$ ms, which is small compared to the total reverberation time of the cavity (> 250 ms), and T expands from 10 ms (for the wave mixing to be sufficient) to 250 ms (where ambient noise starts to dominate).

The real part of the two-point correlation function $C(\omega, \mathrm{d}r)$ is plotted in Figure 2.3(a) at frequency $f = 5000$ Hz, and for all frequencies inside and outside the metamaterial in Figure 2.3(b, c). In Figure 2.3(b), the normalization coefficient calculated for the denominator of equation [2.1] is plotted (black line) from the

averaged intensity measured from all receiving points inside the metamaterial. This explains why it reaches higher values in the passband (where the wavefield propagates inside the metamaterial) than in the stopband (where almost no energy penetrates into the metamaterial).

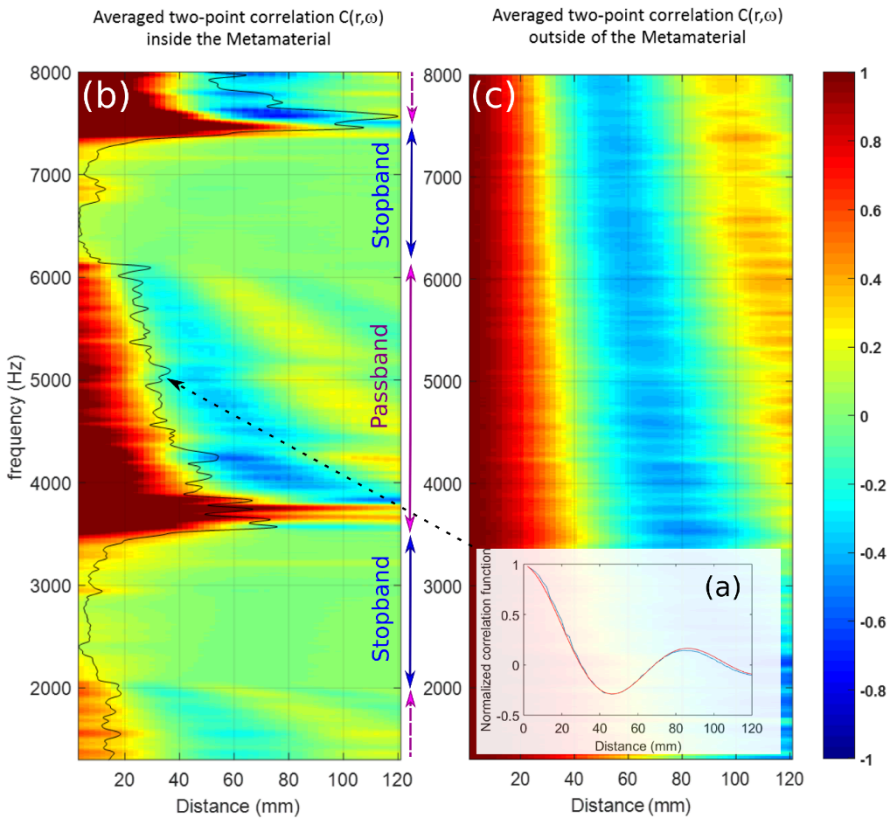

Figure 2.3. *(a) Real part of the averaged two-point correlation function (normalized) measured at 5 kHz for all of the receiver pairs located inside the metamaterial region (blue). The modeled plate Green's function is plotted in red. (b) Averaged two-point correlation versus frequency measured inside the metamaterial (c) and outside the metamaterial. The black line in (b) corresponds to the averaged intensity versus frequency measured inside the metamaterial. For a color version of this figure, see www.iste.co.uk/romero/metamaterials.zip*

We then model $C(\omega, \mathrm{d}r)$ calculated in the passbands with the two-dimensional Green's function for an infinite plate $G_0(\omega, \mathrm{d}r)$ defined from the Bessel and Hankel functions of the second kind [FAH 04] as:

$$C(\omega, \mathrm{d}r) \propto G_0(\omega, \mathrm{d}r) = H_0^{(2)}(k_B \mathrm{d}r) - i\frac{2}{\pi} K_0(k_B \mathrm{d}r), \qquad [2.4]$$

where $k_{eff} = \omega / c_{eff}$ is the effective propagating wavenumber of the A_0 waves with effective velocity $c_{eff} = \Re(c_{eff}) + i\Im(c_{eff})$. In practice, $\Re(c_{eff})$ corresponds to the effective velocity for wave propagation, and $\Im(c_{eff})$ is linked to the scattering attenuation (as the intrinsic attenuation is negligible here), and provides a measurement of the elastic mean free path $\frac{\mid c_{eff} \mid^2}{\omega \Im(c_{eff})}$, which is classically defined in a multiple scattering field theory as the attenuation of the coherent wavefield [DER 01a, DER 01b]. In Figure 2.4(a), the wave propagation properties in the passband of the metamaterial are summarized as a single dispersion curve (blue dots) computed as $\tilde{k}_{eff} = \Re(k_{eff}) = \frac{\omega \Re(c_{eff})}{\mid c_{eff} \mid^2}$. The dispersion relations of the A_0 Lamb mode calculated with the same procedure outside the metamaterial area are superimposed for comparison (purple dots). The mean free path l in the passband (not shown) is much larger than the effective wavelength, as $\tilde{k}_{eff} l \gg 1$, which confirms that no scattering attenuation pollutes the wavefield in this frequency band.

In recent years, we have developed an analytical approach to describe the physics properties of multi-resonant metamaterials for Lamb waves propagating in plates (see [WIL 15]). This theoretical approach neglects the in-plane wavefield component (which cannot be measured by the laser vibrometer) and the flexural resonance of the rods. The metamaterial consists of a 10×10 uniform, periodic array of long rods attached to the surface of a plate that forms the substrate in which anti-symmetric A_0 Lamb waves are excited. It was then shown that the A_0 Lamb wave propagation through the metamaterial can be accurately modeled using a simplified approach that replaces the two-dimensional array with an one-dimensional beam with a linear array of 10 rods. The wave propagation problem is solved rigorously for this one-dimensional system by formulating a scattering matrix at a single rod, found from the boundary conditions at the rod/beam interface, and including both evanescent and propagating waves in the beam. To predict the transmission through the linear array of rods, this scattering matrix is used to set up an eigenvalue problem, along with the boundary conditions between the adjacent unit cells. The eigenvalues are determined exactly, and then they are approximated to a long wavelength expansion to determine the simple expression for the effective wavenumber k_{eff} :

$$k_{eff} = k_p \left[\frac{M_b}{M} \frac{\tan(k_b L_b)}{k_b L_b} + 1 \right]^{1/4}. \qquad [2.5]$$

In equation [2.5], k_p is the A_0 wavenumber in the free plate, M_b is the total mass of a rod, and M is the mass of the $L \times L$ plate area, where $L = 2$ cm corresponds to the averaged inter-rod distance, with $M_b/M = 8.02$ in the present configuration. Finally, the rod length is $L_b = 61$ cm, and we have $k_b = \omega/c_b$ with c_b defined as the non-dispersive wave velocity in the rod, calculated from Young's modulus E_b and density ρ_b, such that $c_b = 5055$ m.s^{-1}.

The dispersion relation shows bending and anti-bending branches that are modeled through a tangential dependence on the rod length. Both the rod length and the additive mass on the plate drive the hybridization effect of this locally resonant metamaterial.

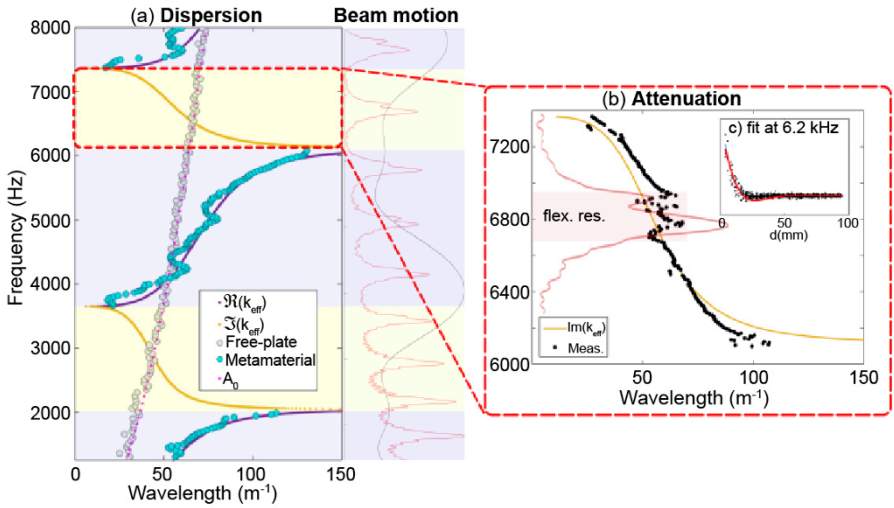

Figure 2.4. *Frequency–wavenumber representation of the plate-plus-rod system. (a) The dispersion curves are obtained for a source outside the metamaterial, and are computed from the averaged two-point correlation function inside (blue dots) and outside (gray dots) the metamaterial region. Theoretical results are represented with solid purple (passband) and yellow (stopband) lines. (b) The attenuation inside the second bandgap is computed from a source located within the metamaterial region. The inset shows the real part of the wavefield at frequency f = 6400 Hz for every receiver, as a function of the distance to the source. For a color version of this figure, see www.iste.co.uk/romero/metamaterials.zip*

In Figure 2.4(a), the modeled dispersion relation (purple line) is compared to the experimental dispersion curve (blue dots) inside the metamaterial, as calculated from

$C(\omega, \mathrm{d}r)$, with excellent agreement demonstrated. When the set of multi-resonant rods is restricted to compressional vibrations that have similar polarizations as the A_0 Lamb wave out-of-plane displacements in the plate, this produces two wide stopbands in the frequency domain from 0 kHz to 10 kHz. Note that the stopband and passband boundaries depend on the minima and maxima of the rod impedance (Figure 2.5(c)), calculated as a vertical force on the plate, as shown by Williams *et al*. [WIL 15]:

$$Z_b = -i\rho_b A_b c_b \tan(k_b L_b) \qquad [2.6]$$

where A_b is the cross-section of one rod.

To confirm this result, the rod response is measured at the tip of a single rod that is attached to the plate but isolated from the metamaterial (Figure 2.5(a)). One accelerometer is attached at the tip of the rod to measure the vertical displacement of the field inside the rod (black arrow). The flexural motion of the rod is measured using a laser vibrometer that is horizontally directed towards the rod tip (red arrow). A set of three accelerometers are glued to the plate at the bottom of the rod to deconvolve the plate motion from the rod response.

When excited by a piezo source attached to the plate in the far field, the rod response shows both low-Q compressional resonances measured from the vertical motion captured at the accelerometer, and high-Q flexural resonances measured from the horizontal motion recorded by the laser vibrometer (Figure 2.5(b)). COMSOL simulation was performed for a single rod attached to the free plate, and this provides the modal deformation both along the rod and on the plate at three frequencies close to the flexural or compressional resonances (Figure 2.5(d–f)). Two observations can be made from these numerical simulations. First, the modal deformations of the single rod in Figure 2.5(e, f) are in agreement with the forced free-impedance calculations (equation [2.6]) obtained in the framework of the theoretical approach (Figure 2.5(c)) led by Williams *et al*. [WIL 15], which confirms the point-like normal force behavior of each rod of the metamaterial on the plate at these frequencies. Second, the plate deformation is maximal at a frequency close to the start of the passband (i.e. compressional resonance; Figure 2.5(e)) and minimal at a frequency close to the start of the stopband (i.e. compressional anti-resonance; Figure 2.5(f)). When generalized to the metamaterial behavior, the plate would appear to be clamped (i.e. no displacement) at the start of the bandgap, and on the contrary, the plate would be allowed to move freely (i.e. maximum displacement) at the start of the passband. Again, this is in agreement with the general wave phenomena observed with the plate-plus-rod system.

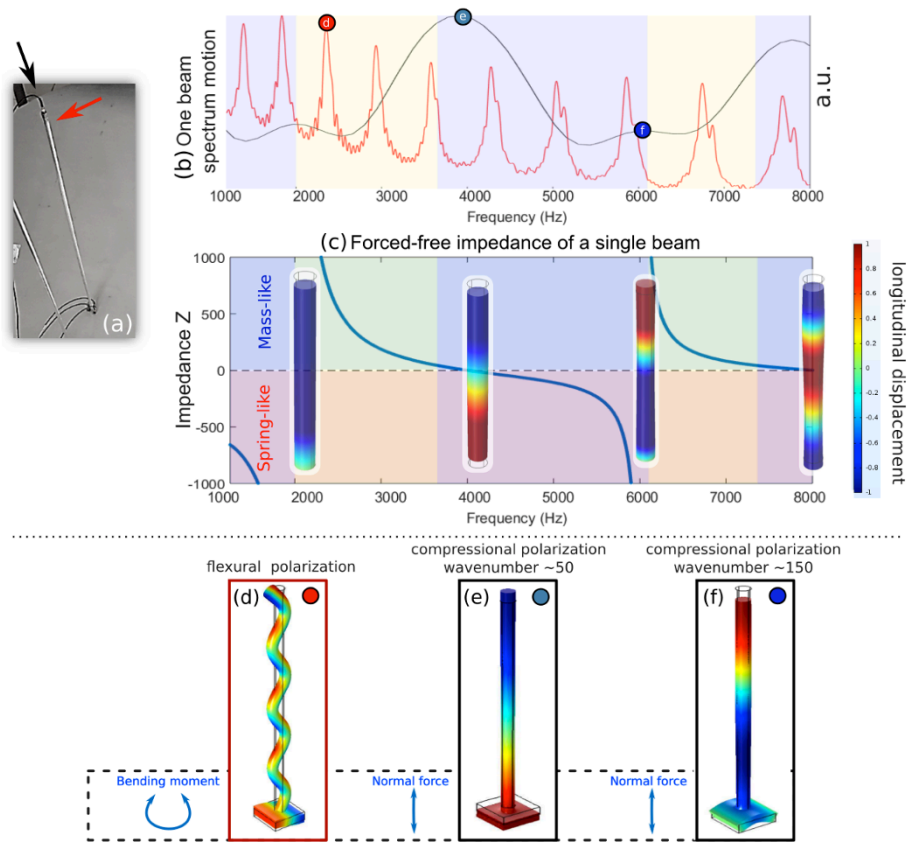

Figure 2.5. *Impedance and mechanical coupling of a single rod attached to the plate. (a) Instrumentation of a single rod for longitudinal (black arrow) and flexural (red arrow) motion. (b) Spectrum motion of a single rod, the out-of-plan motion is shown in black and the in-plan motion in red. (c) Driving point impedance calculation at the base of a single rod attached to the plate, when the rod displacement is limited to longitudinal (vertical) motion. (d–f) Bloch-waves polarization obtained from COMSOL simulation for a single rod attached to a plate, and extracted at different frequencies close to the compressional or flexural resonances. For a color version of this figure, see www.iste.co.uk/romero/metamaterials.zip*

When compared to the dispersion curve in Figure 2.4, we observe that the bandgap starts almost at the anti-resonance and ends almost at the resonance of the rod impedance, as expected from equation [2.5]. The "almost" here is determined by the distance between the beams (or more precisely, the average square root of the mean surface occupied by a beam in the metamaterial) and the mass of the beam M_b, through the M_b/M ratio in equation [2.5]. At the anti-resonance (Figure 2.5(e)), the

plate appears to be clamped by the collection of rods, and no motion is allowed in the metamaterial region, which defines the start of the bandgap. On the contrary, the plate motion induced by the bar is maximal at the resonance (Figure 2.5(d)), which means that the metamaterial no longer prevents the propagation of A_0 Lamb waves in the plate.

In a second step, the piezo source is placed at the center of the metamaterial to better understand and characterize the wave propagation in the frequency bandgap (Figure 2.6(a)). As shown in Figure 2.1, for a source outside the metamaterial, the average spectral intensity is computed over the whole frequency bandwidth for the source inside (Figure 2.6(b)). In the stopbands, the spectral intensity is now higher inside the metamaterial. Note also the presence of spectral peaks in the stopbands that correspond to the flexural resonances of the rods, the importance of which in the complete description of the plate-plus-rod system will be discussed in section 2.4.

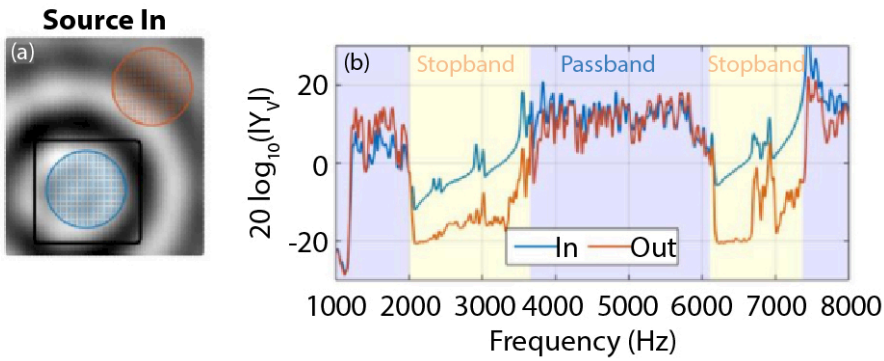

Figure 2.6. *Radiated field from the source inside the metamaterial (black square) together with where the energy averaging is performed (blue, red circles). (b) The averaged energy inside the metamaterial region (blue) and the averaged energy transmitted outside the metamaterial region (red). For a color version of this figure, see www.iste.co.uk/romero/metamaterials.zip*

In Figure 2.7, the field pattern is plotted at frequency $f = 6400$ Hz (inside the stopband, but distant from flexural resonance) when the source is located either outside or inside the metamaterial. For the source located outside the metamaterial (Figure 2.7(a)), the spatially uniform speckle pattern carries the footprint of the wavefield reverberation in the finite-size plate, and as expected, no field penetrates inside the metamaterial.

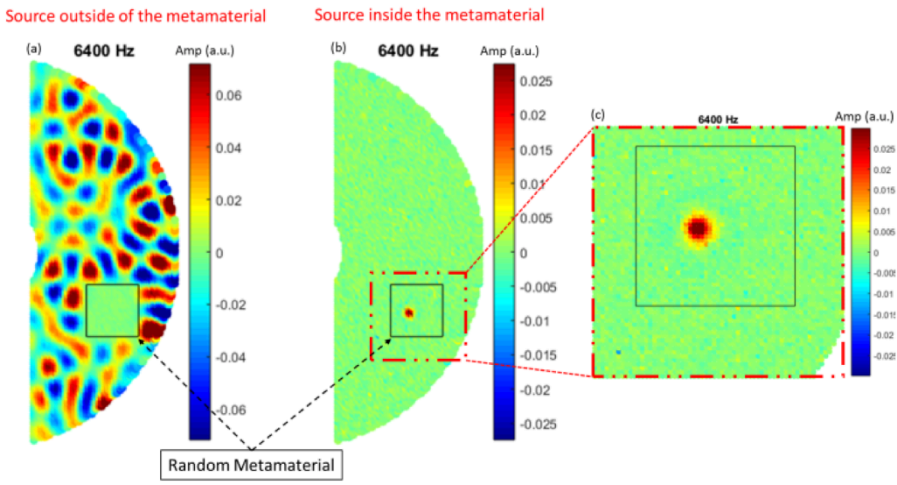

Figure 2.7. *Spatial representation of the Fourier transform (real part) of the wavefield at $f = 6400$ Hz. The spatial sampling in the x and y directions is 8 mm, and the source is located outside the metamaterial (black square). (b) As for (a), with the source inside the metamaterial. (c) New experiment restricted to the metamaterial region (red dashed square in (b)) with a source at the same position and a spatial sampling in the x and y directions of 4 mm. The source behaves as a monopole in the stopband. For a color version of this figure, see www.iste.co.uk/romero/metamaterials.zip*

This confirms the isotropic behavior of the metamaterial with a random distribution of rods at the subwavelength scale. When the source is located inside the metamaterial (Figure 2.7(b)), the wavefield intensity is trapped around the source position in r_0 as an evanescent wave, and as confirmed from the spectral intensity in Figure 2.6(b), no energy escapes from the metamaterial. A new experiment was performed with a finer spatial sampling, as in Figure 2.7(a, b) (Δx = $\Delta y = 8$ mm in Figure 2.7(a, b); $\Delta x = \Delta y = 4$ mm in Figure 2.7(c)) on a zone restricted to the metamaterial area (Figure 2.7(c)).

In Figure 2.4(c), the real part of the wavefield is plotted as a function of the distance to the source in r_0 at frequency $f = 6400$ Hz. In the absence of reverberation, this function is modeled as the two-dimensional Green's function for the plate, as calculated previously (equation [2.4]), with $dr = \mid \overrightarrow{r} - \overrightarrow{r}_0 \mid$. As evanescent waves dominate the wavefield around the source, we now have $\tilde{k}_{eff} l \sim 1$, which means that the attenuation length inside the metamaterial is larger than the wavelength of the propagating waves. In practice, Williams *et al.* [WIL 15] predicted

from their theoretical approach that $\tilde{k}_{eff} = |\ \Re(k_e ff)\ | = |\ \Im(k_{eff})\ |$ in the stopband, which is confirmed by our experimental results obtained with a source inside the metamaterial (Figure 2.4(b)). Note, however, that the presence of flexural frequencies disrupts the match of the experimental wavenumber results for $\tilde{k}_{eff}$ with the theoretical approach limited to A_0 Lamb waves interacting with compressional resonances.

2.4. The role played by flexural resonances of the rods

As the main physical properties of the locally resonant metamaterial have been explained from the coupling of the vertically polarized A_0 waves and compressional resonances in the rod, what might be the role of the flexural resonances in the complete description of the plate-plus-rod complex wave system? To define this, the same experiment was performed with a plate of width $h = 2$ mm (instead of $h = 6$ mm previously), with a finite bandwidth approach limited to the first bandgap between 0.5 kHz and 5 kHz (Figure 2.8). As the plate stiffness varies as h^3, the wavefield on the 2 mm plate is expected to be more sensitive to bending motions induced by the vertical rods on the plate [ROU 17, RUP 15]. This effect is clearly observed for the dispersion curve $\tilde{k}_{eff}$ measured inside the forest of rods attached to this plate with lower stiffness (Figure 2.8(b)). Sub-bending and sub-anti-bending branches are observed in the previously defined passbands (< 2 kHz, >4 kHz) at each flexural resonance of the rod, which means that the flexural motion of the rods can no longer be omitted from the interpretation of the dispersion curve. In a similar way, we also observe that flexural resonances lead to transmission bands inside the main bandgap, which means that waves can both penetrate and escape from the metamaterial region using the coupled in-plane/out-of-plane bending motion induced at the points where the rods are attached to the plate (Figure 2.5(d)).

These two effects are illustrated for the experimental results given in Figures 2.9 and 2.10. The wavefield at frequency $f = 6700$ Hz inside one stopband is shown in Figure 2.9(a, b) for two separate experiments with point-like sources located inside the metamaterial. In Figure 2.9(b), the source is located at the same position as in Figure 2.7(c). Compared to Figure 2.7(c), where only local evanescent waves were observed, the presence of a flexural resonance frequency of the rods at $f = 6700$ Hz (see Figure 2.5(b)) completely modifies the wavefield pattern. First, the wavefield is no longer trapped inside the metamaterial, and we observe some energy leakage outside the metamaterial, as expected from the averaged spectral density shown in Figure 2.6(b). Second, the wavefield around the source behaves as a dipole instead of a monople, as previously observed for the bandgap only 300 Hz away (Figure 2.7 (b, c)). This dipolar pattern is in agreement with the flexural deformation of the rods that is excited by evanescent waves emitted by the source inside the metamaterial that favor a bending motion of the plate (Figure 2.5(d)).

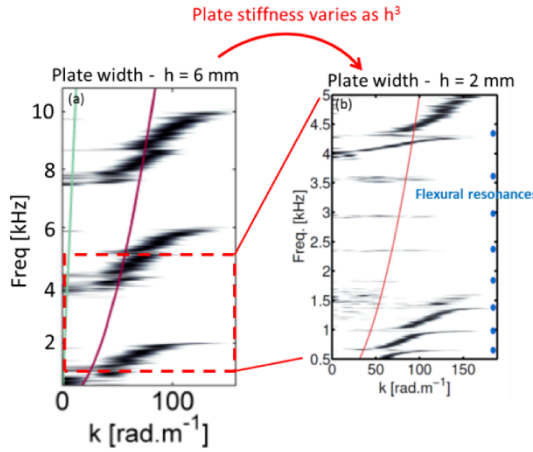

Figure 2.8. *Influence of plate stiffness on the coupling between the rods and the plate at flexural resonances. (a) Dispersion curve obtained experimentally with h = 6 mm wide plate. (b) As for (a), with an h = 2 mm wide plate on a restricted part of the frequency spectrum (red dashed square in (a)). For the thinner plate, the plate-plus-rod system shows a stronger interaction with the flexural resonances of the rods, inside and outside the frequency bandgaps. For a color version of this figure, see www.iste.co.uk/romero/metamaterials.zip*

No interpretation of the shape of the dipole can be given at this stage, as this probably depends on the local (but random) organization of the rods around the local source. Note that this dipolar pattern can be observed at each flexural resonance frequency of the rods inside the stopband. In other words, since the out-of-plane A_0 type mode is forbidden inside the metamaterial, the low-amplitude flexural waves locally excited by evanescent waves at the rod/plate interface can now be observed with an obvious propagation from rod to rod that finally results in a leakage outside the metamaterial region.

A similar effect is shown in Figure 2.10. The source is either located inside or outside the metamaterial (as in Figure 2.7), and we choose to display the wavefield at $f = 6125$ Hz, which corresponds to the start of the stopband (expected at $f_0 = 6190$ Hz according to the theoretical prediction of Williams *et al.* [WIL 15]). The wavefield intensity should be very low at this frequency, as attenuation dominates in this frequency band (Figure 2.4(b)) and the plate behaves as if it is clamped by the rod anti-resonance (Figure 2.5(e)). However, as there is one flexural resonance frequency of the rods nearby (Figure 2.5(b)), some of the energy still

penetrates into the metamaterial and traverses it from one side to the other. As shown in Figure 2.10(a), the energy flux into the metamaterial appears to be transported from rod to rod through evanescent waves generated at the rod/plate interface. Note, however, that these trapped waves are not observed approximately $f = 2050$ Hz at the start of the first stopband, where there is no flexural resonance frequency.

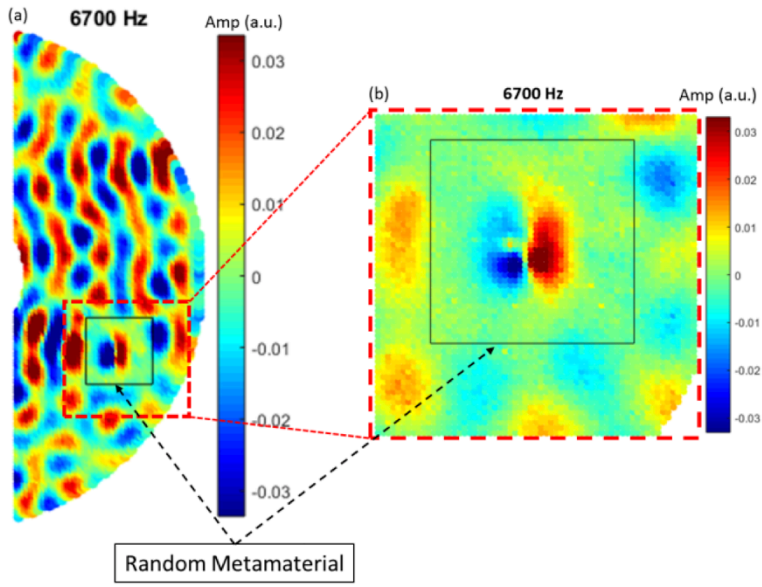

Figure 2.9. *Spatial representation of the Fourier transform (real part) of the wavefield at $f = 6700$ Hz. (a) The wavefield pattern shows energy leakage in a stopband through one flexural resonance. The source is located inside the metamaterial (black square) and the spatial sampling in the x and y directions is 8 mm. (b) New experiment restricted to the metamaterial region (red dashed square in (b)) with better spatial sampling (4 mm). The source behaves as a dipole at the flexural resonance of the rods. For a color version of this figure, see www.iste.co.uk/romero/metamaterials.zip*

When the source is located inside the metamaterial, exactly the same field pattern is measured (Figure 2.10(b)), which confirms that this localized mode can exist independent of the source excitation. In the past, similar localized modes have been observed for microwaves scattered by dense and random distributions of local dielectric scatterers [LAU 07, MOR 07]. These results appear to constitute the unambiguous signature of the existence of strongly localized modes in two-dimensional locally resonant metamaterials.

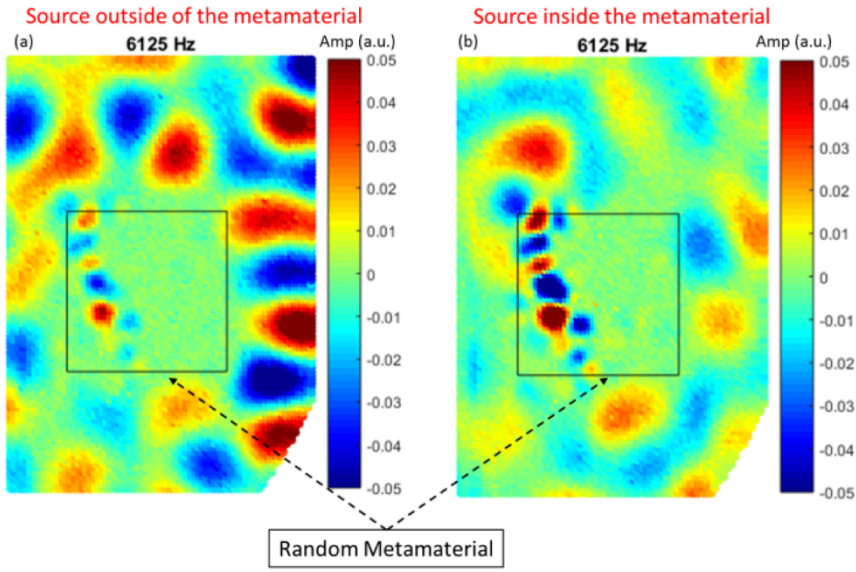

Figure 2.10. *Spatial representation of the Fourier transform (real part) of the wavefield at $f = 6125$ Hz. The wavefield pattern demonstrates energy leakage at the edge of a stopband at $f = 6125$ Hz for a source located either outside (a) or inside (b) the metamaterial. Note that the localized mode shape inside the metamaterial (black square) is independent of the source location. For a color version of this figure, see www.iste.co.uk/romero/metamaterials.zip*

Finally, in Figure 2.11, we investigate the time-domain effects related to the different quality factors of the flexural and compressional resonances of the rods. As shown in Figure 2.11(b) (green), compressional resonances have low Q-factors, which mean that they re-inject the energy that they capture on short time scales. Indeed, compressional resonances correspond to a vertical velocity in the rod that easily couples with the vertically polarized A_0 Lamb mode in the plate. On the contrary, flexural resonances show high Q-factors (Figure 2.11(c), green), which means that flexural vibrations are trapped in the rod for longer times before this energy is fully radiated back into the plate. Time–frequency analysis of the signals recorded inside the metamaterial confirms these results. The spectrogram in Figure 2.11(a) shows, for example, that at late recording times, there is still higher wavefield intensity around flexural resonances. Moreover, when the dispersion curve is calculated for a finite duration time window in the early part of the recordings, we retrieve the dispersion curve associated with compressional resonances, as described in Figure 2.4(a). However, when the dispersion curve is computed from the same time window shifted to a later reverberation time, the role of the flexural resonances

becomes dominant, in agreement with the theoretical predictions from Colquitt *et al.* [COL 17] for a full-elastic plate-plus-rod system (Figure 2.5(b, c), blue and red dotted lines).

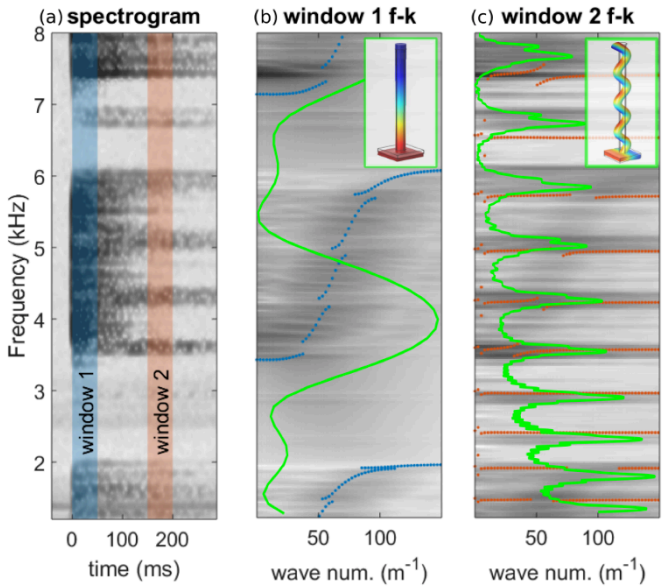

Figure 2.11. *Frequency–time dependence showing the rod resonance contributions to the wavefield. (a) Spectrogram of a signal recorded inside the metamaterial region. (b) Spatial Fourier transform of the wavefield at an early time of propagation (blue colored time window 1 in (a)). The blue dotted line is the predicted dispersion relation for the out-of-plane polarization. (c) Spatial Fourier transform of the wavefield for the late reverberation time (red colored time window 2 in (a)). The red dotted line is the predicted dispersion relation for the in-plane polarization. The associated compressional or flexural motions of the rods are shown in green and are superimposed on the selected time windows, together with relevant examples of modal deformation. For a color version of this figure, see www.iste.co.uk/romero/metamaterials.zip*

This frequency–time analysis helps to separate the effects due to compressional resonances from those due to flexural ones. For example, approximately $f = 6125$ Hz, the energy leakage inside the metamaterial (Figure 2.10(a)) mostly appears after 100 ms of propagation, which represents the time needed to load the high quality factor of the flexural resonance. On the contrary, the monopole created by the source inside the metamaterial at approximately 6400 Hz (Figure 2.7(b)) is instantaneous, and so it should be associated with the low quality factor compressional resonance.

2.5. Conclusion

In this chapter, we have experimentally revisited the multimodal interactions of an aluminum beam "forest" glued on a thin elastic plate. This multi-resonant medium is a laboratory scale analog of a real forest, which can behave as a seismic metamaterial. For both systems, the resonant cell supports compressional or flexural resonant modes, which interact differently on the wave substrate. Studying the laboratory system gives some clues to the mechanical signature of such a system.

For longitudinal resonances, the driving point impedance of a single rod dictates the homogenized behavior of the aluminum forest. The bandgap and the highly dispersive curve inside the passband are the two main features of this metasurface. Using different source locations inside and outside the rod forest helps to quantify these effects. On top of this behavior, the high quality factor flexural resonances add some disturbances, like bandgap leakage with outlandish spatial distribution of the energy.

Finally, the time dependence of the system is studied through short window analysis of the reverberating coda. Directly related to the quality factor of each resonance, we have shown that the hybridization of the flexural waves inside the metamaterial evolves over space and time.

2.6. References

[ACH 13] ACHAOUI Y., LAUDE V., BENCHABANE S. *et al.*, "Local resonances in phononic crystals and in random arrangements of pillars on a surface", *Journal of Applied Physics*, vol. 114, no. 10, p. 104503, AIP, 2013.

[BRÛ 14] BRÛLÉ S., JAVELAUD E., ENOCH S. *et al.*, "Experiments on seismic metamaterials: Molding surface waves", *Physical Review Letters*, vol. 112, no. 13, p. 133901, APS, 2014.

[CHR 12] CHRISTENSEN J., DE ABAJO F.J.G., "Anisotropic metamaterials for full control of acoustic waves", *Physical Review Letters*, vol. 108, no. 12, p. 124301, APS, 2012.

[COL 14] COLOMBI A., ROUX P., RUPIN M., "Sub-wavelength energy trapping of elastic waves in a metamaterial", *The Journal of the Acoustical Society of America*, vol. 136, no. 2, pp. EL192–EL198, ASA, 2014.

[COL 16a] COLOMBI A., COLQUITT D., ROUX P. *et al.*, "A seismic metamaterial: The resonant metawedge", *Scientific Reports*, vol. 6, p. 27717, Nature Publishing Group, 2016.

[COL 16b] COLOMBI A., GUENNEAU S., ROUX P. *et al.*, "Transformation seismology: Composite soil lenses for steering surface elastic Rayleigh waves", *Scientific Reports*, vol. 6, p. 25320, Nature Publishing Group, 2016.

[COL 16c] COLOMBI A., ROUX P., GUENNEAU S. *et al.*, "Forests as a natural seismic metamaterial: Rayleigh wave bandgaps induced by local resonances", *Scientific Reports*, vol. 6, p. 19238, Nature Publishing Group, 2016.

[COL 17] COLQUITT D., COLOMBI A., CRASTER R. *et al.*, "Seismic metasurfaces: Sub-wavelength resonators and Rayleigh wave interaction", *Journal of the Mechanics and Physics of Solids*, vol. 99, pp. 379–393, Elsevier, 2017.

[COW 11] COWAN M.L., PAGE J.H., SHENG P., "Ultrasonic wave transport in a system of disordered resonant scatterers: Propagating resonant modes and hybridization gaps", *Physical Review B*, vol. 84, no. 9, p. 094305, APS, 2011.

[DER 01a] DERODE A., TOURIN A., FINK M., "Random multiple scattering of ultrasound. I. Coherent and ballistic waves", *Physical Review E*, vol. 64, no. 3, p. 036605, APS, 2001.

[DER 01b] DERODE A., TOURIN A., FINK M., "Random multiple scattering of ultrasound. II. Is time reversal a self-averaging process?", *Physical Review E*, vol. 64, no. 3, p. 036606, APS, 2001.

[FAH 04] FAHY F., WALKER J., *Advanced Applications in Acoustics, Noise and Vibration*, CRC Press, Boca Raton, 2004.

[FAN 06] FANG N., XI D., XU J. *et al.*, "Ultrasonic metamaterials with negative modulus", *Nature Materials*, vol. 5, no. 6, p. 452, Nature Publishing Group, 2006.

[GUE 07] GUENNEAU S., MOVCHAN A., PÉTURSSON G. *et al.*, "Acoustic metamaterials for sound focusing and confinement", *New Journal of Physics*, vol. 9, no. 11, p. 399, IOP Publishing, 2007.

[LAU 07] LAURENT D., LEGRAND O., SEBBAH P. *et al.*, "Localized modes in a finite-size open disordered microwave cavity", *Physical Review Letters*, vol. 99, no. 25, p. 253902, APS, 2007.

[LEM 11] LEMOULT F., FINK M., LEROSEY G., "Acoustic resonators for far-field control of sound on a subwavelength scale", *Physical Review Letters*, vol. 107, no. 6, p. 064301, APS, 2011.

[LEM 13] LEMOULT F., KAINA N., FINK M. *et al.*, "Wave propagation control at the deep subwavelength scale in metamaterials", *Nature Physics*, vol. 9, no. 1, p. 55, Nature Publishing Group, 2013.

[LER 09] LEROY V., STRYBULEVYCH A., SCANLON M. *et al.*, "Transmission of ultrasound through a single layer of bubbles", *The European Physical Journal E*, vol. 29, no. 1, pp. 123–130, Springer, 2009.

[LIU 00] LIU Z., ZHANG X., MAO Y. *et al.*, "Locally resonant sonic materials", *Science*, vol. 289, no. 5485, pp. 1734–1736, American Association for the Advancement of Science, 2000.

[MOR 07] MORTESSAGNE F., LAURENT D., LEGRAND O. *et al.*, "Direct observation of localized modes in an open disordered microwave cavity", *Acta Physica Polonica – Series A General Physics*, vol. 112, no. 4, pp. 665–672, Panstwowe Wydawnictwo Naukowe (PWN), 2007.

[PEN 99] PENDRY J.B., HOLDEN A.J., ROBBINS D.J. *et al.*, "Magnetism from conductors and enhanced nonlinear phenomena", *IEEE Transactions on Microwave Theory and Techniques*, vol. 47, no. 11, pp. 2075–2084, IEEE, 1999.

[PSA 02] PSAROBAS I., MODINOS A., SAINIDOU R. *et al.*, "Acoustic properties of colloidal crystals", *Physical Review B*, vol. 65, no. 6, p. 064307, APS, 2002.

[ROU 17] ROUX P., RUPIN M., LEMOULT F. *et al.*, "New trends toward locally-resonant metamaterials at the mesoscopic scale", in MAIER S.A. (ed.), *Handbook of Metamaterials and Plasmonics*, vol. 2, World Scientific, 2017.

[ROU 18] ROUX P., BINDI D., BOXBERGER T. *et al.*, "Toward seismic metamaterials: The METAFORET project", *Seismological Research Letters*, vol. 89, no. 2A, pp. 582–593, Seismological Society of America, 2018.

[ROY 00] ROYER D., DIEULESAINT E., *Elastic Waves in Solids I: Free and Guided Propagation*, trans. by MORGAN D.P., Springer-Verlag, New York, 2000.

[RUP 14] RUPIN M., LEMOULT F., LEROSEY G. *et al.*, "Experimental demonstration of ordered and disordered multiresonant metamaterials for Lamb waves", *Physical Review Letters*, vol. 112, no. 23, p. 234301, APS, 2014.

[RUP 15] RUPIN M., ROUX P., LEROSEY G. *et al.*, "Symmetry issues in the hybridization of multi-mode waves with resonators: An example with Lamb waves metamaterial", *Scientific Reports*, vol. 5, p. 13714, Nature Publishing Group, 2015.

[RUP 17] RUPIN M., ROUX P., "A multi-wave elastic metamaterial based on degenerate local resonances", *The Journal of the Acoustical Society of America*, vol. 142, no. 1, pp. EL75–EL81, ASA, 2017.

[SMI 00] SMITH D.R., PADILLA W.J., VIER D. *et al.*, "Composite medium with simultaneously negative permeability and permittivity", *Physical Review Letters*, vol. 84, no. 18, p. 4184, APS, 2000.

[WIL 15] WILLIAMS E.G., ROUX P., RUPIN M. *et al.*, "Theory of multiresonant metamaterials for A_0 Lamb waves", *Physical Review B*, vol. 91, no. 10, p. 104307, APS, 2015.

3

Slow Sound and Critical Coupling to Design Deep Subwavelength Acoustic Metamaterials for Perfect Absorption and Efficient Diffusion

The control of both the absorption and the diffusion of sound constitutes two prominent research lines in audible acoustics. The acoustic absorbers and diffusers developed up to now are efficient in the high frequency range with sizes comparable to the wavelength of the working frequency. On the contrary, in the low frequency regime, huge dimensions leading to oversized treatments and high manufacture costs arise. In this chapter, we discuss acoustic metamaterials showing efficient absorption and diffusion at low frequencies with a deep subwavelength size. On the one hand, by exploiting the slow sound effect, the resonance frequencies of the system can be shifted down to the low frequency range and the phase shift of the reflection coefficient can be perfectly tuned. On the other hand, the critical coupling conditions are introduced to achieve a perfect impedance matching allowing perfect absorption conditions. We will show in detail both an ultra-thin absorber and ultra-thin diffusers working in the low frequency regime.

3.1. Introduction

Acoustics metamaterials have recently revolutionized the field of acoustics and mechanics due to their extraordinary functionalities giving rise to breakthroughs in the material design strategy. Common wall treatments are made of flat panels with poor efficiency at low frequencies to attenuate, absorb or diffuse acoustic waves.

Chapter written by Vicente ROMERO-GARCÍA, Noé JIMÉNEZ and Jean-Philippe GROBY.

Fundamentals and Applications of Acoustic Metamaterials: From Seismic to Radio Frequency,
First Edition. Edited by Vicente Romero-García and Anne-Christine Hladky-Hennion.

In order to be efficient at low frequencies, we have to solve a complex problem: reducing the geometric dimensions of the structure while increasing the density of states at low frequencies and finding the good conditions to match or tune the acoustic impedance.

Acoustic metamaterials have been proposed as a successful approach for increasing the density of states at low frequencies with reduced dimensions. Recently, several possibilities based on these systems have been used to design sound absorbing structures or efficient diffusers which can simultaneously present subwavelength dimensions and very good efficiency. On the one hand, the design of subwavelength structures can be achieved by using different strategies. One of them consists of using space-coiling structures [CAI 14, LI 16]. Another way is to use subwavelength resonators as membranes [YAN 08, MEI 12] or Helmholtz resonators (HRs) [MER 15, ACH 16]. Recently, a new type of subwavelength metamaterial based on the concept of slow sound propagation has been used for the same purpose [GRO 15, GRO 16]. This last type of metamaterial makes use of its strong dispersion for generating slow sound conditions inside the material [THE 14] and, therefore, drastically decreasing working frequency. Hence, the structure thickness becomes deeply subwavelength. On the other hand, the impedance matching of such open, lossy and resonant structures can be achieved by the well-known critical coupling condition [ROM 16b, JIM 17b, JIM 18, BLI 08]. These open systems, at the resonant frequency, are characterized by both the leakage rate of energy (i.e. the coupling of the resonant elements with the propagating medium) and the intrinsic losses of the resonator. The balance between the leakage and the losses activates the condition of critical coupling, trapping the energy around the resonant elements and generating a maximum of energy absorption. In the case of transmission systems, degenerate critically coupled resonators with symmetric and antisymmetric resonances should be used to perfectly absorb the incoming energy by trapping the energy in the resonant element, i.e. without reflection or transmission [PIP 14, YAN 15]. In the case of a purely reflecting system, either symmetric or antisymmetric resonances that are critically coupled can be used to obtain perfect absorption of energy by a perfect trapping of energy around the resonators [MA 14, ROM 16a].

In this chapter, we discuss two types of acoustic metamaterial, both based on slow sound and critical coupling conditions, showing efficient absorption [JIM 16a, JIM 17d, JIM 17c] and diffusion [JIM 17a] at low frequencies with a deep subwavelength size. In both cases, the system will consist of a 2D flat panel composed of a periodic distribution of slits loaded by a finite array of HR. By exploiting the slow sound effect, the resonance frequencies of the system can be shifted down to the low frequency range and the phase shift of the reflection coefficient can be perfectly tuned. On the contrary, the critical coupling conditions are introduced to achieve a perfect impedance matching allowing perfect absorption conditions. We will show in detail both an ultra-thin absorber and ultra-thin diffusers both working in the low frequency regime.

3.2. Building block of the acoustic metamaterial: finite slit loaded with Helmholtz resonators

We consider a 2D flat panel composed of a periodic distribution of slits of width h separated a distance d and distributed in the x_1 direction as shown in Figure 3.1(a). Each slit is loaded by a finite array of M Helmholtz resonators (HRs) separated with lattice constant (distance between HRs) a. The HRs considered in this work can be either 2D (Figure 3.1(b)), made of a combination of slits with a squared cross-sectional neck and a cavity with length and width dimensions $l_{\mathbf{n}}$ and $w_{\mathbf{n}}$, $l_{\mathbf{c}}$ and $w_{\mathbf{c}}$ respectively; or 3D (Figure 3.1(c)), made of square cross-sectional tubes, with neck and cavity widths w_n and w_c, and lengths l_n and l_c respectively. The system made by the slit with the loaded HRs (Figure 3.1(d)) is considered as the building block of the acoustic metamaterial described in this chapter.

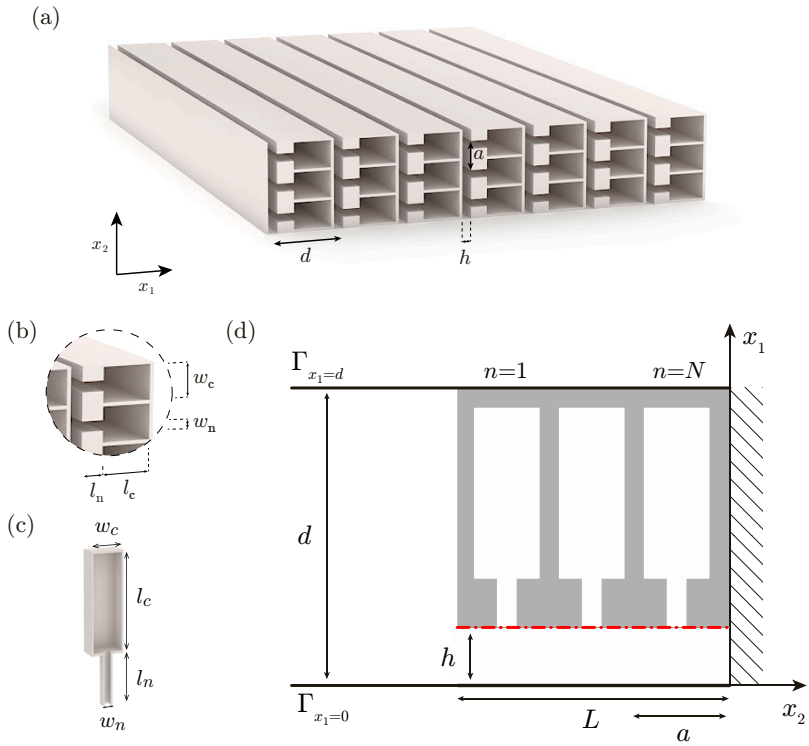

Figure 3.1. *(a) Conceptual view of the thin panel placed on a rigid wall with three layers of 2D Helmholtz resonators. (b) and (c) Conceptual views of 2D and 3D HRs respectively. (d) Scheme of the unit cell of the panel composed of a set of N Helmholtz resonators. Symmetry boundary conditions are applied at boundaries $\Gamma_{x_1=d}$ and $\Gamma_{x_1=0}$*

3.2.1. *Theoretical modeling: transfer-matrix method*

The transfer matrix is used to relate the sound pressures and normal acoustic particle velocities at the beginning and at the end of each unit cell. The transfer matrix of the n-th unit cell, $\mathbf{T}^n$, of length L, extending from $x_2 = 0$ to $x_2 = L$ is written as

$$\begin{bmatrix} P^n \\ V^n \end{bmatrix}_{y=0} = \mathbf{T}^n \begin{bmatrix} P^n \\ V^n \end{bmatrix}_{y=L} = \begin{bmatrix} T_{11}^n & T_{12}^n \\ T_{21}^n & T_{22}^n \end{bmatrix} \begin{bmatrix} P^n \\ V^n \end{bmatrix}_{y=L} . \quad [3.1]$$

For an identical set of M resonators, the transfer matrix $\mathbf{T}^n$ is written as

$$\mathbf{T}^n = \begin{bmatrix} T_{11}^n & T_{12}^n \\ T_{21}^n & T_{22}^n \end{bmatrix} = \mathbf{M}_{\Delta l_{\text{slit}}}^n \left(\mathbf{M}_{\mathbf{s}}^n \mathbf{M}_{\text{HR}}^n \mathbf{M}_{\mathbf{s}}^n\right)^M .$$

Here, the transfer matrix for each lattice step in the n-th slit, $\mathbf{M}_{\mathbf{s}}^n$, is written as

$$\mathbf{M}_{\mathbf{s}}^n = \begin{bmatrix} \cos\left(k_{\mathbf{s}}^n \frac{a}{2}\right) & iZ_{\mathbf{s}}^n \sin\left(k_{\mathbf{s}}^n \frac{a}{2}\right) \\ \frac{i}{Z_{\mathbf{s}}^n} \sin\left(k_s^n \frac{a}{2}\right) & \cos\left(k_{\mathbf{s}}^n \frac{a}{2}\right) \end{bmatrix}, \quad [3.2]$$

where the slit characteristic impedance is written as $Z_{\mathbf{s}}^n = \sqrt{\kappa_{\mathbf{s}}^n \rho_{\mathbf{s}}^n}/S_{\mathbf{s}}^n$ and $S_{\mathbf{s}}^n$ is equal to h^n in the 2D HRs and equal to $h^n\, a$ in the 3D HRs. The resonators are introduced as punctual scatters by a transfer matrix $\mathbf{M}_{\text{HR}}^n$ as

$$\mathbf{M}_{\text{HR}}^n = \begin{bmatrix} 1 & 0 \\ 1/Z_{\text{HR}}^n & 1 \end{bmatrix}, \quad [3.3]$$

and the radiation correction of the n-th slit to the free space as

$$\mathbf{M}_{\Delta l_{\text{slit}}}^n = \begin{bmatrix} 1 & Z_{\Delta l_{\text{slit}}}^n \\ 0 & 1 \end{bmatrix}, \quad [3.4]$$

with the characteristic radiation impedance of the n-th slit $Z_{\Delta l_{\text{slit}}}^n = -i\omega \Delta l_{\text{slit}}^n \rho_0/\phi_t^n S_0$, where S_0 is equal to d for 2D and equal to $d\, a$ for 3D, ρ_0 is the air density and Δl_{slit}^n is the proper end correction that will be described later.

The reflection coefficient of the rigidly backed slit can be directly calculated from the elements of the matrix $\mathbf{T}^n$ as

$$R^n = \frac{T_{11}^n - Z_0 T_{21}^n}{T_{11}^n + Z_0 T_{21}^n}. \qquad [3.5]$$

with $Z_0 = \rho_0 c_0 / S_0$, and finally the absorption as $\alpha^n = 1 - |R^n|^2$.

Finally, the effective parameters of each slit can be obtained from the transfer-matrix elements as follows:

$$k_{\text{eff}}^n = \frac{1}{L}\cos^{-1}\left(\frac{T_{11}^n + T_{22}^n}{2}\right), \quad Z_{\text{eff}}^n = \sqrt{\frac{T_{12}^n}{T_{21}^n}}. \qquad [3.6]$$

In the case of different HRs, the total transfer matrix of the whole system can be obtained by the product of the transfer matrices of each layer of the material. Thus, the total transfer-matrix method of the system is given by

$$\mathbf{T}^n = \begin{bmatrix} T_{11}^n & T_{12}^n \\ T_{21}^n & T_{22}^n \end{bmatrix} = \mathbf{M}_{\Delta l_{\text{slit}}}^n \prod_{m=1}^{M} \left(\mathbf{M}_{\mathbf{s}}^n \mathbf{M}_{\text{HR}}^{n,m} \mathbf{M}_{\mathbf{s}}^n\right).$$

where the matrix $\mathbf{M}_{\text{HR}}^{n,m}$ is calculated for each m resonator in each n slit.

3.2.1.1. *Viscothermal losses model*

The viscothermal losses in the system are considered in both the HRs and in the slits by using its effective complex and frequency-dependent parameters. Considering that only plane waves propagate inside the metamaterial, the effective parameters of the ducts that conform 2D resonators and the slits of width w are given by [STI 91]:

$$\rho_{\text{eff}} = \rho_0 \left[1 - \frac{\tanh\left(\frac{w}{2}G_\rho\right)}{\frac{w}{2}G_\rho}\right]^{-1}, \qquad [3.7]$$

$$\kappa_{\text{eff}} = \kappa_0 \left[1 + (\gamma - 1)\frac{\tanh\left(\frac{w}{2}G_\kappa\right)}{\frac{w}{2}G_\kappa}\right]^{-1}, \qquad [3.8]$$

with $G_\rho = \sqrt{i\omega\rho_0/\eta}$ and $G_\kappa = \sqrt{i\omega \text{Pr}\rho_0/\eta}$, and where γ is the specific heat ratio of air, P_0 is the atmospheric pressure, Pr is the Prandtl number, η is the dynamic viscosity, ρ_0 is the air density and $\kappa_0 = \gamma P_0$ is the air bulk modulus. The effective parameters of the n-th main slit, $\rho_{\mathbf{s}}^n$ and $\kappa_{\mathbf{s}}^n$, are obtained by setting $w = h^n$ in equations [3.7–3.8]. The viscothermal losses inside the two-dimensional resonators neck and cavity are modeled in the same way by these effective parameters, $\rho_{\mathbf{n}}^{n,m}$,

$\kappa_{\mathbf{n}}^{n,m}$ and $\rho_{\mathbf{c}}^{n,m}$, $\kappa_{\mathbf{c}}^{n,m}$ respectively, by setting $w = w_{\mathbf{n}}^{n,m}$ and $w = w_{\mathbf{c}}^{n,m}$ for the m-th resonator located at the n-th slit.

In the case of 3D HRs, the propagation in a rectangular cross-sectional tube can be described by its complex and frequency-dependent density and bulk modulus, and considering that plane waves propagate inside can be expressed as [STI 91]:

$$\rho_t = -\frac{\rho_0 a^2 b^2}{4G_\rho^2 \sum_{k\in\mathbb{N}} \sum_{m\in\mathbb{N}} \left[\alpha_k^2\beta_m^2\alpha_k^2 + \beta_m^2 - G_\rho^2\right]^{-1}}\,, \qquad [3.9]$$

$$\kappa_t = \frac{\kappa_0}{\gamma + \frac{4(\gamma-1)G_\kappa^2}{a^2b^2} \sum_{k\in\mathbb{N}} \sum_{m\in\mathbb{N}} \left[\alpha_k^2\beta_m^2\alpha_k^2 + \beta_m^2 - G_\kappa^2\right]^{-1}}\,, \qquad [3.10]$$

with the constants $\alpha_k = 2(k+1/2)\pi/a$ and $\beta_m = 2(m+1/2)\pi/b$, and the dimensions of the duct a and b being either the neck, $a = b = w_n$ or the cavity, $a = b = w_c$ of the HRs.

3.2.1.2. *Resonator impedance and end corrections*

Using the effective parameters for the neck and cavity elements given by equations [3.7–3.8], the impedance of a Helmholtz resonator, including a length correction due to the radiation can be written as [THE 14]:

$$Z_{\mathrm{HR}}^{n,m} = -\imath \frac{c_n c_c - Z_n k_n \Delta l c_n s_c/Z_c - Z_n s_n s_c/Z_c}{s_n c_c/Z_n - k_n \Delta l s_n s_c/Z_c + c_n s_c/Z_c}\,, \qquad [3.11]$$

where $c_n = \cos(k_n l_n)$, $c_c = \cos(k_c l_c)$, $s_n = \sin(k_n l_n)$, $s_c = \sin(k_c l_c)$ in which note superscripts were omitted for the sake of simplicity. $l_{\mathbf{n}}^{n,m}$ and $l_{\mathbf{c}}^{n,m}$ are the neck and cavity lengths, $k_{\mathbf{n}}^{n,m}$ and $k_{\mathbf{c}}^{n,m}$ are the effective wavenumbers, $Z_{\mathbf{n}}^{n,m}$ and $Z_{\mathbf{c}}^{n,m}$ are the effective characteristic impedance in the neck and cavities respectively, and $\Delta l^{n,m}$ is the correction length for the HRs. These correction lengths are deduced from the addition of two correction lengths $\Delta l^{n,m} = \Delta l_1^{n,m} + \Delta l_2^{n,m}$ as

$$\Delta l_1^{n,m} = 0.41\left[1 - 1.35\frac{w_{\mathbf{n}}^{n,m}}{w_{\mathbf{c}}^{n,m}} + 0.31\left(\frac{w_{\mathbf{n}}^{n,m}}{w_{\mathbf{c}}^{n,m}}\right)^3\right] w_{\mathbf{n}}^{n,m}\,, \qquad [3.12]$$

$$\Delta l_2^{n,m} = 0.41\Big[1 - 0.235\frac{w_{\mathbf{n}}^{n,m}}{w_{\mathbf{s}}^{n}} - 1.32\left(\frac{w_{\mathbf{n}}^{n,m}}{w_{\mathbf{s}}^{n}}\right)^2 + 1.54\left(\frac{w_{\mathbf{n}}^{n,m}}{w_{\mathbf{s}}^{n}}\right)^3 - 0.86\left(\frac{w_{\mathbf{n}}^{n,m}}{w_{\mathbf{s}}^{n}}\right)^4\Big] w_{\mathbf{n}}^{n,m}\,. \qquad [3.13]$$

The first length correction, $\Delta l_1^{n,m}$, is due to pressure radiation at the discontinuity from the neck duct to the cavity of the Helmholtz resonator [KER 87], while the second correction, $\Delta l_2^{n,m}$, comes from the radiation at the discontinuity from the neck to the principal waveguide [DUB 99]. This correction only depends on the radius of the waveguides, so it becomes important when the duct length is comparable to the radius, i.e. for small neck lengths and for frequencies where $k_{\mathbf{n}}^{n,m} w_{\mathbf{n}}^{n,m} \ll 1$.

Another important end correction comes from the radiation from the slits to the free air. The radiation correction for a periodic distribution of slits can be expressed as [MEC 08]:

$$\Delta l_{\text{slit}}^n = h^n \sigma^n \sum_{n=1}^{\infty} \frac{\sin^2\left(n\pi\sigma^n\right)}{\left(n\pi\sigma^n\right)^3}. \qquad [3.14]$$

with $\sigma^n = h^n/d$. Note for $0.1 \leq \sigma^n \leq 0.7$, this expression reduces to $\Delta l_{\text{slit}}^n \approx -\sqrt{2}\ln\left[\sin \pi\sigma^n/2\right]/\pi$.

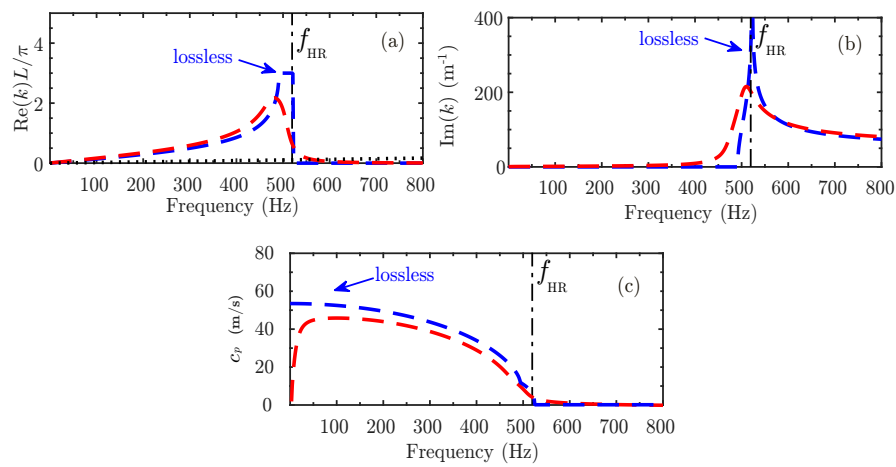

Figure 3.2. *(a) and (b) Real and imaginary parts of the dispersion relation calculated by the TMM for a metamaterial with parameters $h = 1.2$ mm, $a = 1.2$ cm, $w_n = a/6$, $w_c = a/2$, $d = 7$ cm, $l_n = d/3$ and $l_c = d - h - l_n$. Blue lines represent the lossless case, while red lines represent the lossy case. Black dotted lines represent the dispersion relation of the main slit without HRs. (c) Phase speed calculated by TMM for the lossless case (blue) and including thermo-viscous losses (red). For a color version of this figure, see www.iste.co.uk/romero/metamaterials.zip*

3.2.2. *Infinite main slit: dispersion relation and slow sound effect*

We first consider the dispersion properties inside the unit cell. In order to do that we consider a unit cell made of an infinite number of resonators with periodicity a. In this case, by applying periodic boundary conditions in a single periodicity of the unit cell, we can evaluate the dispersion relation inside the main slit with the presence of the resonators. Figure 3.2(a) and (b) show the real and imaginary parts of the dispersion relation calculated by the TMM for both the lossless and lossy cases. The first feature of this dispersion relation is that a bandgap can be observed above the resonant frequency of the HRs, f_{HR}. Below the resonance frequency of the HRs, a dispersive band is observed and the wavenumber is increased with respect to the wavenumber in air. Note also that the maximum wavenumber inside the slit is limited by the discreteness to the value $k_{\max} = \pi N/L$, as shown by the TMM calculations (dashed blue curve in Figure 3.2(b)). Interestingly, the imaginary part of this dispersion relation in the lossy case becomes important around the resonance frequency even in the case where the real part of the dispersion relation is not in the bandgap. However, the losses are less important when we are far from the resonant frequency of the HRs, f_{HR}.

Figure 3.2(c) shows the real part of the phase velocity in the slit, calculated both in the lossless and lossy cases. In this regime, slow sound conditions are produced due to the strong dispersion introduced by the resonators. In the lossless case, zero phase velocity can be observed for frequencies just below f_{HR}. In the lossy case, the losses limit the minimum value of the group velocity [THE 14]; however, in our system, slow sound velocity can be achieved in the dispersive band below f_{HR}. The average sound speed in the low frequency range is much lower (50 m/s) than the speed of sound in air (black dotted line in the main slit).

3.2.3. *Finite slits*

In reality, the unit cells used in the analyzed acoustic metamaterials will be of finite size, therefore, in general we will use the scattering matrix of the unit cells in order to study the scattering properties of the system. In particular, in the problems analyzed in this chapter, i.e. in the reflection problems, the reflection coefficient which represents the scattering coefficient of the system is of particular interest. In this section, we show the different possibilities for tuning this reflection coefficient with finite unit cells.

3.2.3.1. *Managing the amplitude of the reflection coefficient: critical coupling condition*

In the complex frequency plane, the reflection coefficient has pairs of zeros and poles that are complex conjugates one from another in the lossless case. In the $\exp(-\imath\omega t)$ sign convention, the zeros are located in the positive imaginary plane. The imaginary part of the complex frequency of the poles of the reflection coefficient represents the energy leakage of the system into the free space [ROM 16a]. Once the intrinsic losses are introduced in the system, the zeros of the reflection coefficient move downwards to the real frequency axis [ROM 16b]. For a given frequency, if the intrinsic losses perfectly balance the energy leakage of the system, a zero of the reflection coefficient is exactly located on the real frequency axis and therefore perfect absorption, $\alpha = 1 - |R|^2 = 1$, can be obtained. This condition is known as the critical coupling [ROM 16a, ROM 16b, BLI 08, PIP 14, YAN 15, MA 14].

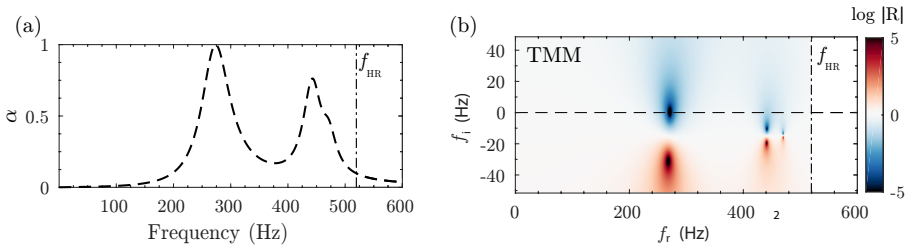

Figure 3.3. *(a) Absorption of a panel made of $N = 3$ resonators calculated by the TMM. The dashed-dotted line marks the resonant frequency of the HRs. (b) Complex frequency planes of the reflection coefficient calculated by TMM where f_r and f_i are the real and imaginary parts of the complex frequency respectively. For a color version of this figure, see www.iste.co.uk/romero/metamaterials.zip*

Figure 3.3(a) shows the absorption predicted by the TMM when the geometry of the system has been tuned to introduce the exact amount of intrinsic losses that exactly compensates the energy leakage of the system at 275 Hz for $N = 3$. In this situation, as shown in Figure 3.3(b), the lower frequency zero is located on the real axis, leading to a peak of perfect absorption. In addition, as we have $N = 3$ resonators, two other secondary peaks of absorption are observed at higher frequencies, for example 442 Hz and 471 Hz. Their corresponding zeros are located close to the real axis and, although the critical coupling condition is not exactly fulfilled, high absorption values can be observed at these frequencies. By using these concepts of slow sound and critical coupling, we theoretically and experimentally show in section 3.3 the possibilities of an acoustic metamaterial panel with deep subwavelength thickness for perfect and omnidirectional absorption.

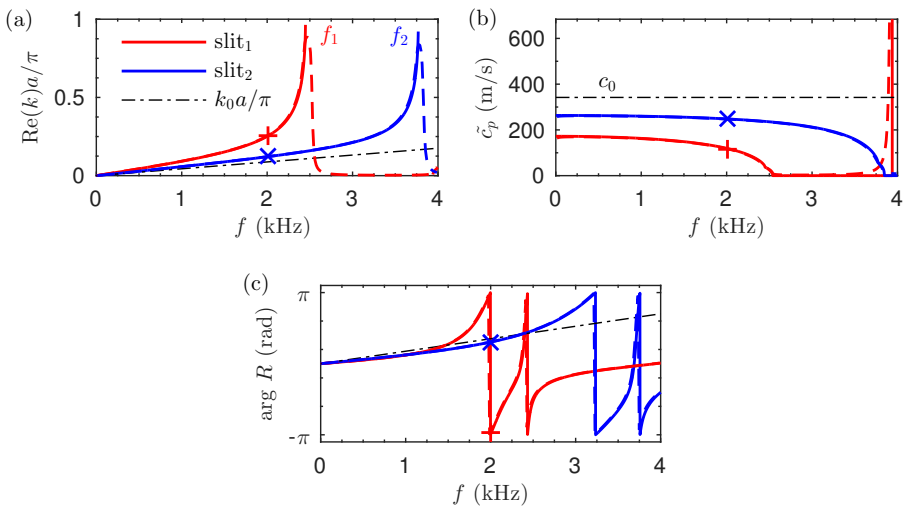

Figure 3.4. *(a) Dispersion relation inside the (blue) first and (red) second slits of a metadiffuser for the lossless case (continuous lines) and accounting for the thermo-viscous losses (dashed lines), and wavenumber in air (dashed-dotted). The resonance frequencies of the HR are shown as f_1 and f_2. (b) Corresponding phase speed. (c) Phase of the reflection coefficient for each individual slit. Image reproduced from [JIM 17a]. For a color version of this figure, see www.iste.co.uk/romero/metamaterials.zip*

3.2.3.2. *Managing the phase of the reflection coefficient*

Figure 3.4(a) shows the dispersion relations inside two different slits, $n = 1$ and $n = 2$, obtained by using HRs with the geometrical parameters listed in Table 3.2. Far from the resonance frequency, at the frequency marked by the symbols in Figure 3.4(a) and (b), the effect of losses is negligible as seen in the previous section 3.2.2. If now we consider a finite slit made of $M = 2$ resonators, due to the different slow sound velocity in the different slit, the phase of the reflection coefficient of each slit can be easily tuned by modifying the properties of the HRs. The phase of the reflection coefficient produced by each finite slit is shown in Figure 3.4(c). We can see that for some frequencies, the phase of the reflection coefficient of both slits (blue and red lines) is strongly modified when compared to the reflection phase of a slit without HRs (dashed line). At 2 kHz, the first slit (red curve) reacts inverting the phase of the incoming wave, while for the second slit (blue curve), this occurs at 3.2 kHz.

In this way, by tuning the geometry of the unit cell, a specific phase profile can be tailored, while the total thickness of the panel can be greatly reduced when compared with a quarter wavelength resonator of length L. By using these features, we will show in section 3.4 that the phase profile of Schroeder diffusers can be mimicked by a subwavelength metadiffuser in a given frequency band. Therefore, by tuning the geometry of a metadiffuser, we can maximize sound diffusion in a broad frequency band for room acoustics applications using a deep subwavelength panel.

3.3. Ultra-thin acoustic metamaterial absorbers

3.3.1. *Monochromatic frequency absorber*

In section 3.2.3.1, the critical coupling conditions have been used to design a perfect absorber for a thickness of $L = 3a = \lambda/34.5$. In this section, we will go further and, by using an optimization method (sequential quadratic programming (SQP) method [POW 78]), the geometry of the system will be tuned in order to minimize the thickness of the material, providing structures with perfect absorption and deep subwavelength dimensions.

The TMM was used in the optimization to consider the discreteness effects on the reflection coefficient. The resulting structure from the optimization procedure is shown in Figure 3.5(a): a sample with a single layer of resonators, $N = 1$ with $h = 2.63$ mm, $d = 14.9$ cm, $a = L = d/13 = 1.1$ cm, $w_n = 2.25$ mm, $w_c = 4.98$ mm, $l_n = 2.31$ cm and $l_c = 12.33$ cm. The width of the impedance tube used for measurements, d, makes it possible to fit 13 resonators in the transversal dimension as shown Figure 3.5(a). The sample was built using stereolithography techniques using a photosensitive epoxy polymer (Accura 60®, 3D Systems Corporation, Rock Hill, SC 29730, USA), where the acoustic properties of the solid phase are $\rho_0 = 1210$ kg/m^3, $c_0 = [1570, 1690]$ m/s. The structure presents a peak of perfect absorption at $f = 338.5$ Hz (different from that of the HR, $f_{\mathrm{HR}} = 370$ Hz) with a thickness $L = \lambda/88$.

Figure 3.5(b) shows the absorption coefficient at normal incidence calculated with the TMM, predicted numerically by FEM and measured experimentally. At $f = 338.5$ Hz, perfect absorption can be observed. The maximum absorption measured experimentally was $\alpha = 0.97$, as shown in the inset of Figure 3.5(b). This small discrepancy between the measurements and the models can be caused by experimental reasons including the non-perfect fitting of the slit on the impedance tube and the excitation of plate modes of the solid medium that composes the metamaterial.

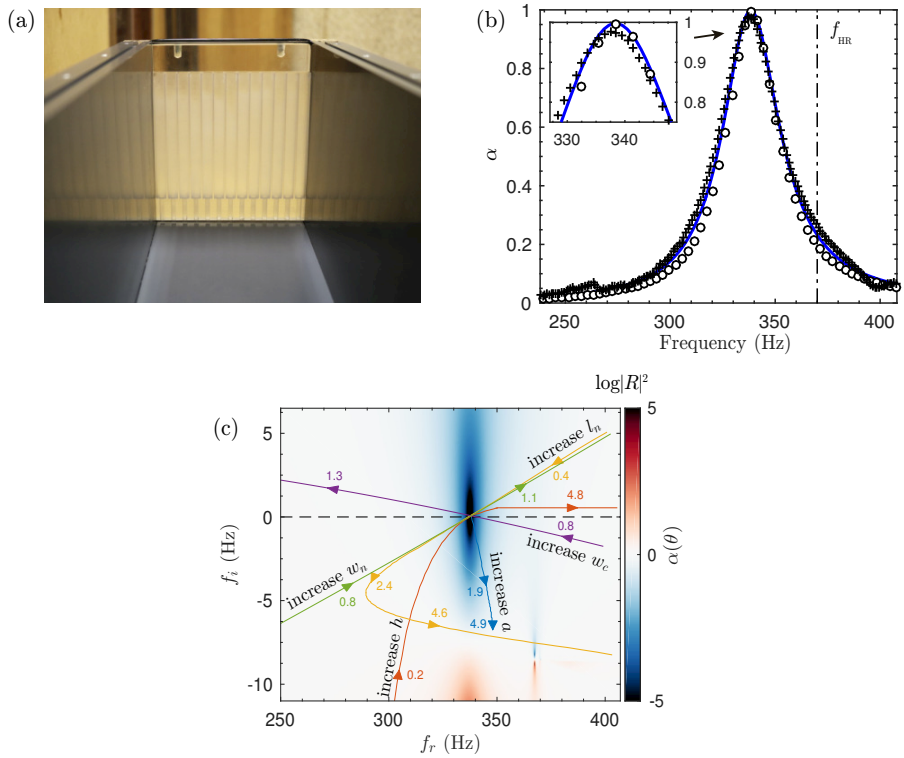

Figure 3.5. *(a) Photograph of the experimental setup with a vertical unit cell, $N = 1$, in the interior of the impedance tube. The translucent resin makes it possible to see the array of HRs. Picture shows the tube open, but it was closed for the experiments. (b) Absorption of the system measured experimentally (crosses), calculated by the transfer-matrix method (continuous blue) and finite element method (circles). (c) Representation of the reflection coefficient in the complex frequency plane for the optimized sample. Each line shows the trajectory of its zero by changing a geometry parameter. For a color version of this figure, see www.iste.co.uk/romero/metamaterials.zip*

On the contrary, Figure 3.5(c) shows the corresponding reflection coefficient in the complex frequency plane. The color map corresponds to the case in which the critical coupling condition is fulfilled, i.e. the zero of the reflection coefficient is exactly located on the real frequency axis. As long as the intrinsic losses depend on the geometry of the resonators and the thickness of the slits, we also represent in Figure 3.5(c) the trajectory of this zero as the geometry of the system is modified. The crossing of the trajectories with the real frequency axis implies that perfect absorption can be achieved with this system at this particular frequency. It can be

seen that the trajectories linked to the resonators' geometry, w_n, w_c, l_n have a strong effect in the real part of the complex frequency of the zero, as they modify the HRs' resonant frequency. In the case of l_n, due to the geometric constraint $d \geq h + l_n + l_c$, increasing the length of the neck also implies the reduction in the cavity and the trajectory of the zero is twisted. The trajectory of the slit thickness, h, shows that the intrinsic losses are excessively increased for very narrow slits and the critical coupling condition cannot be fulfilled. For very wide slits, the geometrical constraints also imply the reduction in the size of the resonators and therefore the resonant frequency is increased. Finally, the trajectory linked to the lattice size, a, shows how the depth of the slit, $L = Na$, is mainly linked to the intrinsic losses of the system: the peak absorption frequency is almost independent of a, it mostly depends on the resonator resonant frequency. Moreover, as the slow sound conditions are caused by the local resonance of the HRs, the periodicity of the array of HRs is not a necessary condition for these perfect absorbing panels. However, considering periodicity allows us to design and tune the system using the present analytical methods.

Finally, Figure 3.6 shows the absorption of the metamaterial panel as a function of the angle of incidence. It can be observed that almost perfect absorption is obtained for a broad range of angles, being $\alpha > 0.90$ for incident waves with $\theta < 60°$. The inset of Figure 3.5 shows the absorption in diffuse field [COX 09] calculated as $\alpha_{\text{diff}} = 2\int_0^{\pi/2} \alpha(\theta)\cos(\theta)\sin(\theta)\mathrm{d}\theta$ where, at the working frequency, it reaches a value of $\alpha_{\text{diff}} = 0.93$, showing the quasi-omnidirectional behavior of the absorption in this subwavelength structure.

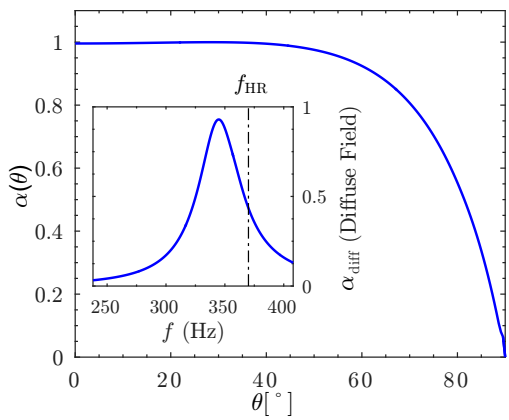

Figure 3.6. *Absorption peak as a function of the angle of incidence calculated by the transfer-matrix method (continuous blue). The inset shows the absorption coefficient in diffuse field as a function of frequency*

3.3.2. *Rainbow-trapping absorber*

Perfect acoustic absorption has been reported in the previous section by means of rigidly backed subwavelength structures by using slow sound and HRs. The interest now is focused on developing perfect and broadband absorption. When the system is not rigidly backed and transmission is allowed, obtaining perfect absorption becomes challenging because the scattering matrix of the system presents two different eigenvalues. In order to obtain perfect absorption, both eigenvalues must vanish at the same frequency [MER 15]. This implies that symmetric and antisymmetric modes must be simultaneously critically coupled at a given frequency [PIP 14]. When the eigenvalues are both zero but at different frequencies, then the system cannot present perfect absorption, but quasi-perfect absorption can be achieved by approaching the symmetric and antisymmetric modes using strong dispersion [JIM 17d]. Perfect acoustic absorption in transmission problems can be obtained by using degenerate resonators, exciting a monopolar and a dipolar mode at the same frequency [YAN 15]. Using elastic membranes decorated with designed patterns of rigid platelets [MEI 12], very selective low-frequency perfect absorption can be observed. Another strategy consists of using asymmetric graded materials, e.g. chirped layered porous structures [JIM 16b], but these structures' lack of subwavelength resonances and therefore their thickness is of the order of half of the incoming wavelength. A final configuration to achieve perfect absorption in transmission consists of breaking the symmetry of the structure by making use of double-interacting resonators, after which perfect absorption was observed in waveguides at a particular frequency [MER 15].

In this section, we address the problem of perfect and broadband acoustic absorption using deep subwavelength structures in non-rigidly backed panels by extending the results shown in the previous section. To do so, we design panels composed of monopolar resonators with graded dimensions, namely *rainbow-trapping absorbers*, as shown in Figure 3.7(a). The rainbow-trapping phenomenon, i.e. the localization of energy due to a gradual reduction of the group velocity in graded structures, has been observed in optics [TSA 07], acoustics [ZHU 13, ROM 13] and elastodynamics [COL 16]. However, losses were not accounted for and therefore absorption was not studied in these works. In the present configuration, a set of graded HRs are used, allowing one to reduce, in addition to the thickness of the panels, the dimension of the unit cell to the deep subwavelength regime. In particular, the structures are composed of a rigid panel, of thickness L, periodically perforated with series of identical waveguides of variable square cross-section loaded by an array of N HRs of different dimensions, as shown in Figure 3.7(a and b). Each waveguide is therefore divided into N segments of length $a^{[n]}$, width $h_1^{[n]}$ and height $h_3^{[n]}$. The HRs are located in the middle of each waveguide section. The *rainbow-trapping absorber* (RTA) was composed of $N = 9$ HRs for the experimental tests, as shown in Figure 3.7(b). The geometrical parameters of both

structures were tuned using optimization methods (sequential quadratic programming (SQP) [POW 78]). In the case of the rainbow-trapping absorber, the cost function was $\varepsilon_{\mathrm{RTA}} = \int_{f_1}^{f_N} |R^-|^2 + |T|^2 df$, i.e. to maximize the absorption in a broad frequency bandwidth, which was chosen from $f_1 = 300$ to $f_N = 1000$ Hz. In the case of the RTA, the length of the panel was constrained to $L = 11.3$ cm, i.e. a panel 10 times thinner than the wavelength at 300 Hz. The geometrical parameters for the RTA $(N = 9)$, measured experimentally, corresponding to Figure 3.7(b), are listed in Table 3.1. The total structure thickness is $L = \sum a^{[n]} = 113$ mm, and its height and the width of the unit cell are $d_3 = 48.7$ mm and $d_1 = 14.6$ mm respectively.

The idea here is to create a frequency-cascade of bandgaps and critically coupled resonators in order to generate a rainbow-trapping effect. The process is as follows: first, we tune the deepest resonator $(n = 1)$ in the waveguide to reduce the transmission above a frequency f_1; second, a second resonator with slightly higher resonance frequency, f_2, is placed in the preceding segment of the waveguide. The geometry of this resonator and the section of the waveguide are tuned to impedance match the system at this frequency. Therefore, the reflection vanishes and a peak of perfect absorption is achieved in the same way as in the previous section. Note that the latter HR also reduces the transmission at even higher frequencies. Thus the process can be repeated by extending the waveguide with more segments, each one with a tuned HR with a resonance frequency higher than the preceding one.

Following this process, a rainbow-trapping absorber is designed using $N = 9$ resonators. Due to machine precision of the available 3D printing system (the minimum step was 0.1 mm), the optimal RTA cannot be accurately manufactured. The main limitation is related to the loss of accuracy of the diameters of the small necks that compose the HRs. Under this technological constraint, we design an RTA using $N = 9$ HRs and quantizing the dimensions of all the geometrical elements that compose the structure to the machine precision. The manufactured sample is shown in Figure 3.7(b) and the quantized geometrical parameters are listed in Table 3.1. Figure 3.7(c–d) show the absorption, reflection and transmission of the device calculated with the TMM, FEM and measured experimentally. Note that both reflection and transmission coefficients are plotted in terms of amplitude and not in terms of energy in order to emphasize the fact that the transmission does not vanish apart from the perfect absorption frequency band. The deepest resonator $(n = 1)$ presents a resonance frequency of $f_1 = f_{\mathrm{gap}} = 259$ Hz, causing the transmission to drop. A set of nine resonators were tuned following the process previously described, with increasing resonance frequencies ranging from 330 to 917 Hz. As a result of the frequency-cascade process, the impedance of the structure in the working frequency range is matched with the exterior medium while the transmission vanishes. As a result, the RTA presents a flat and quasi-perfect absorption coefficient in this frequency range (see Figure 3.7(c)). Excellent agreement is found between the TMM

predictions and FEM simulations, while good agreement is observed between the experimental measurements and both models. It can be observed that at low frequencies, there are small differences between the measurements and the models. These disagreements are mainly caused by imperfections in the sample manufacturing, by imperfect fitting of the structure to the impedance tube, by the possible evanescent coupling between adjacent waveguides and adjacent HRs, and/or by the limitations of the viscothermal model used at the joints between waveguide sections.

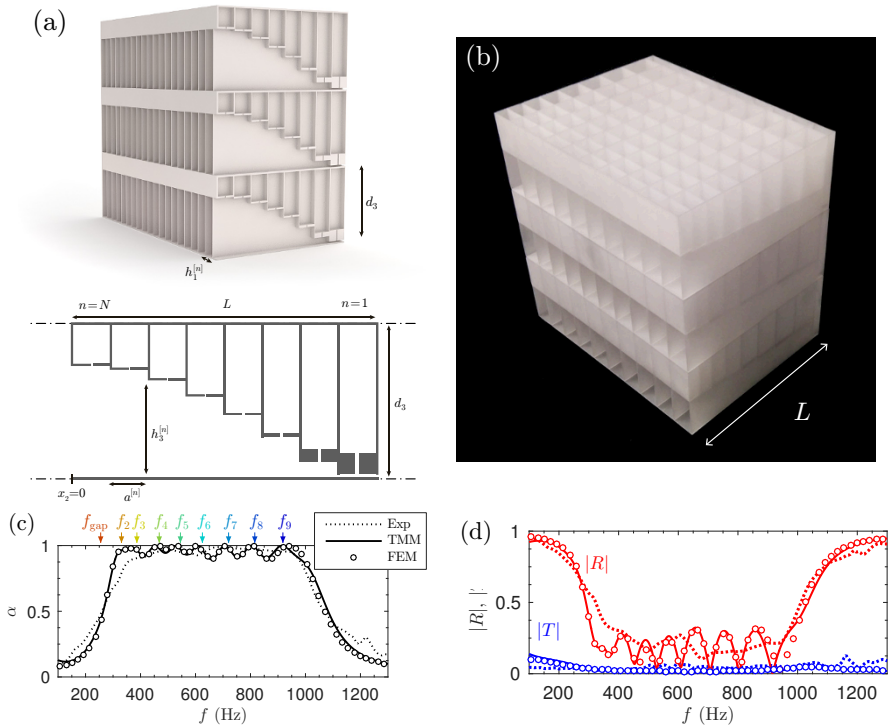

Figure 3.7. *(a) Conceptual view of a rainbow-trapping absorber (RTA) with $N = 8$ HRs. Scheme showing the geometrical variables for RTA. (b) Photograph of the sample containing 10×3 unit cells. (c) Absorption obtained by using the TMM (continuous line), FEM simulations (circles) and measured experimentally (dotted line). (d) Corresponding reflection (red curves) and transmission (blue curves) coefficients in amplitude. For a color version of this figure, see www.iste.co.uk/romero/metamaterials.zip*

n	$a^{[n]}$ (mm)	$h_3^{[n]}$ (mm)	$h_1^{[n]}$ (mm)	$l_{\mathbf{n}}^{[n]}$ (mm)	$l_{\mathbf{c}}^{[n]}$ (mm)	$w_{\mathbf{n}}^{[n]}$ (mm)	$w_{\mathbf{c},1}^{[n]}$ (mm)	$w_{\mathbf{c},2}^{[n]}$ (mm)
9	7.9	25.6	14.0	1.1	21.4	1.2	14.0	7.2
8	9.5	24.2	14.0	1.0	22.8	1.2	14.0	9.0
7	11.0	22.8	14.0	1.7	23.6	1.4	14.0	10.6
6	12.6	21.6	14.0	0.7	25.9	1.0	14.0	12.0
5	14.1	20.2	14.0	1.5	26.5	1.2	14.0	13.6
4	15.7	18.8	14.0	1.1	28.3	1.0	14.0	15.2
3	17.3	17.4	14.0	1.6	29.2	1.0	14.0	16.8
2	18.8	16.0	14.0	1.1	31.2	0.8	14.0	18.4
1	6.4	1.0	1.0	3.0	44.7	0.6	14.0	5.6

Table 3.1. *Geometrical parameters for the RTA ($N = 9$). Table reproduced from [JIM 17c]*

3.4. Metadiffusers

The far-field polar pressure distribution can characterize the performance of a diffuser. For a finite panel of side $2b$, the far-field polar pressure distribution, $p_s(\theta)$, of a locally reacting reflecting surface with a spatially dependent reflection coefficient, $R(x)$, can be calculated using the Fraunhofer integral as [COX 94]

$$p_s(\theta) = \int_{-b}^{b} R(x) e^{jk_0 x \sin\theta} dx, \qquad [3.15]$$

where θ is the polar angle and k_0 is the wavenumber in air. Note that the scattered pressure in the far-field is essentially a Fourier transform of the reflected field along the surface. Therefore, structures whose reflection coefficient distributions present a uniform magnitude Fourier transform with good sound diffusion properties [SCH 75].

The diffusion coefficient [ISO 12], d_ϕ, is estimated from a polar response as

$$\delta_\phi = \frac{\left(\int_{-\pi}^{\pi} I_s(\theta) d\theta\right)^2 - \int_{-\pi}^{\pi} I_s(\theta)^2 d\theta}{\int_{-\pi}^{\pi} I_s(\theta)^2 d\theta}, \qquad [3.16]$$

where $I_s(\theta)$ is the polar scattering intensity for a wave with incident angle ϕ. This coefficient is normalized to that of a plane reflector, δ_{flat}, to eliminate the effect of the finite size of the structure as $\delta_n = (\delta_\phi - \delta_{\text{flat}})/(1 - \delta_{\text{flat}})$.

Based on the principles introduced in the section 3.2.3.2, we now present novel deep subwavelength diffusers based on acoustic metamaterials with deep subwavelength dimensions. The system works as follows: first, we consider a rigid

panel of finite length with a set of N slits; second, we modify the dispersion relations inside each slit by loading one of their walls with a set of HRs. The sound propagation in each slit becomes strongly dispersive and the sound speed inside it, c_p, can be drastically reduced. Each slit behaves effectively as a deep subwavelength resonator and, therefore, the effective depth of the slits can be strongly reduced as $L = c_p/4f$ holds. By tuning the geometry of the HRs and the thickness of the slits, the dispersion relations inside each slit can be modified. As a result, the phase of the reflection coefficient can be tailored along the surface, for example to those of a Schroeder phase grating diffuser. Furthermore, by tuning the thermo-viscous losses, which are inherent in the HRs and in the narrow slits, the leakage of the structure can be compensated by the intrinsic losses of the system and perfect absorption can be obtained. Thus, the magnitude of the reflection coefficient can be also tuned, and the behavior of the slits ranges from perfect reflectors to perfect absorbers. Perfect absorbing slits allow the design of ternary sequence diffusers [COX 06] for low frequencies.

3.4.1. *Quadratic residue metadiffusers*

The first numerical sequence mimicked is the one used in quadratic residue diffusers (QRD). The sequence is given by $s_n = n^2 \mathrm{mod} N$, where mod is the least non-negative remainder of the prime number N. If the phase grating diffuser is based on quarter wavelength resonators (wells), the depth of the wells is given by $L_n = s_n \lambda_0 / 2N$, where λ_0 is the design wavelength. Here, we use optimization methods, for example sequential quadratic programming [POW 78], to tune the geometry of the metamaterial so the spatially dependent reflection coefficient matched between the QR-metadiffuser and the QRD only at 2000 Hz. A QRD with $N = 5$ QRD, a total thickness of $L = 27.4$ cm and side $Nd = 35$ cm was designed for a frequency of 500 Hz. Due to the small lateral size of the panel, the response was evaluated at 2000 Hz considering six repetitions of the unit cell in order to clearly generate the characteristic N diffraction grating lobes of the QRD in the far-field. Figure 3.8(a–b) shows the phase and magnitude of the reflection coefficient along the surface the ideal QRD and a QR-metadiffuser of $L = 2$ cm thickness and $M = 2$ HRs of same lateral dimensions. The geometrical parameters for the metadiffuser are listed in Table 3.2 and a scheme of the panel is shown in Figure 3.8(c). Perfect agreement is found between the reflection coefficients of the QR-metadiffuser and the target phase grating QRD. Figure 3.8(g) shows the far-field calculation at 2000 Hz using equation [3.15] for both structures. Excellent agreement is obtained between the polar responses using the TMM. To validate the design, a full-wave numerical solution using the finite element method (FEM) and accounting for the thermo-viscous losses is also provided. The FEM numerical solution agrees with the theoretical prediction, although small discrepancies can be observed. They are caused first because the radiation corrections used in the TMM are only approximate and, second, because the evanescent coupling between near slits in the TMM is not considered while it is implicitly included in the FEM simulations. The near-field

pressure distributions are shown in Figure 3.8(d–f) for the QR-metadiffuser, the QRD and a reference flat surface of the same width, respectively. Excellent agreement is observed between both diffusers, where it is clear how the field is scattered in other directions rather than specular. The presented QR-metadiffuser is 17.1 times thinner than the QRD (34 times smaller than the QRD design wavelength (500 Hz) and 8.5 times smaller than the evaluation wavelength (2000 Hz)).

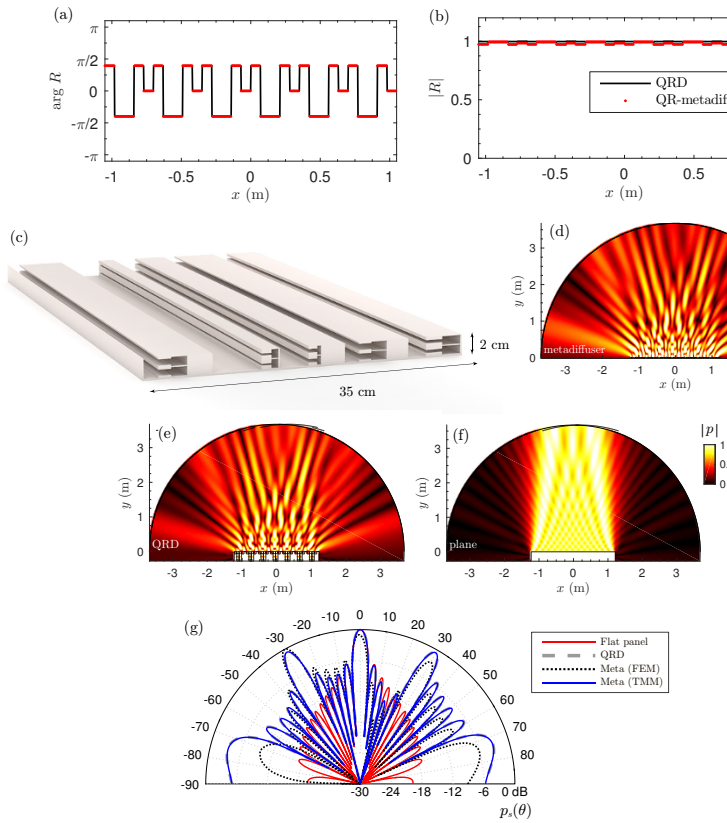

Figure 3.8. *(a) Phase and (b) magnitude of the spatially dependent reflection coefficient of a QRD (black line) and the QR-metadiffuser (red dotted line). (c) Scaled scheme of the QR-metadiffuser with $N = 5$ and $M = 2$. (d) Near-field pressure distribution at 2 kHz of QR-metadiffuser with thickness $L = 2$ cm, (e) phase grating QRD of thickness $L = 27.4$ cm and (f) flat plane reflector. (g) Far-field polar distribution of the QR-metadiffuser obtained by TMM (continuous blue) and FEM (dotted black), the reference QRD (dashed gray), and a plane reflector with same width of the diffusers (continuous red). For a color version of this figure, see www.iste.co.uk/romero/metamaterials.zip*

n	s_n	h (mm)	$l_\mathbf{n}$ (mm)	$l_\mathbf{c}$ (mm)	$w_\mathbf{n}$ (mm)	$w_\mathbf{c}$ (mm)
1	1.0	14.7	13.0	16.4	6.2	9.0
2	4.0	30.9	9.1	4.3	3.5	9.0
3	4.0	30.9	9.1	4.3	3.5	9.0
4	1.0	15.7	13.3	17.0	6.3	9.0
5	0.0	20.3	18.0	20.7	3.2	9.0

Table 3.2. *Geometrical parameters of the QR-metadiffuser. Table reproduced from [JIM 17a]*

3.4.2. *Broadband optimal metadiffusers*

To design a metadiffuser useful for room acoustics, its diffusion must be broad in frequency. Thus, we extended the bandwidth of the optimization procedure, where the cost function to minimize was $\varepsilon = 1 - \int_{f_{\text{low}}}^{f_{\text{high}}} \delta_n df$. In particular, we look for deep subwavelength thickness metadiffusers that present maximum normalized diffusion coefficient in the frequency range from $f_{\text{low}} = 250$ Hz to $f_{\text{high}} = 2000$ Hz. Here, we used a set of $N = 11$ slits separated by $d = 12$ cm, and constrained the thickness of the panel to $L = 3$ cm. The obtained geometrical parameters are listed in Table 3.3. Here, we used square cross-sectional HRs. Figure 3.9(a) shows the scheme of the metadiffuser with the retrieved geometry. First, the polar responses at two frequencies 300 and 2000 Hz are shown in Figure 3.9(b and c). The maximization of the diffusion coefficient implies that the polar responses are uniform. In addition, we show the angular dependence of the near field at shorter distances, for example at 1 and 5 m. Due to the lateral dimension of the structure, which is 1.32 m, equation [3.15] is not accurate at distances much shorter than the Rayleigh distance. However, although the near field does not exactly follow the polar distribution given by equation [3.15], the structure scatters the waves uniformly in broad range of angles when compared with a flat plane of the same dimensions. Figure 3.9(d–g) show the frequency-dependent polar responses in the far field for a reference flat plane with the same width as the metadiffuser, a thick QRD with a design frequency of 250 Hz ($L_{\text{QRD}} = 56$ cm), a thin QRD with the same thickness of the metadiffuser $L_{\text{QRD,thin}} = 3$ cm and the optimized metadiffuser, respectively. Here, we calculated the polar responses using six repetitions of the panel to clearly observe the diffraction grating lobes. First, the scattering of the thin QRD, Figure 3.9(e), is almost the same as a flat plane, Figure 3.9(d). It only starts to scatter waves at different angles above 2 kHz. Second, the deep wells that compose the thick QRD, Figure 3.9(f), resonate near their quarter-wavelength resonances at lower frequencies and, therefore, the

reflection coefficient follows the QR sequence and the panel scatters sound waves into oblique angles. Finally, the optimized metadiffuser, Figure 3.9(g), also shows strong grating lobes, but, in addition, at medium and high frequencies, energy is spread in other directions at low frequencies, for example between 250 and 500 Hz.

n	1	2	3	4	5	6	7	8	9	10	11
h (mm)	5.7	4.9	7.7	82.9	48.4	74.9	20.0	6.6	76.2	29.5	7.6
$l_{\mathbf{n}}$ (mm)	16.3	7.3	37.1	0.0	35.3	22.1	14.7	0.1	0.0	0.1	4.8
$l_{\mathbf{c}}$ (mm)	97.1	106.8	74.2	36.0	35.3	22.1	84.3	112.2	42.7	89.4	106.5
$w_{\mathbf{n}}$ (mm)	6.7	6.5	10.0	29.0	29.0	29.0	14.0	9.5	29.0	27.6	6.2
$w_{\mathbf{c}}$ (mm)	29.0	29.0	29.0	29.0	29.0	29.0	29.0	29.0	29.0	29.0	29.0

Table 3.3. *Geometrical parameters used for the broadband metadiffuser using N different slits. Table reproduced from [JIM 17a]*

The normalized diffusion coefficient shown in Figure 3.9(h) quantifies this behavior. It is observed that over the optimized range, the diffusion coefficient of the metadiffuser takes values with a mean value of about $\delta_n = 0.65$, with peaks of $\delta_n = 0.9$. When compared to the thick QRD, its frequency band is extended to one octave below. The corresponding absorption is shown in Figure 3.9(f). Here, the wide slits that form the QRD produce almost no losses, while the thermo-viscous losses produced in the narrow ducts that comprise the ultra-thin metamaterial lead to some peaks of absorption at the resonance of the cavities. These losses can be reduced if the thickness of the panel is increased, but here we presented a structure whose thickness is 46 times smaller than the wavelength. It is worth noting here that the size of some of neck of the resonators is almost the same as their cavities, as can be observed in Figure 3.9(a). In these cases, the resonator acts as a coiled QWR and the losses in these wide ducts are decreased. The resonance frequency of these QWR is higher than the corresponding HRs, contributing to the high frequency diffusion, while, in contrast, the HRs introduce spatial changes on the reflection coefficient at low frequencies. Moreover, the position of the low frequency absorption peaks can be engineered to solve other typical problems in room acoustics, as placing them at the resonant modes of small control rooms to produce a flatter spectral response or reduce sound coloration in the reverberation. This can be achieved using multi-objective optimization techniques.

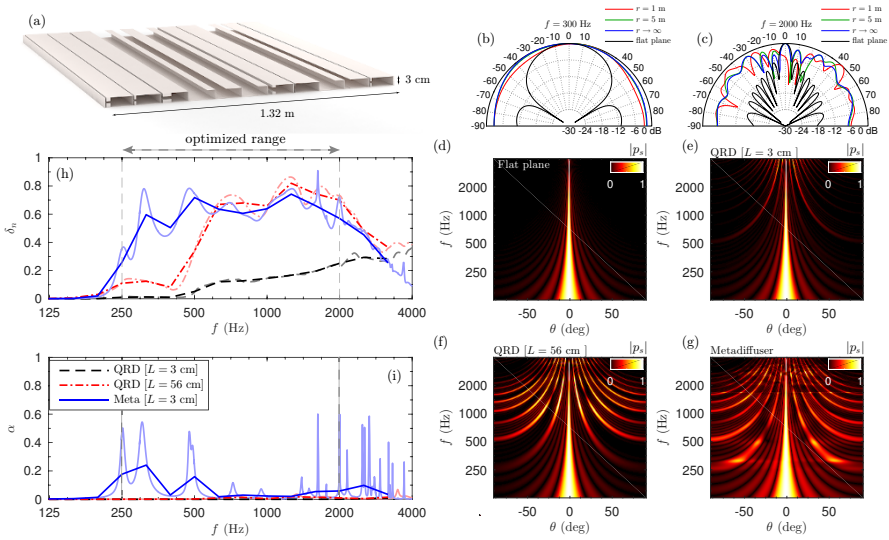

Figure 3.9. *(a) Scheme of the analyzed metadiffuser. (b) and (c) show the polar responses at two frequencies, 300 and 2000 Hz respectively. Far-field polar response as a function of the frequency for (d) reference flat plane, (e) $N = 11$ QRD panel with a total thickness of 3 cm, (f) QRD panel with a total thickness of 56 cm and (g) an optimized metadiffuser thickness of 3 cm. (h) Normalized diffusion coefficient or the 3 cm QRD (dashed black), 32 cm QRD (dashed-dotted red) and optimized metadiffuser using the TMM (blue) integrated in third of octaves. The third octave integration is shown in thick lines according to ISO 17497-2:2012 [ISO 12]. (i) Corresponding absorption. For a color version of this figure, see www.iste.co.uk/romero/metamaterials.zip*

3.5. Conclusions

Realistic panels for sound perfect absorption and diffusion with subwavelength sizes are designed in this chapter with simple structures made of bricks with Helmholtz resonators. The theoretical modeling based on the transfer-matrix method considering the viscothermal losses has been described in detail. Two examples of perfect absorbers and metadiffusers have been described.

Perfect absorption of sound is achieved at 338.5 Hz with a panel thickness of $L = \lambda/88 = 1.1$ cm and without added porous material. It is worth noting here that the total panel size in the vertical dimension is also subwavelength $d = \lambda/6.5 = 14.5$ cm. The subwavelength feature of the presented structure provides

perfect absorption for a wide range of incident angles. This almost omnidirectional sound absorber can be used in practical applications where the omnidirectional feature is mandatory. These promising results have been used to study different configurations producing broadband perfect absorption with deep subwavelength structures, named rainbow-trapping absorbers. We reported flat and perfect absorption over a frequency range covering from 300 to 1000 Hz, i.e. almost two octaves, using a rainbow-trapping absorber (RTA) composed of nine resonators and 10 times smaller than the wavelength at 300 Hz (11.3 cm).

Metadiffusers, a novel design of locally reacting surfaces with tailored acoustic scattering, were also presented. The propagation inside the metamaterial presents strong dispersion and the sound speed can be significantly reduced so that each slit effectively behaves as a deep subwavelength resonator. Thus, by tuning the material geometry, the dispersion of acoustic waves in the slits is modified and the spatially dependent reflection coefficient can be tailored to specific functions with a uniform magnitude Fourier transform. In these conditions, the grating lobes produced by a periodic arrangement of the panel all have the same energy. The acoustic energy can be scattered in other directions than specular. It was also shown that the structures can be optimized to work in a broad frequency range covering three octaves. In particular, we presented a diffuser of 3 cm thickness working from 250 to 2000 Hz, demonstrating the potential of the metadiffusers to be used in critical listening environments due to their deep subwavelength nature: the thickness of the panels was 1/46 to 1/20 times the design wavelength, i.e. between about a twentieth and a tenth of the thickness of traditional designs. In the context of smart building design and sustainability, metadiffusers can be used to save space and to produce lightweight materials, improving the performance of the acoustic solutions using less resources. Moreover, the proposed designs have the potential to meet the aesthetic requirements that are mandatory for modern auditoria design.

3.6. Acknowledgments

This work is based on work from COST Action DENORMS – CA15125, supported by COST (European Cooperation in Science and Technology). The authors acknowledge financial support from the Metaudible Project no. ANR-13-BS09-0003, cofounded by ANR and FRAE.

3.7. References

[ACH 16] ACHILLEOS V., RICHOUX O., THEOCHARIS G., "Coherent perfect absorption induced by the nonlinearity of a Helmholtz resonator", *Journal of the Acoustical Society of America*, vol. 140, no. 1, 2016.

[BLI 08] BLIOKH K.Y., BLIOKH Y.P., FREILIKHER V *et al.* "Unusual resonators: Plasmonics, metamaterials, and random media", *Reviews of Modern Physics*, vol. 80, no. 4, p. 1201, 2008.

[CAI 14] CAI X., GUO Q., HU G. *et al.*, "Ultrathin low-frequency sound absorbing panels based on coplanar spiral tubes or coplanar Helmholtz resonators", *Applied Physics Letters*, vol. 105, no. 12, p. 121901, 2014.

[COL 16] COLOMBI A., COLQUITT D., ROUX P. *et al.*, "A seismic metamaterial: The resonant metawedge", *Scientific Reports*, vol. 6, 2016.

[COX 94] COX T.J., LAM Y., "Prediction and evaluation of the scattering from quadratic residue diffusers", *Journal of the Acoustical Society of America*, vol. 95, no. 1, pp. 297–305, 1994.

[COX 06] COX T.J., ANGUS J.A., D'ANTONIO P., "Ternary and quadriphase sequence diffusers", *Journal of the Acoustical Society of America*, vol. 119, no. 1, pp. 310–319, 2006.

[COX 09] COX T.J., D'ANTONIO P., *Acoustic Absorbers and Diffusers: Theory, Design and Application*, CRC Press, Boca Raton, 2009.

[DUB 99] DUBOS V., KERGOMARD J., KHETTABI A. *et al.*, "Theory of sound propagation in a duct with a branched tube using modal decomposition", *Acta Acustica United With Acustica*, vol. 85, no. 2, pp. 153–169, 1999.

[GRO 15] GROBY J.-P., HUAND W., LARDEAU A. *et al.*, "The use of slow sound to design simple sound absorbing materials", *Journal of Applied Physics*, vol. 117, no. 124903, 2015.

[GRO 16] GROBY J.-P., POMMIER R., AURÉGAN Y., "Use of slow sound to design perfect and broadband passive sound absorbing materials", *Journal of the Acoustical Society of America*, vol. 139, no. 4, pp. 1660–1671, 2016.

[ISO 12] ISO 17497–2:2012, Acoustics – Sound-scattering properties of surfaces – Part 2: Measurement of the directional diffusion coefficient in a free field, ISO standard, International Organization for Standardization, Geneva, Switzerland, 2012.

[JIM 16a] JIMÉNEZ N., HUANG W., ROMERO-GARCÍA V. *et al.*, "Ultra-thin metamaterial for perfect and quasi-omnidirectional sound absorption", *Applied Physics Letters*, vol. 109, no. 121902, 2016.

[JIM 16b] JIMÉNEZ N., ROMERO-GARCÍA V., CEBRECOS A. *et al.*, "Broadband quasi perfect absorption using chirped multi-layer porous materials", *AIP Advances*, vol. 6, no. 12, p. 121605, 2016.

[JIM 17a] JIMÉNEZ N., COX T.J., ROMERO-GARCÍA V. *et al.*, "Metadiffusers: Deep-subwavelength sound diffusers", *Scientific Reports*, no. 7, p. 5389, 2017.

[JIM 17b] JIMÉNEZ N., GROBY J.-P., PAGNEUX V. *et al.*, "Iridescent perfect absorption in critically-coupled acoustic metamaterials using the transfer matrix method", *Applied Sciences*, vol. 7, no. 6, p. 618, 2017.

[JIM 17c] JIMÉNEZ N., ROMERO-GARCÍA V., PAGNEUX V. *et al.*, "Rainbow-trapping absorbers: Broadband, perfect and asymmetric sound absorption by subwavelength panels with transmission", *Scientific Reports*, no. 7, p. 135595, 2017.

[JIM 17d] JIMÉNEZ N., ROMERO-GARCÍA V., PAGNEUX V. *et al.*, "Quasiperfect absorption by subwavelength acoustic panels in transmission using accumulation of resonances due to slow sound", *Physical Review B*, vol. 95, p. 014205, 2017.

[JIM 18] JIMÉNEZ N., ROMERO-GARCÍA V., GROBY J.-P., "Perfect absorption of sound by Rigidly-Backed High-Porous materials", *Acta Acustica United with Acustica*, vol. 104, no. 3, pp. 396–409, 2018.

[KER 87] KERGOMARD J., GARCIA A., "Simple discontinuities in acoustic waveguides at low frequencies: Critical analysis and formulae", *Journal of Sound and Vibration*, vol. 114, no. 3, pp. 465–479, 1987.

[LI 16] LI Y., ASSOUAR B.M., "Acoustic metasurface-based perfect absorber with deep subwavelength thickness", *Applied Physics Letters*, vol. 108, no. 6, p. 063502, 2016.

[MA 14] MA G., YANG M., XIAO S. *et al.*, "Acoustic metasurface with hybrid resonances", *Nature Materials*, vol. 13, no. 9, pp. 873–878, 2014.

[MEC 08] MECHEL F.P., *Formulas of Acoustics*, 2nd edition, Springer Science & Business Media, Springer-Verlag, Berlin, Heidelberg, 2008.

[MEI 12] MEI J., MA G., YANG M. *et al.*, "Dark acoustic metamaterials as super absorbers for low-frequency sound", *Nature Communications*, vol. 3, p. 756, 2012.

[MER 15] MERKEL A., THEOCHARIS G., RICHOUX O. *et al.*, "Control of acoustic absorption in one-dimensional scattering by resonant scatterers", *Applied Physics Letters*, vol. 107, no. 24, p. 244102, 2015.

[PIP 14] PIPER J.R., LIU V., FAN S., "Total absorption by degenerate critical coupling", *Applied Physics Letters*, vol. 104, no. 25, p. 251110, 2014.

[POW 78] POWELL M.J., "A fast algorithm for nonlinearly constrained optimization calculations", *Numerical Analysis*, pp. 144–157, 1978.

[ROM 13] ROMERO-GARCÍA V., PICÓ R., CEBRECOS A. *et al.*, "Enhancement of sound in chirped sonic crystals", *Applied Physics Letters*, vol. 102, no. 9, p. 091906, 2013.

[ROM 16a] ROMERO-GARCÍA V., THEOCHARIS G., RICHOUX O. *et al.*, "Perfect and broadband acoustic absorption by critically coupled sub-wavelength resonators", *Scientific Reports*, vol. 6, p. 19519, 2016.

[ROM 16b] ROMERO-GARCÍA V., THEOCHARIS G., RICHOUX O. *et al.*, "Use of complex frequency plane to design broadband and sub-wavelength absorbers", *Journal of the Acoustical Society of America*, vol. 139, no. 6, p. 3395, 2016.

[SCH 75] SCHRÖDER M.R., "Diffuse sound reflection by maximum- length sequences", *Journal of the Acoustical Society of America*, vol. 57, no. 1, pp. 149–150, 1975.

[STI 91] STINSON M.R., "The propagation of plane sound waves in narrow and wide circular tubes, and generalization to uniform tubes of arbitrary cross-sectional shape", *Journal of the Acoustical Society of America*, vol. 89, no. 2, pp. 550–558, 1991.

[THE 14] THEOCHARIS G., RICHOUX O., ROMERO-GARCÍA V. *et al.*, "Limits of slow sound propagation and transparency in lossy, locally resonant periodic structures", *New Journal of Physics*, vol. 16, no. 9, p. 093017, 2014.

[TSA 07] TSAKMAKIDIS K.L., BOARDMAN A.D., HESS O., "Trapped rainbow storage of light in metamaterials", *Nature*, vol. 450, no. 7168, pp. 397–401, 2007.

[YAN 08] YANG Z., MEI J., YANG M. *et al.*, "Membrane-type acoustic metamaterial with negative dynamic mass", *Physical Review Letters*, vol. 101, no. 20, p. 204301, 2008.

[YAN 15] YANG M., MENG C., FU C. *et al.*, "Subwavelength total acoustic absorption with degenerate resonators", *Physical Review Letters*, vol. 107, no. 10, p. 104104, 2015.

[ZHU 13] ZHU J., CHEN Y., ZHU X. *et al.*, "Acoustic rainbow trapping", *Scientific Reports*, vol. 3, 2013.

PART 2

Principles and Fundamentals of Acoustic Metamaterials

Fundamentals and Applications of Acoustic Metamaterials: From Seismic to Radio Frequency,
First Edition. Edited by Vicente Romero-García and Anne-Christine Hladky-Hennion.

4

Homogenization of Thin 3D Periodic Structures in the Time Domain – Effective Boundary and Jump Conditions

This chapter focuses on the derivation of effective models for the propagation of acoustic waves in the presence of structures that are periodic at a subwavelength scale and that have in addition a subwavelength thickness. In the context of acoustics, we consider the most usual case of rigid inclusions in a fluid matrix, typically air or water. We focus on two typical cases. The first, termed *structured wall*, corresponds to a set of periodic inclusions in the vicinity of a rigid wall or in contact with it, for instance, a rough surface (with periodic roughnesses). The second, termed *structured film*, corresponds to one layer or a few layers of periodically distributed inclusions. Because of the small thickness of the structure, the classical methods of the homogenization theory cannot be used. Classically, the homogenization aims to describe the overall behavior of the wave propagating in the bulk of a periodic structure, and the analysis is performed far from its boundaries. It results that the periodically heterogeneous character of the medium at a small scale can be averaged resulting in an effective homogeneous medium. When the structure is reduced in thickness to one or few inclusions, the "far from boundaries" does not exist and the periodicity of the heterogeneity cannot be exploited across the structure, since it has been lost. In other words, there is no "propagation" through the inclusions; rather, local scattering effects affect the wave propagation in the surrounding fluid. These effects are often referred to as *boundary layer effects*, since they are confined near the wall or the film; they correspond to the layers where the evanescent field can be strong, while it vanishes when moving far away from the structure. To account for the loss in periodicity in one direction, and for the associated boundary layer effects, two approaches are possible. In the first, so-called *boundary layer correctors* are

Chapter written by Agnès MAUREL, Kim PHAM and Jean-Jacques MARIGO.

introduced which depend on the small scale along the structure and vanish exponentially far from it; these correctors are added to the homogenized solution that depends on the large scale only. The second approach considers a solution that is valid in the vicinity of the structure (hence depending on the small scale), which has to match the homogenized solution that is valid far from the structure. In both cases, the solution depending on the small scale aims to provide averaged information.

In the context of the waves, the first derivation of effective jump conditions is due to Sanchez-Hubert and Sanchez-Palencia in 1982 [SAN 82]. This work focused on the scattering of acoustic waves by a set of holes perforating a rigid wall of zero thickness. Therefore, such approaches have been applied in the context of electromagnetic, elastic/seismic and acoustic waves. To avoid a long introduction, the table below summarizes some (most) of these contributions. We distinguish the context of waves and the chosen approach (boundary layer correctors *versus* matched solutions, although both are equivalent).

	Boundary correctors	Matched solutions
Electro-magnetism	[DEL 91]*, [ABB 95],[ABB 96], [HOL 00a]*, [HOL 00b]*, [PRO 03], [POI 06], [HOL 16]*	[AMM 99], [DEL 10]*, [ASL 11], [DEL 12]*, [TOU 12], [DEL 13]*, [DEL 15]*, [HEW 16], [MAU 16], [MAR 16c], [GAL 17]
Elasto-dynamics	[BOU 06]*, [BOU 15]*, [SCH 16]*	[CAP 13]*, [MAR 17], [PHA 17]
Acoustics	[LUK 09], [TLE 09], [ROH 09], [ROH 10], [BEN 15], [SCH 17]	[BON 04], [BON 05], [CLA 13], [BEN 13], [MAR 16a], [MAR 16b], [CHA 16], [POP 16], [MER 17]

In the context of electromagnetic and elastic waves, we indicate by a star * the works which account for the additional complexity of dealing with the (polarized) Maxwell equations or Navier equations. Eventually, we also mention works focusing on the numerical implementation of effective conditions in the harmonic regime [BON 04, BON 05, DEL 10, BEN 12, MAR 16b, RIV 17] and in the time domain [CAP 13, LOM 17], and works presenting experimental inspections of the effective conditions [GAO 16, SCH 17, GAL 17]. Our list of references may appear short, but we restricted it to (i) studies performed in the dynamic case, thus omitting the large amount of literature dedicated to the static one, and (ii) works focusing on effective conditions for structured surfaces or interfaces, thus omitting the even larger amount of literature dedicated to effective conditions across homogeneous interfaces. If we have missed additional references, we wish to apologize.

Main results and motivations

We consider acoustic waves propagating in a fluid in the presence of a set of rigid inclusions in three dimensions. With p the pressure and $\mathbf{u}$ the velocity, the acoustic propagation is governed by linearized Euler equations:

$$\begin{cases} \chi \dfrac{\partial p}{\partial t} + \mathrm{div}\mathbf{u} = 0, \quad \rho \dfrac{\partial \mathbf{u}}{\partial t} = -\nabla p, \\ \mathbf{u} \cdot \mathbf{n}_{|\Gamma} = 0, \end{cases} \tag{4.1}$$

where Γ denotes the boundaries between the fluid and the rigid inclusions (and $\mathbf{n}$ the local normal vector to these boundaries); ρ and χ denote the mass density and the isentropic compressibility of the fluid. The time is t and the space is associated with the coordinate $\mathbf{x} = (x_1, x_2, x_3)$, with $(\mathbf{e}_1, \mathbf{e}_2, \mathbf{e}_3)$ being the associated unit vectors. The structure contains a set of rigid inclusions periodically located in the (x_2, x_3)-plane, with spacings h_2 and h_3 being of the same order of magnitude. Besides, the resulting two-dimensional array has a typical thickness e along x_1 of the same order of magnitude as h_2 and h_3. In the low-frequency regime, the typical array spacing $h = \sqrt{h_1 h_2}$ is much smaller than the typical wavelength $1/k$ imposed by the source (k is the typical wavenumber). We can establish the following effective conditions corresponding to the configurations reported in Figure 4.1, specifically:

(a) **Effective boundary condition for a structured rigid wall:**

$$u_1^{\mathrm{ef}} = h\varphi \frac{\partial u_1^{\mathrm{ef}}}{\partial x_1} + hA_{\alpha\beta} \frac{\partial u_\alpha^{\mathrm{ef}}}{\partial x_\beta},$$

with three coefficients to be calculated A_{22}, A_{33} and $A_{23} = A_{32}$.

(b) **Effective jump conditions for a structured film:**

$$\begin{cases} [p^{\mathrm{ef}}] = hB_i \dfrac{\partial \overline{p^{\mathrm{ef}}}}{\partial x_i}, \\ [u_1^{\mathrm{ef}}] = h\varphi \dfrac{\partial \overline{u_1^{\mathrm{ef}}}}{\partial x_1} + hC_{i\alpha} \dfrac{\partial \overline{u_i^{\mathrm{ef}}}}{\partial x_\alpha}. \\ \text{with six coefficients to be calculated } B_1, B_2, B_3, C_{22}, C_{33}, C_{23}, \\ (\text{with } C_{23} = C_{32}, C_{12} = B_2, C_{13} = B_3), \end{cases} \tag{4.2}$$

and where we denote

$$i, j = 1, 2, 3, \text{and } \alpha, \beta = 2, 3,$$

(this convention for Latin and Greek indices is kept throughout the chapter), and repeated indices mean summation. The effective conditions involve several coefficients: the scalar φ, the vector $\mathbf{B}$ and the tensors A and C, which we will define in the following. Eventually, in the jump conditions, we define the jumps and the mean values of any field f that is discontinuous across the equivalent interface using f^+ and f^- its limits on the both sides and

$$[f] = f^+ - f^-, \quad \overline{f} = \frac{1}{2}\left(f^- + f^+\right).$$

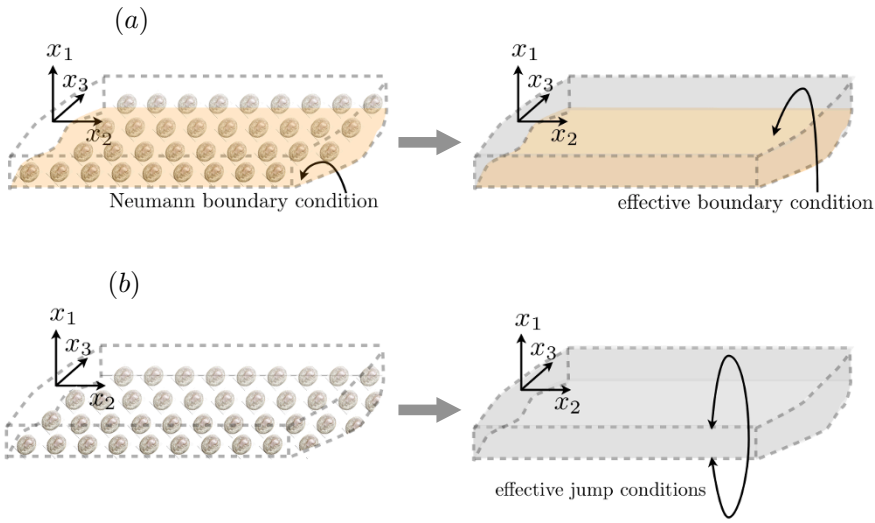

Figure 4.1. *(a) Structured wall composed of an array of rigid inclusions over a rigid wall. (b) Structured film in a surrounding fluid. In both cases, the arrow indicates the homogenization process leading to an effective boundary condition for (a) and effective jump conditions for (b), see* [4.2]

We have said that the effective boundary condition in equations [4.2] requires the calculation of three parameters and the effective jump conditions require the calculation of six parameters. These parameters are deduced from static *elementary* problems (see forthcoming equations [4.11] and [4.21]), which correspond to simple problems of potential flows through or along the structure, driven by a unit velocity along $\mathbf{e}_i$ far from it. Eventually, we will see in the concluding remarks that fewer parameters are involved for simple geometries of the inclusions.

Closely related references

Such configurations have been studied in several references. For structured walls, the two-dimensional case has been considered in [TLE 09] for polarized electromagnetic waves over a conducting wall (which is the electromagnetic counterpart of a rigid wall) covered by a thin dielectric layer containing perfectly conducting inclusions. The case of rough surfaces has been studied in [TOU 12] for polarized electromagnetic waves over roughnesses with double periodicity, and in [MAR 16a] for acoustic waves over rectangular grooves. The three-dimensional case has been considered by Holloway and Kuester for Maxwell equations [HOL 00a, HOL 00b]. For the structured films: in [SAN 82], the case of a rigid wall perforated by holes was considered, with a particular focus on critical cases appearing for specific scalings of the array spacing and hole diameter. The two- and three-dimensional cases were considered in this reference. In the two-dimensional case, the configuration of zero-thickness conducting strips (invariant in one direction) has been analyzed in [DEL 91] for the Maxwell equation. The same geometry has been considered in [BON 04, BON 05] for acoustic waves. The case of arrays of rigid/perfectly conducting inclusions have been discussed in [MAU 16, MAR 16a, MAR 16c]. The same configuration has been considered in [HOL 16] for Maxwell equations. Eventually, the study in [BEN 13] (a perforated wall) is particular in this list since it is assumed that $h = O(1)$, while $e \to 0$ is the small parameter.

Summary

This chapter is organized as follows:

In section 4.1, we set the different ingredients needed to conduct the asymptotic analysis; this starts with the definition of a small parameter ε, which is used to differentiate between the rapid variations of the evanescent field and the slow variations of the propagating field. In the matched asymptotic expansion technique, two different expansions of the solution (termed *outer* and *inner* expansions) are sought which are valid far and close to the inclusions. The corresponding outer and inner problems are complemented using *matching conditions*, which tell us that the two solutions coincide in some intermediate region.

The procedure is then straightforward. The expansions are plugged in equations [4.1] resulting in two hierarchies of problems (outer and inner) at each order in ε, which are linked through the matching conditions. In sections 4.2 and 4.3, they are solved up to $O(\varepsilon^2)$, providing the desired effective boundary condition and effective jump conditions, respectively.

In section 4.4 we inspect the equation of energy conservation in the effective problems. This is of particular interest if we have in mind a numerical

implementation in the time domain; indeed, the problem has to be associated with a positive energy supported by the effective surface, or by the effective interface, in order to avoid numerical instabilities.

We aim to give a simple presentation of the two-scale matched asymptotic analysis. The calculations are detailed and hopefully easy to follow. Hence, there are no prerequisites except possibly some patience.

4.1. The asymptotic analysis – two scale expansions and matching conditions

4.1.1. *Two scales and two regions*

The asymptotic analysis starts with the definition of a small parameter ε. In our case, it is a measure h of the spacing, and the smallness is measured in comparison to the typical wavelength $1/k$ imposed by the source. The structuration is two dimensional, with spacings h_2 along $\mathbf{e}_2$ and h_3 along $\mathbf{e}_3$, and it has a typical thickness e. We consider that (h_2, h_3, e) are of the same order of magnitude; hence, without loss of generality, we set

$$\varepsilon = h = \sqrt{h_2 h_3} \ll 1, \quad e = O(\varepsilon), k = O(1).$$

Owing to this separation of the scales, we define two systems of coordinates: the *macroscopic scale* $\mathbf{x}$ which is associated with the scale of the wavelength, and the *microscopic scale* $\mathbf{y}$ which is associated with the scale of the structuration, with

$$\mathbf{y} = \frac{\mathbf{x}}{\varepsilon},$$

and $\mathbf{y}$ aims to disappear in the homogenized problem. Typically, the coordinate $\mathbf{x}$ allows us to move over long distances along the structure in the (x_2, x_3)-plane and to move far away from it in the x_1-direction. In the vicinity of the inclusions, once $\mathbf{x}' = (x_2, x_3)$ has fixed a given inclusion, $\mathbf{y}$ describes small displacements around it (Figure 4.2). This is why, although $\mathbf{x}$ and $\mathbf{y}$ are linked, they will be considered as independent coordinates (until we remember that they are linked). This is also why $\mathbf{y}' = (y_2, y_3)$ is bounded in

$$\mathsf{Y}(y_1) \subset \mathsf{Y}_\infty = \{y_2 \in (0, h_2/h), y_3 \in (0, h_3/h)\},$$

with $\mathsf{Y}(y_1)$ containing the fluid only. We can consider that y_1 is unbounded, specifically $y_1 \in (0, +\infty)$ for the structured wall and $y_1 \in (-\infty, +\infty)$ for the structured film, and we can anticipate that we will have to specify something when y_1

goes to infinity. It follows that in $\mathbf{y}$ coordinate, the problem is set on a strip $\mathcal{Y}_\infty$ and in practice, we can also consider

$$(a): \mathcal{Y}(y_1^m) = \{y_1 \in (0, y_1^m), \mathbf{y}' \in \mathsf{Y}(y_1)\}, \qquad \mathcal{Y} = \lim_{y_1^m \to +\infty} \mathcal{Y}(y_1^m),$$
$$(b): \mathcal{Y}(y_1^m) = \{y_1 \in (-y_1^m, y_1^m), \mathbf{y}' \in \mathsf{Y}(y_1)\}, \qquad \mathcal{Y} = \lim_{y_1^m \to +\infty} \mathcal{Y}(y_1^m),$$

and we denote by $\mathcal{V}(y_1^m)$ the volume of $\mathcal{Y}(y_1^m)$ and by $\mathcal{S}(y_1)$ the surface of $\mathsf{Y}(y_1)$. Note that by construction $\mathcal{S}(y_1) = 1$ if no inclusion intersects $\mathsf{Y}(y_1)$.

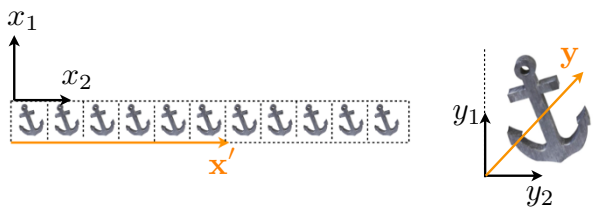

Figure 4.2. *The two systems of coordinate in the vicinity of the inclusions (here shown in 2D). The macroscopic coordinate $\mathbf{x}' = (x_2, x_3)$ allows for long-distance displacements along the inclusions; once a given inclusion has been fixed, $\mathbf{y} = (y_1, y_2, y_3)$ describes short-distance displacement around it*

4.1.2. *The hierarchies of equations in the inner and outer regions*

Now, we can define two regions and the expansions of the fields in these regions. The *outer region* is the one where only the propagating wave exists, that is, far enough from the structure to consider that the evanescent field is negligible. This field vanishes exponentially with a spatial decay of the order of ε, hence the outer region corresponds to $|x_1| \gg \varepsilon$. There, only the macroscopic coordinate is needed; accordingly, the pressure and velocity are expanded in the form

$$\text{Outer region:} \quad \begin{cases} p = p^0(\mathbf{x}, t) + \varepsilon p^1(\mathbf{x}, t) + \cdots, \\ \mathbf{u} = \mathbf{u}^0(\mathbf{x}, t) + \varepsilon \mathbf{u}^1(\mathbf{x}, t) + \cdots. \end{cases} \qquad [4.3]$$

The *inner region* corresponds to the region in the vicinity of the inclusions and it has an extent much smaller than the typical wavelength, $|x_1| \ll 1/k$. There, to account for the evanescent field, the coordinate $\mathbf{y}$ is needed and, as previously said, $\mathbf{x}'$ is kept as an additional coordinate to account for long-distance displacements along the structure. Thus, the expansions are sought in the form

$$\text{Inner region:} \quad \begin{cases} p = q^0(\mathbf{y}, \mathbf{x}', t) + \varepsilon q^1(\mathbf{y}, \mathbf{x}', t) + \cdots, \\ \mathbf{u} = \mathbf{v}^0(\mathbf{y}, \mathbf{x}', t) + \varepsilon \mathbf{v}^1(\mathbf{y}, \mathbf{x}', t) + \cdots. \end{cases} \qquad [4.4]$$

As a result, the differential operator reads differently in the two regions, with

$$\begin{cases} \text{in the outer region:} & \nabla \to \nabla_{\mathbf{x}}, \\ \text{in the inner region:} & \nabla \to \nabla_{\mathbf{x}'} + \dfrac{1}{\varepsilon}\nabla_{\mathbf{y}}. \end{cases} \quad [4.5]$$

In the following, the expansions [4.3] and [4.4] will be plugged into equations [4.1] using equations [4.5], and a hierarchy of equations will be obtained by identifying the terms with the same power of ε (in the inner and outer regions). Specifically, we obtain that linearized Euler equations apply for the outer terms at each order, namely

$$\chi \frac{\partial p^n}{\partial t} + \mathrm{div}_{\mathbf{x}} \mathbf{u}^n = 0, \quad \rho \frac{\partial \mathbf{u}^n}{\partial t} = -\nabla_{\mathbf{x}} p^n, \quad n = 0, 1, \cdots, \quad [4.6]$$

but the boundary conditions on the rigid inclusions (and on the rigid wall) do not apply since the outer terms are only valid far from the structure. Next, in the inner region, the hierarchy of equations is read as

$$\begin{cases} \mathrm{div}_{\mathbf{y}} \mathbf{v}^0 = 0, \quad \nabla_{\mathbf{y}} q^0 = 0, \\ \chi \dfrac{\partial q^n}{\partial t} + \mathrm{div}_{\mathbf{x}} \mathbf{v}^n + \mathrm{div}_{\mathbf{y}} \mathbf{v}^{n+1} = 0, \quad \rho \dfrac{\partial \mathbf{v}^n}{\partial t} = -\nabla_{\mathbf{x}} q^n - \nabla_{\mathbf{y}} q^{n+1}, \quad n = 0, 1, \cdots. \end{cases} \quad [4.7]$$

As in the classical homogenization, the hierarchy of equations in the inner problem starts with $\nabla_{\mathbf{y}} q^0 = 0$, whence q^0 does not depend on $\mathbf{y}$. This simple result is given for free and it is essential to enter serenely in the resolution of the equations, order by order.

4.1.3. *The matching conditions*

At this stage, the inner and outer problems have to be complemented by boundary conditions. Indeed, as y_1 is unbounded when moving away from the inclusions, there are missing boundary conditions for $|y_1| \to +\infty$. Reversely, in the outer region, boundary conditions when approaching the structure are missing; those are precisely the conditions that we are looking for. These conditions are provided simultaneously by the so-called *matching conditions*, which tell us that the outer and inner solutions coincide in an intermediate region. To get an idea, this intermediate region can be seen as the region where $x_1 \sim O(\sqrt{\varepsilon}) \to 0$ in the outer problem, yielding $y_1 = x_1/\varepsilon \sim O(1/\sqrt{\varepsilon}) \to +\infty$ in the inner problem. Using $x_1 = \varepsilon y_1$ in [4.3], and re-expanding in power of ε, provides the matching conditions at the order 1:

$$p^0(0^{\pm}, \mathbf{x}', t) = \lim_{y_1 \to \pm\infty} q^0(\mathbf{y}, \mathbf{x}', t), \quad \mathbf{u}^0(0^{\pm}, \mathbf{x}', t) = \lim_{y_1 \to \pm\infty} \mathbf{v}^0(\mathbf{y}, \mathbf{x}', t), \quad [4.8]$$

and at the order 2:

$$\begin{cases} p^1(0^{\pm},\mathbf{x}',t) = \lim\limits_{y_1\to\pm\infty}\left(q^1(\mathbf{y},\mathbf{x}',t) - y_1\dfrac{\partial p^0}{\partial x_1}(0^{\pm},\mathbf{x}',t)\right), \\ \mathbf{u}^1(0^{\pm},\mathbf{x}',t) = \lim\limits_{y_1\to\pm\infty}\left(\mathbf{v}^1(\mathbf{y},\mathbf{x}',t) - y_1\dfrac{\partial \mathbf{u}^0}{\partial x_1}(0^{\pm},\mathbf{x}',t)\right). \end{cases} \quad [4.9]$$

It is worth noting that the relations above already tell us that, far from the structure, (i) the inner fields $(q^0, \mathbf{v}^0)$ do not depend on $\mathbf{y}'$ anymore, which is quite intuitive, and (ii) the fields $(q^1, \mathbf{v}^1)$ have a linear dependence in y_1, which is less intuitive.

4.2. Effective boundary condition on a structured rigid wall

We start with the case of a structured wall, that is, for inclusions located in the vicinity of a rigid wall, or in contact with it (Figure 4.3). We can establish the effective boundary condition on an equivalent, or effective, surface Σ_e; see [4.2]. As previously said, in the outer region above and far away for the inclusions, [4.6] applies for each term of [4.3]. In the inner region, we can use [4.7] along with [4.4]; note that the matching conditions apply for $y_1 \to +\infty$ only, while the presence of the rigid wall imposes a vanishing normal velocity at $y_1 = -e/h$.

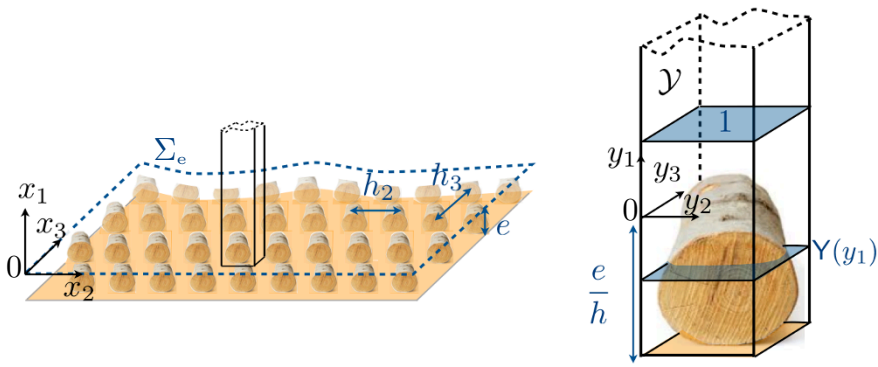

Figure 4.3. *A structured rigid wall: array of inclusions in the vicinity of a rigid wall. The elementary cell $\mathcal{Y}$ contains single inclusions in $\mathbf{y}$ coordinate, with $y_1 \in (-e/h, +\infty)$ (with $h = \sqrt{h_1 h_2}$)*

4.2.1. *A trivial boundary condition at the order 1*

We start with [4.7] at the leading order. As already said, $\nabla_{\mathbf{y}} q^0 = 0$ tells us that q^0 does not depend on $\mathbf{y}$, whence

$$\boxed{q^0 = p^0(0, \mathbf{x}', t),}$$

from the matching condition [4.8]. Next, integrating the relation $\mathrm{div}_{\mathbf{y}} \mathbf{v}^0 = 0$ over $\mathcal{Y}$ leaves us with

$$0 = \int_{\mathcal{Y}} \mathrm{div}_{\mathbf{y}} \mathbf{v}^0(\mathbf{y}, \mathbf{x}', t) \mathrm{d}\mathbf{y} = \int_{\mathsf{Y}(+\infty)} v_1^0(+\infty, \mathbf{y}', \mathbf{x}', t) \mathrm{d}\mathbf{y}' = u_1^0(0, \mathbf{x}', t), \qquad [4.10]$$

$$\boxed{u_1^0(0, \mathbf{x}', t) = 0,}$$

where we used (i) the Neumann boundary conditions on the rigid inclusions and on the rigid wall and (ii) the matching condition [4.8] for $\mathbf{v}^0$. At the dominant order, only the rigid wall is seen by the wave and we need to go to the next order to capture the boundary layer effects due to the presence of the inclusions.

4.2.2. *A less trivial boundary condition at the order 2*

We already know that $q^0(\mathbf{x}', t) = p^0(0, \mathbf{x}', t)$ is independent of $\mathbf{y}$, and from [4.7], the resolution at the second order starts with the problem on $(q^1, \mathbf{v}^0)$. Specifically from [4.7], we have

$$(S) \begin{cases} \text{In } \mathcal{Y}\text{: } \mathrm{div}_{\mathbf{y}} \mathbf{v}^0 = 0, \quad \rho \dfrac{\partial \mathbf{v}^0}{\partial t} = -\nabla_{\mathbf{y}} q^1 - \nabla_{\mathbf{x}'} p^0(0, \mathbf{x}', t), \\ \text{b.c.:} \quad \mathbf{v}^0 \cdot \mathbf{n}_{|\Gamma} = 0, \quad \text{and } v_1^0 = 0, \quad \text{at } y_1 = -e/h, \\ \qquad q^1, \mathbf{v}^0 \ \mathbf{y}'\text{-periodic}, \\ \qquad \lim\limits_{y_1 \to +\infty} \rho \dfrac{\partial}{\partial t} \mathbf{v}^0 = -\nabla_{\mathbf{x}'} p^0(0, \mathbf{x}', t). \end{cases}$$

The boundary conditions, with vanishing normal velocity on the rigid inclusions and on the wall, are supplemented by the conditions of $\mathbf{y}'$-periodicity and by the matching condition [4.8] for $\mathbf{v}^0$, which ensures that the above problem (S) is well posed. It is worth noting that we wrote the matching condition accounting for (i) the

condition $u_1^0(0,\mathbf{x}',t) = 0$ that we have obtained previously and (ii) the relation $\rho\partial_t u_\alpha^0 = -\partial_{x_\alpha} p^0$ from [4.6].

It can be noticed that the relation $\mathrm{div}_{\mathbf{y}}\mathbf{v}^0 = 0$ has been used twice. In the preceding section, we used it once integrated over $\mathcal{Y}$, which has provided the boundary condition for u_1^0. Here it is used again in a strong form. This is the game, when conducting the analysis, between getting averaged information (over $\mathcal{Y}$), which is at the end the information that is sought, and getting information on the local behavior of the inner terms which encapsulate the boundary layer effects.

The system (S) is set on $(q^1,\mathbf{v}^0)$ in $\mathbf{y}$ coordinate (and time t) where $\mathbf{x}'$ appears as a parameter. This means that, although $\nabla_{\mathbf{x}'}p^0(0,\mathbf{x}',t)$ is unknown, it plays the role of an external forcing in (S). Moreover, as (S) holds for any $\nabla_{\mathbf{x}'}p^0(0,\mathbf{x}',t)$, we can invoke the linearity of the problem with respect to $\partial_{x_\alpha}p^0(0,\mathbf{x}',t)$, and set the following decompositions:

$$(D)\quad \begin{cases} q^1(\mathbf{y},\mathbf{x},t) = \dfrac{\partial p^0}{\partial x_\alpha}(0,\mathbf{x}',t)Q_\alpha(\mathbf{y}) + \langle q^1\rangle(\mathbf{x}',t), \\ \rho\dfrac{\partial \mathbf{v}^0}{\partial t}(\mathbf{y},\mathbf{x},t) = -\dfrac{\partial p^0}{\partial x_\alpha}(0,\mathbf{x}',t)\,\nabla_{\mathbf{y}}\left(Q_\alpha(\mathbf{y}) + y_\alpha\right), \end{cases}$$

where $Q_\alpha(\mathbf{y})$, of zero mean over $\mathcal{Y}$ (denoted $\langle Q_\alpha\rangle$), are solutions of the elementary problems:

$$\begin{cases} \text{In } \mathcal{Y}\text{: } \Delta_{\mathbf{y}}Q_\alpha = 0, \\ \text{b.c.: } \nabla_{\mathbf{y}}(Q_\alpha + y_\alpha)\cdot\mathbf{n}_{|\Gamma} = 0, \quad \text{and} \quad \dfrac{\partial Q_\alpha}{\partial y_1} = 0, \text{ at } y_1 = -e/h, \\ \qquad Q_\alpha, \nabla_{\mathbf{y}}Q_\alpha \ \mathbf{y}'\text{-periodic}, \\ \qquad \lim\limits_{y_1\to+\infty}\nabla Q_\alpha = \mathbf{0}. \end{cases} \qquad [4.11]$$

The invoked "linearity" means that, once the Q_α satisfies the elementary problems, $(q^1,\mathbf{v}^0)$ satisfies (S) for any $\nabla_{\mathbf{x}'}p^0(0,\mathbf{x}',t)$. For instance, the problem on Q_2 is obtained by setting, in (S), $q^1 = Q_2$ for $\partial_{x_2}p^0(0,\mathbf{x}',t) = 1$ and $\partial_{x_3}p^0(0,\mathbf{x}',t) = 0$. The interest in solving the elementary problems rather than (S) is obvious. Indeed, (S) is a time-dependent problem which has to be solved for specific source and radiation conditions (since p^0 and its spatial derivatives have to be determined). On the contrary, the elementary problems are static problems which depend only on the microstructure. As such, (i) they can be solved more easily than

the initial problem and (ii) they can be solved once and for all independently of the specific scattering problem that will be considered afterwards.

We can observe that, once the elementary problems have been solved, they provide the effective parameters, which enter in the effective boundary conditions. In the present case, we are looking for a boundary condition on $u_1^1(0,\mathbf{x}',t)$ (we already know that $u_1^0(0,\mathbf{x}',t)=0$). To that aim, we integrate over $\mathcal{Y}(y_1^m)$ the time derivative version of the equation of mass conservation in [4.7] for $n=0$, namely

$$\rho\frac{\partial}{\partial t}\int_{\mathcal{Y}(y_1^m)}\left(\chi\frac{\partial p^0}{\partial t}(0,\mathbf{x}',t)+\mathrm{div}_{\mathbf{x}'}\mathbf{v}^0+\mathrm{div}_{\mathbf{y}}\mathbf{v}^1\right)\mathrm{d}\mathbf{y}=0, \qquad [4.12]$$

where we again used that $q^0(\mathbf{x}',t)=p^0(0,\mathbf{x}',t)$. This step is the second iteration of the averaging process, which we have already done in the preceding section by integrating the relation $\mathrm{div}_{\mathbf{y}}\mathbf{v}^0=0$. It is here slightly more involved (and as such it will provide a slightly less trivial condition). Let us calculate each of the above integrals.

– The first integral involves a term that is independent of $\mathbf{y}$, whence

$$\rho\frac{\partial}{\partial t}\int_{\mathcal{Y}(y_1^m)}\chi\frac{\partial p^0}{\partial t}(0,\mathbf{x}',t)\mathrm{d}\mathbf{y}=\Delta_{\mathbf{x}}p^0(0,\mathbf{x}',t)\,\mathcal{V}(y_1^m), \qquad [4.13]$$

where we used [4.6] for $n=0$, and with $\mathcal{V}(y_1^m)$ being the volume of $\mathcal{Y}(y_1^m)$ (obviously $\mathcal{V}(y_1^m)$ diverges for $y_1^m\to+\infty$).

– The second integral in [4.12] is calculated owing to the decomposition of $\mathbf{v}^0$ in (D) and we get

$$\begin{aligned}\rho\frac{\partial}{\partial t}\int_{\mathcal{Y}(y_1^m)}\mathrm{div}_{\mathbf{x}'}\mathbf{v}^0\mathrm{d}\mathbf{y}=&-\frac{\partial^2 p^0}{\partial x_\alpha\partial x_\beta}(0,\mathbf{x}',t)\int_{\mathcal{Y}(y_1^m)}\frac{\partial Q_\alpha}{\partial y_\beta}\mathrm{d}\mathbf{y}\\&-\Delta_{\mathbf{x}'}p^0(0,\mathbf{x}',t)\,\mathcal{V}(y_1^m).\end{aligned} \qquad [4.14]$$

– Eventually, the third integral is evaluated owing to the matching condition [4.9] for $\mathbf{v}^1$ in the limit of large y_1^m, and leaves us with

$$\begin{aligned}\rho\frac{\partial}{\partial t}\int_{\mathcal{Y}(y_1^m)}\mathrm{div}_{\mathbf{y}}\mathbf{v}^1\mathrm{d}\mathbf{y}&\underset{y_1^m\to+\infty}{\sim}\rho\frac{\partial}{\partial t}\int_{\mathrm{Y}(y_1^m)}\left(u_1^1(0,\mathbf{x}',t)+y_1^m\frac{\partial u_1^0}{\partial x_1}(0,\mathbf{x}',t)\right)\mathrm{d}\mathbf{y}',\\&\underset{y_1^m\to+\infty}{\sim}\rho\frac{\partial}{\partial t}\left(u_1^1(0,\mathbf{x}',t)+y_1^m\frac{\partial u_1^0}{\partial x_1}(0,\mathbf{x}',t)\right).\end{aligned} \qquad [4.15]$$

With our choice of the origin at a distance e/h above the rigid wall (in $\mathbf{y}$ coordinate), we have $\mathcal{V}(y_1^m) = y_1^m + \varphi$, with

$$\boxed{\varphi \text{ the volume of the fluid for } y_1 \in (-e/h, 0), \text{ (and } 0 \leq \varphi \leq e/h),}$$

whence $\varphi = e/h - \mathcal{V}_{\text{inc}}$, with $\mathcal{V}_{\text{inc}}$ being the actual volume of the inclusion rescaled by h^2. Gathering the three integrals above, the terms linear in y_1^m cancel, which leaves us with

$$\rho \frac{\partial u_1^1}{\partial t}(0, \mathbf{x}', t) = -\varphi \frac{\partial^2 p^0}{\partial x_1^2}(0, \mathbf{x}', t) - A_{\alpha\beta} \frac{\partial^2 p^0}{\partial x_\alpha \partial x_\beta}(0, \mathbf{x}', t), \qquad [4.16]$$

and eventually with

$$\boxed{u_1^1(0, \mathbf{x}', t) = \varphi \frac{\partial u_1^0}{\partial x_1}(0, \mathbf{x}', t) + A_{\alpha\beta} \frac{\partial u_\alpha^0}{\partial x_\beta}(0, \mathbf{x}', t),} \qquad [4.17]$$

where

$$\boxed{A_{\alpha\beta} = -\int_{\mathcal{Y}} \frac{\partial Q_\alpha}{\partial y_\beta} \mathrm{d}\mathbf{y}.} \qquad [4.18]$$

It is worth noting that $A_{\alpha\beta}$ is finite since $\nabla_{\mathbf{y}} Q_\alpha$ vanishes when $y_1 \to +\infty$ (it vanishes exponentially).

REMARK 4.1.– The expression of $\mathcal{V}(y_1^m)$ in [4.14]–[4.15] depends on the choice of the origin $y_1 = 0$ with respect to the position of the actual wall. In any case, $\mathcal{V}(y_1^m)$ can be written as $\mathcal{V}(y_1^m) = y_1^m + \eta$, with η a constant. We can see that a positive value of η is suitable when the energy is considered (see section 4.4) and our choice of the origin with $\eta = \varphi$ ensures that the inclusion is entirely comprised in $y_1 = (-e/h, 0)$.

4.2.3. *Construction of a unique problem*

The hierarchy of problems on $(p^0, \mathbf{u}^0)$ and $(p^1, \mathbf{u}^1)$ can be solved iteratively. In the present case, the problem on $(p^0, \mathbf{u}^0)$ corresponds to the problem of scattering over a rigid wall on its own (but shifted to a new position). Once the solution $(p^0, \mathbf{u}^0)$ has been calculated for a given source and appropriate radiation conditions, it can be used to feed the problem on $(p^1, \mathbf{u}^1)$, being that of the scattering over a wall with boundary condition [4.17] being dependent on $\mathbf{u}^0$. It is more convenient, for several reasons that we cannot detail here, to build a unique problem on $(p^{\text{ef}}, \mathbf{u}^{\text{ef}})$ such that p^{ef} and $\mathbf{u}^{\text{ef}}$ admit the same expansions as $(p^0+\varepsilon p^1)$ and $(\mathbf{u}^0+\varepsilon\mathbf{u}^1)$ up to $O(\varepsilon^2)$, hence the same expansions as p and $\mathbf{u}$ up to $O(\varepsilon^2)$. This unique problem on $(p^{\text{ef}}, \mathbf{u}^{\text{ef}})$ is such that $(p^{\text{ef}}, \mathbf{u}^{\text{ef}})$ satisfies the linearized Euler equation in the fluid and the effective boundary condition

$$\boxed{u_1^{\text{ef}}(0, \mathbf{x}', t) = h\varphi \frac{\partial u_1^{\text{ef}}}{\partial x_1}(0, \mathbf{x}', t) + hA_{\alpha\beta} \frac{\partial u_\alpha^{\text{ef}}}{\partial x_\beta}(0, \mathbf{x}', t),}$$

which was announced in [4.2]. This is because, denoting $\mathbf{u}^a = \mathbf{u}^0+\varepsilon\mathbf{u}^1$ (with $\varepsilon = h$), we have from [4.17] that

$$\begin{aligned} u_1^a(0, \mathbf{x}', t) &= h\varphi \frac{\partial(u_1^a - \varepsilon u_1^1)}{\partial x_1}(0, \mathbf{x}', t) + hA_{\alpha\beta} \frac{\partial(u_\alpha^a - \varepsilon u_\alpha^1)}{\partial x_\beta}(0, \mathbf{x}', t) \\ &= h\varphi \frac{\partial u_1^a}{\partial x_1}(0, \mathbf{x}', t) + hA_{\alpha\beta} \frac{\partial u_\alpha^a}{\partial x_\beta}(0, \mathbf{x}', t) + O(\varepsilon^2), \end{aligned}$$

and obviously, $p^a = p^0 + \varepsilon p^1$ and $\mathbf{u}^a$ satisfy linearized Euler equations.

4.3. Effective jump conditions across a structured film

We now move on to the case where the thin structure is surrounded by the fluid (Figure 4.4). In this case, we are looking for an effective problem in which the whole structure has been replaced by effective transmission, or jump, conditions.

As discussed previously, equations [4.6] apply at each order in the outer regions above and below the inclusions (and far enough from them) and equations [4.7] apply in the inner region. The difference is that the condition of vanishing normal velocity on the rigid wall is replaced by matching conditions at $y_1 \to -\infty$ given by [4.8]–[4.9].

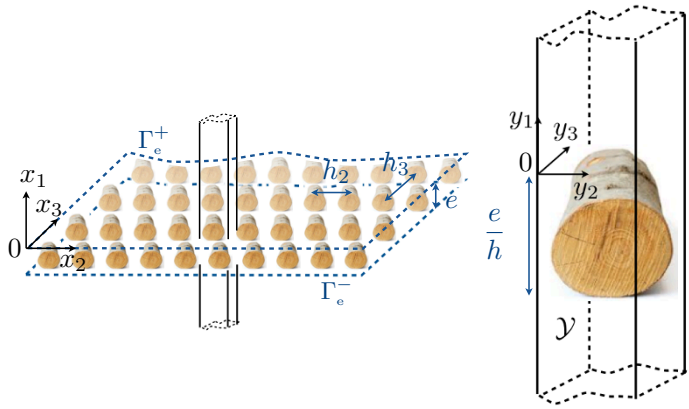

Figure 4.4. *A structured film: array of inclusions in a surrounding fluid. The elementary cell contains a single inclusion in* $\mathbf{y}$*-coordinate, with* $y_1 \in (-\infty, +\infty)$

4.3.1. *Jump conditions at the order 1*

As in the preceding section, we start with $\nabla_{\mathbf{y}} q^0 = \mathbf{0}$, hence

$$q^0(\mathbf{x}', t) = p^0(0^{\pm}, \mathbf{x}', t). \qquad [4.19]$$

Next, integrating over $\mathcal{Y}$ the relation $\mathrm{div}_{\mathbf{y}} \mathbf{v}^0 = 0$ leaves us with

$$\begin{aligned} 0 &= \int_{\mathrm{Y}(+\infty)} v_1^0(\mathbf{y}, \mathbf{x}', t)\, \mathrm{d}\mathbf{y}' - \int_{\mathrm{Y}(-\infty)} v_1^0(\mathbf{y}, \mathbf{x}', t)\, \mathrm{d}\mathbf{y}' \\ &= u_1^0(0^+, \mathbf{x}', t) - u_1^0(0^-, \mathbf{x}', t). \end{aligned}$$

It follows that the jump conditions read as

$$\boxed{\left[p^0\right]_{(0)} = \left[u_1^0\right]_{(0)} = 0,} \qquad [4.20]$$

which means that the array is not seen by the wave and the usual continuities of the pressure and of the normal velocity apply at the dominant order.

4.3.2. *Jump conditions at the order 2*

To conduct the analysis at the second order, we start with the problem on $(q^1, \mathbf{v}^0)$, which is slightly modified with respect to its *alter ego* (S); it reads as

$$(s)\begin{cases} \text{In } \mathcal{Y}\text{: } \operatorname{div}_{\mathbf{y}} \mathbf{v}^0 = 0, \quad \rho \dfrac{\partial \mathbf{v}^0}{\partial t} = -\nabla_{\mathbf{y}} q^1 - \nabla_{\mathbf{x}'} p^0(0, \mathbf{x}', t), \\ \text{b.c.: } \quad \mathbf{v}^0 \cdot \mathbf{n}_{|\Gamma} = 0, \quad q^1, \mathbf{v}^0 \ \mathbf{y}\text{'-periodic}, \\ \qquad \lim\limits_{y_1 \to \pm\infty} \rho \dfrac{\partial}{\partial t} \mathbf{v}^0 = -\nabla_{\mathbf{x}} p^0(0, \mathbf{x}', t). \end{cases}$$

We have used that $\nabla_{\mathbf{x}} p^0$ is continuous at $x_1 = 0$ from the preceding section, since (i) $\partial_{x_1} p^0 = -\rho \partial_t u_1^0$ is continuous at $x_1 = 0$ because u_1^0 is continuous at $x_1 = 0$, and (ii) $\nabla_{\mathbf{x}'} p^0$ is continuous because $p^0(0, \mathbf{x}', t)$ is continuous. The system (s) is linear with respect to $\partial_{x_i} p^0(0, \mathbf{x}', t)$ and we use the decomposition

$$(d)\begin{cases} q^1(\mathbf{y}, \mathbf{x}', t) = \dfrac{\partial p^0}{\partial x_i}(0, \mathbf{x}', t) Q_i(\mathbf{y}) + \langle q^1 \rangle(\mathbf{x}', t), \\ \rho \dfrac{\partial \mathbf{v}^0}{\partial t}(\mathbf{y}, \mathbf{x}', t) = -\dfrac{\partial p^0}{\partial x_i}(0, \mathbf{x}', t) \nabla_{\mathbf{y}} Q_i(\mathbf{y}) - \nabla_{\mathbf{x}'} p^0(0, \mathbf{x}', t), \end{cases}$$

where the elementary solutions Q_i, of zero average, are solutions of the elementary problems:

$$\begin{cases} \text{In } \mathcal{Y}\text{: } \Delta_{\mathbf{y}} Q_1 = 0, \\ \text{b.c.: } \quad \nabla_{\mathbf{y}} Q_1 \cdot \mathbf{n}_{|\Gamma} = 0, \qquad Q_1, \nabla_{\mathbf{y}} Q_1 \ \mathbf{y}\text{'-periodic}, \\ \qquad \lim\limits_{y_1 \to \pm\infty} \nabla_{\mathbf{y}} Q_1 = \mathbf{e}_1, \end{cases}$$

$$\begin{cases} \text{In } \mathcal{Y}\text{: } \Delta_{\mathbf{y}} Q_\alpha = 0, \\ \text{b.c.: } \quad \nabla_{\mathbf{y}} (Q_\alpha + y_\alpha) \cdot \mathbf{n}_{|\Gamma} = 0, \ Q_\alpha, \nabla_{\mathbf{y}} Q_\alpha \ \mathbf{y}\text{'-periodic}, \\ \qquad \lim\limits_{y_1 \to \pm\infty} \nabla_{\mathbf{y}} Q_\alpha = \mathbf{0}. \end{cases} \qquad [4.21]$$

Again, as soon as the Q_i are solutions of the elementary problems, $(q^1, \mathbf{v}^0)$ are solutions of (s) for any $\nabla_{\mathbf{x}} p^0(0, \mathbf{x}', t)$. Moreover, and as already stressed, the elementary problems are simple static problems which depend only on the considered microstructure.

In the previous section, a boundary condition on u_1^1 was sought; here, we want to derive jumps in p^1 and u_1^1 (we already know that p^0 and u_1^0 have zero jumps). Owing to the matching conditions [4.9] for p^1, along with the decomposition (d), the jump in the pressure simply follows from the limits Q_i when $y_1 \to \pm\infty$. The limits of the Q_i are known from the limits of their gradients up to constants; specifically from [4.21] they read as

$$\boxed{Q_1 \underset{y\to\pm\infty}{\sim} y_1 + B_1^{\pm}, \quad Q_\alpha \underset{y\to\pm\infty}{\sim} B_\alpha^{\pm},}$$

and the values of the $B_i^{\pm}$ are known once the elementary problems have been solved. It is easy to see that the term linear in y_1 in the matching condition [4.9] for p^1 is compensated by the term linear in Q_1 when $y_1 \to \pm\infty$, and we obtain that

$$\begin{cases} p^1(0^-, \mathbf{x}', t) = B_1^- \dfrac{\partial p^0}{\partial x_1}(0, \mathbf{x}', t) + B_\alpha^- \dfrac{\partial p^0}{\partial x_\alpha}(0, \mathbf{x}', t) + \langle q^1 \rangle(\mathbf{x}', t), \\ p^1(0^+, \mathbf{x}', t) = B_1^+ \dfrac{\partial p^0}{\partial x_1}(0, \mathbf{x}', t) + B_\alpha^+ \dfrac{\partial p^0}{\partial x_\alpha}(0, \mathbf{x}', t) + \langle q^1 \rangle(\mathbf{x}', t). \end{cases}$$

The jump in p^1 immediately follows, of the form

$$\boxed{\left[p^1\right]_{(0)} = \hat{B}_i \frac{\partial p^0}{\partial x_i}(0, \mathbf{x}', t),} \qquad [4.22]$$

with

$$\boxed{\hat{B}_i = B_i^+ - B_i^-.}$$

We still have to determine the jump in u_1^1, and to do so we integrate over $\mathcal{Y}$ the relation $\chi \partial_t p^0(0, \mathbf{x}', t) + \operatorname{div}_{\mathbf{x}'} \mathbf{v}^0 + \operatorname{div}_{\mathbf{y}} \mathbf{v}^1 = 0$ from [4.7], once differentiated with respect to time t; see [4.12] (and here, only the definition of $\mathcal{Y}$ has changed). We find

three integrals which have essentially the same forms as in the preceding section and for the same reasons; see [4.13]–[4.15]. Specifically:

– The first integral is given by

$$\rho\frac{\partial}{\partial t}\int_{\mathcal{Y}(y_1^m)}\chi\frac{\partial p^0}{\partial t}(0,\mathbf{x}',t)\mathrm{d}\mathbf{y}=\Delta_{\mathbf{x}}p^0(0,\mathbf{x}',t)\,\mathcal{V}(y_1^m),$$

and $\mathcal{V}(y_1^m)=2y_1^m-\mathcal{V}_{\text{inc}}$ still diverges when $y_1^m\to+\infty$. In the following, and to draw a parallel with the case of a structured wall, we use $\mathcal{V}_{\text{inc}}=e/h-\varphi$; this will be helpful when the final jumps are specified.

– The second integral is calculated owing to the decomposition of $\mathbf{v}^0$ in (d), and thus it involves a term in $\partial_{x_1}p^0_{|x_1=0}$ which was zero in the preceding section, namely

$$\begin{aligned}\rho\frac{\partial}{\partial t}\int_{\mathcal{Y}(y_1^m)}\mathrm{div}_{\mathbf{x}'}\mathbf{v}^0\mathrm{d}\mathbf{y}=&-\frac{\partial^2 p^0}{\partial x_\alpha\partial x_i}(0,\mathbf{x}',t)\int_{\mathcal{Y}(y_1^m)}\frac{\partial Q_i}{\partial y_\alpha}\mathrm{d}\mathbf{y}\\&-\Delta_{\mathbf{x}'}p^0(0,\mathbf{x}',t)\,\mathcal{V}(y_1^m).\end{aligned}$$

– The third integral is evaluated owing to the matching conditions [4.9] at $y_1=\pm y_1^m$ in the limit of large y_1^m, which leaves us with

$$\begin{aligned}\rho\frac{\partial}{\partial t}\int_{\mathcal{Y}(y_1^m)}\mathrm{div}_{\mathbf{y}}\mathbf{v}^1\mathrm{d}\mathbf{y}&\underset{y_1^m\to+\infty}{\sim}\rho\frac{\partial}{\partial t}\int_{\Upsilon(y_1^m)}\left(u_1^1+y_1^m\frac{\partial u_1^0}{\partial x_1}\right)_{|x_1=0^+}\\&-\rho\frac{\partial}{\partial t}\int_{\Upsilon(-y_1^m)}\left(u_1^1-y_1^m\frac{\partial u_1^0}{\partial x_1}\right)_{|x_1=0^-}\\&\underset{y_1^m\to+\infty}{\sim}\rho\frac{\partial}{\partial t}\left(\left[u_1^1\right]_{(0)}+2y_1^m\frac{\partial u_1^0}{\partial x_1}(0,\mathbf{x}',t)\right).\end{aligned}$$

It is worth noting that we made use of the continuity of $\partial_{x_1}u_1^0$ at $x_1=0$; this continuity is given by the conservation of the momentum in [4.7], with $\partial_{x_1}u_1^0=-\partial_{x_\alpha}u_\alpha^0-\chi\partial_t p^0$ (and both $\partial_{x_\alpha}u_\alpha^0$ and $\partial_t p^0$ are continuous). Gathering the three integrals yields the jump condition on u_1^1 of the form

$$\rho\frac{\partial}{\partial t}\left[u_1^1\right]_{(0)}=-\rho\frac{\partial}{\partial t}\left(\frac{e}{h}-\varphi\right)\frac{\partial u_1^0}{\partial x_1}(0,\mathbf{x}',t)+\frac{\partial^2 p^0}{\partial x_i\partial x_\alpha}(0,\mathbf{x}',t)\int_{\mathcal{Y}}\frac{\partial Q_i}{\partial y_\alpha}\mathrm{d}\mathbf{y},$$

which can be rewritten, omitting the time derivative, as

$$\boxed{\left[u_1^1\right]_{(0)}=-\left(\frac{e}{h}-\varphi\right)\frac{\partial u_1^0}{\partial x_1}(0,\mathbf{x}',t)+C_{i\alpha}\frac{\partial u_i^0}{\partial x_\alpha}(0,\mathbf{x}',t),}\qquad[4.23]$$

where

$$\boxed{C_{i\alpha} = -\int_{\mathcal{Y}} \frac{\partial Q_i}{\partial y_\alpha}(\mathbf{y})\mathrm{d}\mathbf{y}.} \qquad [4.24]$$

REMARK 4.2.– In [4.23], the coefficient $-(e/h-\varphi)$ associated with $\partial_{x_1} u_1^0(0,\mathbf{x}',t)$ is negative since $(e/h-\varphi)$ represents the (rescaled) volume of the inclusion. *We will see below that this jump condition has to be slightly modified, or better said, can be slightly modified in order to obtain jump conditions with the suitable property of positive energy.*

4.3.3. *An alternative form of the effective jump conditions on a unique problem*

In the previous section, we wrote the effective boundary condition on a surface Σ_e at a distance e of the actual rigid plane (in $\mathbf{x}$ coordinate). Here we do a similar choice by writing the jumps across an *enlarged interface* of non-zero thickness (up to now they have been expressed across a zero-thickness interface at $x_1 = 0$). In both cases, these choices will be discussed in the last part of this chapter, where the energy conservation in the homogenized problems will be considered. For the time being, we just decide to write the jumps between $x_1 = -e$ and $x_1 = 0$. To begin with, we consider $p^a = p^0 + \varepsilon p^1$, and its values at both sides of the enlarged interface

$$\begin{cases} p^a(-e,\mathbf{x}',t) = p^0(-e,\mathbf{x}',t) + \varepsilon p^1(-e,\mathbf{x}',t) \\ \qquad\qquad\quad = p^0(0,\mathbf{x}',t) + \varepsilon\left(-\dfrac{e}{h}\dfrac{\partial p^0}{\partial x_1}(0,\mathbf{x}',t) + p^1(0^-,\mathbf{x}',t)\right) + O(\varepsilon^2), \\ p^a(0^+,\mathbf{x}',t) = p^0(0,\mathbf{x}',t) + \varepsilon p^1(0^+,\mathbf{x}',t), \end{cases}$$

by using a Taylor expansion of $p^0(-e,\mathbf{x}',t)$ and of $p^1(-e,\mathbf{x}',t)$ in the vicinity of $x_1 = 0^-$ (and remember that $\varepsilon = h$). For $x_1 \in (-e,0)$, both fields are continuous, such that the Taylor expansions are valid. It follows that the new jump $[p^a]$ becomes

$$[p^a] = p^a(0^+,\mathbf{x}',t) - p^a(-e,\mathbf{x}',t) = \varepsilon\left(\left[p^1\right]_{(0)} + \frac{e}{h}\frac{\partial p^0}{\partial x_1}(0,\mathbf{x}',t)\right) + O(\varepsilon^2)$$

$$= \varepsilon\left(\hat{B}_i\frac{\partial p^0}{\partial x_i}(0,\mathbf{x}',t) + \frac{e}{h}\frac{\partial p^0}{\partial x_1}(0,\mathbf{x}',t)\right) + O(\varepsilon^2), \qquad [4.25]$$

where we used that p^0 is continuous from [4.19] and where $\left[p^1\right]_{(0)}$ is given by [4.22]. We also define the mean value of p^a on the interface by

$$\overline{p^a} = \frac{1}{2}\left(p^a(-e,\mathbf{x}',t) + p^a(0^+,\mathbf{x}',t)\right) = \overline{p^0} + \varepsilon\overline{p^1}. \qquad [4.26]$$

For now, it is sufficient to use that

$$\varepsilon \frac{\partial p^0}{\partial x_i}(0, \mathbf{x}', t) = \varepsilon \frac{\partial \overline{p^a}}{\partial x_i} + O(\varepsilon^2), \qquad [4.27]$$

which is obvious, along with [4.25], to get

$$[p^a] = \varepsilon \left(\hat{B}_i \frac{\partial \overline{p^a}}{\partial x_i} + \frac{e}{h} \frac{\partial \overline{p^a}}{\partial x_1} \right) + O(\varepsilon^2).$$

The same applies for $\mathbf{u}^a = \mathbf{u}^0 + \varepsilon \mathbf{u}^1$, resulting in an additional term $\varepsilon e/h \partial_{x_1} u_1^0(0, \mathbf{x}', t)$ in the jumps of u_1^1 (the calculation is similar and straightforward).

Now, we consider $(p^{\text{ef}}, \mathbf{u}^{\text{ef}})$ satisfying the linearized Euler equation for $x_1 \in (-\infty, -e) \cup (0, +\infty)$ and the jump conditions

$$\boxed{[p^{\text{ef}}] = \varepsilon B_i \frac{\partial \overline{p^{\text{ef}}}}{\partial x_i}, \qquad [u_1^{\text{ef}}] = \varepsilon \left(\varphi \frac{\partial \overline{u_1^{\text{ef}}}}{\partial x_1} + C_{i\alpha} \frac{\partial \overline{u_i^{\text{ef}}}}{\partial x_\alpha} \right),}$$

given in [4.2], and with

$$\boxed{B_1 = \hat{B}_1 + e/h, \text{and } B_\alpha = \hat{B}_\alpha}$$

(in [4.22]) and $C_{i\alpha}$ in [4.24]. It is easy to see that p^{ef} and $\mathbf{u}^{\text{ef}}$ admit the same expansions as p^a and $\mathbf{u}^a$ up to $O(\varepsilon^2)$, hence the same expansions as p and $\mathbf{u}$ up to $O(\varepsilon^2)$.

4.4. Considerations on the equation of energy conservation

In this section, we inspect the equation of energy conservation in the homogenized problem. We consider a bounded domain Ω which we can see as a computational domain where the effective problems are solved (Figure 4.5). The boundary $\partial\Omega$ contains the physical boundary Σ with the exterior; in the case (a), it also contains Σ_{e} where the effective boundary condition applies, and in the case (b), it contains $\Gamma_{\text{e}} = \Gamma_{\text{e}}^+ \cup \Gamma_{\text{e}}^-$, across which the jump conditions apply. Hence, $\partial\Omega = \Sigma \cup \Sigma_{\text{e}}$ and $\partial\Omega = \Sigma \cup \Gamma_{\text{e}}^+ \cup \Gamma_{\text{e}}^-$, respectively.

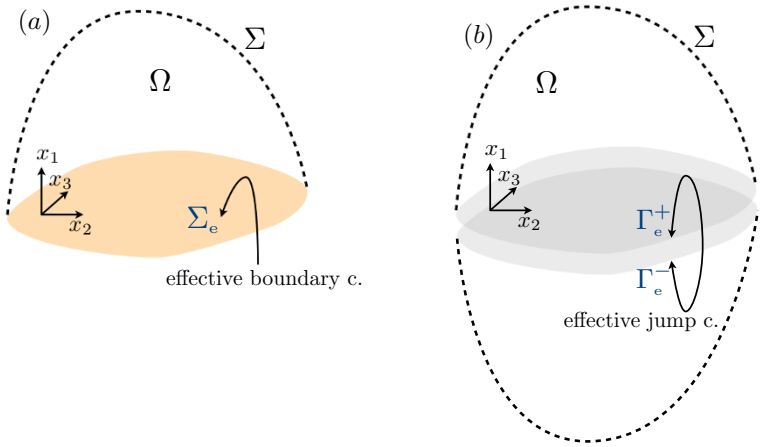

Figure 4.5. *Conservation of the energy in the effective problems. The conservation of energy is written in a bounded domain Ω, the boundary of which interrogates the effective conditions, on Σ_e for a structured wall (case (a)) and across $\Gamma_e = \Gamma_e{}^+ \cup \Gamma_e{}^-$ for a structured film (case (b))*

The equation of energy conservation is obtained from linearized Euler equations [4.1] by multiplying the equation of mass conservation by p and the equation of momentum conservation by $\mathbf{u}$ and by summing and integrating over Ω. We get the classical equation of energy conservation of the form

$$\begin{cases} \dfrac{d}{dt}\displaystyle\int_\Omega \mathcal{E}\,\mathrm{d}\mathbf{y} + \Phi = 0, \\ \text{with } \mathcal{E} = \dfrac{1}{2}\left(\chi p^2 + \rho u^2\right) \text{ the acoustic energy,} \\ \text{and } \Phi = \displaystyle\int_{\partial\Omega} p\mathbf{u}\cdot\mathbf{n}\,\mathrm{d}s \text{ the flux of the Poynting vector.} \end{cases} \qquad [4.28]$$

In general, the material boundaries of $\partial\Omega$ (a rigid wall or a material interface) do not contribute to Φ, and only the ingoing and outgoing fluxes across Σ have to be accounted for; hence, in the absence of such fluxes (e.g. Σ is a rigid wall), the acoustic energy is conserved in Ω. In the effective problems, the boundaries Σ_e or $\Gamma_e{}^\pm$ contribute to the fluxes, and we term these contributions Φ^{ef}; this is because the effective condition on Σ_e has non-vanishing $\mathbf{u}\cdot\mathbf{n}$ and non-vanishing p, and the fluxes through $\Gamma_e{}^\pm$ are not equilibrated because of the effective jumps. It is meaningful to show that the effective problems are associated with energies which, in the absence of fluxes across Σ, are conserved. To show this, Φ^{ef} has to be written as the time derivative of an effective energy $\mathcal{E}^{ef}$ supported by Σ_e or Γ_e. Besides, $\mathcal{E}^{ef}$ has to be positive. Loosely speaking, this ensures that, in the absence of fluxes through Σ, the

total energy $(\mathcal{E} + \mathcal{E}^{\text{ef}})$ is conserved in time, without possible time variations of $\mathcal{E}$ compensated by opposite time variations of $\mathcal{E}^{\text{ef}}$, which would foster numerical (and unphysical) instabilities. We can see that Φ^{ef} takes the following forms:

$$\Phi^{\text{ef}} = \frac{d}{dt}\mathcal{E}^{\text{ef}}, \quad \text{with:}$$

(a) **Effective energy supported by Σ_{e}:**

$$\mathcal{E}^{\text{ef}} = \frac{h}{2}\int_{\Sigma_{\text{e}}} \left(\varphi\chi\, p^2 + \rho\left(A_2 u_2^2 + A_3 u_3^2 - 2A_{23}u_2u_3\right)\right) \mathrm{d}\mathbf{x}', \qquad [4.29]$$

(b) **Effective energy supported by Γ_{e}:**

$$\mathcal{E}^{\text{ef}} = \frac{h}{2}\int_{\Gamma_{\text{e}}} \left(\varphi\chi\, \overline{p}^2 + \rho B_1 \overline{u_1}^2 + \rho\left(C_2\, \overline{u_2}^2 + C_3\, \overline{u_3}^2 - 2C_{23}\overline{u_2}\ \overline{u_3}\right)\right) \mathrm{d}\mathbf{x}',$$

where we defined $A_\alpha = \varphi - A_{\alpha\alpha}$ and $C_\alpha = \varphi - C_{\alpha\alpha}$. Hence, $\mathcal{E}^{\text{ef}} \geq 0$ if, for (a): $A_\alpha \geq 0$, $A_2A_3 - A_{23}^2 \geq 0$ and for (b): $B_1 \geq 0$, $C_\alpha \geq 0$, $C_2C_3 - C_{23}^2 \geq 0$.

In [4.29], we have omitted to specify that we are working with the effective fields and we have used $(p^{\text{ef}}, \mathbf{u}^{\text{ef}}) \to (p, \mathbf{u})$ for simplicity; we can keep this notation in this section.

4.4.1. *Energy $\mathcal{E}^{\text{ef}}$ supported by the effective surface Σ_{e}*

With $\mathbf{n}$ the normal exterior to $\partial\Omega$ in [4.28], it is easy to see that the flux on Σ_{e} reads as

$$\Phi^{\text{ef}} = -\int_{\Sigma_{\text{e}}} p(0, \mathbf{x}', t) u_1(0, \mathbf{x}', t) \mathrm{d}\mathbf{x}', \qquad [4.30]$$

and accounting for the boundary condition in [4.2], we get

$$\Phi^{\text{ef}} = -h\int_{\Sigma_{\text{e}}} p\left(\varphi\frac{\partial u_1}{\partial x_1} + A_{\alpha\beta}\frac{\partial u_\alpha}{\partial x_\beta}\right) \mathrm{d}\mathbf{x}'. \qquad [4.31]$$

We consider the two contributions in the above integral.

- $$\Phi_1^{\text{ef}} = -h\varphi \int_{\Sigma_e} p\,\frac{\partial u_1}{\partial x_1}\mathrm{d}\mathbf{x}' = h\varphi \int_{\Sigma_e} p\left(\chi\frac{\partial p}{\partial t} + \frac{\partial u_\alpha}{\partial x_\alpha}\right)\mathrm{d}\mathbf{x}'$$
$$= h\frac{\varphi\chi}{2}\frac{d}{dt}\int_{\Sigma_e} p^2\mathrm{d}\mathbf{x}' - h\varphi\int_{\Sigma_e}\frac{\partial p}{\partial x_\alpha}\,u_\alpha\mathrm{d}\mathbf{x}' + \text{b.t.}$$
$$= \frac{h\varphi}{2}\frac{d}{dt}\int_{\Sigma_e}\left(\chi\,p^2 + \rho\,{u_\alpha}^2\right)\mathrm{d}\mathbf{x}' + \text{b.t.},$$

where we first used the relation $\mathrm{div}\mathbf{u} + \chi\partial_t p = 0$, and after an integration by part of $p\partial_{x_\alpha}u_\alpha$, we used that $\partial_{x_\alpha}p = -\rho\partial_t u_\alpha$. It is worth noting that the integration by parts makes boundary terms (b.t.) appear at both extremities of Σ_e; they are disregarded here.

- $$\Phi_2^{\text{ef}} = -hA_{\alpha\beta}\int_{\Sigma_e} p\,\frac{\partial u_\alpha}{\partial x_\beta}\mathrm{d}\mathbf{x}' = -\rho\,hA_{\alpha\beta}\int_{\Sigma_e}\frac{\partial u_\beta}{\partial t}\,u_\alpha\mathrm{d}\mathbf{x}' + \text{b.t.},$$

using the same relations as for the first contributions. Eventually, with $A_{23} = A_{32}$ (see [A1.1] in Appendix 1), $\Phi^{\text{ef}} = \Phi_1^{\text{ef}} + \Phi_2^{\text{ef}}$ can be written as stated in [4.29].

4.4.2. *Energy $\mathcal{E}^{\text{ef}}$ supported by the effective interface Γ_e*

This case is similar to the previous one, now with

$$\Phi^{\text{ef}} = -\int_{\Gamma_e}[pu_1]\,\mathrm{d}\mathbf{x}' = -\int_{\Gamma_e}\left([p]\,\overline{u_1} + \overline{p}\,[u_1]\right)\mathrm{d}\mathbf{x}', \qquad [4.32]$$

hence, from [4.2],

$$\Phi^{\text{ef}} = -h\int_{\Gamma_e}\left(B_i\frac{\partial\overline{p}}{\partial x_i}\,\overline{u_1} + \overline{p}\left(\varphi\frac{\partial\overline{u_1}}{\partial x_1} + C_{i\alpha}\frac{\partial\overline{u_i}}{\partial x_\alpha}\right)\right)\mathrm{d}\mathbf{x}'. \qquad [4.33]$$

Again, we consider each term in the above integral, namely

- $$\Phi_1^{\text{ef}} = -hB_i\int_{\Gamma_e}\frac{\partial\overline{p}}{\partial x_i}\,\overline{u_1} = \rho\frac{hB_1}{2}\frac{d}{dt}\int_{\Gamma_e}\overline{u_1}^2 - hB_\alpha\int_{\Gamma_e}\frac{\partial\overline{p}}{\partial x_\alpha}\,\overline{u_1}.$$

The first term for $i = 1$ makes the time derivative of $\overline{u_1}^2$ since $\partial_{x_1}p = -\rho\partial_t\overline{u_1}$. For the time being, the second term in B_α is left as it is.

- $$\Phi_2^{\text{ef}} = -h\varphi\int_{\Gamma_e}\overline{p}\,\frac{\partial\overline{u_1}}{\partial x_1} = h\varphi\int_{\Gamma_e}\overline{p}\left(\chi\frac{\partial\overline{p}}{\partial t} + \frac{\partial\overline{u_\alpha}}{\partial x_\alpha}\right)$$
$$= h\frac{\varphi\chi}{2}\frac{d}{dt}\int_{\Gamma_e}\overline{p}^2 - h\varphi\int_{\Gamma_e}\frac{\partial\overline{p}}{\partial x_\alpha}\,\overline{u_\alpha} + \text{b.t.}$$
$$= \frac{h\varphi}{2}\frac{d}{dt}\int_{\Gamma_e}\left(\chi\,\overline{p}^2 + \rho\,\overline{u_\alpha}^2\right) + \text{b.t.},$$

where we used that $\mathrm{div}\mathbf{u} + \chi\partial_t p = 0$, then an integration by part of $\overline{p}\partial_{x_\alpha}\overline{u_\alpha}$, and eventually that $\partial_{x_\alpha}\overline{p} = -\rho\partial_t\overline{u_\alpha}$.

- $$\Phi_3^{\text{ef}} = -hC_{i\alpha}\int_{\Gamma_e}\overline{p}\,\frac{\partial\overline{u_i}}{\partial x_\alpha} = -hC_{1\alpha}\int_{\Gamma_e}\overline{p}\,\frac{\partial\overline{u_1}}{\partial x_\alpha} - hC_{\alpha\beta}\int_{\Gamma_e}\overline{p}\,\frac{\partial\overline{u_\alpha}}{\partial x_\beta}$$
$$= hC_{1\alpha}\int_{\Gamma_e}\frac{\partial\overline{p}}{\partial x_\alpha}\,\overline{u_1} - \rho\,hC_{\alpha\beta}\int_{\Gamma_e}\frac{\partial\overline{u_\beta}}{\partial t}\,\overline{u_\alpha}.$$

We see that the first terms in $C_{1\alpha}$ compensate the terms in B_α in Φ_1^{ef} (since $C_{1\alpha} = B_\alpha$, see [A1.2]). Gathering all the terms leaves us with the form announced in [4.29].

4.4.3. *Positiveness of the effective energies*

As previously mentioned, to show that $\mathcal{E}^{\text{ef}} \geq 0$ in [4.29](b), we have to show that $B_1 \geq 0$, $C_\alpha = \varphi - C_{\alpha\alpha} \geq 0$ and $C_2C_3 - C_{23}^2 \geq 0$ (and in (a), the demonstration for (A_α, A_{23}) is the similar). It is worth noting that in this context, φ has a fuzzy definition: it represented the volume fraction of the fluid in some vicinity of the inclusions dictated by effective thickness e, and the latter is chosen arbitrarily. However, with $\varphi = e/h - \mathcal{V}_{\text{inc}}$ ($\mathcal{V}_{\text{inc}}$ the volume of an inclusion), we have imposed that e is larger than the actual dimension, say e_1, along x_1 of the inclusions in order to ensure that $\varphi \geq 0$. Our guess is that setting $e = e_1$ is sufficient to ensure that $\mathcal{E}^{\text{ef}} \geq 0$. In this case, we will prove below that (i) $B_1 \geq 0$ and (ii) for any reals (a_2, a_3), $a_2^2C_2 + a_3^2C_3^2 - 2a_2a_3C_{23} \geq 0$ (the quadratic form is positive, which is equivalent to the conditions $C_\alpha \geq 0$ and $C_2C_3 - C_{23}^2 \geq 0$).

4.4.3.1. *Property (i) – $B_1 \geq 0$*

With $\Delta Q_1 = 0$, we have that

$$0 = \int_{\mathcal{Y}} Q\,\Delta Q_1 \mathrm{d}\mathbf{y} = -\int_{\mathcal{Y}} \nabla Q\cdot\nabla(Q_1 - y_1)\,\mathrm{d}\mathbf{y} - \int_{\mathcal{Y}}\frac{\partial Q}{\partial y_1}\mathrm{d}\mathbf{y} + \int_{\partial\mathcal{Y}} Q\nabla Q_1\cdot\mathbf{n}\,\mathrm{d}s$$

for any Q, termed *admissible field*, such as Q is continuous and $\nabla Q \to \mathbf{0}$ when $|y_1| \to \infty$. The last integral over $\partial\mathcal{Y}$ equals $(Q(+\infty) - Q(-\infty))$ since $\nabla Q_1\cdot\mathbf{n}$ vanishes on Γ, on the periodic boundaries and it has only non-zero contributions on $\mathsf{Y}(\pm\infty)$, where $\nabla Q_1\cdot\mathbf{n} = \pm 1$. We denote $B(Q) = (Q(+\infty, \mathbf{y}') - Q(-\infty, \mathbf{y}'))$; hence we have for any admissible field Q that

$$0 = \int_{\mathcal{Y}} \nabla Q\cdot\nabla(Q_1 - y_1)\mathrm{d}\mathbf{y} + \int_{\mathcal{Y}}\frac{\partial Q}{\partial y_1}\mathrm{d}\mathbf{y} - B(Q), \qquad [4.34]$$

which applies for $Q = Q_1 - y_1$ (and $B(Q) = \hat{B}_1 = B_1 - e/h$), but this does not help us to show that $B_1 \geq 0$). However, this tells us that $(Q_1 - y_1)$ satisfies the Dirichlet principle, specifically

$$E(Q_1 - y_1) \leq E(Q), \text{ with } E(Q) = \int_{\mathcal{Y}} \left(\frac{1}{2} |\nabla Q|^2 + \int_{\mathcal{Y}} \frac{\partial Q}{\partial y_1} \right) \mathbf{dy} - B(Q), \quad [4.35]$$

for any admissible field Q. To find a bound for B_1, it is now sufficient to (i) calculate $E(Q_1 - y_1)$ and (ii) choose a field Q and its associated $E(Q)$.

– *Expression of* $E(Q_1 - y_1)$: applying [4.34] to $Q = (Q_1 - y_1)$, we get that

$$\int_{\mathcal{Y}} |\nabla (Q_1 - y_1)|^2 \mathbf{dy} + \int_{\mathcal{Y}} \frac{\partial (Q_1 - y_1)}{\partial y_1} \mathbf{dy} - \left(B_1 - \frac{e}{h} \right) = 0.$$

Next, evaluating $0 = \int_{\mathcal{Y}} y_1 \Delta Q_1 \mathbf{dy}$, it is straightforward to show that

$$\int_{\mathcal{Y}} \frac{\partial (Q_1 - y_1)}{\partial y_1} \mathbf{dy} = \mathcal{V}_{\text{inc}}.$$

Reporting the above results in [4.34] leaves us with

$$E(Q_1 - y_1) = \frac{1}{2} \left(\mathcal{V}_{\text{inc}} + \frac{e}{h} - B_1 \right). \quad [4.36]$$

– *Energy of a particular admissible field*: we choose Q depending on y_1 only, with

$$Q(\mathbf{y}) = \begin{cases} 0, & y_1 \in (-\infty, -e/h), \\ b(hy_1/e + 1), & y_1 \in (-e/h, 0), \\ b, & y_1 \in (0, +\infty), \end{cases}$$

hence $|\nabla Q| = \partial_{y_1} Q = bh/e$ in $(-e/h, 0)$ (zero otherwise), and $B(Q) = b$ in [4.34]. At this stage, b is a free parameter. With $(e/h - \mathcal{V}_{\text{inc}}) = \varphi$ the volume of the subset of $\mathcal{Y}$ comprised in $y_1 \in (-e/h, 0)$, it is easy to see that the minimum of $E(Q)$ is reached for $b = e\mathcal{V}_{\text{inc}}/h\varphi$ and

$$\min E(Q) = -\frac{1}{2} \frac{\mathcal{V}_{\text{inc}}^2}{\varphi}. \quad [4.37]$$

It is now sufficient to write that $E(Q_1 - y_1) \leq E(Q)$ to find that

$$B_1 \geq \frac{e^2}{h^2 \varphi}, \quad [4.38]$$

which shows that $B_1 \geq 0$.

4.4.3.2. *Property (ii) – for any reals* (a_2, a_2), $a_2^2 C_2 + a_3^2 C_3 - 2a_2 a_3 C_{23} \geq 0$

To establish this property, we introduce the field Q defined as

$$Q(\mathbf{y}) = a_2 Q_2(\mathbf{y}) + a_3 Q_3(\mathbf{y}), \qquad [4.39]$$

and the associated field $\mathbf{U}$ as

$$\mathbf{U} = \nabla \left(Q(\mathbf{y}) + a_2 y_2 + a_3 y_3 \right), \qquad [4.40]$$

which, from [4.21], satisfies div$\mathbf{U} = 0$, $\mathbf{U} \cdot \mathbf{n}_{|\Gamma} = 0$ and $\lim_{y_1 \to \pm\infty} \mathbf{U} = a_2 \mathbf{e}_2 + a_3 \mathbf{e}_3$. The Thomson variational principle tells us that $\mathbf{U}$ satisfies

$$E^*(\mathbf{U}) \leq E^*(\mathbf{V}), \quad E^*(\mathbf{V}) = \frac{1}{2} \int_{\mathcal{Y}} |\mathbf{V} - (a_2 \mathbf{e}_2 + a_3 \mathbf{e}_3)|^2, \qquad [4.41]$$

for any admissible velocity field $\mathbf{V}$ that is divergence-free and that satisfies $\mathbf{V} \cdot \mathbf{n}_{|\partial\mathcal{Y}} = \mathbf{U} \cdot \mathbf{n}_{|\partial\mathcal{Y}}$. As previously, it is now sufficient to (i) calculate $E^*(\mathbf{U})$ and (ii) choose a field $\mathbf{V}$ and its associated $E^*(\mathbf{V})$.

– *Expression of* $E^*(\mathbf{U})$: with $C_{\alpha\beta} = \int_{\mathcal{Y}} \nabla Q_\alpha \cdot \nabla Q_\beta \, \mathbf{dy}$ (see [4.24] and [A1.1]) and $E^*(\mathbf{U}) = \int_{\mathcal{Y}} |\nabla Q|^2 \mathbf{dy}$, we obtain

$$E^*(\mathbf{U}) = \frac{1}{2} \left[\varphi(a_2^2 + a_3^2) - \underbrace{\left(a_2^2 C_2 + a_3^2 C_3 - 2a_2 a_3 C_{23} \right)}_{Q.F.} \right], \qquad [4.42]$$

since $C_\alpha = (\varphi - C_{\alpha\alpha})$, and we recover our quadratic form $Q.F.$.

– *Energy of a particular admissible field*: to ensure that $\mathbf{V}$ satisfies $\mathbf{V} \cdot \mathbf{n}_{|\Gamma} = 0$ (and the inclusions are in $(-e/h, 0)$) and $\lim_{y_1 \to \pm\infty} \mathbf{V} = a_2 \mathbf{e}_2 + a_3 \mathbf{e}_3$, a trivial admissible field is $\mathbf{V}(\mathbf{y}) = \mathbf{0}$ for $y_1 \in (-e/h, 0)$, and $\mathbf{V} = a_2 \mathbf{e}_2 + a_3 \mathbf{e}_3$ otherwise. We get

$$E^*(\mathbf{V}) = \frac{\varphi}{2}(a_2^2 + a_3^2),$$

and it immediately follows that the quadratic form

$$\left(a_2^2 C_2 + a_3^2 C_3 - 2a_2 a_3 C_{23} \right) \geq 0 \qquad [4.43]$$

is positive.

4.5. Concluding remarks

We have presented a two-scale homogenization to encapsulate the effect of rigid inclusions in the vicinity of a rigid wall (case (a)) or forming a structured film (case (b)) in effective conditions. These effective conditions avoid dealing with the small scale of the inclusions in the actual problems, their effects being encapsulated in effective parameters. The interest of such approaches is twofold. On the one hand, the effective problems are much simpler than the actual ones precisely because the small scale has disappeared; they are much easier to solve numerically and in some cases, explicit solutions are available. The gain in the numerical cost increases when the size of the microstructure decreases, and it is even more important when the numerical implementation of the effective problems is considered in the transient regime. On the other hand, the effective conditions are obtained using a deductive approach; this means that the form of the effective conditions is not postulated *a priori*. As such, the number of parameters entering in the effective conditions is reduced to its minimum and more importantly the values of these parameters are known and they depend only the shape of the microstructure.

In the case of rigid inclusions reported in this chapter, we have shown that (a) for a structured wall, only four parameters are necessary, among which three have to be calculated numerically from two elementary problems, and (b) for a structured film, eight parameters are necessary, among which seven are deduced from three elementary problems. Besides, in practice, further simplifications arise for particular shapes of inclusions, which produce particular forms of the elementary solutions Q_i. It is worth noting that we can get insight into the form of the Q_i remarking that Q_1 and $(Q_\alpha + y_\alpha)$ correspond to the velocity potentials for a perfect fluid flowing across or along the array of inclusions with a unitary velocity at $y_1 \to \pm\infty$ along $\mathbf{e}_1$ and $\mathbf{e}_\alpha$ respectively. The simplest cases are as follows:

– The inclusions have a symmetry, say $y_3 \to -y_3$. Then Q_1, Q_2 are even and Q_3 is odd (up to a constant) with respect to y_3, resulting in (a) $A_{23} = 0$ and (b) $B_3 = C_{23} = 0$.

– The inclusions have zero thickness along y_1, typically a perforated wall. Then, $Q_2 = Q_3 = 0$ (the elementary problems correspond to a fluid flowing in the (y_2, y_3)-plane without being perturbed by the inclusions). Then, we have for (a) $A_{22} = A_{33} = A_{23} = 0$ and for (b) $B_2 = B_3 = C_{22} = C_{33} = C_{23} = 0$.

– In the 2D case, the inclusion is infinite along y_3. Then $\frac{\partial}{\partial y_3} = 0$, from which $Q_3 = 0$ (since $n_3 = 0$), resulting in (a) $A_{23} = A_{33} = 0$, and (b) $B_3 = C_{23} = C_{33} = 0$.

4.6. References

[ABB 95] ABBOUD T., AMMARI H., "Diffraction par un réseau courbe bipériodique. Homogénéisation", *Comptes rendus de l'Académie des sciences. Série 1, Mathématique*, vol. 320, no. 3, pp. 301–306, Elsevier, 1995.

[ABB 96] ABBOUD T., AMMARI H., "Diffraction at a curved grating: TM and TE cases, homogenization", *Journal of Mathematical Analysis and Applications*, vol. 202, no. 3, pp. 995–1026, Elsevier, 1996.

[AMM 99] AMMARI H., LATIRI-GROUZ C., "Conditions aux limites approchées pour les couches minces périodiques", *ESAIM: Mathematical Modelling and Numerical Analysis*, vol. 33, no. 4, pp. 673–692, EDP Sciences, 1999.

[ASL 11] ASLANYÜREK B., HADDAR H., ŞAHINTÜRK H., "Generalized impedance boundary conditions for thin dielectric coatings with variable thickness", *Wave Motion*, vol. 48, no. 7, pp. 681–700, Elsevier, 2011.

[BEN 12] BENDALI A., LAURENS S., TORDEUX S. *et al.*, "Numerical study of acoustic multiperforated plates", *ESAIM: Proceedings*, vol. 37, pp. 166–177, EDP Sciences, 2012.

[BEN 13] BENDALI A., FARES M., PIOT E. *et al.*, "Mathematical justification of the Rayleigh conductivity model for perforated plates in acoustics", *SIAM Journal on Applied Mathematics*, vol. 73, no. 1, pp. 438–459, SIAM, 2013.

[BEN 15] BENDALI A., POIRIER J.-R., "Scattering by a highly oscillating surface", *Mathematical Methods in the Applied Sciences*, vol. 38, no. 13, pp. 2785–2802, Wiley Online Library, 2015.

[BON 04] BONNET-BENDHIA A., DRISSI D., GMATI N., "Simulation of muffler's transmission losses by a homogenized finite element method", *Journal of Computational Acoustics*, vol. 12, no. 03, pp. 447–474, World Scientific, 2004.

[BON 05] BONNET-BEN DHIA A., DRISSI D., GMATI N., "Mathematical analysis of the acoustic diffraction by a muffler containing perforated ducts", *Mathematical Models and Methods in Applied Sciences*, vol. 15, no. 07, pp. 1059–1090, World Scientific, 2005.

[BOU 06] BOUTIN C., ROUSSILLON P., "Wave propagation in presence of oscillators on the free surface", *International Journal of Engineering Science*, vol. 44, no. 3, pp. 180–204, Elsevier, 2006.

[BOU 15] BOUTIN C., SCHWAN L., DIETZ M.S., "Elastodynamic metasurface: Depolarization of mechanical waves and time effects", *Journal of Applied Physics*, vol. 117, no. 6, p. 064902, AIP Publishing, 2015.

[CAP 13] CAPDEVILLE Y., MARIGO J.-J., "A non-periodic two scale asymptotic method to take account of rough topographies for 2-D elastic wave propagation", *Geophysical Journal International*, vol. 192, no. 1, pp. 163–189, Oxford University Press, 2013.

[CHA 16] CHAMAILLARD M., Effective boundary conditions for thin periodic coatings, PhD thesis, Université Paris Saclay, 2016.

[CLA 13] CLAEYS X., DELOURME B., "High order asymptotics for wave propagation across thin periodic interfaces", *Asymptotic Analysis*, vol. 83, nos 1–2, pp. 35–82, IOS Press, 2013.

[DEL 91] DELYSER R.R., KUESTER E.F., "Homogenization analysis of electromagnetic strip gratings", *Journal of Electromagnetic Waves and Applications*, vol. 5, no. 11, pp. 1217–1236, Taylor & Francis, 1991.

[DEL 10] DELOURME B., Modèles et asymptotiques des interfaces fines et périodiques en électromagnétisme, PhD thesis, UPMC, Paris, 2010.

[DEL 12] DELOURME B., HADDAR H., JOLY P., "Approximate models for wave propagation across thin periodic interfaces", *Journal de mathématiques pures et appliquées*, vol. 98, no. 1, pp. 28–71, Elsevier, 2012.

[DEL 13] DELOURME B., HADDAR H., JOLY P., "On the well-posedness, stability and accuracy of an asymptotic model for thin periodic interfaces in electromagnetic scattering problems", *Mathematical Models and Methods in Applied Sciences*, vol. 23, no. 13, pp. 2433–2464, World Scientific, 2013.

[DEL 15] DELOURME B., "High-order asymptotics for the electromagnetic scattering by thin periodic layers", *Mathematical Methods in the Applied Sciences*, vol. 38, no. 5, pp. 811–833, Wiley Online Library, 2015.

[GAL 17] GALLAS B., MAUREL A., MARIGO J.-J. *et al.*, "Light scattering by periodic rough surfaces: Equivalent jump conditions", *JOSA A*, vol. 34, no. 12, pp. 2181–2188, Optical Society of America, 2017.

[GAO 16] GAO Y., Experimental study and application of homogenization based on metamaterials, PhD thesis, UPMC, Paris, 2016.

[HEW 16] HEWETT D.P., HEWITT I.J., "Homogenized boundary conditions and resonance effects in Faraday cages", *Proceedings of the Royal Society A*, vol. 472, The Royal Society, p. 20160062, 2016.

[HOL 00a] HOLLOWAY C.L., KUESTER E.F., "Equivalent boundary conditions for a perfectly conducting periodic surface with a cover layer", *Radio Science*, vol. 35, no. 3, pp. 661–681, American Geophysical Union (AGU), 2000.

[HOL 00b] HOLLOWAY C.L., KUESTER E.F., "Impedance-type boundary conditions for a periodic interface between a dielectric and a highly conducting medium", *IEEE Transactions on Antennas and Propagation*, vol. 48, no. 10, pp. 1660–1672, IEEE, 2000.

[HOL 16] HOLLOWAY C.L., KUESTER E.F., "A homogenization technique for obtaining generalized sheet-transition conditions for a metafilm embedded in a magnetodielectric interface", *IEEE Transactions on Antennas and Propagation*, vol. 64, no. 11, pp. 4671–4686, IEEE, 2016.

[LOM 17] LOMBARD B., MAUREL A., MARIGO J.-J., "Numerical modeling of the acoustic wave propagation across a homogenized rigid microstructure in the time domain", *Journal of Computational Physics*, vol. 335, pp. 558–577, Elsevier, 2017.

[LUK 09] LUKEŠ V., ROHAN E., "Computational analysis of acoustic transmission through periodically perforated interfaces", *Applied and Computational Mechanics*, vol. 3, pp. 111–120, University of West Bohemia, 2009.

[MAR 16a] MARIGO J.-J., MAUREL A., "Homogenization models for thin rigid structured surfaces and films", *The Journal of the Acoustical Society of America*, vol. 140, no. 1, pp. 260–273, ASA, 2016.

[MAR 16b] MARIGO J.-J., MAUREL A., "An interface model for homogenization of acoustic metafilms", in MAIER S.A., *Handbook of Metamaterials and Plasmonics*, vol. 2, World Scientific, 2016.

[MAR 16c] MARIGO J.-J., MAUREL A., "Two-scale homogenization to determine effective parameters of thin metallic-structured films", *Proceedings of the Royal Society A*, vol. 472, p. 20160068, The Royal Society, 2016.

[MAR 17] MARIGO J.-J., MAUREL A., PHAM K. *et al.*, "Effective dynamic properties of a row of elastic inclusions: The case of scalar shear waves", *Journal of Elasticity*, vol. 128, no. 2, pp. 1–25, Springer, 2017.

[MAU 16] MAUREL A., MARIGO J.-J., OURIR A., "Homogenization of ultrathin metallo-dielectric structures leading to transmission conditions at an equivalent interface", *JOSA B*, vol. 33, no. 5, pp. 947–956, Optical Society of America, 2016.

[MER 17] MERCIER J.-F., MARIGO J.-J., MAUREL A., "Influence of the neck shape for Helmholtz resonators", *The Journal of the Acoustical Society of America*, vol. 142, no. 6, pp. 3703–3714, ASA, 2017.

[PHA 17] PHAM K., MAUREL A., MARIGO J.-J., "Two scale homogenization of a row of locally resonant inclusions – the case of anti-plane shear waves", *Journal of the Mechanics and Physics of Solids*, vol. 106, pp. 80–94, Elsevier, 2017.

[POI 06] POIRIER J.-R., BENDALI A., BORDERIES P., "Impedance boundary conditions for the scattering of time-harmonic waves by rapidly varying surfaces", *IEEE Transactions on Antennas and Propagation*, vol. 54, no. 3, pp. 995–1005, IEEE, 2006.

[POP 16] POPIE V., Modélisation asymptotique de la réponse acoustique de plaques perforées dans un cadre linéaire avec étude des effets visqueux, PhD thesis, ISAE, Toulouse, 2016.

[PRO 03] PROEKT L., CANGELLARIS A.C., "Investigation of the impact of conductor surface roughness on interconnect frequency-dependent ohmic loss", *53rd Electronic Components and Technology Conference Proceedings*, IEEE, pp. 1004–1010, 2003.

[RIV 17] RIVAS C., SOLANO M.E., RODRÍGUEZ R. *et al.*, "Asymptotic model for finite-element calculations of diffraction by shallow metallic surface-relief gratings", *JOSA A*, vol. 34, no. 1, pp. 68–79, Optical Society of America, 2017.

[ROH 09] ROHAN E., LUKEŠ V., "Sensitivity analysis for the optimal perforation problem in acoustic transmission", *Applied and Computational Mechanics*, vol. 3, pp. 163–176, University of West Bohemia, 2009.

[ROH 10] ROHAN E., LUKEŠ V., "Homogenization of the acoustic transmission through a perforated layer", *Journal of Computational and Applied Mathematics*, vol. 234, no. 6, pp. 1876–1885, Elsevier, 2010.

[SAN 82] SANCHEZ-HUBERT J., SANCHEZ-PALENCIA E., "Acoustic fluid flow through holes and permeability of perforated walls", *Journal of Mathematical Analysis and Applications*, vol. 87, no. 2, pp. 427–453, Elsevier, 1982.

[SCH 16] SCHWAN L., BOUTIN C., PADRÓN L. *et al.*, "Site-city interaction: Theoretical, numerical and experimental crossed-analysis", *Geophysical Journal International*, vol. 205, no. 2, pp. 1006–1031, Oxford University Press, 2016.

[SCH 17] SCHWAN L., UMNOVA O., BOUTIN C., "Sound absorption and reflection from a resonant metasurface: Homogenisation model with experimental validation", *Wave Motion*, vol. 72, pp. 154–172, Elsevier, 2017.

[TLE 09] TLEMCANI M., "A two-scale asymptotic analysis of a time-harmonic scattering problem with a multi layered thin periodic domain", *Communications in Computational Physics*, vol. 6, no. 4, p. 758, 2009.

[TOU 12] TOURNIER S., Contribution à la modélisation de la diffusion électromagnétique par des surfaces rugueuses à partir de méthodes rigoureuses, PhD thesis, ISAE, Toulouse, 2012.

5

The Plane Wave Expansion Method

The plane wave expansion (PWE) method allows the calculation of dispersion curves (i.e. the relation linking the frequency to the wave number for any propagating mode) of periodic structures made of, for example, elastic materials such as phononic crystals. The method is presented with many details in the case of bulk phononic crystals (i.e. structures of infinite extent) and its advantages and drawbacks are discussed. It is also shown that it can be used for analyzing the evanescence of waves inside the phononic band gaps and for drawing the equifrequency contours of any periodic structure.

5.1. Introduction

Propagation of elastic waves in composite materials exhibiting a periodic structure constitutes a very old topic in physics. We can mention the work, among others, of Lord Rayleigh in 1887, where the author showed the existence of band gaps in periodically stratified media [RAY 87]. However, since the beginning of the 1990s and the pioneering works of M. M. Sigalas *et al.* [SIG 92] and M.S. Kushwaha *et al.* [KUS 93] on phononic crystals, this topic received a renewed interest. These artificial composite materials whose physical characteristics (density, elastic moduli...) are periodic functions of the position have been proven to exhibit very peculiar propagation properties such as frequency band gaps, negative refraction and self-collimation phenomena, [DEY 13] among others. Studies of the propagation of elastic waves in periodic structures require solving, with a high level of accuracy, the equations of propagation of elastic waves. Different theoretical tools were then proposed. We can mention the PWE method, the finite difference time domain (FDTD) method, the multiple scattering (MS) method and the finite element (FE) method, [DEY 13] as different examples.

Chapter written by Jérôme VASSEUR.

Fundamentals and Applications of Acoustic Metamaterials: From Seismic to Radio Frequency,
First Edition. Edited by Vicente Romero-García and Anne-Christine Hladky-Hennion.

In the first part of this chapter, considering very simple periodic structures such as one-dimensional infinite atomic when chains, we recall briefly the concepts that are necessary for studying when more complex periodic structures such as the phononic crystals – namely the unit cell, the direct lattice, the reciprocal lattice, the Brillouin zones, the dispersion curves and the band gaps. The second part of the chapter focuses on the PWE method. Starting from the equations of propagation of elastic waves in an homogeneous elastic material, the basic principles of the PWE method are presented and application of this method to two-dimensional periodic structures is reported with many details. Limitations of the PWE method are discussed. Finally, it is shown that the method can be used for analyzing the evanescence of waves inside the phononic band gaps and for drawing the equifrequency surfaces of periodic structures.

5.2. One-dimensional atomic chains

5.2.1. *One-dimensional atomic chain with one atom by unit cell*

We consider first a very simple periodic structure, namely an infinite one-dimensional linear chain of atoms of identical mass m, connected by springs with constant stiffness β and oriented along the x direction. The equilibrium position of atom n is $x_{n,eq} = na$, where a is the distance between two adjacent atoms in their equilibrium position. Atoms are assumed free to move slightly around their respective equilibrium position. Their position, at any date t, is given as $x_n(t) = na + u_n(t)$ with $|u_n(t)| << |x_n(t)|$ and $u_n = x_n - x_{n,eq}$ is the displacement of the n^{th} atom from the equilibrium position. In that case, the unit cell (see Figure 5.1) that can be repeated along direction x with periodicity a contains only one atom and the lattice spacing a defines the periodicity of the chain along the x axis. Newton's second law applied to atom n considering interaction between first neighbors gives

$$m\frac{\partial^2 u_n}{\partial t^2} = -\beta(u_n - u_{n-1}) + \beta(u_{n+1} - u_n) = \beta(u_{n+1} + u_{n-1} - 2u_n). \qquad [5.1]$$

Seeking solutions of equation [5.1] in the form of sinusoidal propagating waves of amplitude U_0 such as $u_n(t) = U_0 e^{i(kna-\omega t)}$, where k is the wave number and ω the circular frequency, equation [5.1] becomes

$$-m\omega^2 = \beta(e^{ika} + e^{-ika} - 2) = 2\beta(\cos(ka) - 1) = -4\beta \sin^2\left(\frac{ka}{2}\right). \qquad [5.2]$$

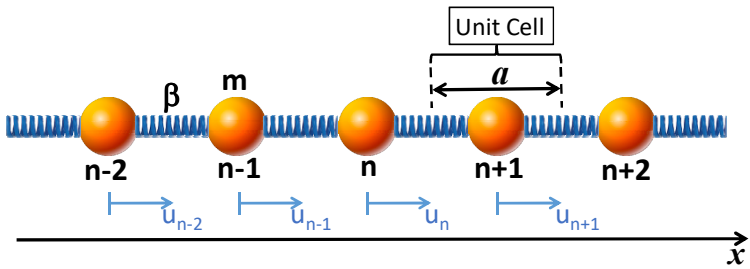

Figure 5.1. *Schematic illustration of the infinite atomic chain made of identical atoms of mass m with a lattice parameter a. β is the stiffness of the spring linking atoms*

We deduce from equation [5.2] the dispersion relation of the atomic chain, i.e. the relation linking the circular frequency ω to the wave number k in the form

$$\omega(k) = \sqrt{\frac{4\beta}{m}} |\sin\left(\frac{ka}{2}\right)|. \qquad [5.3]$$

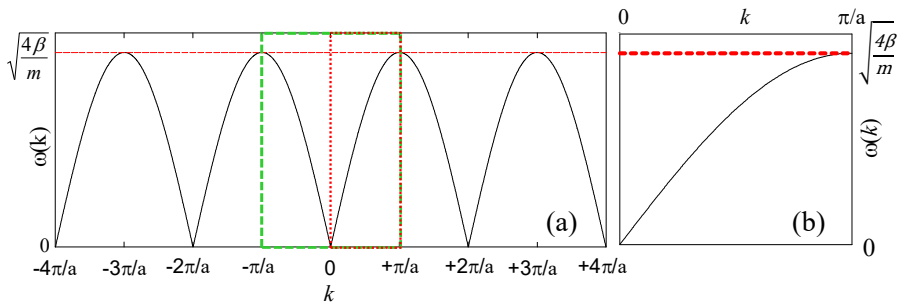

Figure 5.2. *(a) Dispersion relation of the infinite atomic chain made of identical atoms (see Figure 5.1). The green and red boxes represent the first Brillouin zone and the irreducible Brillouin zone, respectively. (b) Dispersion relation plotted in the irreducible Brillouin zone. For a color version of this figure, see www.iste.co.uk/romero/metamaterials.zip*

Figure 5.2(a) shows the dispersion relation $\omega(k)$. We note that $|\sin\left(\frac{ka}{2}\right)|$ being a π-periodic function,

$$|\sin\left(\frac{ka}{2}\right)| = |\sin\left(\frac{ka}{2} + \pi\right)| = |\sin\left(\frac{a}{2}(k + \frac{2\pi}{a})\right)|, \qquad [5.4]$$

$\omega(k)$ is then a periodic function of k with periodicity $G = \frac{2\pi}{a}$ and $\omega(k+nG) = \omega(k)$, where n is an integer. We deduce that a propagating mode of wave number k and a mode with wave number $(k+G)$ are exactly the same mode. The periodicity $G = \frac{2\pi}{a}$ in the wave number space is associated with the "reciprocal lattice" of the chain, while the lattice parameter a characterizes its "direct lattice".

Due to the periodicity of the dispersion relation in the reciprocal space, the useful information concerning the vibration modes that can propagate in the chain is contained in the waves with wave numbers lying between the limits $-\pi/a$ and $+\pi/a$. This range of wave numbers centered on $k = 0$ is named the *first Brillouin zone* of the reciprocal lattice. Therefore, the dispersion relation is also symmetric with respect of the plane $k = 0$ and we may restrict the study to the *irreducible Brillouin zone*, i.e. the domain of wave numbers ranging from 0 to $+\pi/a$ (see Figure 5.2-(b)).

5.2.2. *One-dimensional atomic chain with two atoms by unit cell*

We can now take a closer look at a more complicated structure : an infinite one-dimensional linear chain with two atoms of different masses in the unit cell (see Figure 5.3). The lattice parameter is $2a$ and all the springs are supposed to have the same stiffness β. Atoms of mass m_1 and m_2 are named $even$ and odd atoms and are labeled with integers $2n$ and $2n+1$, respectively. With the same assumptions as that of section 5.2.1, we can write the equations of motion for $even$ and odd atoms in the form

$$\begin{cases} m_1 \frac{\partial^2 u_{2n}}{\partial t^2} &= -\beta(u_{2n} - u_{2n-1}) + \beta(u_{2n+1} - u_{2n}) \\ &= \beta(u_{2n+1} + u_{2n-1} - 2u_{2n}), \\ m_2 \frac{\partial^2 u_{2n+1}}{\partial t^2} &= -\beta(u_{2n+1} - u_{2n}) + \beta(u_{2n+2} - u_{2n+1}) \\ &= \beta(u_{2n+2} + u_{2n} - 2u_{2n+1}). \end{cases} \quad [5.5]$$

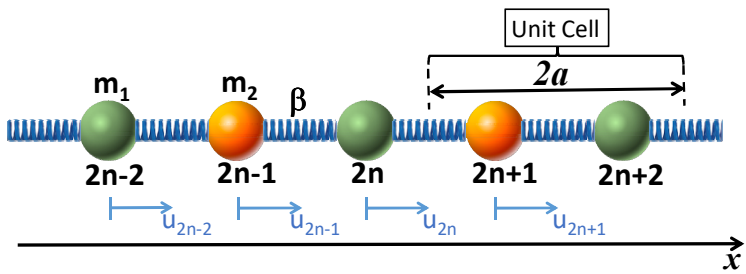

Figure 5.3. *Schematic illustration of the infinite atomic chain made of two atoms of masses m_1 and m_2 in the unit cell with a lattice parameter $2a$. β is the stiffness of the spring linking atoms*

Seeking solutions of equation [5.5] in the form

$$\begin{cases} u_{2n}(t) = Ae^{i(k(2n)a-\omega t)}, \\ u_{2n+1}(t) = Be^{i(k(2n+1)a-\omega t)}, \end{cases} \quad [5.6]$$

where A and B are amplitude terms, we obtain a set of two equations that can be recast in the following matrix form:

$$\begin{pmatrix} (2\beta - m_1\omega^2) & -2\beta\cos(ka) \\ 2\beta\cos(ka) & -(2\beta - m_2\omega^2) \end{pmatrix} \begin{pmatrix} A \\ B \end{pmatrix} = \begin{pmatrix} 0 \\ 0 \end{pmatrix}. \quad [5.7]$$

Equation [5.7] admits non-trivial solutions if the determinant of the matrix vanishes. This gives

$$\omega^4 - 2\beta\left(\frac{m_1 + m_2}{m_1 m_2}\right) + \frac{4\beta^2 \sin^2(ka)}{m_1 m_2} = 0, \quad [5.8]$$

and we deduce

$$\omega(k) = \sqrt{\beta\left(\frac{m_1 + m_2}{m_1 m_2}\right)\left[1 \pm \sqrt{1 - 4\frac{m_1 m_2 \sin^2(ka)}{(m_1 + m_2)^2}}\right]}. \quad [5.9]$$

Consequently, equation [5.8] admits two real solutions $\omega_-(k)$ and $\omega_+(k)$ that are periodic in wave number, k, with a period of $+\pi/a$, and the first Brillouin zone corresponds to the wave numbers varying between $-\pi/2a$ and $+\pi/2a$. We note that because the unit cell in the direct lattice of the chain is twice larger than that of the monoatomic chain, the first Brillouin zone is twice smaller. Figure 5.4 shows the behavior of the dispersion relations plotted in the irreducible Brillouin zone (k between 0 and $+\pi/2a$) as a function of the ratio m_2/m_1 greater than or equal to 1. We can observe that for $m_2 = m_1$, we can recover the dispersion relation of the infinite monoatomic chain, but the band is folded in a smaller irreducible Brillouin zone. Moreover, for increasing mass ratio, a band gap appears at the edge of the irreducible Brillouin zone, and higher is the mass ratio, larger is the band gap.

In this section, concepts of main importance such as the unit cell, the direct lattice and the reciprocal lattice have been defined for very simple 1D periodic structures. Such concepts can be generalized to much more complicated periodic structures such as the phononic crystals. We suggest to readers of this chapter to consult some solid-state physics text books such as references [ASH 76, KIT 04], where complete report on these concepts of crystallography are available.

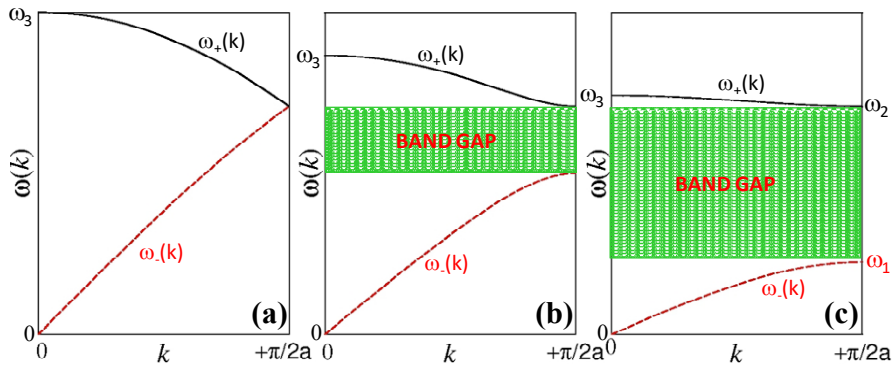

Figure 5.4. *Dispersion relations of the infinite atomic chain made of two atoms of masses m_1 and m_2 in the unit cell with a lattice parameter $2a$ plotted in the irreducible Brillouin zone for (a) $m_2 = m_1$, (b) $m_2 = 2m_1$ and (c) $m_2 = 10m_1$. Circular frequencies ω_1, ω_2 and ω_3 are equal to $\sqrt{2\beta/m_2}$, $\sqrt{2\beta/m_1}$ and $\sqrt{2\beta(m_1+m_2)/m_1m_2}$, respectively*

5.3. The plane wave expansion method

5.3.1. *Plane wave expansion method for bulk phononic crystals*

5.3.1.1. *Equations of propagation of elastic waves in heterogeneous materials*

We consider an heterogeneous elastic medium of infinite extent along the three spatial directions (x_1, x_2, x_3), made of constituent materials with specific crystallographic symmetry (isotropic, cubic, ...). The Cartesian coordinates system refers to an orthonormal basis $(O, \vec{e_1}, \vec{e_2}, \vec{e_3})$. At every point, $\vec{r}$, the medium is characterized by the material parameters, namely the mass density $\rho(\vec{r})$ and the elastic moduli $C_{ijk\ell}(\vec{r})$. The elements of the stress tensor T_{ij} and those of the strain tensor $S_{k\ell}$ are related through Hooke's law [ROY 99]

$$T_{ij}(\vec{r}) = \sum_{kl} C_{ijk\ell}(\vec{r}) S_{k\ell}(\vec{r}), \qquad [5.10]$$

where each index, i, j, k, ℓ varies between 1 and 3. We can note that in this relation the stress and the strain tensors are of rank 2 with $3^2 = 9$ elements, while the tensor of elastic moduli is of rank 4 with $3^4 = 81$ elements. Constituent materials are assumed to be linear materials (limit of small strains) and the elements of the strain tensor are expressed as $S_{k\ell}(\vec{r}) = \frac{1}{2}\left(\frac{\partial u_k(\vec{r})}{\partial x_\ell} + \frac{\partial u_\ell(\vec{r})}{\partial x_k}\right)$, where $u_i(\vec{r}), i = 1, 2, 3$ refers to the components of the displacement vector $\vec{u}$ in (x_1, x_2, x_3) cartesian coordinates system. The elements of the elastic moduli tensor $C_{ijk\ell}$ must satisfy $C_{ijk\ell} = C_{jik\ell}$ because

$T_{ij} = T_{ji}$ and $C_{ijk\ell} = C_{ij\ell k}$ because $S_{k\ell} = S_{\ell k}$ and thermodynamic laws impose $C_{ijk\ell} = C_{k\ell ij}$ [ROY 99]. Then, in terms of displacements, Hooke's law is written as

$$\begin{aligned} T_{ij}(\vec{r}) &= \frac{1}{2}\sum_{kl} C_{ijk\ell}(\vec{r})\frac{\partial u_k(\vec{r})}{\partial x_\ell} + \frac{1}{2}\sum_{kl} C_{ijk\ell}\frac{\partial u_\ell(\vec{r})}{\partial x_k} \\ &= \frac{1}{2}\sum_{kl} C_{ijk\ell}(\vec{r})\frac{\partial u_k(\vec{r})}{\partial x_\ell} + \frac{1}{2}\sum_{kl} C_{ij\ell k}\frac{\partial u_\ell(\vec{r})}{\partial x_k}, \end{aligned} \quad [5.11]$$

and since $C_{ijk\ell} = C_{ij\ell k}$, the two summations on the right are equal, so that

$$T_{ij}(\vec{r}) = \sum_{k\ell} C_{ijk\ell}(\vec{r})\frac{\partial u_k(\vec{r})}{\partial x_\ell}. \quad [5.12]$$

In the absence of external forces, Newton's second law gives the equations of motion as follows:

$$\rho(\vec{r})\frac{\partial^2 u_i(\vec{r})}{\partial t^2} = \sum_j \frac{\partial T_{ij}(\vec{r})}{\partial x_j} = \sum_j \frac{\partial}{\partial x_j}\left[\sum_{k\ell} C_{ijk\ell}(\vec{r})\frac{\partial u_k(\vec{r})}{\partial x_\ell}\right]. \quad [5.13]$$

The tensor of elastic moduli contains, *a priori*, 81 elements, but due to the symmetries of this tensor ($C_{ijk\ell} = C_{jik\ell}$, $C_{ijk\ell} = C_{ij\ell k}$, $C_{ijk\ell} = C_{k\ell ij}$), this number reduces to 21 and Hooke's law can be rewritten in the following matrix form:

$$\begin{pmatrix} T_{11} \\ T_{22} \\ T_{33} \\ T_{23} \\ T_{31} \\ T_{12} \end{pmatrix} = \begin{pmatrix} C_{1111} & C_{1122} & C_{1133} & C_{1123} & C_{1131} & C_{1112} \\ C_{1122} & C_{2222} & C_{2233} & C_{2223} & C_{2231} & C_{2212} \\ C_{1133} & C_{2233} & C_{3333} & C_{3323} & C_{3331} & C_{3312} \\ C_{1123} & C_{2223} & C_{3323} & C_{2323} & C_{2331} & C_{2312} \\ C_{1131} & C_{2231} & C_{3331} & C_{2331} & C_{3131} & C_{3112} \\ C_{1112} & C_{2212} & C_{3312} & C_{2312} & C_{3112} & C_{1212} \end{pmatrix} \begin{pmatrix} S_{11} \\ S_{22} \\ S_{33} \\ 2S_{23} \\ 2S_{31} \\ 2S_{12} \end{pmatrix}. \quad [5.14]$$

This latter equation can be rewritten using the Voigt notation : *a pair of indices ij is replaced by a single index m* as follows:

$$\begin{aligned} (11) &\leftrightarrow 1, \\ (22) &\leftrightarrow 2, \\ (33) &\leftrightarrow 3, \\ (23) \text{ or } (32) &\leftrightarrow 4, \\ (31) \text{ or } (13) &\leftrightarrow 5, \\ (12) \text{ or } (21) &\leftrightarrow 6, \end{aligned} \quad [5.15]$$

and equation [5.14] becomes

$$\begin{pmatrix} T_1 \\ T_2 \\ T_3 \\ T_4 \\ T_5 \\ T_6 \end{pmatrix} = \begin{pmatrix} C_{11} & C_{12} & C_{13} & C_{14} & C_{15} & C_{16} \\ C_{12} & C_{22} & C_{23} & C_{24} & C_{25} & C_{26} \\ C_{13} & C_{23} & C_{33} & C_{34} & C_{35} & C_{36} \\ C_{14} & C_{24} & C_{34} & C_{44} & C_{45} & C_{46} \\ C_{15} & C_{25} & C_{35} & C_{45} & C_{55} & C_{56} \\ C_{16} & C_{26} & C_{36} & C_{46} & C_{56} & C_{66} \end{pmatrix} \begin{pmatrix} S_1 \\ S_2 \\ S_3 \\ 2S_4 \\ 2S_5 \\ 2S_6 \end{pmatrix}. \quad [5.16]$$

In the particular case of constituent materials of cubic crystallographic symmetry, only three independent elastic moduli C_{11}, C_{12} and C_{44} are involved and Hooke's law is written in the matrix form

$$\begin{pmatrix} T_1 \\ T_2 \\ T_3 \\ T_4 \\ T_5 \\ T_6 \end{pmatrix} = \begin{pmatrix} C_{11} & C_{12} & C_{12} & 0 & 0 & 0 \\ C_{12} & C_{11} & C_{12} & 0 & 0 & 0 \\ C_{12} & C_{12} & C_{11} & 0 & 0 & 0 \\ 0 & 0 & 0 & C_{44} & 0 & 0 \\ 0 & 0 & 0 & 0 & C_{44} & 0 \\ 0 & 0 & 0 & 0 & 0 & C_{44} \end{pmatrix} \begin{pmatrix} S_1 \\ S_2 \\ S_3 \\ 2S_4 \\ 2S_5 \\ 2S_6 \end{pmatrix}. \quad [5.17]$$

The case of isotropic material can be considered as a particular case of cubic material imposing $C_{12} = C_{11} - 2C_{44}$ and only two independent elastic moduli C_{11} and C_{44} are necessary to describe the elastic behaviour of the material.

In what follows, we will limit ourselves to constituent materials of cubic crystallographic symmetry and combining equations [5.13] and [5.17], we can write the equation of motion in this case as follows:

$$\begin{aligned} \rho\frac{\partial^2 u_1}{\partial t^2} &= \frac{\partial T_{11}}{\partial x_1} + \frac{\partial T_{12}}{\partial x_2} + \frac{\partial T_{13}}{\partial x_3} \\ &= \frac{\partial}{\partial x_1}\big(C_{11}S_1 + C_{12}(S_2 + S_3)\big) + \frac{\partial}{\partial x_2}(C_{44}.2S_6) + \frac{\partial}{\partial x_3}(C_{44}.2S_5) \\ &= \frac{\partial}{\partial x_1}\Big[C_{11}\frac{\partial u_1}{\partial x_1} + C_{12}\big(\frac{\partial u_2}{\partial x_2} + \frac{\partial u_3}{\partial x_3}\big)\Big] \\ &+ \frac{\partial}{\partial x_2}\Big[C_{44}\big(\frac{\partial u_1}{\partial x_2} + \frac{\partial u_2}{\partial x_1}\big)\Big] + \frac{\partial}{\partial x_3}\Big[C_{44}\big(\frac{\partial u_1}{\partial x_3} + \frac{\partial u_3}{\partial x_1}\big)\Big], \end{aligned} \quad [5.18]$$

$$\rho\frac{\partial^2 u_2}{\partial t^2} = \frac{\partial T_{21}}{\partial x_1} + \frac{\partial T_{22}}{\partial x_2} + \frac{\partial T_{23}}{\partial x_3}$$
$$= \frac{\partial}{\partial x_1}\left[C_{44}\left(\frac{\partial u_1}{\partial x_2} + \frac{\partial u_2}{\partial x_1}\right)\right] + \frac{\partial}{\partial x_2}\left[C_{11}\frac{\partial u_2}{\partial x_2} + C_{12}\left(\frac{\partial u_1}{\partial x_1} + \frac{\partial u_3}{\partial x_3}\right)\right] \quad [5.19]$$
$$+ \frac{\partial}{\partial x_3}\left[C_{44}\left(\frac{\partial u_2}{\partial x_3} + \frac{\partial u_3}{\partial x_2}\right)\right],$$

and

$$\rho\frac{\partial^2 u_3}{\partial t^2} = \frac{\partial T_{31}}{\partial x_1} + \frac{\partial T_{32}}{\partial x_2} + \frac{\partial T_{33}}{\partial x_3}$$
$$= \frac{\partial}{\partial x_1}\left[C_{44}\left(\frac{\partial u_1}{\partial x_3} + \frac{\partial u_3}{\partial x_1}\right)\right] + \frac{\partial}{\partial x_2}\left[C_{44}\left(\frac{\partial u_2}{\partial x_3} + \frac{\partial u_3}{\partial x_2}\right)\right] \quad [5.20]$$
$$+ \frac{\partial}{\partial x_3}\left[C_{11}\frac{\partial u_3}{\partial x_3} + C_{12}\left(\frac{\partial u_1}{\partial x_1} + \frac{\partial u_2}{\partial x_2}\right)\right].$$

In equations [5.18], [5.19] and [5.20], for the sake of simplification, dependence of ρ, u_i and C_{mn} on $\vec{r}$ has been omitted. Equations [5.18], [5.19] and [5.20] show that the equations of propagation of elastic waves in a heterogeneous elastic material of infinite extent are three coupled differential equations of order 2. In the case where the inhomogeneities are distributed periodically in space as in phononic crystals, these three coupled equations can be solved using the plane wave expansion (PWE) method.

5.3.1.2. *Basic principles of the PWE method for bulk phononic crystals*

We consider a 3D periodic structure for which the direct lattice (DL), of specific geometry, is characterized by its unit cell (UC). The reciprocal lattice (RL) vectors [ASH 76, KIT 04] are $\vec{G}(G_1, G_2, G_3)$ with respect to the orthonormal basis $(O, \vec{e_1}, \vec{e_2}, \vec{e_3})$. We search for sinusoidally time-varying solutions of the equations of propagation in the form $\vec{u}(\vec{r}, t) = \vec{u}(\vec{r})e^{-i\omega t}$, where ω is the circular frequency. Due to the periodicity of the structure, the Bloch–Floquet theorem states that $\vec{u}(\vec{r})$ can be written in the form

$$\vec{u}(\vec{r}) = e^{i\vec{K}.\vec{r}}\vec{U}_{\vec{K}}(\vec{r}), \quad [5.21]$$

where $\vec{K}(K_1, K_2, K_3)$ is the Bloch wave vector and $\vec{U}_{\vec{K}}(\vec{r})$ has the periodicity of the direct lattice. Then $\vec{U}_{\vec{K}}(\vec{r})$ can be developed in Fourier series as

$$\vec{U}_{\vec{K}}(\vec{r}) = \sum_{\vec{G'}} \vec{U}_{\vec{K}}(\vec{G'})e^{i\vec{G'}.\vec{r}} \text{ where } \vec{G'} \in (RL) \quad [5.22]$$

and

$$\vec{u}(\vec{r},t) = e^{-i\omega t}\sum_{\vec{G}'}\vec{U}_{\vec{K}}(\vec{G}')e^{i(\vec{G}'+\vec{K}).\vec{r}}. \qquad [5.23]$$

The material parameters, mass density $\rho(\vec{r})$ and elastic moduli $C_{mn}(\vec{r})$, are periodic functions of the position, i.e. $\rho(\vec{r}+\vec{R}) = \rho(\vec{r})$ and $C_{mn}(\vec{r}+\vec{R}) = C_{mn}(\vec{r})$, where $\vec{R} \in (DL)$, which can be expanded in Fourier series so that

$$\eta(\vec{r}) = \sum_{\vec{G}''}\eta(\vec{G}'')e^{i\vec{G}''.\vec{r}}, \qquad [5.24]$$

where $\vec{G}'' \in (RL)$ and $\eta \equiv \rho$ or C_{mn}. Note that the Fourier coefficients $\eta(\vec{G}'')$ in equation [5.24] are defined as

$$\eta(\vec{G}'') = \frac{1}{V_{(U.C.)}}\iiint_{(U.C.)}\eta(\vec{r})e^{-i\vec{G}''.\vec{r}}d^3\vec{r}, \qquad [5.25]$$

where the integral is performed on the volume $V_{(U.C.)}$ of the $(U.C)$ of the direct lattice.

Inserting equations [5.23] and [5.24] in equations [5.18], [5.19] and [5.20] gives the Fourier transform of the equations of motion. For example, doing these substitutions in the left-hand side of equation [5.18], we obtain

$$\rho(\vec{r})\frac{\partial^2 u_1(\vec{r})}{\partial t^2} = -\omega^2 e^{i(\vec{K}.\vec{r}-\omega t)}\sum_{\vec{G}',\vec{G}''}\rho(\vec{G}'')U_{1,\vec{K}}(\vec{G}')e^{i(\vec{G}'+\vec{G}'').\vec{r}} \qquad [5.26]$$

where $U_{1,\vec{K}}$ is the component of $\vec{U}_{\vec{K}}$ along $\vec{e_1}$. Proceeding in the same way, in the first term of the right-hand side of equation [5.18] gives

$$\begin{aligned}
&\frac{\partial}{\partial x_1}\left[C_{11}(\vec{r})\frac{\partial u_1(\vec{r})}{\partial x_1}\right] \\
&= e^{-i\omega t}\frac{\partial}{\partial x_1}\Big[\sum_{\vec{G}',\vec{G}''}C_{11}(\vec{G}'')e^{i\vec{G}''.\vec{r}}[i(K_1+G_1')].e^{i(\vec{K}+\vec{G}').\vec{r}}U_{1,\vec{K}}(\vec{G}')\Big] \\
&= e^{-i\omega t}\frac{\partial}{\partial x_1}\Big[\sum_{\vec{G}',\vec{G}''}C_{11}(\vec{G}'')[i(K_1+G_1')].e^{i(\vec{K}+\vec{G}'+\vec{G}'').\vec{r}}U_{1,\vec{K}}(\vec{G}')\Big] \\
&= -e^{i(\vec{K}.\vec{r}-\omega t)}\Big[\sum_{\vec{G}',\vec{G}''}C_{11}(\vec{G}'')[(K_1+G_1')(K_1+G_1'+G_1'')].e^{i(\vec{G}'+\vec{G}'').\vec{r}} \\
&.U_{1,\vec{K}}(\vec{G}')\Big]
\end{aligned} \qquad [5.27]$$

and so on for the other terms of the right-hand side of equation [5.18]. Finally, the Fourier transform of equation [5.18] is written as

$$
\begin{aligned}
&-\omega^2 e^{i(\vec{K}.\vec{r}-\omega t)} \sum_{\vec{G}',\vec{G}''} \rho(\vec{G}'')U_{1,\vec{K}}(\vec{G}')e^{i(\vec{G}'+\vec{G}'').\vec{r}} \\
&= -e^{i(\vec{K}.\vec{r}-\omega t)}. \sum_{\vec{G}',\vec{G}''} e^{i(\vec{G}'+\vec{G}'').\vec{r}} \Bigg\{ \Bigg[C_{11}(\vec{G}'')(K_1+G_1')(K_1+G_1'+G_1'') \\
&\quad + C_{44}[(\vec{G}'')\Big[(K_2+G_2')(K_2+G_2'+G_2'') \\
&\quad + (K_3+G_3')(K_3+G_3'+G_3'')\Big]\Bigg] U_{1,\vec{K}}(\vec{G}') \\
&\quad + \Bigg[C_{12}(\vec{G}'')(K_2+G_2')(K_1+G_1'+G_1'') \\
&\quad + C_{44}(\vec{G}'')(K_1+G_1')(K_2+G_2'+G_2'')\Bigg] U_{2,\vec{K}}(\vec{G}') \\
&\quad + \Bigg[C_{12}(\vec{G}'')(K_3+G_3')(K_1+G_1'+G_1'') \\
&\quad + C_{44}(\vec{G}'')(K_1+G_1')(K_3+G_3'+G_3'')\Big] U_{3,\vec{K}}(\vec{G}') \Bigg\}. \qquad [5.28]
\end{aligned}
$$

After simplification by $-e^{i(\vec{K}.\vec{r}-\omega t)}$, multiplying both sides of equation [5.28] by $e^{-i\vec{G}.\vec{r}}$, where $\vec{G} \in (RL)$, gives terms of the form $e^{i(\vec{G}'+\vec{G}''-\vec{G}).\vec{r}}$. Because

$$
\begin{aligned}
&\frac{1}{V_{(U.C.)}} \iiint_{(U.C.)} e^{i(\vec{G}'+\vec{G}''-\vec{G}).\vec{r}} d^3\vec{r} = \delta_{(\vec{G}'+\vec{G}''-\vec{G}),\vec{0}} \\
&= \begin{cases} 1 \text{ if } \vec{G}'+\vec{G}''-\vec{G} = \vec{O} \\ 0 \text{ if } \vec{G}'+\vec{G}''-\vec{G} \neq \vec{O} \end{cases} \qquad [5.29]
\end{aligned}
$$

integration over $V_{(U.C.)}$ of equation [5.28] gives

$$\omega^2 \sum_{\vec{G'}} \rho(\vec{G}-\vec{G'})U_{1,\vec{K}}(\vec{G'}) = \sum_{\vec{G'}} \Bigg\{ \Bigg[C_{11}(\vec{G}-\vec{G'})(K_1+G_1').(K_1+G_1) + C_{44}[(\vec{G}-\vec{G'})(K_2+G_2')(K_2+G_2) + (K_3+G_3')(K_3+G_3)] \Bigg] .U_{1,\vec{K}}(\vec{G'}) + \Big[C_{12}(\vec{G}-\vec{G'})(K_2+G_2')(K_1+G_1) + C_{44}(\vec{G}-\vec{G'})(K_1+G_1')(K_2+G_2) \Big] .U_{2,\vec{K}}(\vec{G'}) + \Big[C_{12}(\vec{G}-\vec{G'})(K_3+G_3')(K_1+G_1) + C_{44}(\vec{G}-\vec{G'})(K_1+G_1')(K_3+G_3) \Big] .U_{3,\vec{K}}(\vec{G'}) \Bigg\}. \quad [5.30]$$

Indeed, equation [5.29] imposes to keep only the terms in equation [5.28] such that $\vec{G''} = \vec{G} - \vec{G'}$.

Applying the same algebra for equations [5.19] and [5.20], we obtain that the Fourier transforms of the equations of propagation form a set of three coupled equations given as

$$\begin{cases} \omega^2 \sum_{\vec{G'}} B^{(11)}_{\vec{G},\vec{G'}} U_{1,\vec{K}}(\vec{G'}) = & [5.31a] \\ = \sum_{\vec{G'}} \left\{ A^{(11)}_{\vec{G},\vec{G'}} U_{1,\vec{K}}(\vec{G'}) + A^{(12)}_{\vec{G},\vec{G'}} U_{2,\vec{K}}(\vec{G'}) + A^{(13)}_{\vec{G},\vec{G'}} U_{3,\vec{K}}(\vec{G'}), \right\} & \\ \omega^2 \sum_{\vec{G'}} B^{(22)}_{\vec{G},\vec{G'}} U_{2,\vec{K}}(\vec{G'}) = & [5.31b] \\ = \sum_{\vec{G'}} \left\{ A^{(21)}_{\vec{G},\vec{G'}} U_{1,\vec{K}}(\vec{G'}) + A^{(22)}_{\vec{G},\vec{G'}} U_{2,\vec{K}}(\vec{G'}) + A^{(23)}_{\vec{G},\vec{G'}} U_{3,\vec{K}}(\vec{G'}), \right\} & \\ \omega^2 \sum_{\vec{G'}} B^{(33)}_{\vec{G},\vec{G'}} U_{3,\vec{K}}(\vec{G'}) = & [5.31c] \\ = \sum_{\vec{G'}} \left\{ A^{(31)}_{\vec{G},\vec{G'}} U_{1,\vec{K}}(\vec{G'}) + A^{(32)}_{\vec{G},\vec{G'}} U_{2,\vec{K}}(\vec{G'}) + A^{(33)}_{\vec{G},\vec{G'}} U_{3,\vec{K}}(\vec{G'}), \right\} & \end{cases}$$

where

$$
\begin{cases}
B^{(11)}_{\vec{G},\vec{G}'} = B^{(22)}_{\vec{G},\vec{G}'} = B^{(33)}_{\vec{G},\vec{G}'} = \rho(\vec{G}-\vec{G}'), & \text{[5.32a]}\\
A^{(11)}_{\vec{G},\vec{G}'} = C_{11}(\vec{G}-\vec{G}')(G_1+K_1)(G'_1+K_1)+ & \text{[5.32b]}\\
+C_{44}(\vec{G}-\vec{G}')\Big[(G_2+K_2)(G'_2+K_2)+(G_3+K_3)(G'_3+K_3)\Big], & \\
A^{(12)}_{\vec{G},\vec{G}'} = C_{12}(\vec{G}-\vec{G}')(G_1+K_1)(G'_2+K_2)+ & \text{[5.32c]}\\
+C_{44}(\vec{G}-\vec{G}')(G'_1+K_1)(G_2+K_2), & \\
A^{(13)}_{\vec{G},\vec{G}'} = C_{12}(\vec{G}-\vec{G}')(G_1+K_1)(G'_3+K_3)+ & \text{[5.32d]}\\
+C_{44}(\vec{G}-\vec{G}')(G'_1+K_1)(G_3+K_3), & \\
A^{(21)}_{\vec{G},\vec{G}'} = C_{12}(\vec{G}-\vec{G}')(G'_1+K_1)(G_2+K_2)+ & \text{[5.32e]}\\
+C_{44}(\vec{G}-\vec{G}')(G'_2+K_2)(G_1+K_1), & \\
A^{(22)}_{\vec{G},\vec{G}'} = C_{11}(\vec{G}-\vec{G}')(G_2+K_2)(G'_2+K_2)+ & \text{[5.32f]}\\
+C_{44}(\vec{G}-\vec{G}')\Big[(G_1+K_1)(G'_1+K_1)+(G_3+K_3)(G'_3+K_3)\Big], & \\
A^{(23)}_{\vec{G},\vec{G}'} = C_{12}(\vec{G}-\vec{G}')(G_2+K_2)(G'_3+K_3)+ & \text{[5.32g]}\\
+C_{44}(\vec{G}-\vec{G}')(G'_2+K_2)(G_3+K_3), & \\
A^{(31)}_{\vec{G},\vec{G}'} = C_{12}(\vec{G}-\vec{G}')(G'_1+K_1)(G_3+K_3)+ & \text{[5.32h]}\\
+C_{44}(\vec{G}-\vec{G}')(G_1+K_1)(G'_3+K_3), & \\
A^{(32)}_{\vec{G},\vec{G}'} = C_{12}(\vec{G}-\vec{G}')(G'_2+K_2)(G_3+K_3)+ & \text{[5.32i]}\\
+C_{44}(\vec{G}-\vec{G}')(G_2+K_2)(G'_3+K_3), & \\
A^{(33)}_{\vec{G},\vec{G}'} = C_{11}(\vec{G}-\vec{G}')(G_3+K_3)(G'_3+K_3)+ & \text{[5.32j]}\\
+C_{44}(\vec{G}-\vec{G}')\Big[(G_1+K_1)(G'_1+K_1)+(G_2+K_2)(G'_2+K_2)\Big]. &
\end{cases}
$$

Equation [5.31] can be recast in the following matrix form:

$$\omega^2 \begin{pmatrix} B^{(11)}_{\vec{G},\vec{G}'} & 0 & 0 \\ 0 & B^{(22)}_{\vec{G},\vec{G}'} & 0 \\ 0 & 0 & B^{(33)}_{\vec{G},\vec{G}'} \end{pmatrix} \begin{pmatrix} U_{1,\vec{K}}(\vec{G}') \\ U_{2,\vec{K}}(\vec{G}') \\ U_{3,\vec{K}}(\vec{G}') \end{pmatrix}$$
$$= \begin{pmatrix} A^{(11)}_{\vec{G},\vec{G}'} & A^{(12)}_{\vec{G},\vec{G}'} & A^{(13)}_{\vec{G},\vec{G}'} \\ A^{(21)}_{\vec{G},\vec{G}'} & A^{(22)}_{\vec{G},\vec{G}'} & A^{(23)}_{\vec{G},\vec{G}'} \\ A^{(31)}_{\vec{G},\vec{G}'} & A^{(32)}_{\vec{G},\vec{G}'} & A^{(33)}_{\vec{G},\vec{G}'} \end{pmatrix} \begin{pmatrix} U_{1,\vec{K}}(\vec{G}') \\ U_{2,\vec{K}}(\vec{G}') \\ U_{3,\vec{K}}(\vec{G}') \end{pmatrix} \quad [5.33]$$

or

$$\omega^2 \overleftrightarrow{B}\vec{\mathcal{U}} = \overleftrightarrow{A}\vec{\mathcal{U}} \quad [5.34]$$

where $\overleftrightarrow{A}$ and $\overleftrightarrow{B}$ are square matrices and $\vec{\mathcal{U}}$ a vector whose sizes depend on the number of reciprocal lattice vectors taken into account in the Fourier series. The numerical resolution of this generalized eigenvalue equation is performed for a fixed value of the wave vector $\vec{K} = (K_1, K_2, K_3)$ and for $\vec{K}$ describing the contour of the irreducible Brillouin zone of the array of inclusions. Then we obtain a set of eigenfrequencies $\omega(\vec{K})$.

Equation [5.33] is general and constitutes the basis equation for applying the PWE method to the calculation of the dispersion curves of a three-dimensional periodic structure with a specific geometry. For lower dimensions, this *master* equation can be simplified, cancelling some components of the wave vectors and of the reciprocal lattice vectors. This is the object of the next part in which we will consider the particular case of bulk two-dimensional phononic crystals.

5.3.1.3. *PWE method for bulk two-dimensional phononic crystals*

A bulk two-dimensional phononic crystal consists of a two-dimensional array of parallel cylindrical scatterers (of specific cross section : circular, square, elliptical, hexagonal ...) made of an elastic material A embedded in an elastic matrix B (see Figure 5.5). Materials A and B are supposed to be of cubic crystallographic symmetry.

Due to the infinite length of the cylinders along the x_3 axis, there exists an invariance by translation along x_3 and the material parameters (density and elastic moduli) and the displacement field does not depend on x_3. This forces us to consider that G_3 and G'_3 vanishes in the equation [5.31]. Moreover, we can limit the

propagation of waves to the transverse plane (x_1Ox_2) and this imposes $K_3 = O$. As a matter of fact in equation [5.32], terms $A^{(13)}_{\vec{G},\vec{G}'}$, $A^{(23)}_{\vec{G},\vec{G}'}$, $A^{(31)}_{\vec{G},\vec{G}'}$ and $A^{(32)}_{\vec{G},\vec{G}'}$ vanish and equation [5.33] becomes

$$\omega^2 \begin{pmatrix} B^{(11)}_{\vec{G},\vec{G}'} & 0 & 0 \\ 0 & B^{(22)}_{\vec{G},\vec{G}'} & 0 \\ 0 & 0 & B^{(33)}_{\vec{G},\vec{G}'} \end{pmatrix} \begin{pmatrix} U_{1,\vec{K}}(\vec{G}') \\ U_{2,\vec{K}}(\vec{G}') \\ U_{3,\vec{K}}(\vec{G}') \end{pmatrix}$$

$$= \begin{pmatrix} A^{(11)}_{\vec{G},\vec{G}'} & A^{(12)}_{\vec{G},\vec{G}'} & 0 \\ A^{(21)}_{\vec{G},\vec{G}'} & A^{(22)}_{\vec{G},\vec{G}'} & 0 \\ 0 & 0 & A^{(33)}_{\vec{G},\vec{G}'} \end{pmatrix} \begin{pmatrix} U_{1,\vec{K}}(\vec{G}') \\ U_{2,\vec{K}}(\vec{G}') \\ U_{3,\vec{K}}(\vec{G}') \end{pmatrix}, \qquad [5.35]$$

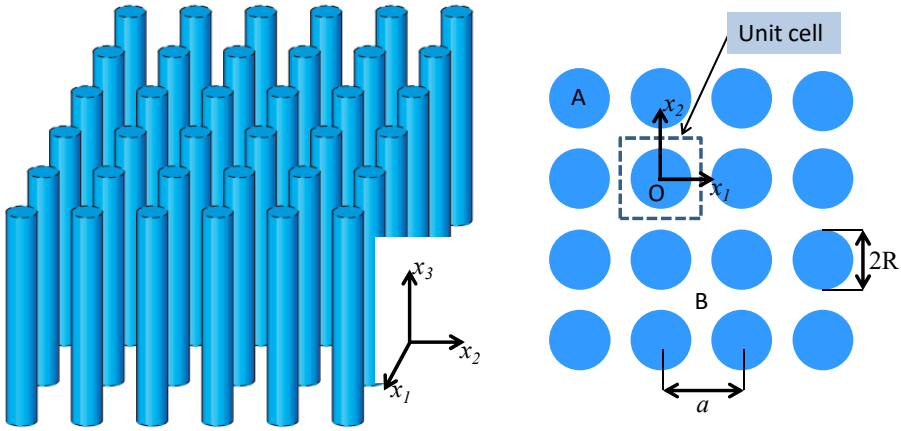

Figure 5.5. *Left panel: Two-dimensional phononic crystal made of a square array (lattice parameter a) of circular cylinders A of radius R embedded in a matrix B. The cylinders are oriented along the x_3 axis and are assumed infinite along this direction. The structure is periodic along x_1 and x_2; Right panel: Cross section in the transverse $(x_1, 0, x_2)$ plane of the 2D phononic crystal*

where

$$
\begin{cases}
B^{(11)}_{\vec{G},\vec{G}'} = B^{(22)}_{\vec{G},\vec{G}'} = B^{(33)}_{\vec{G},\vec{G}'} = \rho(\vec{G}-\vec{G}'), & \text{[5.36a]}\\
A^{(11)}_{\vec{G},\vec{G}'} = C_{11}(\vec{G}-\vec{G}')(G_1+K_1)(G'_1+K_1) + & \text{[5.36b]}\\
+C_{44}(\vec{G}-\vec{G}')(G_2+K_2)(G'_2+K_2), & \\
A^{(12)}_{\vec{G},\vec{G}'} = C_{12}(\vec{G}-\vec{G}')(G_1+K_1)(G'_2+K_2) + & \text{[5.36c]}\\
+C_{44}(\vec{G}-\vec{G}')(G'_1+K_1)(G_2+K_2), & \\
A^{(21)}_{\vec{G},\vec{G}'} = C_{12}(\vec{G}-\vec{G}')(G'_1+K_1)(G_2+K_2) + & \text{[5.36d]}\\
+C_{44}(\vec{G}-\vec{G}')(G'_2+K_2)(G_1+K_1), & \\
A^{(22)}_{\vec{G},\vec{G}'} = C_{11}(\vec{G}-\vec{G}')(G_2+K_2)(G'_2+K_2) + & \text{[5.36e]}\\
+C_{44}(\vec{G}-\vec{G}')(G_1+K_1)(G'_1+K_1), & \\
A^{(33)}_{\vec{G},\vec{G}'} = C_{44}(\vec{G}-\vec{G}')\Big[(G_1+K_1)(G'_1+K_1) + & \text{[5.36f]}\\
+(G_2+K_2)(G'_2+K_2)\Big]. &
\end{cases}
$$

Equation [5.35] involves *super-diagonal matrices* and can be separated into two independent matrix equations:

$$
\omega^2 \begin{pmatrix} B^{(11)}_{\vec{G},\vec{G}'} & 0 \\ 0 & B^{(22)}_{\vec{G},\vec{G}'} \end{pmatrix} \begin{pmatrix} U_{1,\vec{K}}(\vec{G}') \\ U_{2,\vec{K}}(\vec{G}') \end{pmatrix} = \begin{pmatrix} A^{(11)}_{\vec{G},\vec{G}'} & A^{(12)}_{\vec{G},\vec{G}'} \\ A^{(21)}_{\vec{G},\vec{G}'} & A^{(22)}_{\vec{G},\vec{G}'} \end{pmatrix} \begin{pmatrix} U_{1,\vec{K}}(\vec{G}') \\ U_{2,\vec{K}}(\vec{G}') \end{pmatrix}, \quad [5.37]
$$

and

$$
\omega^2 \sum_{\vec{G}'} B^{(33)}_{\vec{G},\vec{G}'} U_{3,\vec{K}}(\vec{G}') = \sum_{\vec{G}'} A^{(33)}_{\vec{G},\vec{G}'} . U_{3,\vec{K}}(\vec{G}'). \quad [5.38]
$$

Equations [5.37] and [5.38] show that propagation modes in the 2D bulk phononic crystal decouple. Equation [5.37] corresponds to modes polarized in the transverse plane (x_1Ox_2) (often named XY modes) while equation [5.38] characterizes modes (often named Z modes) with a displacement field oriented along the x_3 direction.

Equations [5.36] involve the Fourier coefficients $\rho(\vec{G}-\vec{G}')$ and $C_{mn}(\vec{G}-\vec{G}')$, with $(mn)\equiv(11),\ (44)$ and (12) defined by equations [5.25]. For two-dimensional phononic crystals, equations [5.25] must be rewritten as

$$\eta(\vec{G}-\vec{G}')=\frac{1}{\Sigma_{(U.C.)}}\iint_{(U.C.)}\eta(\vec{r})e^{-i(\vec{G}-\vec{G}').\vec{r}}d^2\vec{r},\ \eta\equiv\rho \text{ or } C_{mn}, \qquad [5.39]$$

where $\Sigma_{(U.C.)}$ is the area of the two-dimensional unit cell in the (x_1Ox_2) plane and

$$\begin{aligned}\eta(\vec{G}-\vec{G}')=&\frac{1}{\Sigma_{(U.C.)}}\iint_{(A_{(UC)})}\eta_A.e^{-i(\vec{G}-\vec{G}').\vec{r}}d^2\vec{r}\\&+\frac{1}{\Sigma_{(U.C.)}}\iint_{(B_{(UC)})}\eta_B.e^{-i(\vec{G}-\vec{G}').\vec{r}}d^2\vec{r},\end{aligned} \qquad [5.40]$$

where the integrals are performed on the areas filled by materials A and B inside the (UC), and η_A (resp. η_B) denotes the value of parameter η for material A (resp. B). Equation [5.40] can be rewritten as

$$\begin{aligned}\eta(\vec{G}-\vec{G}')=&\frac{1}{\Sigma_{(U.C.)}}\iint_{(A_{(UC)})}\eta_A.e^{-i(\vec{G}-\vec{G}').\vec{r}}d^2\vec{r}\\&-\frac{1}{\Sigma_{(U.C.)}}\iint_{(A_{(UC)})}\eta_B.e^{-i(\vec{G}-\vec{G}').\vec{r}}d^2\vec{r}\\&+\frac{1}{\Sigma_{(U.C.)}}\iint_{(A_{(UC)})}\eta_B.e^{-i(\vec{G}-\vec{G}').\vec{r}}d^2\vec{r}\\&+\frac{1}{\Sigma_{(U.C.)}}\iint_{(B_{(UC)})}\eta_B.e^{-i(\vec{G}-\vec{G}').\vec{r}}d^2\vec{r}\\=&(\eta_A-\eta_B)\Big\{\frac{1}{\Sigma_{(U.C.)}}\iint_{(A_{(UC)})}e^{-i(\vec{G}-\vec{G}').\vec{r}}d^2\vec{r}\Big\}\\&+\eta_B\Big\{\frac{1}{\Sigma_{(U.C.)}}\iint_{(UC)}e^{-i(\vec{G}-\vec{G}').\vec{r}}d^2\vec{r}\Big\}.\end{aligned} \qquad [5.41]$$

Because

$$\frac{1}{\Sigma_{(U.C.)}}\iint_{(UC)}e^{-i(\vec{G}-\vec{G}').\vec{r}}d^2\vec{r}=\delta_{(\vec{G}-\vec{G}'),\vec{0}}=\begin{cases}1 \text{ if } (\vec{G}-\vec{G}')=\vec{O}\\0 \text{ if } (\vec{G}-\vec{G}')\neq\vec{O}\end{cases} \qquad [5.42]$$

and defining the quantity $F(\vec{G}-\vec{G}')$ as

$$F(\vec{G}-\vec{G}')=\frac{1}{\Sigma_{(U.C.)}}\iint_{(A_{(UC)})}e^{-i(\vec{G}-\vec{G}').\vec{r}}d^2\vec{r}, \qquad [5.43]$$

Equation [5.40] becomes

$$\eta(\vec{G}-\vec{G}') = (\eta_A - \eta_B).F(\vec{G}-\vec{G}') + \eta_B.\delta_{(\vec{G}-\vec{G}'),\vec{0}} \ , \qquad [5.44]$$

where $F(\vec{G}-\vec{G}')$ is the structure factor that depends on the geometry of the cross section of the cylindrical inclusion.

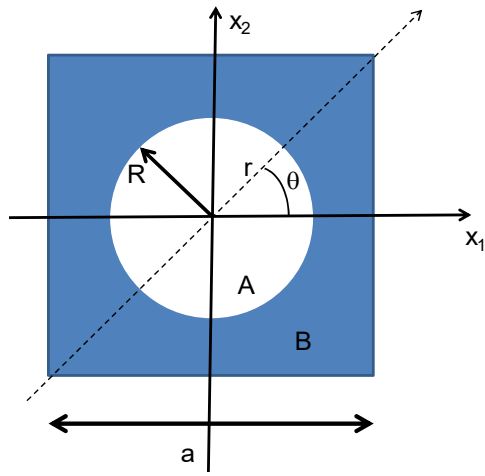

Figure 5.6. *Unit cell in the transverse plane $(x_1 0 x_2)$ of the two-dimensional phononic crystal made of a square array of cylinders of circular cross section. The area of the unit cell is a^2*

For example, if we consider inclusions of circular cross section (see Figure 5.6), the structure factor can be calculated using polar coordinates (r,θ) as

$$\begin{aligned} F(\vec{G}-\vec{G}') &= \frac{1}{\Sigma_{(U.C.)}} \iint_{(A_{(UC)})} e^{-i(\vec{G}-\vec{G}').\vec{r}} d^2\vec{r} \\ &= \frac{1}{a^2}\int_0^R \int_0^{2\pi} e^{-i|\vec{G}-\vec{G}'|r\cos\theta} r.dr.d\theta = \frac{1}{a^2}\int_0^R 2\pi r dr J_0(|\vec{G}-\vec{G}'|r) \\ &= \frac{2\pi}{(a^2|\vec{G}-\vec{G}'|^2)}\int_0^{|\vec{G}-\vec{G}'|R} (|\vec{G}-\vec{G}'|r)J_0(|\vec{G}-\vec{G}'|r)d(|\vec{G}-\vec{G}'|r) \\ &= \frac{2\pi}{(a^2|\vec{G}-\vec{G}'|^2)}(|\vec{G}-\vec{G}'|R)J_1(|\vec{G}-\vec{G}'|R) = f\frac{2J_1(|\vec{G}-\vec{G}'|R)}{|\vec{G}-\vec{G}'|R}, \end{aligned} \qquad [5.45]$$

where $f = \dfrac{\pi R^2}{a^2}$ $(0 \leq f \leq \dfrac{\pi}{4})$ is the filling factor of inclusions (i.e. the ratio between the area of the cross section of the cylinder and the surface of the unit cell) and J_0 and J_1 are Bessel's functions of the first kind of orders 0 and 1, respectively. When $(\vec{G} - \vec{G'}) = \vec{0}$,

$$F(\vec{0}) = \frac{1}{\Sigma_{(U.C.)}} \iint_{(A_{(UC)})} d^2\vec{r} = \frac{\pi R^2}{a^2} = f, \qquad [5.46]$$

and we can rewrite equation [5.44] as

$$\eta(\vec{G} - \vec{G'}) = \begin{cases} f\eta_A + (1-f)\eta_B = \overline{\eta} \text{ if } (\vec{G} - \vec{G'}) = \vec{O} \\ (\eta_A - \eta_B).F(\vec{G} - \vec{G'}) \text{ if } (\vec{G} - \vec{G'}) \neq \vec{O} \end{cases}. \qquad [5.47]$$

where $\overline{\eta}$ is an average value on the unit cell of parameter η.

The structure factor depends on the reciprocal lattice vectors and on the geometry of the inclusions. We may consider the cross section of other geometries and for cylinders of square cross section of side length ℓ, for example,

$$\begin{aligned} F(\vec{G} - \vec{G'}) &= \frac{1}{\Sigma_{(U.C.)}} \iint_{(A_{(UC)})} e^{-i(\vec{G}-\vec{G'}).\vec{r}} d^2\vec{r} \\ &= \frac{1}{a^2} \int_{-\frac{\ell}{2}}^{+\frac{\ell}{2}} e^{-i(G_1 - G'_1).x_1} dx_1 . \int_{-\frac{\ell}{2}}^{+\frac{\ell}{2}} e^{-i(G_2 - G'_2).x_2} dx_2 \\ &= f . \left[\frac{\sin\left[(G_1 - G'_1)\frac{\ell}{2}\right]}{(G_1 - G'_1)\frac{\ell}{2}} \right] . \left[\frac{\sin\left[(G_2 - G'_2)\frac{\ell}{2}\right]}{(G_2 - G'_2)\frac{\ell}{2}} \right]. \end{aligned} \qquad [5.48]$$

Other authors have considered elliptical or hexagonal [WAN 07] cross sections and analytical expressions of the structure factor can be derived in these cases. However, for much more complicated geometry, calculation of the structure factor can be performed numerically via a numerical resolution of the surface integral involved in equation [5.43], but computational time will be increased significantly. On the other hand, cylindrical inclusions made of different materials (for example, made of concentric cylindrical slabs) can be considered. This requires us to rewrite equation [5.41] properly and take into account this peculiar geometry.

Equation [5.38] governs the Z modes propagating in the bulk 2D phononic crystal and can be rewritten as

$$\omega^2 \sum_{\vec{G}'} \rho(\vec{G}-\vec{G}')U_{3,\vec{K}}(\vec{G}') = \sum_{\vec{G}'} C_{44}(\vec{G}-\vec{G}')\Big[(G_1+K_1)(G_1'+K_1)+(G_2+K_2)(G_2'+K_2)\Big]U_{3,\vec{K}}(\vec{G}'). \quad [5.49]$$

If in equation [5.49], we single out the term $\vec{G} = \vec{G}'$ in the summation, then this equation can be recast as

$$\omega^2\Big\{\rho(\vec{0})U_{3,\vec{K}}(\vec{G}) + \sum_{\vec{G}'\neq\vec{G}} \rho(\vec{G}-\vec{G}')U_{3,\vec{K}}(\vec{G}')\Big\} = C_{44}(\vec{0})\Big[(G_1+K_1)(G_1+K_1)+(G_2+K_2)(G_2+K_2)\Big]U_{3,\vec{K}}(\vec{G}) + \sum_{\vec{G}'\neq\vec{G}} C_{44}(\vec{G}-\vec{G}')\Big[(G_1+K_1)(G_1'+K_1)+(G_2+K_2)(G_2'+K_2)\Big]U_{3,\vec{K}}(\vec{G}') \quad [5.50]$$

and

$$\omega^2\Big\{\overline{\rho}U_{3,\vec{K}}(\vec{G}) + (\rho_A-\rho_B)\sum_{\vec{G}'\neq\vec{G}} F(\vec{G}-\vec{G}')U_{3,\vec{K}}(\vec{G}')\Big\} = \overline{C_{44}}(\vec{G}+\vec{K})^2.U_{3,\vec{K}}(\vec{G}) + (C_{44A}-C_{44B})\sum_{\vec{G}'\neq\vec{G}} F(\vec{G}-\vec{G}')\Big[(G_1+K_1)(G_1'+K_1) + (G_2+K_2)(G_2'+K_2)\Big]U_{3,\vec{K}}(\vec{G}'). \quad [5.51]$$

Considering the dimensionless vectors $\vec{g} = \frac{a}{2\pi}\vec{G}$, $\vec{g}' = \frac{a}{2\pi}\vec{G}'$ and $\vec{k} = \frac{a}{2\pi}\vec{K}$, equation [5.51] becomes

$$\omega^2\overline{\rho}\Big\{U_{3,\vec{k}}(\vec{g}) + \frac{(\rho_A-\rho_B)}{\overline{\rho}}\sum_{\vec{g}'\neq\vec{g}} F(\vec{g}-\vec{g}')U_{3,\vec{k}}(\vec{g}')\Big\}$$

$$= \overline{C_{44}}(\frac{2\pi}{a})^2\Big\{(\vec{g}+\vec{k})^2.U_{3,\vec{k}}(\vec{g}) + \frac{(C_{44A}-C_{44B})}{\overline{C_{44}}}\sum_{\vec{g}'\neq\vec{g}}F(\vec{g}-\vec{g}')(\vec{g}+\vec{k})(\vec{g}'+\vec{k})U_{3,\vec{k}}(\vec{g}')\Big\} \quad [5.52]$$

that can be rewritten as

$$\Omega^2\Big\{U_{3,\vec{k}}(\vec{g}) + \Delta\rho\sum_{\vec{g}'\neq\vec{g}}F(\vec{g}-\vec{g}')U_{3,\vec{k}}(\vec{g}')\Big\} = (\vec{g}+\vec{k})^2.U_{3,\vec{k}}(\vec{g}) + \Delta C_{44}\sum_{\vec{g}'\neq\vec{g}}F(\vec{g}-\vec{g}')(\vec{g}+\vec{k})(\vec{g}'+\vec{k})U_{3,\vec{k}}(\vec{g}') \quad [5.53]$$

where

$$\Omega = \frac{\omega}{(\frac{2\pi}{a})\sqrt{\frac{\overline{C_{44}}}{\overline{\rho}}}}\ ,\ \Delta C_{44} = \frac{(C_{44A}-C_{44B})}{\overline{C_{44}}}\ ,\ \text{and}\ \Delta\rho = \frac{(\rho_A-\rho_B)}{\overline{\rho}}$$

are dimensionless quantities. The same transformations can be done for equation [5.37] governing the XY modes of propagation. Equation [5.53] shows that it is convenient to compute the dimensionless frequency Ω versus the dimensionless Bloch wave vector $\vec{k}$. For example, in the case of a square array of cylindrical inclusions, the $2D$ dimensionless vectors $\vec{g}$ (resp. $\vec{g}'$) are $\vec{g} = \ell\vec{e_1} + m\vec{e_2}$ (resp. $\vec{g}' = \ell'\vec{e_1} + m'\vec{e_2}$), where ℓ and m (resp. ℓ' and m') are integers (see [VAS 94]). In the course of the numerical resolution of equations [5.37] and [5.38], we consider $-MT \leq (\ell,\ell') \leq +MT$ and $-MT \leq (m,m') \leq +MT$ where MT is a positive integer, i.e. $(2MT+1)^2$ $\vec{g}$ or $\vec{g}'$ vectors are taken into account in the truncated Fourier series. This gives $(2MT+1)^2$ (resp. $2(2MT+1)^2$) real eigenfrequencies for the Z modes (resp. the XY modes) for a given reduced wave vector $\vec{k}$ describing the principal directions of propagation in the irreducible Brillouin zone (at point Γ, X and M of the irreducible Brillouin zone of the square array, $\vec{k}$ is $\vec{k_\Gamma} = (0,0)$, $\vec{k_X} = (\frac{1}{2},0)$ and $\vec{k_M} = (\frac{1}{2},\frac{1}{2})$, respectively [VAS 94]). Solving for equation [5.53] needs to resolve a generalized eigen values problem for each value of $\vec{k}$. The size of the matrices involved in this problem and then the choice of the values of the integer MT is of crucial importance for insuring the convergency of the Fourier series and consequently to optimize the precision on the numerical values of the eigen frequencies Ω. This will be discussed in the next section.

5.3.2. *Limits of the PWE method*

The PWE method constitutes a useful tool for calculating band structures of phononic crystals. It is relatively easy to implement the method numerically and the main difficulty lies in correctly writing the matrices involved in the generalized eigenvalues problem to solve. There exists many numerical codes (in Fortran and C languages, in Matlab software, etc.) of band structure calculations based on the PWE method that are freely available on the Internet (many of them were developed for photonic crystals, but they can be easily transposed to phononic crystals). The method is general in the sense that it can be applied for 1D, 2D and 3D structures, with inclusions of different shapes distributed on arrays of various geometries. Inclusions and matrix can be made of materials of much more complicated crystallographic symmetry than the isotropic or the cubic ones [LIN 11]. Moreover, not only passive elastic constituent materials, but also active ones such as piezoelectric [WIL 02] or magneto-elastic [BOU 12] materials may be taken into account. However, the method presents some limits linked with convergency problems of the truncated Fourier series and the choice of constitutive materials.

5.3.2.1. *Convergency of the truncated Fourier series*

As already mentioned at the end of section 5.3.1.3, while the Fourier series are assumed infinite theoretically, a finite number of reciprocal lattice vectors must be taken into account in the course of the numerical calculations. We analyze here the effect of this truncation of the series on the calculated eigen values. For that, we consider the particular case of a phononic crystal made of very contrasted constituent materials, namely a square array of steel cylinders embedded in an epoxy matrix for a filling factor of inclusions $f = 0.55$. One limits the study to the Z modes of propagation defined by equation [5.53]. Figure 5.7 presents the first 10 bands of these band structures. These are calculated along the principal directions of propagation of the irreducible Brillouin zone for different values of the integer MT, – namely for $MT = 6, 8$, 10 and 12. While the overall shape of the band structure remains almost the same, we observe that the location in frequency of some bands (for Ω around 0.2, 0.45 and 1.0 for examples) is strongly influenced by the value of MT, this effect being larger for Ω. This slow convergency results mainly from the difficulty to reproduce accurately a strongly discontinuous function such as the density or an elastic modulus as a summation of a finite number of sinusoidal continuous functions [SÖZ 92]. This is often referred to as the "Gibbs phenomenon" and can be clearly viewed in Figure 5.8, where the function

$$\rho_{truncated}(\vec{r}) = \sum_{|\vec{G}| \leq G_{max}} \rho(\vec{G}) e^{i\vec{G}.\vec{r}} \qquad [5.54]$$

(with $G_{max} = \frac{2\pi}{a}\sqrt{MT^2 + MT^2} = \frac{2\pi}{a}.MT\sqrt{2}$) has been plotted for different numbers of reciprocal lattice vectors (i.e. for $MT = 6$, 8, 10 and 12). We observe that whatever the value of MT, the function $\rho_{truncated}$ is rather different from $\rho(\vec{r})$.

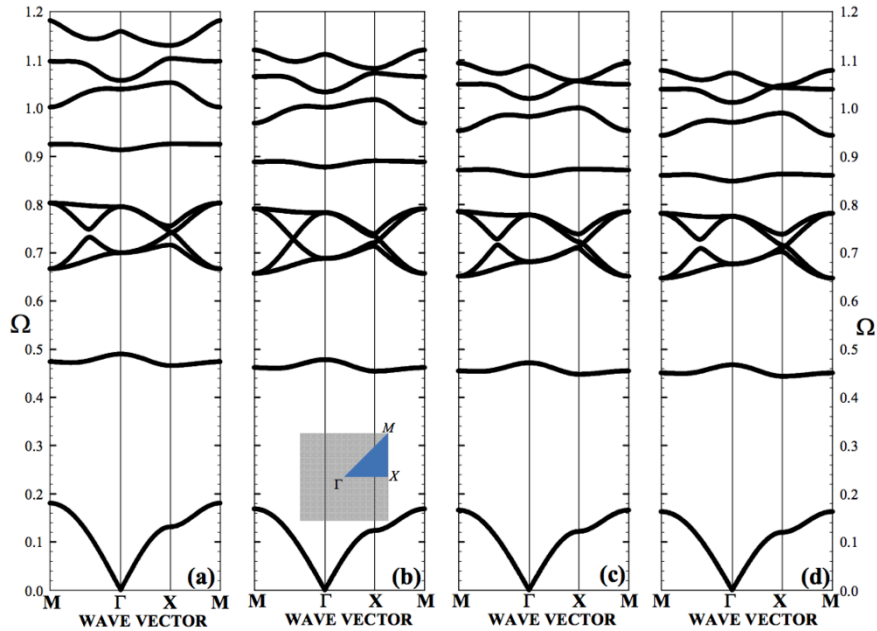

Figure 5.7. *Z modes band structure for a square array of steel circular cylinders embedded in an epoxy matrix for $MT = 6$ (a), $MT = 8$ (b), $MT = 10$ (c), and $MT = 12$ (d). $\rho_A = 7780\ kg.m^{-3}$, $C_{44,A} = 8.1.10^{10}\ N.m^{-2}$, $\rho_B = 1142\ kg.m^{-3}$, $C_{44,B} = 0.148.10^{10}\ N.m^{-2}$ and $f = 0.55$. The inset represents the square Brillouin zone*

Then when using the PWE method, it is necessary to fix a value of MT allowing a good compromise between convergency and calculation time. Convergency of the truncated Fourier series is of main importance when considering very different constituent materials such as steel and epoxy. In this case, a value of MT at least equal to 10 is necessary for obtaining acceptable values of the eigenfrequencies. Some authors have proposed alternative scheme aiming at speeding up the convergency of the PWE algorithm ([CAO 04] and Chapter 11 of [DEY 13]).

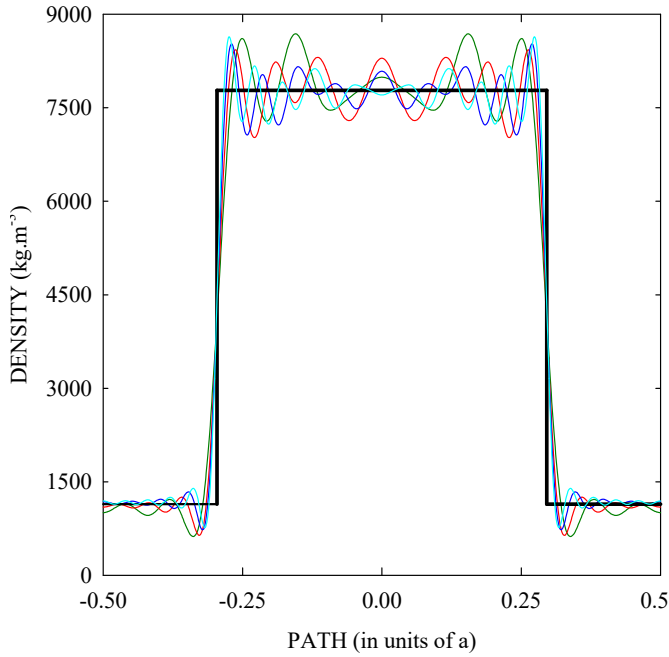

Figure 5.8. *$\rho(\vec{r})$ (black) and $\rho(\vec{r})_{truncated}$ with $MT = 6$ (green), $MT = 8$ (red), $MT = 10$ (blue), $MT = 12$ (cyan) for a square array of steel cylinders embedded in an epoxy matrix along the path $x_1 = x_2$ in the unit cell (see Figure 5.6); $f = 0.55$. For a color version of this figure, see www.iste.co.uk/romero/metamaterials.zip*

5.3.2.2. *Choice of the materials*

In the preceding sections, it was assumed that all the constituent materials are purely elastic solids. However, we may consider phononic crystals made of materials of different nature, for example, a fluid (liquid or gas) and a solid and we can question the reliability of the PWE method in this case. Let us consider a 2D phononic crystal made of hollow cylinders drilled in a solid matrix and filled with a liquid. We may intuitively modelize the fluid as an isotropic "solid" material with $C_{44} = 0$, because a transverse vibration does not exist inside a liquid. However, the PWE method still assumes a finite non-vanishing displacement amplitude for this transverse mode in the cylinders and considering $C_{44} = 0$ in the fluid will introduce numerical instabilities in the PWE code. As a matter of example, we report in Figure 5.9 the XY modes band structure of a square array of hollow cylinders drilled in an aluminum matrix and filled with liquid mercury. Liquid mercury was modeled as a solid isotropic material with $C_{44} = 0$, values of ρ and C_{11} being those of *real* mercury. PWE calculations reveal the existence of flat bands, which number increases when the number of reciprocal lattice vectors taken into account in the

Fourier series increases, and bands without clear physical meaning. The absence of these modes in the band structure which were worked out using another method of calculation (for example, the finite element method via the COMSOL software where solid material and fluid constituent are modeled with their real elastic characteristics – two elastic moduli for the solid and the compressibility modulus for the fluid) shows unambiguously that the PWE additional modes are fictitious [TAN 00]. Z. Hou *et al.* [HOU 06] argued that these fictitious modes result from an incorrect use of the Bloch theorem in the application of the PWE method in such mixed solid/fluid phononic crystals. Note that the boundary conditions between the solid and the liquid are strictly satisfied in the finite element calculations, while the PWE method does not take into account these conditions.

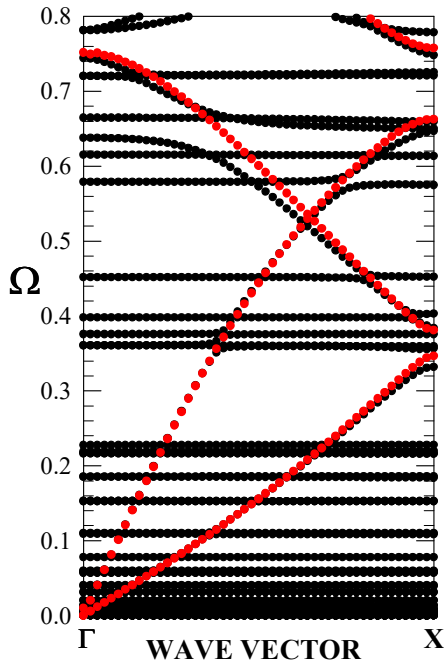

Figure 5.9. *XY band structure along the ΓX direction of the irreducible Brillouin zone of a square array of hollow cylinders drilled in an aluminum matrix and filled with liquid mercury for $f = 0.4$; black dots: PWE calculations where mercury has been considered as an isotropic solid with $C_{44} = 0$ and $MT = 8$, red dots : finite element results where mercury has been considered as a real fluid. The PWE method leads to unphysical modes in this case and fails to predict accurately the propagating modes in the mixed fluid/solid 2D structure. $\rho_A = 13600\ kg.m^{-3}$, $C_{11,\,A} = 2.86\ 10^{10}\ N.m^{-2}$, $\rho_B = 2700\ kg.m^{-3}$, $C_{44,\,B} = 2.61\ 10^{10}\ N.m^{-2}$, $C_{11,\,B} = 11.09\ 10^{10}\ N.m^{-2}$. For a color version of this figure, see www.iste.co.uk/romero/metamaterials.zip*

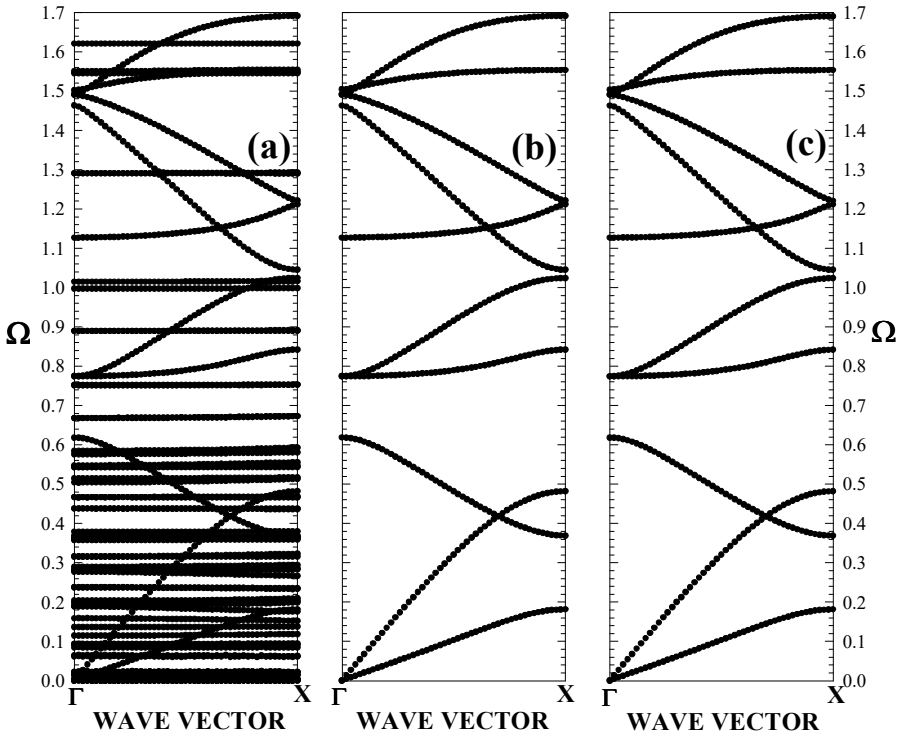

Figure 5.10. *XY band structure along the ΓX direction of the irreducible Brillouin zone of a square array of hollow circular cylinders drilled in an aluminum matrix for $f = 0.4$; (a) PWE calculations where the medium inside the cylinders is air with $C_{44} = 0$, $C_{11} = 1.49\ 10^5 N.m^{-2}$, $\rho = 1.3\ kg.m^{-3}$ and $MT = 6$; (b) PWE calculations where the medium inside the cylinders is the LIM with $C_{11} = C_{44} = 10^6\ N.m^{-2}$, $\rho = 10^{-4}\ kg.m^{-3}$ and $MT = 6$; (c) Finite elements method (see text for details)*

Moreover, phononic crystals made of holes drilled in a solid matrix present many advantages because they can be manufactured quite easily. For the reasons reported previously, if we model air inside the cylinders as a solid material with vanishing C_{44}, we obtain fictitious flat bands in the band structure as it is depicted in Figure 5.10(a) where the XY band structure for a square array of holes drilled in an aluminum matrix is reported. However, it was shown [VAS 08] that for an accurate use of the PWE method in this case, it is preferable to replace air inside the cylinders by vacuum and to model vacuum as a pseudo-solid material with very low elastic

moduli and density. Indeed, modeling vacuum by a material with vanishing density and elastic moduli leads to unphysical solutions to the eigenvalue problem. For the sake of simplicity, this low impedance medium (LIM) was supposed elastically isotropic and was characterized by a longitudinal speed of sound C_ℓ, and a transversal speed of sound C_t or equivalently by two elastic moduli, $C_{11} = \rho.{C_\ell}^2$ and $C_{44} = \rho {C_t}^2$. The choice of the values of these parameters is governed by the boundary condition between any solid material and a vacuum. Indeed, we know that this interface must be free of stress and this requires that $C_{11} = 0$ and $C_{44} = 0$ rigorously in a vacuum. Then, using the LIM to model the vacuum in the PWE computations, the nonvanishing values of these parameters must be as small as possible and we considered that the ratio between the elastic moduli of the LIM and those of any other solid material constituting the phononic crystal must approach zero. We imposed C_ℓ and C_t to be much larger than the speeds of sound in usual solid materials, in order to limit propagation of acoustic waves to the solid. Large speeds of sound and small elastic moduli impose a choice of a very low mass density for the LIM. More specifically, we choose $\rho = 10^{-4}$ kg.m^{-3} and $C_\ell = C_t = 10^5$ m.s^{-1}, i.e. the acoustic impedances of the LIM are equal to 10 kg.m^{-2}.s^{-1}. With these values, $C_{11} = C_{44} = 10^6$ N.m^{-2} and the elastic constants of the LIM are approximately 10^4 times lower than those of any usual solid material that are typically of the order of 10^{10} N.m^{-2}. The values we have chosen for C_{11} and C_{44} are a compromise to achieve satisfactory convergence of the PWE method and still satisfy boundary conditions. C_{11} and C_{44} were assumed the same for convenience. Figure 5.10(b) presents the same band structure as in Figure 5.10(a) but the medium inside the hollow cylinders is modeled with the LIM. We observe that the flat bands that appeared in Figure 5.10(a) are removed. The results obtained with the finite element method, where only the space occupied by the aluminum matrix has been discretized, reported in Figure 5.10(c), show a very good agreement with those of Figure 5.10(b). This shows that the PWE method is suitable for calculating the band structure of phononic crystals made of holes drilled inside a solid matrix provided the medium inside the holes is replaced by the LIM.

Many experimental works were dealing with phononic crystals, often named as sonic crystals, where solid inclusions are surrounding with air. Again considering air as a solid with $C_{44} = 0$ leads to unphysical results. Nevertheless, due to the huge contrast between the physical characteristics of the solid and those of air, the solid inclusions can be assumed infinitely hard with a high density and high elastic moduli. This implies that the sound does not penetrate such inclusions, and hence the propagation of acoustic waves is predominant in air in which only longitudinal waves can propagate. The periodic structure made of rigid inclusions in air can then be

considered as an inhomogeneous fluid and the equation of propagation of longitudinal acoustic waves in such medium [KUS 98a] is written as

$$-\frac{1}{C_{11}(\vec{r})}\frac{\partial^2 p(\vec{r},t)}{\partial t^2} = -\frac{\omega^2}{C_{11}(\vec{r})}p(\vec{r}) = \vec{\nabla}.\Big(\frac{1}{\rho(\vec{r})}\vec{\nabla}p(\vec{r},t)\Big) \qquad [5.55]$$

where $p(\vec{r},t) = e^{i\omega t}p(\vec{r})$ is the acoustic pressure field inside the heterogeneous fluid. In a periodic fluid medium, equation [5.55] can be Fourier transformed to give

$$\omega^2 \sum_{\vec{G}'} C_{11}^{-1}(\vec{G}-\vec{G}')p_{\vec{K}}(\vec{G}') = \sum_{\vec{G}'} \rho^{-1}(\vec{G}-\vec{G}')\Big[(G_1+K_1)(G_1'+K_1)+ \\ +(G_2+K_2)(G_2'+K_2)+(G_3+K_3)(G_3'+K_3)\Big]p_{\vec{K}}(\vec{G}'). \qquad [5.56]$$

We note that in the case of a 2D array of rigid cylindrical inclusions surrounded by air (i.e. for $G_3 = G_3' = K_3 = 0$), equation [5.56] becomes

$$\omega^2 \sum_{\vec{G}'} C_{11}^{-1}(\vec{G}-\vec{G}')p_{\vec{K}}(\vec{G}') = \sum_{\vec{G}'} \rho^{-1}(\vec{G}-\vec{G}')\Big[(G_1+K_1)(G_1'+K_1) \\ +(G_2+K_2)(G_2'+K_2)\Big]p_{\vec{K}}(\vec{G}') \qquad [5.57]$$

and it is fully analog to the equation of propagation of Z modes in an elastic solid 2D phononic crystal (provided ρ, C_{44} and $U_{3,\vec{K}}$ in equation [5.49] play the roles of C_{11}^{-1}, ρ^{-1} and $p_{\vec{k}}$ in equation [5.57]). Considering these analogies and using a numerical code written for the Z modes, it is very easy to calculate the band structure reported in Figure 5.11 for a square array of steel cylinders in air. Due to the existence of a large acoustic stop band in the audible frequency range, application of these sonic crystals as sound barriers was largely investigated by many authors [GOF 03, PEI 16].

The reliability of the assumption of infinitely rigid inclusions when the matrix of the phononic crystal is made of air was validated (see Figure 2 of reference [VAS 09]). We may note that this assumption leads to unreliable results in most of the cases (array of inclusions, filling factor of inclusions, etc.) when considering a fluid matrix whose physical characteristics are larger than that of air, such as water. We can also remark that equation [5.56] can be used for calculating band structures of phononic crystals composed of only fluid constituents such as periodic arrays of air inclusions in water [KUS 98a, KUS 98b].

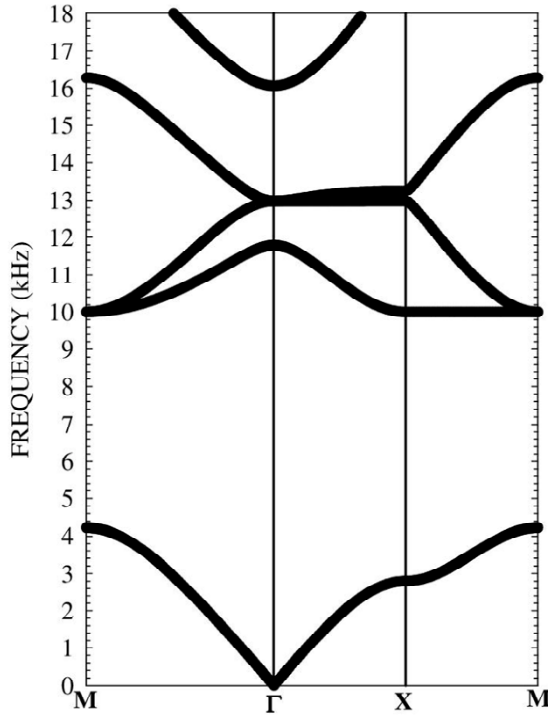

Figure 5.11. *PWE band structure of a square array of circular steel cylinders placed in air with $a = 2.7$ cm and $R = 1.29$ cm. PWE calculations were done considering the assumption of infinitely rigid solid inclusions and with $MT = 10$. Notes the existence of a large absolute stop band in the audible frequency range*

5.3.3. *Modified PWE method for complex band structures*

In classical PWE expansion methods (see section 5.3.1.2), we calculate a set of real eigenfrequencies $\omega(\vec{K})$ for a specific wave vector $\vec{K}$. That means that only propagating modes with a real wave vector can be deduced from the $\omega(\vec{K})$ PWE method. Then a modified PWE method has been proposed that allows the calculation of not only the propagating modes, but also the evanescent modes [ROM 10a, ROM 10b]. The wave vector for evanescent waves possesses a non vanishing imaginary part. We have seen previously that the Fourier transform of the equation of propagation of elastic waves in a phononic crystal leads to the resolution of a generalized eigenvalue equation in the form $\omega^2 \overleftrightarrow{B}\vec{\mathcal{U}} = \overleftrightarrow{A}\vec{\mathcal{U}}$.

The matrix elements of $\overleftrightarrow{A}$ and $\overleftrightarrow{B}$ involve terms depending on the components of the wave vector $\vec{K}$. It is always possible to rewrite matrix $\overleftrightarrow{A}$ as $\overleftrightarrow{A} = {K_\alpha}^2\overleftrightarrow{A_1} + K_\alpha\overleftrightarrow{A_2} + \overleftrightarrow{A_3}$, where K_α is one of the components of the wave vector, and $\overleftrightarrow{A_1}$, $\overleftrightarrow{A_2}$ and $\overleftrightarrow{A_3}$ are matrices of the same size as $\overleftrightarrow{A}$. The generalized eigenvalue equation $\omega^2\overleftrightarrow{B}\vec{\mathcal{U}} = \overleftrightarrow{A}\vec{\mathcal{U}}$ may be recast as ${K_\alpha}^2\overleftrightarrow{A_1}\vec{\mathcal{U}} = (\omega^2\overleftrightarrow{B} - K_\alpha\overleftrightarrow{A_2} - \overleftrightarrow{A_3}).\vec{\mathcal{U}}$ and we can write

$$K_\alpha \begin{pmatrix} \overleftrightarrow{I} & \overleftrightarrow{0} \\ \overleftrightarrow{0} & \overleftrightarrow{A_1} \end{pmatrix} \begin{pmatrix} \vec{\mathcal{U}} \\ K_\alpha\vec{\mathcal{U}} \end{pmatrix} = \begin{pmatrix} 0 & \overleftrightarrow{I} \\ \omega^2\overleftrightarrow{B} - \overleftrightarrow{A_3} & -\overleftrightarrow{A_2} \end{pmatrix} \begin{pmatrix} \vec{\mathcal{U}} \\ K_\alpha\vec{\mathcal{U}} \end{pmatrix}, \quad [5.58]$$

where $\overleftrightarrow{I}$ is the identity matrix. Equation [5.58] is nothing else than a generalized eigenvalue equation, where the eigenvalues are the component K_α of the wave vector. For a specific value of the circular frequency ω, we calculate a set of complex eigenvalues K_α. The size of the matrices occurring on the left and right sides of equation [5.58] is twice that of matrices $\overleftrightarrow{A}$ and $\overleftrightarrow{B}$. We may illustrate these general ideas by considering the peculiar case of the Z elastic modes propagating in a bulk $2D$ phononic crystal made of a square array of lattice parameter a, of cylindrical inclusions embedded in a solid matrix. If we assume that $K_3 = 0$, then these modes are given by equation [5.53], where ω depends on the two variables K_1 and K_2. Consider the propagation of elastic waves along the ΓX direction of the irreducible Brillouin zone for which $K_2 = 0$ and $0 \leq \mathfrak{Re}(K_1) \leq \frac{\pi}{a}$.

Equation [5.53] gives

$$\omega^2 \sum_{\vec{G}'} \rho(\vec{G} - \vec{G}')U_{3,\vec{K}}(\vec{G}') = \sum_{\vec{G}'} C_{44}(\vec{G} - \vec{G}')\Big[(G_1 + K_1)(G_1' + K_1) + G_2.G_2'\Big].U_{3,\vec{K}}(\vec{G}') \quad [5.59]$$

and this can be rewritten as

$$\begin{aligned} {K_1}^2 \sum_{\vec{G}'} C_{44}(\vec{G} - \vec{G}').U_{3,\vec{K}}(\vec{G}') &= \sum_{\vec{G}'} \Big\{\omega^2\rho(\vec{G} - \vec{G}') - (G_1G_1' + G_2G_2')C_{44}(\vec{G} - \vec{G}')\Big\}U_{3,\vec{K}}(\vec{G}') \\ &\quad - K_1 \sum_{\vec{G}'} (G_1 + G_1')C_{44}(\vec{G} - \vec{G}').U_{3,\vec{K}}(\vec{G}') \end{aligned} \quad [5.60]$$

or in matrix form

$$K_1 \begin{pmatrix} \overleftrightarrow{I} & \overleftrightarrow{0} \\ \overleftrightarrow{0} & \overleftrightarrow{A_1} \end{pmatrix} \begin{pmatrix} \vec{\mathcal{U}} \\ K_1\vec{\mathcal{U}} \end{pmatrix} = \begin{pmatrix} 0 & \overleftrightarrow{I} \\ \omega^2\overleftrightarrow{B} - \overleftrightarrow{A_3} & -\overleftrightarrow{A_2} \end{pmatrix} \begin{pmatrix} \vec{\mathcal{U}} \\ K_1\vec{\mathcal{U}} \end{pmatrix}, \quad [5.61]$$

where

$$\begin{cases} B_{\vec{G},\vec{G}'} = \rho(\vec{G} - \vec{G}'), & [5.62a] \\ A_{1\vec{G},\vec{G}'} = C_{44}(\vec{G} - \vec{G}'), & [5.62b] \\ A_{2\vec{G},\vec{G}'} = C_{44}(\vec{G} - \vec{G}')(G_1 + G_1'), & [5.62c] \\ A_{3\vec{G},\vec{G}'} = C_{44}(\vec{G} - \vec{G}').(G_1G_1' + G_2G_2'). & [5.62d] \end{cases}$$

The same transformations of the Fourier transformed equations of propagation can be done easily for XY propagation modes. Numerical resolution of equation [5.61] gives $2N$ (if $N \times N$ is the size of matrices $\overleftrightarrow{A}$ and $\overleftrightarrow{B}$) complex values of $K_1 = \mathfrak{Re}\{K_1\} - i\mathfrak{Im}\{K_1\}$ for any value of ω. Eigenvalues belonging to the irreducible Brillouin zone and corresponding to waves with a vanishing amplitude when $x_1 \to \infty$ may be taken into account, i.e., $0 \leq \mathfrak{Re}\{K_1\} \leq \frac{\pi}{a}$ and $\mathfrak{Im}\{K_1\} \geq 0$. Figure 5.12 presents the band structures calculated by both $\omega(\vec{K})$ and $\vec{K}(\omega)$ methods. This figure shows the ability of the $\vec{K}(\omega)$ method to calculate the evanescent modes. Of particular interest is the existence of additional bands (see right panel of Figure 5.12 for $\Omega \approx 1.1$) not predicted by the classical $\omega(\vec{K})$ method (red dots). These vibrational modes are characterized by a nonvanishing $\mathfrak{Im}\{K_1\}$. $\vec{K}(\omega)$ method requires to consider only one component of the wave vector $\vec{K}$ as eigenvalue. That needs to keep fixed the other component or to write a linear relation between them. For example, along the ΓM direction in the irreducible Brillouin zone of the square array, we can write $K_1 = K_2$ and consider K_1 as the eigenvalue. In the same way, we can deal with any direction of propagation and not only with the high-symmetry directions. Plotting all the values of K_1 and K_2 corresponding to a specific frequency leads to the equifrequency contour (EFC) of the phononic crystal. For example, in Figure 5.13(c) the EFC's calculated at two different frequencies are presented for a triangular array of steel cylinders embedded in epoxy (see Figure 5.13(a)) for which the XY band structure is also given in Figure 5.13(b). We note the perfect circular shape of these EFCs, indicating that this phononic crystal may present peculiar refraction properties [CRO 11]. Moreover, the $\vec{K}(\omega)$ PWE method allows to take into account elastic moduli depending on the frequency and should be applied for calculating the band structures of phononic crystals made of viscoelastic materials [MOI 11].

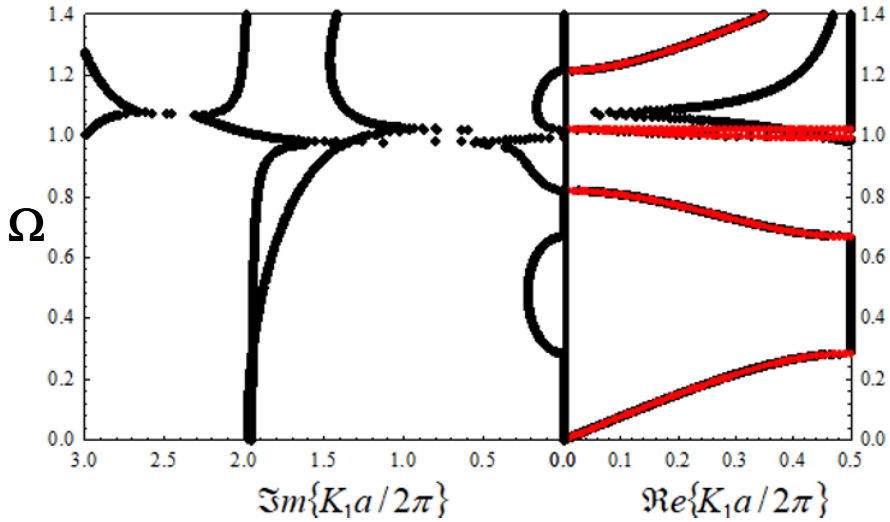

Figure 5.12. *Z modes band structure along the ΓX direction $(K_2 = 0)$ of the irreducible Brillouin zone for a square array of circular holes drilled in a Silicon matrix: Red dots: $\omega(\vec{K})$ method; black dots: $\vec{K}(\omega)$ method. For a color version of this figure, see www.iste.co.uk/romero/metamaterials.zip*

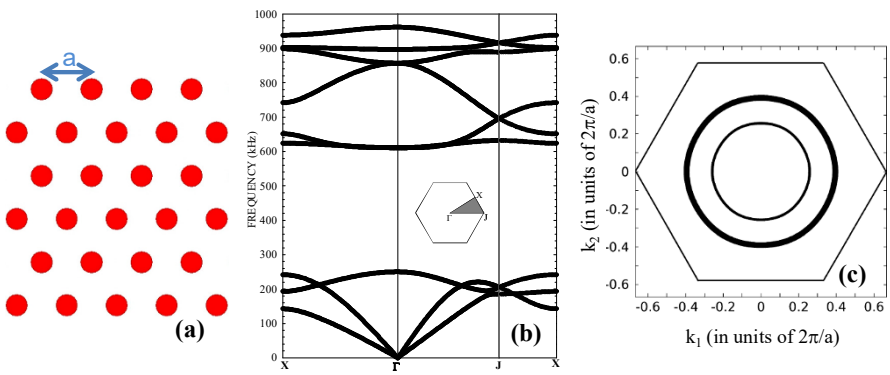

Figure 5.13. *(a) Cross section of the triangular array of circular steel cylinders in epoxy ($a = 2.84$ mm, $R = 1$ mm); (b) $\omega(\vec{K})$ band structure for the XY modes; the inset represents the hexagonal Brillouin zone (c) $\vec{K}(\omega)$ PWE equifrequency contours at 780 kHz (thick solid line) and at 800 kHz (thin solid line)*

5.4. Conclusion

We have reported with many details on the PWE method, which is nowadays a useful and pedagogical tool when searching to compute the dispersion curves of periodic structures such as phononic crystals. The method is quite easy to implement, but presents some limitations regarding the convergency of the Fourier series and the choice of the constituent materials. The method is reliable in the case of phononic crystals made of solid or fluid components, but is not for most of the mixed structures where a fluid component is associated with a solid one. In these cases, other means of calculation such as the finite difference time domain method or the finite element method must be preferred. Nevertheless, we have proposed tricks for accurately dealing with structures made of holes drilled in a solid matrix or constituted of solid inclusions surrounded with air. The classical PWE method can also be extended for analyzing the evanescence of waves inside the band gaps and for calculating the equifrequency surfaces of any periodic structure.

5.5. Acknowledgments

I would like to thank C. Croënne (IEMN, Villeneuve d'Ascq, France) for his help with some numerical calculations.

5.6. References

[ASH 76] ASHCROFT N., MERMIN N., *Solid State Physics*, 8th Edition, Saunders College Publishing, Fort Worth, 1976.

[BOU 12] BOUMATAR O., ROBILLARD J.F., VASSEUR J.O. *et al.*, "Band gap tunability of magneto-elastic phononic crystal", *Journal of Applied Physics*, vol. 111, no. 5, p. 054901, 2012.

[CAO 04] CAO Y., HOU Z., LIU Y., "Convergence problem of plane-wave expansion method for phononic crystals", *Physics Letters A*, vol. 327, no. 2, pp. 247–253, 2004.

[CRO 11] CROENNE C., MANGA E.D., MORVAN B. *et al.*, "Negative refraction of longitudinal waves in a two-dimensional solid-solid phononic crystal", *Physical Review B*, vol. 83, no. 5, p. 054301, 2011.

[DEY 13] DEYMIER P., *Acoustic Metamaterials and Phononic Crystals, Springer Series in Solid-State Sciences 173*, Springer, Berlin-Heidelberg, 2013.

[GOF 03] GOFFAUX C., MASERI F., VASSEUR J.O. *et al.*, "Measurements and calculations of the sound attenuation by a phononic band gap structure suitable for an insulating partition application", *Applied Physics Letters*, vol. 83, no. 2, pp. 281–283, 2003.

[HOU 06] HOU Z., FU X., LIU Y., "Singularity of the Bloch theorem in the fluid/solid phononic crystal", *Physical Review B*, vol. 73, no. 2, p. 024304, 2006.

[KIT 04] KITTEL C., *Introduction to Solid State Physics*, 8th edition, Wiley, USA, 2004.

[KUS 93] KUSHWAHA M., HALEVI P., DOBRZYNSKI L. *et al.*, "Acoustic band structure of periodic elastic composites", *Physical Review Letters*, vol. 71, no. 13, pp. 2022–2025, 1993.

[KUS 98a] KUSHWAHA M., DJAFARI-ROUHANI B., "Giant sonic stop bands in two-dimensional periodic system of fluids", *Journal of Applied Physics*, vol. 84, no. 9, pp. 4677–4683, 1998.

[KUS 98b] KUSHWAHA M., DJAFARI-ROUHANI B., DOBRZYNSKI L., "Sound isolation from cubic arrays of air bubbles in water", *Physics Letters A*, vol. 248, no. 2, pp. 252–256, 1998.

[LIN 11] LIN S.-C.S., HUANG T.J., "Tunable phononic crystals with anisotropic inclusions", *Physical Review B*, vol. 83, no. 17, p. 174303, 2011.

[MOI 11] MOISEYENKO R.P., LAUDE V., "Material loss influence on the complex band structure and group velocity in phononic crystals", *Physical Review B*, vol. 83, no. 6, p. 064301, 2011.

[PEI 16] PEIRÒ-TORRES M., REDONDO J., BRAVO J. *et al.*, "Open noise barriers based on sonic crystals. Advances in noise control in transport infrastructures", *Transportation Research Procedia*, vol. 18, no. Supplement C, pp. 392–398, 2016.

[RAY 87] RAYLEIGH L., "XVII. On the maintenance of vibrations by forces of double frequency, and on the propagation of waves through a medium endowed with a periodic structure", *Philosophical Magazine, Series 5*, vol. 24, no. 147, pp. 145–159, 1887.

[ROM 10a] ROMERO-GARCÍA V., SÁNCHEZ-PÉREZ J., GARCIA-RAFFI L., "Evanescent modes in Sonic Crystals: Complex dispersion relation and supercell approximation", *Journal of Applied Physics*, vol. 108, p. 044907, 2010.

[ROM 10b] ROMERO-GARCÍA V., SÁNCHEZ-PÉREZ J., NEIRA IBÁÑEZ S.C. *et al.*, "Evidences of evanescent Bloch waves in Phononic Crystals", *Applied Physics Letters*, vol. 96, p. 124102, 2010.

[ROY 99] ROYER D., DIEULESAINT E., *Elastic Waves in Solids I, Free and Guided Propagation*, Springer, Berlin-Heidelberg, 1999.

[SÖZ 92] SÖZÜER H.S., HAUS J.W., INGUVA R., "Photonic bands: Convergence problems with the plane-wave method", *Physical Review B*, vol. 45, no. 24, pp. 13962–13972, 1992.

[SIG 92] SIGALAS M., ECONOMOU E., "Elastic and acoustic wave band structure", *Journal of Sound and Vibration*, vol. 158, no. 2, pp. 377–382, 1992.

[TAN 00] TANAKA Y., TOMOYASU Y., TAMURA S., "Band structure of acoustic waves in phononic lattices: Two-dimensional composites with large acoustic mismatch", *Physical Review B*, vol. 62, no. 11, pp. 7387–7392, 2000.

[VAS 94] VASSEUR J.O., DJAFARI-ROUHANI B., DOBRZYNSKI L. *et al.*, "Complete acoustic band-gaps in periodic fibre reinforced composite materials: The carbon/epoxy composite and some metallic systems", *Journal of Physics: Condensed Matter*, vol. 6, no. 42, pp. 8759–8770, 1994.

[VAS 08] VASSEUR J.O., DEYMIER P.A., DJAFARI-ROUHANI B. *et al.*, "Absolute forbidden bands and waveguiding in two-dimensional phononic crystal plates", *Physical Review B*, vol. 77, no. 8, p. 085415, 2008.

[VAS 09] VASSEUR J., DEYMIER P.A., BEAUGEOIS M. *et al.*, "Experimental observation of resonant filtering in a two-dimensional phononic crystal waveguide", *Zeitschrift für Kristallographie*, vol. 220, nos 9–10, pp. 829–835, 2009.

[WAN 07] WANG Y.-Z., LI F.-M., HUANG W.-H. *et al.*, "Effects of inclusion shapes on the band gaps in two-dimensional piezoelectric phononic crystals", *Journal of Physics: Condensed Matter*, vol. 19, no. 49, p. 496204, 2007.

[WIL 02] WILM M., BALLANDRAS S., LAUDE V. *et al.*, "A full 3D plane-wave-expansion model for 1–3 piezoelectric composite structures", *The Journal of the Acoustical Society of America*, vol. 112, no. 3, pp. 943–952, 2002.

6

Introduction to Multiple Scattering Theory

Multiple scattering theory is now an important class of theoretical and computational techniques in the study of photonic, phononic and sonic crystals and related problems. In this chapter, we present the development of this theory and apply it to different simple two-dimensional problems of increasing complexity, from the scattering of acoustic waves by a cluster of impervious obstacles to the scattering of plane acoustic waves by stacks of clusters of periodic arrangement and the calculation of band diagrams. We also provide all the necessary recipes to efficiently implement this method.

6.1. Introduction

Multiple scattering theory most probably originated from Lord Rayleigh [RAY 92] when he studied potential flow through a cubic periodic arrangement of identical circular cylinders. This method, also sometimes called the Rayleigh multipole method, has since been widely developed in different fields of wave physics, from electromagnetism to water waves and acoustics, notably thanks to the rapid development of photonic, phononic and sonic crystals. These crystals usually consist of periodic arrangements of scatterers, most of the time simple shapes such as circular cross-sectional cylinders or spheres, embedded in a dielectric, elastic or fluid medium. Methods that are strongly adapted to particular scattering geometries or profiles are therefore quite advantageous, because they provide highly accurate results with relatively short computation times. Among these methods, multiple scattering theory has been particularly successful. The efficiency of the method is apparent in the application of an ingenious field identity relating the regular field in

Chapter written by Logan SCHWAN and Jean-Philippe GROBY.

Fundamentals and Applications of Acoustic Metamaterials: From Seismic to Radio Frequency,
First Edition. Edited by Vicente Romero-García and Anne-Christine Hladky-Hennion.

the vicinity of any scatterer to fields radiated by scatterers and external sources, and the use of lattice sums in the case of periodic systems [BOT 03]. Multiple scattering is a huge subject with a huge literature. For example, the reader can refer to [MAR 06, BOT 03] for further details or to [TOR 17] for an online course.

The aim of this chapter is not to provide an exhaustive review of the possible applications of this method in acoustics [TOU 00], but rather to provide the basic theoretical elements so the reader can understand and implement this method. Homogenization procedures arising from multiple scattering theory are out of the scope of the present chapter. This method will be developed in detail to solve the scattering problem of acoustic waves by simple two-dimensional configurations consisting of the possibly periodic arrangement of impervious circular cross-sectional cylinders. From this simple example, multiple scattering theory can be derived for more complicated cases involving resonant elements [SCH 18], elastic [SAI 05, WU 08], porous [GRO 08b] or poroelastic [WEI 16, ALE 16] materials, as well as for three-dimensional configurations. This chapter is organized as follows: in section 6.2, basic notions and principles of the theory are presented. The procedure to solve the scattering problem by a cluster of cylindrical obstacles is then presented in section 6.3. Orthogonality relations which enable this problem to be solved, application of the boundary conditions yielding to the scattering matrix and Graf's addition theorem are presented. In particular, the scattering problem of a plane wave and a wave radiated by a line source by a cluster are solved. The scattering of plane waves by a periodic row of obstacles is then presented in section 6.4. While the central role of the Schlömilch series is emphasized for the calculation of the scattering coefficient in the direct space, the link with Bloch waves in the Cartesian coordinate system is clearly established. In section 6.5, scattering by a stack of periodic cluster is presented via the Transfer-Matrix method as well as band diagram calculation. Finally, an example of a sonic crystal is provided in section 6.6, before concluding this chapter. Special attention is paid to clearly stating the domain of validity of every field representation required.

6.2. Statement of the problem

6.2.1. *Notion of multiple scattering*

When an obstacle finds itself in the propagation path of a sound wave, part of the sound is deflected from its original course [LAN 87, MOR 68] as shown in Figure 6.1(a): the sound is said to be scattered by the obstacle. This phenomenon is referred to as *single sound scattering*: apart from the *undisturbed field* that would exist in the absence of the obstacle, another wavefield, called the *scattered field*, is emitted in all directions from the obstacle. The actual wavefield that is observed

outside the obstacle is therefore the superposition of both the undisturbed and scattered fields, which are interfering with one another.

When many obstacles find themselves in the propagation path of the sound wave, the sound is scattered by every obstacle: this is called *multiple sound scattering*, see Figure 6.1(b). Besides the undisturbed field that would exist in the absence of the obstacles, scattered fields spread out from every obstacle. However, the obstacles are in mutual interactions: each of them is submitted not only to the undisturbed field, but also to the fields scattered from all the other obstacles. Multiple scattering theory aims at the complete and exact description of these cross interactions.

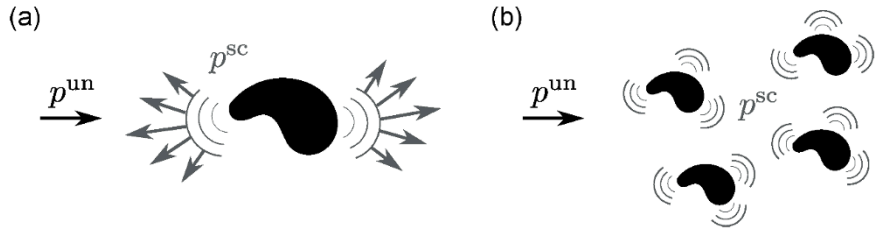

Figure 6.1. *Illustration of (a) single scattering and (b) multiple scattering. p^{un} is the undisturbed field and p^{sc} is the scattered field*

6.2.2. *Helmholtz equation and boundary conditions*

Sound propagation in the presence of the number $\mathcal{N}$ of bounded obstacles arranged in the homogeneous and isotropic propagative medium Ω is studied. Each obstacle is identified by an integer $j \in [\![1, \mathcal{N}]\!]$ and given the name Ω_j. The interface of the obstacle Ω_j with the medium Ω is denoted Γ_j, with the outward normal vector $\mathbf{n}_j$. The position, shape and rheology of each obstacle are supposed to be known, as well as the boundary conditions applied at their surface Γ_j. The analysis is performed in the linear time-harmonic regime at frequencies $\omega/2\pi$ and complex notations are used. The pressure $p\,e^{-\mathrm{i}\omega t}$ and particle velocity $\mathbf{v}e^{-\mathrm{i}\omega t}$ in the medium Ω are governed by the following equations of mass and momentum conservation:

$$\mathrm{div}(\mathbf{v}) = \mathrm{i}\omega p/K \quad \text{and} \quad -\mathrm{i}\omega\rho\mathbf{v} = -\mathbf{grad}(p) \quad \text{in } \Omega, \qquad [6.1]$$

where ρ and K are the density and bulk modulus of the propagative medium Ω. This latter can be made of any fluid or fluid-like materials. For instance, it can be air under ambient conditions, in which case $\rho = 1.213\ \mathrm{kg.m}^{-3}$ and $K = \gamma P_0$, where $\gamma = 1.4$

is the adiabatic constant and $P_0 = 1.013 \times 10^5$ Pa is the atmospheric pressure. Another example is the case where Ω is made of air-saturated porous material with a rigid frame, in which case ρ and K are effective frequency-dependent and complex-valued parameters that account for viscous and thermal effects in the micropores [LEV 77, SAN 80]. In any case, combining the equations [6.1] of mass and momentum conservation, the following relation is derived, that is, the *Helmholtz equation*:

$$\Delta(p) + k^2 p = 0 \quad \text{in } \Omega, \qquad [6.2]$$

where $\Delta(\cdot) = \text{div}(\mathbf{grad}(\cdot))$ is the Laplacian operator and $k = \omega/c$ is the wavenumber, with $c = \sqrt{K/\rho}$ being the sound speed in Ω. To close the problem, equation [6.2] must be supplemented with boundary conditions at the surface Γ_j of the obstacles. Here, the obstacles are supposed to be motionless and impervious to particles in Ω. It implies that the normal component of the particle velocity $\mathbf{v}$ must be zero at each surface Γ_j, that is, $\mathbf{v} \cdot \mathbf{n}_j = 0$ at Γ_j for $j \in [\![1, \mathcal{N}]\!]$. Using the equation of momentum conservation in equation [6.1], it can be written in the following form, called a *boundary condition of the Neumann type*:

$$\forall j \in [\![1, \mathcal{N}]\!], \quad \mathbf{grad}(p) \cdot \mathbf{n}_j = 0 \quad \text{at } \Gamma_j. \qquad [6.3]$$

Other types of boundary conditions could have been considered, for instance, the obstacles could have been permeable to sound waves, as will be described in section 6.3.8, but the simplest case of Neumann boundary conditions given in equation [6.3] will be considered to begin with. In fact, the Helmholtz equation [6.2] and Neumann boundary conditions [6.3] can be found in many domains of physics, such as electromagnetism or optics. As a result, multiple scattering theory is not restricted to acoustics.

6.2.3. *Undisturbed field, scattered fields and radiation condition*

As explained in section 6.2.1, the field p that appears in the Helmholtz equation [6.2] and the boundary conditions [6.3] is the actual pressure in the medium Ω, which consists of the sum between the undisturbed field p^{un} and the total scattered field p^{sc}. This latter consists itself of the superposition of the fields p_j^{sc} scattered by every obstacle Ω_j. Mathematically, the field p hence reads:

$$p(\mathbf{x}) = p^{\text{un}}(\mathbf{x}) + p^{\text{sc}}(\mathbf{x}) \quad \text{where} \quad p^{\text{sc}}(\mathbf{x}) = \sum_{j \in [\![1, \mathcal{N}]\!]} p_j^{\text{sc}}(\mathbf{x}), \qquad [6.4]$$

where $\mathbf{x}$ is the position vector with respect to a given coordinate system $(O, \mathbf{x})$. Since $p^{\text{un}}(\mathbf{x})$ is the wavefield that would exist in the absence of obstacles, it satisfies the Helmholtz equation [6.2], and due to linearity, so does each scattered field $p_j^{\text{sc}}(\mathbf{x})$. In fact, the scattered field $p_j^{\text{sc}}(\mathbf{x})$ is emitted by the obstacle Ω_j in response to $p^{\text{un}}(\mathbf{x})$ so that the sum in equation [6.4] satisfies the boundary conditions [6.3]. The field $p_j^{\text{sc}}(\mathbf{x})$ corresponds to waves propagating outward from the obstacle Ω_j, and vanishing at some distance away from it. To describe this feature, $p_j^{\text{sc}}(\mathbf{x})$ is supposed to satisfy the following relation, called the *Sommerfeld radiation condition*:

$$(r_j)^d \left(\frac{\partial p_j^{\text{sc}}}{\partial r_j} - \mathrm{i}k p_j^{\text{sc}} \right) \to 0 \qquad \text{as } r_j \to \infty, \tag{6.5}$$

where r_j is the distance between a point in space and the center O_j of the obstacle Ω_j, while $d = 1$ or $d = 1/2$ for three-dimensional (3-D) or two-dimensional (2-D) problems respectively. Roughly speaking, equation [6.5] means that p_j^{sc} decays away from the obstacle Ω_j as $1/r_j$ in 3-D problems and as $1/\sqrt{r_j}$ in 2-D problems.

6.2.4. *Wavefunctions in multiple scattering theory*

Central to multiple scattering theory is the question of the coordinate system to describe both the wavefields and the shape of the obstacles. Indeed, the theory relies on the mathematical ability to define a local coordinate system $(O_j, \mathbf{r}_j)$ attached to each obstacle Ω_j in which:

1) two independent families (ψ_n) and (ζ_n) of elementary solutions to the Helmholtz equation *with separated variables* can be defined;

2) the elementary solutions (ψ_n) represent outgoing waves from the obstacle and satisfy the Sommerfeld radiation condition;

3) the elementary solutions (ζ_n) are regular in the vicinity of the obstacle;

4) the boundary Γ_j of the obstacle Ω_j coincides with a line of constant value of one coordinate, while orthogonality conditions are satisfied by (ψ_n) and (ζ_n) regarding their dependence on the other coordinates.

The solutions (ψ_n) and (ζ_n) are called *wavefunctions*. The outgoing wavefunctions (ψ_n) are used as a functional basis to expand the scattered field p_j^{sc} in the form:

$$p_j^{\text{sc}}(\mathbf{r}_j) = \sum_n A_n^j \psi_n(\mathbf{r}_j), \tag{6.6}$$

where the complex amplitudes A_n^j are called the *scattering coefficients* of the obstacle Ω_j. At the same time, the regular wavefunctions (ζ_n) are used to expand, at least in the vicinity of the obstacle Ω_j, the undisturbed field p^{un} and the fields $p^{\text{sc}}_{i\neq j}$ scattered by all the inclusions Ω_i other than Ω_j:

$$p^{\text{un}}(\mathbf{r}_j) = \sum_n U_n \zeta_n(\mathbf{r}_j) \quad \text{and} \quad p^{\text{sc}}_{i\neq j}(\mathbf{r}_j) = \sum_n B_n^{i\neq j} \zeta_n(\mathbf{r}_j), \qquad [6.7]$$

where U_n are coefficients derived from the knowledge of the undisturbed field, and $B_n^{i\neq j}$ are amplitudes which depend on the scattering coefficients $A_n^{i\neq j}$ of the obstacle $\Omega_{i\neq j}$. The relation between the coefficients $B_n^{i\neq j}$ and the scattering coefficients $A_n^{i\neq j}$ are derived from *addition theorems* [BAT 53, ABR 64]. Finally, taking advantage of the adapted shape of the obstacles and using the orthogonality conditions satisfied by (ψ_n) and (ζ_n), the boundary conditions at Γ_j are applied to provide a linear system of equations to be solved for the scattering coefficients A_n^j.

It should be noted here that the condition of separated variables leads to some restrictions on the admissible shapes of the obstacles which can be studied by the multiple scattering theory. Indeed, solutions of the Helmholtz equation with separated variables and adapted to bounded obstacles can be derived in only two kinds of 2-D coordinate systems and four kinds of 3-D coordinate systems [MAR 06]. The admissible shapes for the obstacles corresponding to these coordinate systems are circles and ellipses in 2-D, and four kinds of spheres and ellipsoids in 3-D. In the following, multiple scattering theory is applied to circular boundaries in 2-D problems, but its underlying principles remain applicable to the other geometries.

6.3. Scattering of sound by a cluster of cylindrical obstacles

In this section, multiple sound scattering by a cluster Ω_{cl} composed of $\mathcal{N}$ cylindrical obstacles Ω_j with $j \in [\![1;\mathcal{N}]\!]$ is studied (see Figure 6.2). The axes of the cylinders Ω_j are all parallel and oriented along the direction defined by the unit vector $\mathbf{e}_z$. Only sound propagation in the plane $\mathcal{P} = (O, \mathbf{e}_x, \mathbf{e}_y)$ orthogonal to the axes of the obstacles is considered, where O is the origin of the Cartesian coordinate system $(\mathbf{e}_x, \mathbf{e}_y)$ and $\mathbf{e}_x \wedge \mathbf{e}_y = \mathbf{e}_z$. Consequently, for obstacles sufficiently long, the wavefield can be assumed invariant under any translation along $\mathbf{e}_z$ and the problem can be tackled in the 2-D plane $\mathcal{P}$, where each cylinder Ω_j is supposed to have a circular cross-section with the radius a_j and its center O_j located by the position vector $\mathbf{x}_j = \overrightarrow{OO_j}$.

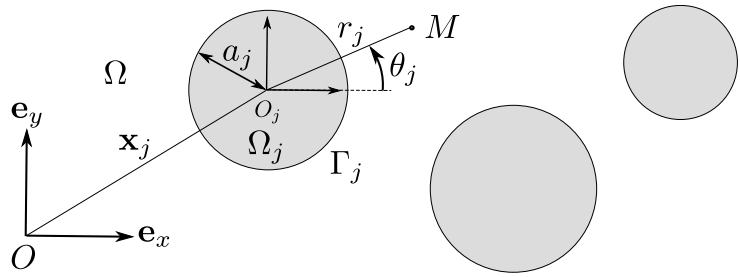

Figure 6.2. *Cluster of $\mathcal{N}$ cylindrical scatterers with circular cross-sections*

6.3.1. *Cylindrical wavefunctions in polar coordinate systems*

The local coordinate system $(O_j, \mathbf{r}_j)$ is attached to the obstacle Ω_j, wherein $\mathbf{r}_j = \overrightarrow{O_j M}$ is the position vector of the point $M \in \mathcal{P}$ as shown in Figure 6.2. Here, polar coordinates $\mathbf{r}_j = (r_j, \theta_j)$ are used, such that $r_j = |\mathbf{r}_j|$ is the distance between the points O_j and M, and θ_j is the polar angle of $\mathbf{r}_j$ counted from $\mathbf{e}_x$. Hence, the boundary Γ_j of the obstacle Ω_j is defined by the line of constant value $r_j = a_j$, with the normal vector $\mathbf{n}_j = \mathbf{r}_j/a_j$ for points $\mathbf{r}_j$ at Γ_j. Furthermore, the Helmholtz equation [6.2] takes the following form when expressing the Laplacian operator with the polar coordinates (r_j, θ_j):

$$\frac{\partial^2 p}{\partial r_j^2} + \frac{1}{r_j}\frac{\partial p}{\partial r_j} + \frac{1}{r_j^2}\frac{\partial^2 p}{\partial \theta_j^2} + k^2 p = 0 \quad \text{in } \Omega. \qquad [6.8]$$

To determine the wavefunctions ψ_n and ζ_n, solutions in the form of separated variables $p(\mathbf{r}_j) = f(\theta_j)g(r_j)$ are studied, where $f(\theta_j)$ and $g(r_j)$ are scalar functions. Substitution of this expression into equation [6.8] leads to:

$$\frac{r_j^2}{g(r_j)}\frac{\partial^2 g(r_j)}{\partial r_j} + \frac{r_j}{g(r_j)}\frac{\partial g(r_j)}{\partial r_j} + k^2 r_j^2 = -\frac{1}{f(\theta_j)}\frac{\partial^2 f(\theta_j)}{\partial \theta_j^2}. \qquad [6.9]$$

The left-hand side of equation [6.9] depends only on the polar coordinate r_j, while its right-hand side depends only on the polar coordinate θ_j. Hence, both sides are equal to the same constant, which is called the *separation constant* and is denoted α^2. Depending on the value of this constant, the functions f and g can be different and they are re-named $f_\alpha(\theta_j)$ and $g_\alpha(r_j)$ to emphasize their dependence on α. Using equation [6.9], the functions $f_\alpha(\theta_j)$ and $g_\alpha(r_j)$ satisfy the differential equations:

$$\frac{\partial^2 f_\alpha}{\partial \theta_j^2} + \alpha^2 f_\alpha = 0, \quad \text{and} \quad \frac{\partial^2 g_\alpha}{\partial r_j} + \frac{1}{r_j}\frac{\partial g_\alpha}{\partial r_j} + \left(k^2 - \frac{\alpha^2}{r_j^2}\right) g_\alpha = 0. \qquad [6.10]$$

The general solution of the differential equation satisfied by $f_\alpha(\theta_j)$ takes the form of exponential functions $e^{\pm \mathrm{i}\alpha\theta_j}$. However, any point $M \in \mathcal{P}$ having the polar coordinates (r_j, θ_j) coincides with the points having the polar coordinates $(r_j, \theta_j + 2\pi n)$ where $n \in \mathbb{Z}$ is an integer. Since the wavefield is uniquely defined at each point of the plane $\mathcal{P}$, the relation $f_\alpha(\theta_j) = f_\alpha(\theta_j + 2\pi n)$ must hold for any integer $n \in \mathbb{Z}$. It means that $f_\alpha(\theta_j)$ is 2π-periodic, which implies that the separation constant can only take integer values $\alpha = n \in \mathbb{Z}$, that is, $f_\alpha(\theta_j) = f_n(\theta_j) = e^{\mathrm{i}n\theta_j}$ with $n \in \mathbb{Z}$.

The differential equation [6.10] satisfied by g_α with $\alpha = n \in \mathbb{Z}$ is called the *Bessel equation* of integer order $n \in \mathbb{Z}$. Any solution of this equation can be written as the linear combination of two independent particular solutions called the *Bessel functions of the first* and *second kind*, and denoted $\mathrm{J}_n(kr_j)$ and $\mathrm{Y}_n(kr_j)$ respectively. The Bessel functions can be seen as decaying standing waves, as testified by their following asymptotic limits as $kr_j \to \infty$, where $\phi_n = n\pi/2 + \pi/4$:

$$\mathrm{J}_n(kr_j) \to \sqrt{\frac{2/\pi}{kr_j}} \cos\left(kr_j - \phi_n\right) \quad \text{and} \quad \mathrm{Y}_n(kr_j) \to \sqrt{\frac{2/\pi}{kr_j}} \sin\left(kr_j - \phi_n\right). \quad [6.11]$$

Like complex exponential functions are formed from sine and cosine functions, the *Hankel functions* $\mathrm{H}_n^{(1)}(kr_j) = \mathrm{J}_n(kr_j) + \mathrm{i}\mathrm{Y}_n(kr_j)$ and $\mathrm{H}_n^{(2)}(kr_j) = \mathrm{J}_n(kr_j) - \mathrm{i}\mathrm{Y}_n(kr_j)$ of the first and second kind and of order n are defined. As linear combinations of Bessel functions, the Hankel functions satisfy the Bessel equation, and using equation [6.11], their asymptotic limits as $kr_j \to \infty$ read:

$$\mathrm{H}_n^{(1)}(kr_j) \to \sqrt{\frac{2/\pi}{kr_j}} e^{\mathrm{i}(kr_j - \phi_n)} \quad \text{and} \quad \mathrm{H}_n^{(2)}(kr_j) \to \sqrt{\frac{2/\pi}{(kr_j)}} e^{-\mathrm{i}(kr_j - \phi_n)}. \quad [6.12]$$

Equation [6.12] shows that Hankel functions are propagating waves with $\mathrm{H}_n^{(1)}(kr_j)$ being outgoing waves and $\mathrm{H}_n^{(2)}(kr_j)$ incoming waves when using the time convention $e^{-\mathrm{i}\omega t}$. Among many mathematical properties satisfied by the Bessel and Hankel functions [BAT 53, ABR 64], the Bessel functions $\mathrm{J}_n(kr_j)$ are found to be regular as $r_j \to 0$, while $\mathrm{Y}_n(kr_j)$, $\mathrm{H}_n^{(1)}(kr_j)$ and $\mathrm{H}_n^{(2)}(kr_j)$ are singular as $r_j \to 0$. These properties lead us to define the cylindrical wavefunctions in the forms:

$$\forall n \in \mathbb{Z}, \quad \psi_n(\mathbf{r}_j) = \mathrm{H}_n^{(1)}(kr_j) e^{\mathrm{i}n\theta_j} \quad \text{and} \quad \zeta_n(\mathbf{r}_j) = \mathrm{J}_n(kr_j) e^{\mathrm{i}n\theta_j}, \quad [6.13]$$

which satisfy all the requirements announced in section 6.2.4. Indeed, they are independent solutions of the Helmholtz equation with separated variables; the wavefunctions $\psi_n(\mathbf{r}_j)$ represent outgoing waves from the obstacle Ω_j and satisfy the Sommerfeld radiation condition [6.5]; the wavefunctions $\zeta_n(\mathbf{r}_j)$ are regular as $r_j \to 0$; the boundary Γ_j of the obstacle Ω_j coincides with the line of constant value

$r_j = a_j$; and the following orthogonality condition holds regarding their dependence on θ_j:

$$\forall\,(m,\,n) \in \mathbb{Z}^2, \quad \int_0^{2\pi} e^{\mathrm{i}m\theta_j} e^{\mathrm{i}n\theta_j}\,\mathrm{d}\theta_j = 2\pi\,\delta(m+n), \qquad [6.14]$$

where δ is the Kronecker delta with $\delta(m+n) = 1$ if $m+n = 0$ while $\delta(m+n) = 0$ otherwise. To simplify notations here and in the following, the Hankel function of the first kind and order n will be denoted $\mathrm{H}_n(kr_j)$ instead of $\mathrm{H}_n^{(1)}(kr_j)$.

6.3.2. *Scattering coefficients and addition theorem*

Following the method presented in section 6.2.4, the field scattered by each obstacle of the cluster Ω_{cl} is now expanded on the functional basis of the outgoing cylindrical wavefunctions. In particular, the fields p_j^{sc} and p_i^{sc} scattered by the two different obstacles Ω_j and Ω_i with $i \neq j$ are expanded in the form:

$$p_j^{\text{sc}}(\mathbf{r}_j) = \sum_{n\in\mathbb{Z}} A_n^j \psi_n(\mathbf{r}_j) \qquad \text{and} \qquad p_i^{\text{sc}}(\mathbf{r}_i) = \sum_{m\in\mathbb{Z}} A_m^i \psi_m(\mathbf{r}_i). \qquad [6.15]$$

Note in equation [6.15] that different letters $(m, n) \in \mathbb{Z}^2$ have been used to index the scattering coefficients and wavefunctions related to Ω_j and Ω_i, but it has no influence on the result. To apply the boundary conditions at the surface $\Gamma_j(r_j = a_j)$ of the obstacle Ω_j, the field p_i^{sc} must be expressed in the polar coordinate system $(O_j, \mathbf{r}_j)$ attached to the obstacle Ω_j. To do so, the position vector $\mathbf{r}_i$ is written as $\mathbf{r}_i = \mathbf{r}_i^j + \mathbf{r}_j$ where $\mathbf{r}_i^j = \overrightarrow{O_iO_j}$ has the polar coordinates $\mathbf{r}_i^j = (r_i^j, \theta_i^j)$ in the coordinate system $(O_i, \mathbf{r}_i)$, with r_i^j being the distance between the O_i and O_j, and θ_i^j being the angle between the vector $\overrightarrow{O_iO_j}$ and the vector $\mathbf{e}_x$ (see Figure 6.3). Then, *Graf's addition theorem* [BAT 53, ABR 64] is used, which states that outgoing wavefunctions $\psi_m(\mathbf{r}_i)$ can be expanded on outgoing or regular wavefunctions $\psi_n(\mathbf{r}_j)$ or $\zeta_n(\mathbf{r}_j)$ depending on the distance r_j:

$$\psi_m(\mathbf{r}_i) = \psi_m(\mathbf{r}_i^j + \mathbf{r}_j) = \begin{cases} \displaystyle\sum_{n\in\mathbb{Z}} \psi_{m-n}(\mathbf{r}_i^j)\,\zeta_n(\mathbf{r}_j) \text{ if } |\mathbf{r}_j| < |\mathbf{r}_i^j|, \\ \displaystyle\sum_{n\in\mathbb{Z}} \zeta_{m-n}(\mathbf{r}_i^j)\,\psi_n(\mathbf{r}_j) \text{ if } |\mathbf{r}_j| > |\mathbf{r}_i^j|. \end{cases} \qquad [6.16]$$

It is worth noting here that since the obstacles have finite non-zero radii a_i, the application of Graf's addition theorem [6.16] will be avoided in the domain $|\mathbf{r}_i^j - a_i| \leq |\mathbf{r}_j| \leq |\mathbf{r}_i^j + a_i|$, where the presence of the obstacle Ω_i prevents the use of cylindrical wavefunctions $\zeta_n(\mathbf{r}_j)$ and $\psi_n(\mathbf{r}_j)$ centered at Ω_j to describe wavefields [FEL 94]. Therefore, the only field expression that is valid in the whole domain Ω is the one

provided in equation [6.15]. This expression will be preferred to evaluate the field in the whole domain Ω.

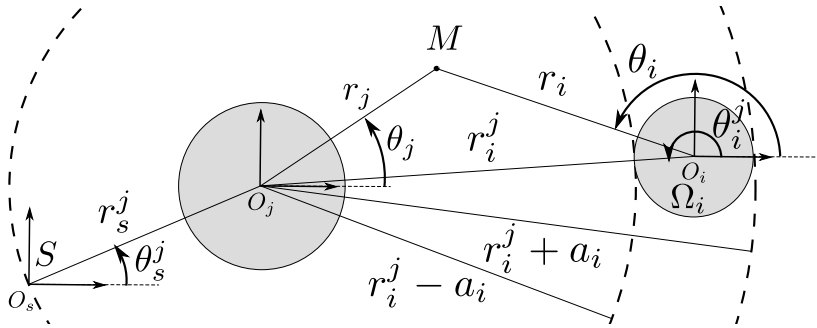

Figure 6.3. *Application of Graf's addition theorem in the case of two circular cross-sectional obstacles and a line source*

Beside their dependence on the wavenumber k, the coefficients $\psi_{m-n}(\mathbf{r}_i^j)$ and $\zeta_{m-n}(\mathbf{r}_i^j)$ in equation [6.16] depend only on the relative position of the centers O_i and O_j of the obstacles. To apply the boundary conditions at $\Gamma_j(r_j = a_j)$, the expansion for $|\mathbf{r}_j| < |\mathbf{r}_i^j|$ in equation [6.16] is used. Substituting that expression into [6.15], the scattered field p_i^{sc} reads as follows in the coordinate system $(O_j, \mathbf{r}_j)$ for points such that $r_j \in [a_j,\, r_i^j - a_i]$:

$$p_i^{\text{sc}}(\mathbf{r}_j) = \sum_{n\in\mathbb{Z}} \sum_{m\in\mathbb{Z}} \mathcal{C}_{nm}^{j,i}\, A_m^i \zeta_n(\mathbf{r}_j) \quad \text{with} \quad \mathcal{C}_{nm}^{j,i} = \psi_{m-n}(\mathbf{r}_i^j). \qquad [6.17]$$

Finally, it is supposed (for the time being) that, at least in the vicinity of the obstacle Ω_j, the undisturbed field p^{un} can be expanded on the functional basis of the regular wavefunctions $\zeta_n(\mathbf{r}_j)$:

$$p^{\text{un}}(\mathbf{r}_j) = \sum_n U_n^j\, \zeta_n(\mathbf{r}_j) \qquad \text{for } a_j \le r_j < r_j^{\lim}, \qquad [6.18]$$

where $r_j^{\lim}$ is the limit distance from O_j up to which the expansion in equation [6.18] holds. The coefficients U_n^j and the limit distance $r_j^{\lim}$ actually depend on the nature of the undisturbed field, and their expression will be given in the cases of the incident plane wave and the line source excitation in sections 6.3.5 and 6.3.6 respectively.

6.3.3. *Application of boundary conditions*

Now that the undisturbed field and the scattered fields have been expressed in the polar coordinate system $(O_j, \mathbf{r}_j)$ attached to the obstacle Ω_j by means of the cylindrical wavefunctions, the boundary condition [6.3] at the surface $\Gamma_j (r_j = a_j)$ can be applied. Substitution of equation [6.4] into the boundary condition [6.3] yields the following relation:

$$\forall j \in [\![1;\mathcal{N}]\!], \quad \forall \mathbf{r}_j \in \Gamma_j, \qquad \frac{\partial}{\partial r_j}\left[p^{\text{un}}(\mathbf{r}_j) + p_j^{\text{sc}}(\mathbf{r}_j) + \sum_{i\neq j} p_i^{\text{sc}}(\mathbf{r}_j) \right] = 0. \qquad [6.19]$$

Here, the distinction is made between the field p_j^{sc} scattered by Ω_j and the external field p_j^{ext} to which Ω_j is submitted. This latter consists of the undisturbed field p^{un} and of the fields p_i^{sc} scattered by all the obstacles $\Omega_{i\neq j}$ other than Ω_j. Using the expansions of the fields p_i^{sc} and p^{un} given in equations [6.17] and [6.18], the external field p_j^{ext} reads as follows when expressed in the polar coordinate system $(O_j, \mathbf{r}_j)$ for points in the vicinity of Ω_j:

$$\forall j \in [\![1;\mathcal{N}]\!], \quad p_j^{\text{ext}}(\mathbf{r}_j) = p^{\text{un}}(\mathbf{r}_j) + \sum_{i\neq j} p_i^{\text{sc}}(\mathbf{r}_j) = \sum_{n\in\mathbb{Z}} \mathcal{E}_n^j \, \zeta_n(\mathbf{r}_j), \qquad [6.20]$$

where

$$\mathcal{E}_n^j = U_n^j + \sum_{i\neq j} \sum_{m\in\mathbb{Z}} \mathcal{C}_{nm}^{j,i} \, A_m^i. \qquad [6.21]$$

Now, using the expansions of the fields p_j^{sc} and p_j^{ext} given in equations [6.15] and [6.20], the boundary condition [6.19] becomes:

$$\forall j \in [\![1;\mathcal{N}]\!], \quad \forall \mathbf{r}_j \in \Gamma_j, \quad \sum_{n\in\mathbb{Z}} \left\{ A_n^j \frac{\partial \psi_n(\mathbf{r}_j)}{\partial r_j} + \mathcal{E}_n^j \frac{\partial \zeta_n(\mathbf{r}_j)}{\partial r_j} \right\} = 0. \qquad [6.22]$$

The expression of the cylindrical wavefunctions $\psi_n(\mathbf{r}_j)$ and $\zeta_n(\mathbf{r}_j)$ given in equation [6.13] is substituted into equation [6.22] to provide the following equation:

$$\forall j \in [\![1;\mathcal{N}]\!], \quad \forall \theta_j, \quad \sum_{n\in\mathbb{Z}} k \left\{ A_n^j \mathrm{H}_n'(ka_j) + \mathcal{E}_n^j \mathrm{J}_n'(ka_j) \right\} e^{\mathrm{i}n\theta_j} = 0. \qquad [6.23]$$

Here, J_n' and H_n' are the derivatives of functions J_n and H_n with respect to their total argument. In particular, the properties of Bessel and Hankel functions [BAT 53, ABR 64] lead to:

$$\mathrm{H}_n' = \left(\mathrm{H}_{n-1} - \mathrm{H}_{n+1}\right)/2 \qquad \text{and} \qquad \mathrm{J}_n' = \left(\mathrm{J}_{n-1} - \mathrm{J}_{n+1}\right)/2. \qquad [6.24]$$

Finally, using the orthogonality of the exponential functions as described by equation [6.14], the term between braces in equation [6.23] is found to be zero for all order $n \in \mathbb{Z}$:

$$\forall j \in [\![1;\mathcal{N}]\!], \quad \forall n \in \mathbb{Z}, \quad A_n^j \mathrm{H}'_n(ka_j) + \mathcal{E}_n^j \mathrm{J}'_n(ka_j) = 0. \qquad [6.25]$$

After division by $\mathrm{H}'_n(ka_j)$, equation [6.25] can be re-written in the form:

$$\forall j \in [\![1;\mathcal{N}]\!], \quad \forall n \in \mathbb{Z}, \quad A_n^j = \mathcal{D}_n^j \, \mathcal{E}_n^j, \quad \text{with} \quad \mathcal{D}_n^j = -\frac{\mathrm{J}'_n(ka_j)}{\mathrm{H}'_n(ka_j)}. \qquad [6.26]$$

Here, the coefficients $\mathcal{D}_n^j$ make the link between the external field coefficients $\mathcal{E}_n^j$ and the scattering coefficients A_n^j of the obstacle Ω_j. The coefficients $\mathcal{D}_n^j$ are actually dictated by the boundary conditions applied at the interface Γ_j and read as equation [6.26] in the case of impervious obstacles. For comparison, their expression in the case of permeable obstacles will be given in section 6.3.8.

6.3.4. *Matrix formulation*

Equations [6.26] and [6.21] represent an algebraic system with an infinite number of equations to solve for the scattering coefficients A_n^j forced by the coefficients U_n^j prescribed by the undisturbed field. This system can be re-written in a matrix form more suitable for computation. To do so, the (infinite) vectors $\boldsymbol{\mathcal{A}}^j$ and $\boldsymbol{\mathcal{U}}^j$ containing the scattering coefficients A_n^j and forcing coefficients U_n^j are defined:

$$\boldsymbol{\mathcal{A}}^j = \{\ldots, A_{n-1}^j, A_n^j, A_{n+1}^j, \ldots\}^T, \qquad [6.27a]$$

$$\boldsymbol{\mathcal{U}}^j = \{\ldots, U_{n-1}^j, U_n^j, U_{n+1}^j, \ldots\}^T, \qquad [6.27b]$$

where ^{T} denotes the transposition. The diagonal matrix $[\boldsymbol{\mathcal{D}}^j]$ with coefficients $\mathcal{D}_n^j$ and the matrix $[\boldsymbol{\mathcal{C}}^{j,i}]$ with coefficients $\mathcal{C}_{nm}^{j,i}$ are also defined:

$$[\boldsymbol{\mathcal{D}}^j] = \mathrm{diag}_{n\in\mathbb{Z}}\left\{\mathcal{D}_n^j\right\}, \quad \text{and} \quad [\boldsymbol{\mathcal{C}}^{j,i}]_{nm} = \mathcal{C}_{nm}^{j,i} = \psi_{m-n}(\mathbf{r}_i^j). \qquad [6.28]$$

With those notations, equations [6.26] and [6.21] can be re-written as follows:

$$\forall j \in [\![1;\mathcal{N}]\!], \quad \boldsymbol{\mathcal{A}}^j = [\boldsymbol{\mathcal{D}}^j]\boldsymbol{\mathcal{E}}^j \quad \text{where} \quad \boldsymbol{\mathcal{E}}^j = \boldsymbol{\mathcal{U}}^j + \sum_{i\neq j} [\boldsymbol{\mathcal{C}}^{j,i}]\boldsymbol{\mathcal{A}}^i. \qquad [6.29]$$

The matrix $[\mathcal{D}^j]$ linking the vector of scattering coefficients $\mathcal{A}^j$ to the vector $\mathcal{E}^j$ of external excitation is called the *single scattering matrix* of the obstacle Ω_j. Equation [6.29] results in a system of $\mathcal{N}$ vectorial equations. They can be gathered in one single vectorial equation by defining the global vectors of scattering and forcing coefficients:

$$\boldsymbol{\mathcal{A}} = \left\{\mathcal{A}^1, \ldots, \mathcal{A}^j, \ldots, \mathcal{A}^{\mathcal{N}}\right\}^T, \quad \boldsymbol{\mathcal{U}} = \left\{\mathcal{U}^1, \ldots, \mathcal{U}^j, \ldots, \mathcal{U}^{\mathcal{N}}\right\}^T, \qquad [6.30]$$

the global identity matrix $[\mathcal{I}]$ and the single scattering matrix $[\mathcal{D}]$:

$$[\mathcal{I}] = \begin{bmatrix} \mathbf{Id} & \mathcal{O} & \mathcal{O} \\ \mathcal{O} & \mathbf{Id} & \mathcal{O} \\ \mathcal{O} & \mathcal{O} & \mathbf{Id} \end{bmatrix} \quad \text{and} \quad [\mathcal{D}] = \begin{bmatrix} [\mathcal{D}^1] & \mathcal{O} & \mathcal{O} \\ \mathcal{O} & [\mathcal{D}^j] & \mathcal{O} \\ \mathcal{O} & \mathcal{O} & [\mathcal{D}^{\mathcal{N}}] \end{bmatrix}, \qquad [6.31]$$

and the following matrix $[\mathcal{C}]$ of coupling between the obstacles:

$$\mathcal{C} = \begin{bmatrix} \mathcal{O} & \mathcal{C}^{1,2} & \mathcal{C}^{1,3} & \cdots & \mathcal{C}^{1,\mathcal{N}} \\ \mathcal{C}^{2,1} & \mathcal{O} & \mathcal{C}^{2,3} & \cdots & \mathcal{C}^{2,\mathcal{N}} \\ \vdots & \mathcal{C}^{j,j-1} & \mathcal{O} & \mathcal{C}^{j,j+1} & \vdots \\ \mathcal{C}^{\mathcal{N}-1,1} & \cdots & \mathcal{C}^{\mathcal{N}-1,\mathcal{N}-2} & \mathcal{O} & \mathcal{C}^{\mathcal{N}-1,\mathcal{N}} \\ \mathcal{C}^{\mathcal{N},1} & \mathcal{C}^{\mathcal{N},2} & \cdots & \mathcal{C}^{\mathcal{N},\mathcal{N}-1} & \mathcal{O} \end{bmatrix}, \qquad [6.32]$$

where **Id** and $\mathcal{O}$ in equations [6.31] and [6.32] are the identity and null matrices having the same size as $[\mathcal{D}^j]$ and $[\mathcal{C}^{j,i}]$. Since $[\mathcal{C}]$ is not diagonal, every scattering coefficient of every obstacle is coupled to any other scattering coefficient of any other obstacle. With those notations, equation [6.29] can be re-written as follows:

$$[\mathcal{I}]\boldsymbol{\mathcal{A}} = [\mathcal{D}]\boldsymbol{\mathcal{E}} \quad \text{where} \quad \boldsymbol{\mathcal{E}} = \boldsymbol{\mathcal{U}} + [\mathcal{C}]\boldsymbol{\mathcal{A}}. \qquad [6.33]$$

Solving for the scattering coefficients $\boldsymbol{\mathcal{A}}$ in equation [6.33] leads to:

$$\boldsymbol{\mathcal{A}} = [\mathcal{M}]\boldsymbol{\mathcal{U}} \quad \text{with} \qquad [\mathcal{M}] = \Big[[\mathcal{I}] - [\mathcal{D}][\mathcal{C}]\Big]^{-1}[\mathcal{D}], \qquad [6.34]$$

where the matrix $\boldsymbol{\mathcal{M}}$ is called the *multiple scattering matrix of the cluster*. It is interesting to note that $\boldsymbol{\mathcal{M}}$ does not depend on the nature of the undisturbed field. However, it requires the inversion of the matrix $[\mathcal{I}] - [\mathcal{D}][\mathcal{C}]$, which is usually performed numerically. Consequently, the infinite sums in equations [6.15], [6.17] and [6.18] must be truncated to $n, m \in [\![-M; M]\!]$ where M is a finite integer. Only convergence studies can confirm that a sufficient number M of wavefunctions have

been considered to assess the fields, but the following numerical recipe can be used as an estimate [BAR 90] in the case of impervious obstacles:

$$M = \text{floor}\left(ka_{\max} + 4.05(ka_{\max})^{1/3}\right) + 10 \quad \text{with} \quad a_{\max} = \max_{j\in[\![1;\mathcal{N}]\!]}(a_j). \qquad [6.35]$$

Finally, equation [6.34] shows that once the forcing coefficients $\boldsymbol{\mathcal{U}}$ are determined, the scattering coefficients in $\boldsymbol{\mathcal{A}}$ can be computed. In sections. 6.3.5 and 6.3.6, the forcing coefficients $\boldsymbol{\mathcal{U}}$ are hence derived for the incident plane wave and the line source excitation respectively.

6.3.5. *Forcing coefficients in the case of an incident plane wave*

If the undisturbed field is a plane wave with unitary amplitude and wave vector $\mathbf{k}$ in the plane $\mathcal{P}$, it reads as follows in the Cartesian coordinate system $(O, \mathbf{e}_x, \mathbf{e}_y)$:

$$p^{\text{un}}(\mathbf{x}) = e^{\mathrm{i}\mathbf{k}\cdot\mathbf{x}} \quad \text{with} \quad \mathbf{k} = k_x\mathbf{e}_x + k_y\mathbf{e}_y \quad \text{and} \quad \mathbf{x} = x\mathbf{e}_x + y\mathbf{e}_y. \qquad [6.36]$$

For the undisturbed field to satisfy the Helmholtz equation, the relation $k_x^2 + k_y^2 = k^2$ must hold. Consequently, they can be written in the form $k_x = k\cos(\vartheta)$ and $k_y = k\sin(\vartheta)$, where the angle ϑ characterizes the direction of propagation of the incident wave. In addition, the position vector is written as $\mathbf{x} = \mathbf{x}_j + \mathbf{r}_j$ with $\mathbf{r}_j = r_j\cos(\theta_j)\mathbf{e}_x + r_j\sin(\theta_j)\mathbf{e}_y$. As a result, equation [6.36] becomes:

$$p^{\text{un}} = e^{\mathrm{i}\mathbf{k}\cdot\mathbf{x}_j}\, e^{\mathrm{i}kr_j\{\cos(\theta_j)\cos(\vartheta)+\sin(\theta_j)\sin(\vartheta)\}} = e^{\mathrm{i}\mathbf{k}\cdot\mathbf{x}_j}\, e^{\mathrm{i}kr_j\cos(\theta_j-\vartheta)}, \qquad [6.37]$$

where $e^{\mathrm{i}\mathbf{k}\cdot\mathbf{x}_j}$ plays the role of a complex amplitude which depends on the position $\mathbf{x}_j$ of the obstacle Ω_j in the global Cartesian coordinate system. Now, the *Jacobi–Anger expansion* [BAT 53, ABR 64] is used to expand the term $e^{\mathrm{i}kr_j\cos(\theta_j-\vartheta)}$ on the Bessel functions:

$$e^{\mathrm{i}kr_j\cos(\theta_j-\vartheta)} = \sum_{n\in\mathbb{Z}} \mathrm{i}^n \mathrm{J}_n(kr_j)e^{\mathrm{i}n(\theta_j-\vartheta)} = \sum_{n\in\mathbb{Z}} \mathrm{i}^n e^{-\mathrm{i}n\vartheta}\zeta_n(\mathbf{r}_j). \qquad [6.38]$$

Substitution of equation [6.38] into [6.37] leads to the following expansion of the undisturbed field on the regular wavefunctions $\zeta_n(\mathbf{r}_j)$ in the polar coordinate system $(O_j, \mathbf{r}_j)$ attached to the obstacle Ω_j:

$$p^{\text{un}}(\mathbf{r}_j) = e^{\mathrm{i}\{\mathbf{k}\cdot\mathbf{x}_j + kr_j\cos(\theta_j-\vartheta)\}} = \sum_{n\in\mathbb{Z}} U_n^j\zeta_n(\mathbf{r}_j) \quad \text{with} \quad U_n^j = \mathrm{i}^n e^{\mathrm{i}(\mathbf{k}\cdot\mathbf{x}_j - n\vartheta)}. \qquad [6.39]$$

Moreover, the expansion [6.39] remains valid for any points such that $r_j \geq a_j$, which means that the limit distance of validity for the expansion [6.39] is $r_j^{\lim} = \infty$.

6.3.6. *Forcing coefficients in the case of a line source*

Another type of undisturbed field which is useful in practice is the case of the line source. In our 2-D problem, it consists of the field created by a source S located at the point O_s in the plane $\mathcal{P}$ as shown in Figure 6.3. The polar coordinate system $(O_s, \mathbf{r}_s)$ attached to the source is defined, with coordinates $\mathbf{r}_s = (r_s, \theta_s)$. Denoting $\mathbf{x}_s = \overrightarrow{OO_s}$ the position vector of the source in the Cartesian coordinate system $(O, \mathbf{x})$, the undisturbed field satisfies the following Helmholtz equation and reads as follows:

$$\Delta(p^{\text{un}}) + k^2 p^{\text{un}} = \delta(\mathbf{x} - \mathbf{x}_s) \qquad \Rightarrow \qquad p^{\text{un}}(\mathbf{r}_s) = \frac{1}{4\text{i}} \text{H}_0(kr_s) = \frac{\psi_0(\mathbf{r}_s)}{4\text{i}}, \quad [6.40]$$

where $\delta(\mathbf{x} - \mathbf{x}_s)$ is the Dirac function which is equal to 1 if $\mathbf{x} = \mathbf{x}_s$ but to 0 otherwise. The position vector $\mathbf{r}_s$ is written as $\mathbf{r}_s = \mathbf{r}_s^j + \mathbf{r}_j$ where $\mathbf{r}_s^j = \overrightarrow{O_s O_j}$ has the coordinates $\mathbf{r}_s^j = (r_s^j, \theta_s^j)$ in the polar coordinate system $(O_s, \mathbf{r}_s)$, with r_s^j being the distance between the source O_s and the center O_j, and θ_s^j being the angle between $\overrightarrow{O_s O_j}$ and $\mathbf{e}_x$. Now, using Graf's addition theorem [6.16], the undisturbed field is expressed in the polar coordinate system $(O_j, \mathbf{r}_j)$ attached to the obstacle Ω_j in the form:

$$p^{\text{un}} = \frac{1}{4\text{i}} \psi_0(\mathbf{r}_s^j + \mathbf{r}_j) = \begin{cases} \frac{1}{4\text{i}} \sum\limits_{n \in \mathbb{Z}} \psi_{0-n}(\mathbf{r}_s^j)\, \zeta_n(\mathbf{r}_j) & \text{if } r_j < r_s^j, \\ \frac{1}{4\text{i}} \sum\limits_{n \in \mathbb{Z}} \zeta_{0-n}(\mathbf{r}_s^j)\, \psi_n(\mathbf{r}_j) & \text{if } r_j > r_s^j. \end{cases} \quad [6.41]$$

To apply the boundary conditions at the surface $\Gamma_j (r_j = a_j)$, only the expansion for $r_j < r_s^j$ is relevant, which means that the undisturbed field is expanded as follows in the vicinity of the obstacle Ω_j with the limit distance of validity $r_j^{\lim} = r_s^j$:

$$p^{\text{un}} = \frac{\text{H}_0(kr_s)}{4\text{i}} = \sum_{n \in \mathbb{Z}} U_n^j \zeta_n(\mathbf{r}_j) \quad \text{with} \quad U_n^j = \frac{\psi_{0-n}(\mathbf{r}_s^j)}{4\text{i}} \quad \text{for } r_j < r_s^j. \quad [6.42]$$

The excitation of a cluster of cylindrical obstacles by a line source is of particular physical interest, because the field that is calculated is nothing but the Green's function of the system. This Green's function can be then used to solve the inverse problem [GRO 08a] consisting of locating and characterizing defects in the cluster or to evaluate the density of state [ASA 03].

6.3.7. *Total scattered field and actual pressure*

Once the forcing coefficients U_n^j are determined from the undisturbed field, and the scattering coefficients A_n^j are computed according to equation [6.34], the total scattered field p^{sc} and the actual field $p = p^{\text{un}} + p^{\text{sc}}$ can be evaluated at any point in space. Combining equations [6.4] and [6.15], the scattered field p^{sc} can be calculated as follows by combining field representation in multiple polar coordinate systems $(O_j, \mathbf{r}_j)$:

$$p^{\text{sc}}(\mathbf{x}) = \sum_{j\in[\![1,\mathcal{N}]\!]} p_j^{\text{sc}}(\mathbf{r}_j) \qquad \text{with} \qquad p_j^{\text{sc}}(\mathbf{r}_j) = \sum_{n\in\mathbb{Z}} A_n^j \psi_n(\mathbf{r}_j) \qquad [6.43]$$

where, for all $j \in [\![1,\mathcal{N}]\!]$, the position vector reads $\mathbf{x} = \mathbf{x}_j + \mathbf{r}_j$. This field representation is the only one that is valid in the whole domain Ω. To express $p^{\text{sc}}(\mathbf{x})$ in one single coordinate system, Graf's addition theorem [6.16] must be used, but attention must be paid to the domain of validity of the field representations. To illustrate this, the barycenter O_{cl} of the cluster is defined, with the position vector :

$$\mathbf{x}_{\text{cl}} = \sum_{j\in[\![1;\mathcal{N}]\!]} \frac{S_j}{S_{\text{cl}}}\mathbf{x}_j \quad \text{with} \quad S_j = \pi a_j^2 \quad \text{and} \quad S_{\text{cl}} = \sum_{j\in[\![1;\mathcal{N}]\!]} S_j, \qquad [6.44]$$

where S_j is the surface area of the Ω_j cross-section, while S_{cl} is the total surface area occupied by the cluster. Then, the polar coordinate system $(O_{\text{cl}}, \mathbf{r}_{\text{cl}})$ is attached to the cluster barycenter, wherein the center O_j of the obstacle Ω_j has the position vector $\mathbf{r}_{\text{cl}}^j = \overrightarrow{O_{\text{cl}}O_j}$. Using Graf's addition theorem [6.16] for points outside the cluster, that is, for $|\mathbf{r}_{\text{cl}}| \geq r_{\text{cl}}^{\min}$ where $r_{\text{cl}}^{\min} = \max_j(|\mathbf{r}_{\text{cl}}^j| + a_j)$, the field scattered by all the obstacles of the cluster in the domain $|\mathbf{r}_{\text{cl}}| \geq r_{\text{cl}}^{\min}$ can be written in the form:

$$p^{\text{sc}}(\mathbf{r}_{\text{cl}}) = \sum_{j\in[\![1;\mathcal{N}]\!]} \sum_{m\in\mathbb{Z}} A_m^j \psi_m(\mathbf{r}_{\text{cl}}^j + \mathbf{r}_{\text{cl}}) = \sum_{n\in\mathbb{Z}} A_n^{\text{cl}} \psi_n(\mathbf{r}_{\text{cl}}), \quad \text{for } |\mathbf{r}_c| \geq r_c^{\min}, \qquad [6.45]$$

where the scattering coefficients A_n^{cl} of the overall cluster read:

$$A_n^{\text{cl}} = \sum_{j\in[\![1;\mathcal{N}]\!]} \sum_{m\in\mathbb{Z}} A_m^j \zeta_{m-n}(\mathbf{r}_{\text{cl}}^j). \qquad [6.46]$$

As a result, for position vectors $|\mathbf{r}_{\text{cl}}| \geq r_{\text{cl}}^{\min}$ outside the cluster, this latter can be treated as an overall structured obstacle, the scattering coefficients of which depend on those from all the obstacles it contains. This procedure is in particular adopted to derive effective parameters of clusters at low frequencies [BER 80, TOR 06].

6.3.8. *Permeable obstacles*

It is worth mentioning here that equation [6.29], or equivalently equation [6.34], encapsulates the whole multiple scattering problem and is not limited to the case of impervious obstacles. Indeed, changing the nature of one or more obstacles Ω_j would only require the re-definition of their associated matrix $[\boldsymbol{\mathcal{D}}^j]$ of single scattering.

To illustrate this idea, the obstacle Ω_j is supposed to be made of homogeneous and isotropic material with the (effective) bulk modulus K_j and density ρ_j. The obstacle Ω_j being then penetrable to sound, the pressure field p_j^{in} develops inside it and must satisfy the Helmholtz equation [6.2] with the wavenumber $k_j = \omega/c_j$, where $c_j = \sqrt{K_j/\rho_j}$ is the sound speed in Ω_j. Since p_j^{in} must be regular over the domain Ω_j, it is expanded on the functional basis of regular cylindrical wavefunctions only, which is called the *Rayleigh hypothesis*:

$$p_j^{\text{in}} = \sum_{n\in\mathbb{Z}} X_n^j\, \zeta_n^j(\mathbf{r}_j) \quad \text{with} \quad \zeta_n^j(\mathbf{r}_j) = \mathrm{J}_n(k_j r_j) e^{in\theta_j}, \tag{6.47}$$

where X_n^j are complex coefficients. The Neumann boundary condition [6.3] at the surface Γ_j is then replaced by the following conditions of continuity for the pressure and the normal component of the particle velocity:

$$\forall \mathbf{r}_j \in \Gamma_j, \quad p_j^{\text{in}} = (p_j^{\text{sc}} + p_j^{\text{ext}}) \quad \text{and} \quad \frac{1}{\rho_j}\frac{\partial p_j^{\text{in}}}{\partial r_j} = \frac{1}{\rho}\frac{\partial (p_j^{\text{sc}} + p_j^{\text{ext}})}{\partial r_j} \tag{6.48}$$

where the field p_j^{sc} scattered by Ω_j and the external field p_j^{ext} to which Ω_j is submitted are given in equations [6.15] and [6.20]. Following the same procedure as that presented in section 6.3.3, application of the boundary conditions [6.48] with the field representations in equations [6.47], [6.15] and [6.20] yields:

$$\forall n \in \mathbb{Z}, \qquad X_n^j\, \mathrm{J}_n(k_j a_j) = A_n^j \mathrm{H}_n(k a_j) + \mathcal{E}_n^j \mathrm{J}_n(k a_j), \tag{6.49a}$$

$$\forall n \in \mathbb{Z}, \qquad \frac{k_j}{\rho_j} X_n^j\, \mathrm{J}'_n(k_j a_j) = \frac{k}{\rho}\left\{ A_n^j \mathrm{H}'_n(k a_j) + \mathcal{E}_n^j \mathrm{J}'_n(k a_j)\right\}. \tag{6.49b}$$

Solving for A_n^j and X_n^j in equation [6.49] provides:

$$A_n^j = \check{D}_n^j \mathcal{E}_n^j \ \text{ with } \ \check{D}_n^j = \frac{-\mathrm{J}'_n(ka_j)\mathrm{J}_n(k_j a_j) + \sigma_j \mathrm{J}_n(ka_j)\mathrm{J}'_n(k_j a_j)}{\mathrm{H}'_n(ka_j)\mathrm{J}_n(k_j a_j) - \sigma_j \mathrm{H}_n(ka_j)\mathrm{J}'_n(k_j a_j)}, \tag{6.50a}$$

$$X_n^j = \Theta_n^j \mathcal{E}_n^j \ \text{ with } \ \Theta_n^j = \frac{\mathrm{J}_n(ka_j)\mathrm{H}'_n(ka_j) - \mathrm{J}'_n(ka_j)\mathrm{H}_n(ka_j)}{\mathrm{H}'_n(ka_j)\mathrm{J}_n(k_j a_j) - \sigma_j \mathrm{H}_n(ka_j)\mathrm{J}'_n(k_j a_j)}, \tag{6.50b}$$

where $\sigma_j = (\rho c)/(\rho_j c_j)$ is the ratio between the impedance ρc in the medium Ω and that $\rho_j c_j$ in the obstacle Ω_j. The relation $A_n^j = \check{D}_n^j \mathcal{E}_n^j$ in equation [6.50a] is similar to that obtained for impervious obstacles in equation [6.26], with in particular $\check{D}_n^j \to D_n^j$ as $\sigma_j \to 0$. Consequently, the procedure described in section 6.3.4 can also be applied in the case of permeable obstacles, replacing D_n^j by $\check{D}_n^j$. It is worth noting that, once again, the resulting single scattering matrix would be diagonal for permeable obstacles. Although this is often the case, it is important to note that structured obstacles can be designed so that single scattering matrices are not diagonal, which formally does not change anything in the procedure described in section 6.3.4. This is, for example, the case of Helmholtz or split-ring resonators [KRY 11, SCH 18].

6.4. Scattering of sound by a periodic row of obstacles: the single grating array

When many identical obstacles are equally spaced along the direction $\mathbf{e}_x$, the idealization of such an array as an infinite periodic row can be pertinent. In this section, sound scattering by a single grating array of cylindrical obstacles with circular cross-sections in the plane $\mathcal{P}$ is studied. It consists of the ℓ-periodic repetition, along the direction $\mathbf{e}_x$, of the cluster Ω_{cl} composed of $\mathcal{N}$ obstacles (see Figure 6.4). The qth repetition of the cluster is denoted Ω_{cl}^q, where $q \in \mathbb{Z}$, while obstacles in the cluster Ω_{cl}^q are indexed by $j \in [\![1;\mathcal{N}]\!]$ and named $\Omega_{j,q}$. Due to the ℓ-periodicity, the obstacles $\Omega_{j,q}$ have their radius a_j independent from q, and their center $O_{j,q}$ located at the following points in the Cartesian coordinate system $(O, \mathbf{e}_x, \mathbf{e}_y)$:

$$\mathbf{x}_{j,q} = \mathbf{x}_j + q\ell\mathbf{e}_x \quad \text{with} \quad q \in \mathbb{Z} \quad \text{and} \quad \mathbf{x}_j = x_j\,\mathbf{e}_x + y_j\,\mathbf{e}_y, \qquad [6.51]$$

where $\mathbf{x}_j$ is the position of the center $O_{j,0}$ in the reference cluster Ω_{cl}^0. To simplify notations in what follows, the convention $\Omega_j = \Omega_{j,0}$ and $O_j = O_{j,0}$ is adopted. In addition, the origin O of the Cartesian Coordinate system is chosen so that the obstacles Ω_j in the reference cluster Ω_{cl}^0 are included in the domain $x \in [-\ell/2;\, \ell/2]$, that is, $|x_j| + a_j < \ell/2$ for all $j \in [\![1;\mathcal{N}]\!]$, while the barycenter O_{cl}^0 of the cluster Ω_{cl}^0 belongs to the axis $(O, \mathbf{e}_x)$. In all this section, the incident field p^{inc} is supposed to be a plane wave of unitary amplitude propagating with the wave vector $\mathbf{k} = k_x\mathbf{e}_x + k_y\mathbf{e}_y$:

$$p^{\text{inc}}(\mathbf{x}) = e^{\mathrm{i}\mathbf{k}\cdot\mathbf{x}} = e^{\mathrm{i}k_x x + \mathrm{i}k_y y}. \qquad [6.52]$$

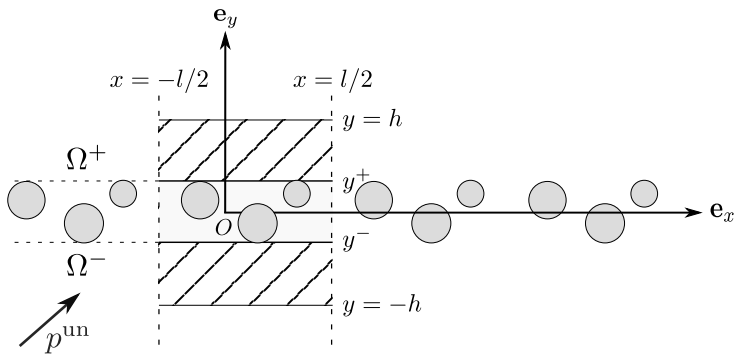

Figure 6.4. *ℓ-periodic repetition of a cluster composed of $\mathcal{N}$ obstacles*

6.4.1. *Quasi-periodicity*

Using the principle of superposition, the actual field p is written as the sum between the undisturbed field $p^{\mathrm{un}} = p^{\mathrm{inc}}$ and the field p^{sc} scattered by the array, this latter being the sum of the fields $p^{\mathrm{sc}}_{j,q}$ scattered by all the obstacles $\Omega_{j,q}$ in the array:

$$p(\mathbf{x}) = p^{\mathrm{un}}(\mathbf{x}) + p^{\mathrm{sc}}(\mathbf{x}) \quad \text{with} \quad p^{\mathrm{sc}}(\mathbf{x}) = \sum_{j\in[\![1;\mathcal{N}]\!]} \sum_{q\in\mathbb{Z}} p^{\mathrm{sc}}_{j,q}(\mathbf{x}). \qquad [6.53]$$

The local coordinate system $(O_{j,q}, \mathbf{r}_{j,q})$ with polar coordinates $\mathbf{r}_{j,q} = (r_{j,q}, \theta_{j,q})$ is then attached to each obstacle $\Omega_{j,q}$ and the scattered field $p^{\mathrm{sc}}_{j,q}$ is expanded on the outgoing cylindrical wavefunctions $\psi_n(\mathbf{r}_{j,q})$ in the form:

$$\forall j \in [\![1;\mathcal{N}]\!], \quad \forall q \in \mathbb{Z}, \quad p^{\mathrm{sc}}_{j,q}(\mathbf{r}_{j,q}) = \sum_{n\in\mathbb{Z}} A^{j,q}_n \psi_n(\mathbf{r}_{j,q}), \qquad [6.54]$$

where $A^{j,q}_n$ are the scattering coefficients of $\Omega_{j,q}$. To reduce the number of scattering coefficients to determine, the periodicity of the array is now exploited. This is only possible, however, if the undisturbed field which forces the scattered fields preserves somehow this periodicity. This is the case of plane waves, for which *quasi-periodicity conditions* can be used, as explained hereafter.

The fact that the undisturbed field in equation [6.52] is a plane wave entails the phase shift $e^{\mathrm{i}k_x\ell}$ between two consecutive clusters Ω^q_{cl} and $\Omega^{q+1}_{\mathrm{cl}}$ of the array. As a result, the scattering coefficients inherit this property in the form $A^{j,q+1}_n = A^{j,q}_n e^{\mathrm{i}k_x\ell}$,

so that the scattering coefficients $A_n^{j,q}$ of the obstacle $\Omega_{j,q}$ can be derived from those of the obstacle Ω_j in the reference cluster Ω_{cl}^0 as follows:

$$\forall j \in [\![1;\mathcal{N}]\!], \quad \forall q \in \mathbb{Z}, \quad A_n^{j,q} = A_n^j e^{\mathrm{i}qk_x\ell} \quad \text{where} \quad A_n^j = A_n^{j,0}. \qquad [6.55]$$

Equation [6.55] is called the *quasi-periodicity condition*. As a result, it is sufficient in equation [6.54] to determine the scattering coefficients A_n^j for the obstacles Ω_j in the reference cluster Ω_{cl}^0 to solve the problem. Indeed, combining equations [6.53] to [6.55], the actual field can be calculated according to:

$$p = p^{\text{un}} + \sum_{j\in[\![1;\mathcal{N}]\!]} \sum_{q\in\mathbb{Z}} p_{j,q}^{\text{sc}} \quad \text{with} \quad p_{j,q}^{\text{sc}}(\mathbf{r}_{j,q}) = \sum_{n\in\mathbb{Z}} A_n^j e^{\mathrm{i}qk_x\ell}\psi_n(\mathbf{r}_{j,q}). \quad [6.56]$$

6.4.2. *Lattice sums and scattering coefficients of the array*

To apply the boundary conditions at the surface Γ_j of the obstacles Ω_j, the field p in equation [6.56] is expanded on cylindrical wavefunctions expressed in the polar coordinate system $(O_j, \mathbf{r}_j)$ where $\mathbf{r}_j = \mathbf{r}_{j,0}$. The distinction is made in equation [6.56] between the field $p_{j,0}^{\text{sc}}$ scattered by the obstacle Ω_j in the reference cluster Ω_{cl}^0, and the external field $p_{j,0}^{\text{ext}}$ to which Ω_j is submitted. In addition, the following contributions to the external field $p_{j,0}^{\text{ext}}$ are identified: (i) the undisturbed field p^{un}; (ii) the intra-cluster external field $p_{j,0}^{\text{intra}}$ made of the fields $p_{i\neq j,0}^{\text{sc}}$ scattered by the obstacles $\Omega_{i\neq j}$ located in the reference cluster Ω_{cl}^0 apart from Ω_j; and (iii) the exo-cluster external field $p_{j,0}^{\text{exo}}$ made of the fields $p_{i,q\neq 0}^{\text{sc}}$ scattered by the obstacles $\Omega_i^{q\neq 0}$ located in the clusters $\Omega_{\text{cl}}^{q\neq 0}$ other than the reference cluster Ω_{cl}^0. Mathematically, it reads:

$$p = p_{j,0}^{\text{sc}} + p_{j,0}^{\text{ext}} \qquad \text{with} \qquad p_{j,0}^{\text{ext}} = p^{\text{un}} + p_{j,0}^{\text{intra}} + p_{j,0}^{\text{exo}} \qquad [6.57]$$

where

$$p_{j,0}^{\text{intra}} = \sum_{i\neq j} p_{i,0}^{\text{sc}} \qquad \text{and} \qquad p_{j,0}^{\text{exo}} = \sum_{i\in[\![1;\mathcal{N}]\!]} \sum_{q\neq 0} p_{i,q}^{\text{sc}}. \qquad [6.58]$$

Now, the fields are expressed in the polar coordinate system attached to Ω_j. Using equation [6.39], the undisturbed field is expanded on the regular wavefunctions $\zeta_n(\mathbf{r}_j)$ as:

$$p^{\text{un}}(\mathbf{r}_j) = \sum_{n\in\mathbb{Z}} U_n^j \zeta_n(\mathbf{r}_j) \quad \text{with} \quad U_n^j = \mathrm{i}^n e^{\mathrm{i}(\mathbf{k}\cdot\mathbf{x}_j - n\vartheta)}, \qquad [6.59]$$

while Graf's addition theorem [6.16] is used to expand the outgoing wavefunctions $\psi_m(\mathbf{r}_{i,q})$ on the regular wavefunctions $\zeta_n(\mathbf{r}_j)$, where $i, j \in [\![1;\mathcal{N}]\!]$:

$$\begin{aligned}\psi_m(\mathbf{r}_{i,q}) &= \psi_m(\mathbf{r}_{i,q}^{j,0} + \mathbf{r}_j) \\ &= \sum_{n\in\mathbb{Z}} \psi_{m-n}(\mathbf{r}_{i,q}^{j,0})\, \zeta_n(\mathbf{r}_j) \quad \text{for } |\mathbf{r}_j| < \min_i |\mathbf{r}_{i,q}^{j,0} - a_i|, \end{aligned} \tag{6.60}$$

where $\mathbf{r}_{i,q}^{j,0} = \overrightarrow{O_{i,q}O_{j,0}}$. Using equation [6.60], the following relations hold close to Ω_j:

$$\forall i \neq j, \qquad p_{i,0}^{\text{sc}}(\mathbf{r}_j) = \sum_{n\in\mathbb{Z}}\sum_{m\in\mathbb{Z}} \mathcal{C}_{nm}^{j,i} A_m^i\, \zeta_n(\mathbf{r}_j), \tag{6.61a}$$

$$\forall i \in [\![1;\mathcal{N}]\!], \qquad \sum_{q\neq 0} p_{i,q}^{\text{sc}}(\mathbf{r}_j) = \sum_{n\in\mathbb{Z}}\sum_{m\in\mathbb{Z}} \mathcal{S}_{nm}^{j,i} A_m^i\, \zeta_n(\mathbf{r}_j), \tag{6.61b}$$

where:

$$\mathcal{C}_{nm}^{j,i} = \psi_{m-n}(\mathbf{r}_{i,0}^{j,0}) \quad \text{and} \quad \mathcal{S}_{nm}^{j,i} = \sum_{q\in\mathbb{Z}, q\neq 0} e^{\mathrm{i}qk_x\ell} \psi_{m-n}(\mathbf{r}_{i,q}^{j,0}). \tag{6.62}$$

Here, $\mathcal{C}_{nm}^{j,i}$ are the coupling coefficients between obstacles Ω_j and $\Omega_{i\neq j}$ in the reference cluster Ω_{cl}^0, and take the same form as the coupling coefficients in equation [6.17] holding for the cluster in the unbounded space. On the contrary, the coefficients $\mathcal{S}_{nm}^{j,i}$ in equation [6.62] are called *lattice sums* and account for the contribution of the fields scattered by the obstacles $\Omega_{i,q}$ located in all the exo-clusters $\Omega_{\text{cl}}^{q\neq 0}$ to the near field close to Ω_j. In particular, the term $\mathcal{S}_{nm}^{j,j}$ that refers to the periodic replicates of obstacle Ω_j in all cells other than the reference cell is often called the *Schlömich series*[1]. Here, the choice has been made to distinguish between intra-cluster and exo-cluster interactions, resulting in the coupling coefficients $\mathcal{C}_{nm}^{j,i}$ and $\mathcal{S}_{nm}^{j,i}$ as defined in equation [6.62], but other field partitions can be adopted in the literature. In particular, conventions defining absolute lattice sums $\hat{\mathcal{S}}_{nm}^{j,j} = \mathcal{S}_{nm}^{j,j}$, and relative lattice sums $\hat{\mathcal{S}}_{nm}^{j,i} = \mathcal{C}_{nm}^{j,i} + \mathcal{S}_{nm}^{j,i}$ for $i \neq j$ are often adopted in the literature

1 The sum can be reduced to $q \leq 1$ due to symmetry in lattice sums. It is worth mentioning that lattice sums are slowly converging in non-dissipative media, in which fields scattered from obstacles even very far from the reference cluster can be significant. That requires accounting for many clusters when truncating the sum in equation [6.62] to $\sum_{q\in[\![-Q;Q]\!],q\neq 0}$. However, mathematical procedures to efficiently evaluate the lattice sums can be found in the literature [TWE 61, MCP 00, LIN 06].

[BOT 00, BOT 03, GRO 11]. Nevertheless, the substitution of equation [6.61] into [6.58] provides:

$$p_{j,0}^{\text{intra}}(\mathbf{r}_j) = \sum_{i\neq j}\sum_{n\in\mathbb{Z}}\sum_{m\in\mathbb{Z}} \mathcal{C}_{nm}^{j,i} A_m^i \, \zeta_n(\mathbf{r}_j), \qquad [6.63a]$$

$$p_{j,0}^{\text{exo}}(\mathbf{r}_j) = \sum_{i\in[\![1;\mathcal{N}]\!]}\sum_{n\in\mathbb{Z}}\sum_{m\in\mathbb{Z}} \mathcal{S}_{nm}^{j,i} A_m^i \, \zeta_n(\mathbf{r}_j). \qquad [6.63b]$$

Combining equations [6.57], [6.59] and [6.63], the external field $p_{j,0}^{\text{ext}}$ is found in the form:

$$p_{j,0}^{\text{ext}}(\mathbf{r}_j) = \sum_{n\in\mathbb{Z}} \mathcal{E}_n^j \zeta_n(\mathbf{r}_j), \qquad [6.64a]$$

$$\text{with} \quad \mathcal{E}_n^j = U_n^j + \sum_{i\neq j}\sum_{m\in\mathbb{Z}} \mathcal{C}_{nm}^{j,i} A_m^i + \sum_{i\in[\![1;\mathcal{N}]\!]}\sum_{m\in\mathbb{Z}} \mathcal{S}_{nm}^{j,i} A_m^i. \qquad [6.64b]$$

Equation [6.64a] is similar to equation [6.20] for the isolated cluster. Hence, the procedure to apply the boundary conditions at Γ_j by means of the single scattering matrices is formally the same as for the isolated cluster, whether the obstacles are impervious as in section 6.3.3 or permeable to sound as in section 6.3.8. Using the similar matrix formulation as in section 6.3.4, without specifying the nature (impervious or permeable) of the obstacles, the final problem can be written in the form:

$$[\boldsymbol{\mathcal{I}}]\boldsymbol{\mathcal{A}} = [\boldsymbol{\mathcal{D}}]\boldsymbol{\mathcal{E}} \quad \text{where} \quad \boldsymbol{\mathcal{E}} = \boldsymbol{\mathcal{U}} + [\boldsymbol{\mathcal{C}}]\boldsymbol{\mathcal{A}} + [\boldsymbol{\mathcal{S}}]\boldsymbol{\mathcal{A}}. \qquad [6.65]$$

Here, $[\boldsymbol{\mathcal{I}}]$ is the identity matrix; $[\boldsymbol{\mathcal{D}}]$ is the matrix of single scattering for the obstacles in the reference cluster Ω_{cl}^0; the vector $\boldsymbol{\mathcal{A}}$ contains the scattering coefficients A_n^j (unknowns of the problem); the vectors $\boldsymbol{\mathcal{E}}$ and $\boldsymbol{\mathcal{U}}$ contains the coefficients $\mathcal{E}_n^j$ and U_n^j of the external and undisturbed fields; $[\boldsymbol{\mathcal{C}}]$ is the matrix of coupling between obstacles in the reference cluster Ω_{cl}^0 (intra-cluster interactions) and takes the same form as in equation [6.32] for the isolated cluster; and the matrix $[\boldsymbol{\mathcal{S}}]$ accounts for the coupling between the obstacles in the reference cluster Ω_{cl}^0 and those in all the other clusters $\Omega_{\text{cl}}^{q\neq 0}$ of the array (exo-cluster interactions). In particular, it reads as follows, where conversely to $\boldsymbol{\mathcal{C}}$, its block-diagonal terms are not $\boldsymbol{O}$:

$$\boldsymbol{\mathcal{S}} = \begin{bmatrix} \boldsymbol{\mathcal{S}}^{1,1} & \cdots & \boldsymbol{\mathcal{S}}^{1,\mathcal{N}} \\ \vdots & \boldsymbol{\mathcal{S}}^{j,i} & \vdots \\ \boldsymbol{\mathcal{S}}^{\mathcal{N},1} & \cdots & \boldsymbol{\mathcal{S}}^{\mathcal{N},\mathcal{N}} \end{bmatrix}, \quad \text{with} \quad \left[\boldsymbol{\mathcal{S}}^{j,i}\right]_{nm} = \mathcal{S}_{nm}^{j,i}. \qquad [6.66]$$

Solving for $\boldsymbol{\mathcal{A}}$ in equation [6.65] leads to:

$$\boldsymbol{\mathcal{A}} = [\boldsymbol{\mathcal{M}}^{\infty}]\boldsymbol{\mathcal{U}} \quad \text{with} \qquad [\boldsymbol{\mathcal{M}}^{\infty}] = \Big[[\boldsymbol{\mathcal{I}}] - [\boldsymbol{\mathcal{D}}]\left([\boldsymbol{\mathcal{C}}] + [\boldsymbol{\mathcal{S}}]\right)\Big]^{-1}[\boldsymbol{\mathcal{D}}], \qquad [6.67]$$

where $[\boldsymbol{\mathcal{M}}^{\infty}]$ is the multiple scattering matrix of the array and relates the vector $\boldsymbol{\mathcal{A}}$ of scattering coefficients for the obstacles in the reference cluster Ω^0_{cl} to the vector $\boldsymbol{\mathcal{U}}$ of forcing coefficients inherited from the plane wave excitation.

From a computational point of view, the infinite sums over the angular modes are truncated as explained in equation [6.35], while the lattice sum that runs over the spatial repetition of the cluster is evaluated independently [TWE 61, MCP 00]. Please note once again that the only field representation that is valid in the whole domain Ω is the one provided in equation [6.56], which implies that the field is represented in the direct, i.e. spatial, domain. Nevertheless, because of the periodicity of the structure and its geometrical features that fit Cartesian coordinate system, field representation in the reciprocal, i.e. wavenumber, domain can be preferred.

6.4.3. *Emergence of Bloch's waves and Wood's anomaly*

When the undisturbed field strikes the array, it is expected that some waves are reflected back while others are transmitted through it. Using equation [6.57], the pressure field can be computed at any point and the reflected and transmitted fields can be identified numerically. However, summing the fields scattered from all the obstacles at many points can be very demanding from the computational point of view, and provides no insight into the collective behavior of the obstacles submitted to the undisturbed field. Here, the field p^{sc} scattered by the array is expanded on plane waves in both half-spaces Ω_+ and Ω_- located above and below the array (grating), that is, at points such that $y > y^+$ and $y < y^-$ respectively, where $y^+ = \max_j(y_j + a_j)$ and $y^- = \min_j(y_j - a_j)$ (see Figure 6.4). Not all wave vectors are admissible for such plane waves. Using the Bloch–Floquet analysis [FLO 83, BLO 28], only the discrete set of wavevectors $k_x^\nu \mathbf{e}_x \pm k_y^\nu \mathbf{e}_y$ is admissible, due to the ℓ-periodicity of the array and to the wavenumber k_x prescribed by the undisturbed field in the direction $\mathbf{e}_x$, where:

$$\forall \nu \in \mathbb{Z}, \quad k_x^\nu = k_x + \frac{2\pi\nu}{\ell} \quad \text{and} \quad k_y^\nu = \sqrt{k^2 - (k_x^\nu)^2} \quad \text{with} \quad \text{Re}(k_y^\nu) \geq 0. \quad [6.68]$$

Consequently, the scattered field p^{sc} is expanded on plane waves as follows:

$$p^{\text{sc}}(x,y) = \begin{cases} \displaystyle\sum_{\nu\in\mathbb{Z}} E_\nu^+ e^{\mathrm{i}k_x^\nu x} e^{\mathrm{i}k_y^\nu y} & \text{if } y > y^+, \\ \displaystyle\sum_{\nu\in\mathbb{Z}} E_\nu^- e^{\mathrm{i}k_x^\nu x} e^{-\mathrm{i}k_y^\nu y} & \text{if } y < y^-, \end{cases} \qquad [6.69]$$

where $E_\nu^\pm$ are the complex amplitudes of the *outgoing plane waves radiated from the array* in the free half-spaces $\Omega_\pm$. These plane waves with wavenumbers given by equation [6.68] are called *Bloch waves*. The present issue is now to find the relation between the Bloch wave amplitudes $E_\nu^\pm$ and the scattering coefficients A_n^j calculated in equation [6.67]. This is done by means of the *Green–Kirchhoff integral theorem* where a *2-D ℓ-periodic Green function* is used. The derivation is somewhat tedious and is provided in detail in Appendix 2 at the end of this chapter. It provides the Bloch wave amplitudes in the form:

$$E_\nu^\pm = \sum_{j\in[\![1;\mathcal{N}]\!]} \sum_{m\in\mathbb{Z}} K_{\nu,m}^{\pm,j}\, A_m^j, \qquad [6.70a]$$

$$\text{with} \qquad K_{\nu,m}^{\pm,j} = \frac{2(-\mathrm{i})^m e^{\pm \mathrm{i} m \vartheta^\nu}}{k_y^\nu \ell} e^{-\mathrm{i}\left(k_x^\nu x_j \pm k_y^\nu y_j\right)}, \qquad [6.70b]$$

where it is recalled that angle ϑ^ν is such that $k_x^\nu = k\cos(\vartheta^\nu)$ and $k_y^\nu = k\sin(\vartheta^\nu)$. Using equation [6.69], the actual field is found in the form:

$$p(x,y) = \begin{cases} \displaystyle\sum_{\nu\in\mathbb{Z}} \{T_\nu^0\, e^{\mathrm{i}k_y^\nu y}\} e^{\mathrm{i}k_x^\nu x} & \text{if } y > y^+, \\ \displaystyle\sum_{\nu\in\mathbb{Z}} \{\delta(\nu) e^{\mathrm{i}k_y^0 y} + R_\nu^0\, e^{-\mathrm{i}k_y^\nu y}\} e^{\mathrm{i}k_x^\nu x} & \text{if } y < y^-, \end{cases} \qquad [6.71]$$

where the incident field $\delta(\nu) e^{-\mathrm{i}k_y^0 y} e^{\mathrm{i}k_x^\nu x}$ represents the undisturbed field in the free half-space $\Omega_-(y < y^-)$, while coefficients $R_\nu^0 = E_\nu^-$ and $T_\nu^0 = \delta(\nu) + E_\nu^+$ are the reflection and transmission coefficients from the single grating array with reference plane at $y = 0$. It is worth mentioning here the contribution of the undisturbed field to the transmission coefficient at the fundamental Bloch mode $\nu = 0$, that is, $T_0^0 = 1 + E_0^+$, while higher Bloch modes $\nu \neq 0$ stem only from the field scattered by the array itself, that is, $T_\nu^0 = E_\nu^+$ for $\nu \neq 0$.

Finally, it is important to note here that the Bloch wave expansion of the scattered field p^{sc} with Bloch wave amplitudes given in equation [6.70] is not valid at every frequency. Indeed, coefficient $K_{\nu,m}^{\pm,j}$ in equation [6.70b] is singular whenever $k_y^\nu = 0$. Using equation [6.68], it happens at the frequencies ω_ν^{W} given by:

$$\omega_\nu^{\text{W}} = \frac{2\pi\nu c/\ell}{\pm 1 - \cos(\theta)}, \quad \text{for } \nu \in \mathbb{Z}. \qquad [6.72]$$

For instance, at normal incidence, $\theta = \pi/2$, the lowest frequency at which $K_{\nu,m}^{\pm,j}$ becomes singular is $\omega_1^{\text{W}} = 2\pi c/\ell$, that is, when the wavelength of the incident wave is equal to the lattice size ℓ. At that frequency, the reflected and transmitted waves remain localized in the vicinity of the array, and propagate along the grating in the direction $\pm\mathbf{e}_x$ (not demonstrated here). In other words, the field is made of evanescent

waves which are guided by the array. This phenomenon is called the *Wood anomaly* [WOO 02, CUT 44].

From a computational point of view, the associated singularity is usually avoided by adding a small imaginary part to k in the vicinity of the Wood anomaly. The infinite sums in equations [6.69] and [6.71] must be truncated to $\nu \in [\![-N^-, N^+]\!]$ with

$$N^{\pm} = \text{floor}\,(3k \mp k_x) + 10, \qquad [6.73]$$

to ensure their convergence.

6.4.4. *Interaction of the array with a plane boundary*

The ability in equation [6.69] to describe the scattered field p^{sc} in terms of Bloch waves opens the possibility of studying the interaction between the single grating array with a plane boundary Γ_b parallel to the grating (see Figure 6.5). Here, the plane boundary Γ_b is supposed to be located at $y = b$, with $b > y^+$ being the distance between the boundary Γ_b and the line $y = 0$ along which the array is arranged. The boundary Γ_b is also supposed to be impervious to particles in Ω, so that $\mathbf{v} \cdot \mathbf{e}_y = 0$ at $y = b$.

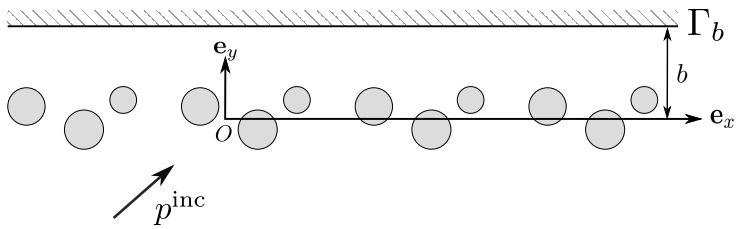

Figure 6.5. *ℓ-period cluster composed of $\mathcal{N}$ obstacles placed against a rigid flat boundary*

In the absence of the array, the incident field $p^{\text{inc}} = e^{\mathrm{i}k_x x + \mathrm{i}k_y y}$ is reflected from the plane boundary $\Gamma_b (y = b)$ into the field $e^{\mathrm{i}k_x x - \mathrm{i}k_y (y-2b)}$, so that the undisturbed field reads:

$$p^{\text{un}}(x,y) = \left\{ e^{\mathrm{i}k_y y} + e^{-\mathrm{i}k_y (y-2b)} \right\} e^{\mathrm{i}k_x x} \quad \text{such that} \quad \frac{\partial p^{\text{un}}}{\partial y} = 0 \text{ at } \Gamma_b. \qquad [6.74]$$

In response to the undisturbed field, the obstacles in the array radiate the field:

$$p^{\text{sc}}(\mathbf{x}) = \sum_{j \in [\![1;\mathcal{N}]\!]} \sum_{q \in \mathbb{Z}} p^{\text{sc}}_{j,q}(\mathbf{x}) \quad \text{with} \quad p^{\text{sc}}_{j,q}(\mathbf{r}_{j,q}) = \sum_{n \in \mathbb{Z}} A^j_n e^{\mathrm{i}q k_x \ell} \psi_n(\mathbf{r}_{j,q}), \qquad [6.75]$$

where the scattering coefficients A_n^j of the obstacles in the reference cluster $\Omega_{\rm cl}^0$ are to be determined. Interferences between the scattered fields $p_{j,q}^{\rm sc}$ give rise to Bloch waves, and the scattered field $p^{\rm sc}$ can be re-written as in equation [6.69]:

$$p^{\rm sc}(x,y) = \begin{cases} \displaystyle\sum_{\nu\in\mathbb{Z}} E_\nu^+ e^{{\rm i}k_x^\nu x + {\rm i}k_y^\nu y} & \text{if } y \in [y^+, b], \\ \displaystyle\sum_{\nu\in\mathbb{Z}} E_\nu^- e^{{\rm i}k_x^\nu x - {\rm i}k_y^\nu y} & \text{if } y < y^-, \end{cases} \qquad [6.76]$$

where the Bloch wave amplitudes E_ν^+ are given in equation [6.70]. However, due to the presence of the plane boundary Γ_b, each Bloch wave $E_\nu^+ e^{{\rm i}k_x^\nu x + {\rm i}k_y^\nu y}$ emitted from the array is reflected back from $\Gamma_b (y = b)$, which radiates the field:

$$p_\Gamma^{\rm sc}(x,y) = \sum_{\nu\in\mathbb{Z}} E_\nu^+ e^{{\rm i}2k_y^\nu b} e^{{\rm i}k_x^\nu x - {\rm i}k_y^\nu y} \quad \text{so that} \quad \frac{\partial(p^{\rm sc} + p_\Gamma^{\rm sc})}{\partial y} = 0 \text{ at } \Gamma_b. \qquad [6.77]$$

Now, the obstacle Ω_j in the reference cluster $\Omega_{\rm cl}^0$ is submitted to the undisturbed field $p^{\rm un}$ given in equation [6.74], to the intra- and exo-cluster fields $p_{j,0}^{\rm intra}$ and $p_{j,0}^{\rm exo}$ given in equation [6.58], and to the field $p_\Gamma^{\rm sc}$ scattered back from the plane boundary Γ_b. To apply the boundary conditions at the surface Γ_j of Ω_j, all of these fields are expanded on regular wavefunctions $\zeta_n(\mathbf{r}_j)$ in the vicinity of Ω_j. Using the Jacobi–Anger expansion detailed in section 6.3.5, the following relation is derived:

$$e^{{\rm i}k_x^\nu x \pm {\rm i}k_y^\nu y} = \sum_{n\in\mathbb{Z}} L_{n,\nu}^{j,\pm}\, \zeta_n(\mathbf{r}_j) \quad \text{with} \quad L_{n,\nu}^{j,\pm} = ({\rm i})^n e^{\mp {\rm i}n\vartheta^\nu} e^{{\rm i}k_x^\nu x_j \pm {\rm i}k_y^\nu y_j}. \qquad [6.78]$$

Quite interestingly, the coefficients $K_{\nu,m}^{\pm,j}$ in equation [6.70b] and $L_{m,\nu}^{j,\pm}$ in equation [6.78] satisfy the relation $K_{\nu,m}^{\pm,j} L_{m,\nu}^{j,\pm} = 2/(k_y^\nu \ell)$. The substitution of equation [6.78] into the expressions of the undisturbed field $p^{\rm un}$ and back-scattered field $p_\Gamma^{\rm sc}$ in equations [6.74] and [6.77], while using equation [6.70a] leads to the following expansions:

$$p^{\rm un}(\mathbf{r}_j) = \sum_{m\in\mathbb{Z}} U_n^j \zeta_n(\mathbf{r}_j) \quad \text{with} \quad U_n^j = L_{n,0}^{j,+} + e^{{\rm i}2k_y b} L_{n,0}^{j,-}, \qquad [6.79a]$$

$$\text{and} \quad p_\Gamma^{\rm sc}(\mathbf{r}_j) = \sum_{i\in[\![1;\mathcal{N}]\!]} \sum_{n\in\mathbb{Z}} \sum_{m\in\mathbb{Z}} \mathcal{B}_{n,m}^{j,i}\, A_m^i\, \zeta_n(\mathbf{r}_j), \qquad [6.79b]$$

$$\text{with} \quad \mathcal{B}_{n,m}^{j,i} = \sum_{\nu\in\mathbb{Z}} L_{n,\nu}^{j,-} K_{\nu,m}^{+,i} e^{{\rm i}2k_y^\nu b}. \qquad [6.79c]$$

Finally, the expansion of the intra- and exo-cluster fields $p_{j,0}^{\text{intra}}$ and $p_{j,0}^{\text{exo}}$ are provided by equation [6.64a], which results in the following external field $p_{j,0}^{\text{ext}}(\mathbf{r}_j)$ close to Ω_j:

$$p_{j,0}^{\text{ext}}(\mathbf{r}_j) = \sum_{n\in\mathbb{Z}} \mathcal{E}_n^j \zeta_n(\mathbf{r}_j), \quad \text{with} \tag{6.80a}$$

$$\mathcal{E}_n^j = U_n^j + \sum_{i\neq j}\sum_{m\in\mathbb{Z}} \mathcal{C}_{nm}^{j,i} A_m^i + \sum_{i\in[\![1;\mathcal{N}]\!]}\sum_{m\in\mathbb{Z}} (\mathcal{S}_{nm}^{j,i} + \mathcal{B}_{n,m}^{j,i}) A_m^i. \tag{6.80b}$$

Application of the boundary conditions at surface Γ_j then proceeds as usual, and leads to the following problem, written here in its matrix formulation (procedure and notations introduced in sections 6.3.4 and 6.4.2):

$$[\boldsymbol{\mathcal{I}}]\boldsymbol{\mathcal{A}} = [\boldsymbol{\mathcal{D}}]\boldsymbol{\mathcal{E}} \quad \text{where} \quad \boldsymbol{\mathcal{E}} = \boldsymbol{\mathcal{U}} + [\boldsymbol{\mathcal{C}}]\boldsymbol{\mathcal{A}} + [\boldsymbol{\mathcal{S}}]\boldsymbol{\mathcal{A}} + [\boldsymbol{\mathcal{B}}]\boldsymbol{\mathcal{A}}, \tag{6.81}$$

where the following matrix $[\boldsymbol{\mathcal{B}}]$ accounts for the coupling between the obstacles in the reference cluster Ω_{cl}^0 and the fields back-scattered from the plane boundary Γ_b:

$$\boldsymbol{\mathcal{B}} = \begin{bmatrix} \boldsymbol{\mathcal{B}}^{1,1} & \dots & \boldsymbol{\mathcal{B}}^{1,\mathcal{N}} \\ \vdots & \boldsymbol{\mathcal{B}}^{j,i} & \vdots \\ \boldsymbol{\mathcal{B}}^{\mathcal{N},1} & \dots & \boldsymbol{\mathcal{B}}^{\mathcal{N},\mathcal{N}} \end{bmatrix}, \quad \text{with} \quad \left[\boldsymbol{\mathcal{B}}^{j,i}\right]_{nm} = \mathcal{B}_{nm}^{j,i}. \tag{6.82}$$

Once the scattering coefficients are calculated from equation [6.81], the actual field $p = p^{\text{un}} + p^{\text{sc}} + p_\Gamma^{\text{sc}}$ can be computed. This example showed that in the presence of the plane interface Γ_b, the undisturbed field is not reduced to the incident field, and the obstacles are submitted to the fields scattered back from Γ_b. In fact, the plane boundary Γ_b acts as an obstacle on its own, with (Bloch) plane waves playing the role of the wavefunctions adapted to its shape. Although Γ_b has been considered here impervious, the approach to account for the interactions between the single grating array and the plane boundary remains general, and the procedure can be extended to the cases of an admittance surface or an interface between two media, for instance.

6.5. Scattering of sound by a multi-grating array

In this section, the cluster Ω_{cl} with $\mathcal{N}$ obstacles in it is repeated ℓ_x-periodically in the direction $\mathbf{e}_x$ to produce a row, and the resulting row is repeated N_y times with the center-to-center spacing ℓ_y in the direction $\mathbf{e}_y$ (see Figure 6.6). Barycenters of the clusters are therefore located at the following points:

$$\mathbf{x}_{\text{cl}}^{(q,g)} = q\ell_x\mathbf{e}_x + g\ell_y\mathbf{e}_y \quad \text{with} \quad q \in \mathbb{Z}, \quad \text{and} \quad g \in [\![0, N_y - 1]\!]. \tag{6.83}$$

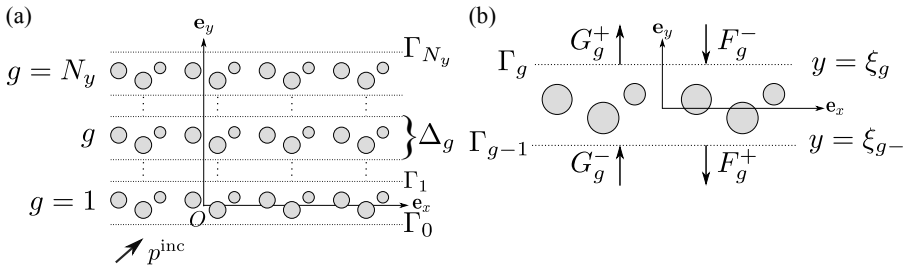

Figure 6.6. *(a) Multi-grating ℓ-periodic cluster composed of $\mathcal{N}$ obstacles and (b) single grating Δ_g*

The cluster at the point $\mathbf{x}_{\text{cl}}^{(q,g)}$ is denoted $\Omega_{\text{cl}}^{(q,g)}$ while the obstacles in $\Omega_{\text{cl}}^{(q,g)}$ are denoted $\Omega_{(j,q,g)}$ with $j \in [\![1, \mathcal{N}]\!]$. The center $O_{(j,q,g)}$ of the obstacle $\Omega_{(j,q,g)}$ is located at the point $\mathbf{x}_{(j,q,g)} = \mathbf{x}_j + q\ell_x\mathbf{e}_x + g\ell_y\mathbf{e}_y$, where $\mathbf{x}_j = x_j\mathbf{e}_x + y_j\mathbf{e}_y$ is the position of $O_{(j,0,0)}$. The radius of obstacle $\Omega_{(j,q,g)}$ is denoted a_j, and the lattice sizes ℓ_x and ℓ_y are supposed to satisfy $\ell_x/2 > \max_j(|x_j| + a_j)$ and $\ell_y/2 > \max_j(|y_j| + a_j)$. To study the scattering of the incident plane wave $p^{\text{inc}}(\mathbf{x}) = e^{\mathrm{i}k_x x + \mathrm{i}k_y(y-\ell_y/2)}$ by such the *multi-grating array*, super clusters $\Omega_{\text{cl}\star}^{q} = \bigcup\left\{\Omega_{\text{cl}}^{(q,g)} | g \in [\![0, N_y - 1]\!]\right\}$ could be defined, and the results from section 6.4 applied to the single grating of super clusters [GRO 08b, GRO 11]. However, it would result in $N_y \times \mathcal{N}$ obstacles in the super cluster, which could require heavy computations, especially when N_y is large. In this section, another approach to the problem is presented. It relies on the transfer matrix formulation for the single grating array (one row), and the association of these transfer matrices to derive the reflected and transmitted fields from the multi-grating array. Another approach relies on the scattering matrix formulation [BOT 00], which is in essence relatively similar but the scattering matrix multiplication might be somewhat tedious.

6.5.1. *Transfer matrix formulation for the single grating*

Here, the single grating $\Delta_g = \bigcup\left\{\Omega_{\text{cl}}^{(q,g)} | q \in \mathbb{Z}\right\}$ is extracted from the multi-grating array and isolated (see Figure 6.6). It is submitted simultaneously to the two incident fields $\hat{p}_g^+$ and $\hat{p}_g^-$ propagating from below and above the grating:

$$\hat{p}_g^+ = \sum_{\nu\in\mathbb{Z}} F_{g,\nu}^+ \, e^{\mathrm{i}k_x^\nu x + \mathrm{i}k_y^\nu(y-\xi_g)} \qquad \text{in } y < y_g^-, \qquad [6.84a]$$

$$\hat{p}_g^- = \sum_{\nu\in\mathbb{Z}} F_{g,\nu}^- \, e^{\mathrm{i}k_x^\nu x - \mathrm{i}k_y^\nu(y-\xi_{g+1})} \qquad \text{in } y > y_g^+, \qquad [6.84b]$$

where $y_g^+ = g\ell_y + \max_j(y_j + a_j)$ and $y_g^- = g\ell_y + \min_j(y_j - a_j)$ delimit domains for Bloch wave expansion outside the grating, $F_{g,\nu}^{\pm}$ are complex amplitudes, and $\xi_g = g\ell_y - \ell_y/2$ define fictive boundaries at $y = \xi_g$ between gratings Δ_{g+1} and Δ_g in the multi-grating array. In response to the incident fields, grating Δ_g produces the fields:

$$p_g^+ = \sum_{\mu\in\mathbb{Z}} G_{g,\mu}^+ \, e^{\mathrm{i}k_x^\mu x + \mathrm{i}k_y^\mu (y-\xi_{g+1})} \qquad \text{in } y > y_g^+, \tag{6.85a}$$

$$p_g^- = \sum_{\mu\in\mathbb{Z}} G_{g,\mu}^- \, e^{\mathrm{i}k_x^\mu x - \mathrm{i}k_y^\mu (y-\xi_g)} \qquad \text{in } y < y_g^-. \tag{6.85b}$$

To determine the amplitudes $G_{g,\mu}^{\pm}$, the results from section 6.4 are used. The obstacle $\Omega_{(j,0,g)}$ in the reference cluster ($q = 0$) of the grating Δ_g produces the scattered field $p^{\text{sc}}_{(j,0,g)}$ in response to the external field $p^{\text{ext}}_{(j,0,g)}$ to which it is submitted, where $p^{\text{ext}}_{(j,0,g)}$ is the superposition of the undisturbed field $p^{\text{un}} = \hat{p}_g^+ + \hat{p}_g^-$, the intra-cluster external field $p^{\text{intra}}_{(j,0,g)}$ and the exo-cluster field $p^{\text{exo}}_{(j,0,g)}$. In the vicinity of $\Omega_{(j,0,g)}$ and in the polar coordinate system $(O_{(j,0,g)}, \mathbf{r}_{(j,0,g)})$ attached to $\Omega_{(j,0,g)}$, they take the form:

$$p^{\text{sc}}_{(j,0,g)}(\mathbf{r}_{(j,0,g)}) = \sum_{n\in\mathbb{Z}} A_n^{(j,0,g)} \psi_n(\mathbf{r}_{(j,0,g)}), \tag{6.86a}$$

$$p^{\text{un}}(\mathbf{r}_{(j,0,g)}) = \sum_{n\in\mathbb{Z}} U_n^{(j,0,g)} \zeta_n(\mathbf{r}_{(j,0,g)}), \tag{6.86b}$$

$$p^{\text{intra}}_{(j,0,g)}(\mathbf{r}_{(j,0,g)}) = \sum_{i\neq j} \sum_{n\in\mathbb{Z}} \sum_{m\in\mathbb{Z}} \mathcal{C}_{nm}^{j,i} A_m^{(i,0,g)} \, \zeta_n(\mathbf{r}_{(j,0,g)}), \tag{6.86c}$$

$$p^{\text{exo}}_{(j,0,g)}(\mathbf{r}_{(j,0,g)}) = \sum_{i\in[\![1;\mathcal{N}]\!]} \sum_{n\in\mathbb{Z}} \sum_{m\in\mathbb{Z}} \mathcal{S}_{nm}^{j,i} A_m^{(i,0,g)} \, \zeta_n(\mathbf{r}_{(j,0,g)}), \tag{6.86d}$$

where intra-cluster coupling coefficients $\mathcal{C}_{nm}^{j,i}$ and lattice sums $\mathcal{S}_{nm}^{j,i}$ are independent of the index g of the grating Δ_g (since they involve the relative positions of the obstacles in the grating) and read as follows, with $\mathbf{r}_{(i,q,g)}^{(j,0,g)} = \overrightarrow{O_{(i,q,g)}O_{(j,0,g)}}$:

$$\mathcal{C}_{nm}^{j,i} = \psi_{m-n}(\mathbf{r}_{(i,0,g)}^{(j,0,g)}) \quad \text{and} \quad \mathcal{S}_{nm}^{j,i} = \sum_{q\in\mathbb{Z}, q\neq 0} e^{\mathrm{i}qk_x\ell_x} \psi_{m-n}(\mathbf{r}_{(i,q,g)}^{(j,0,g)}). \tag{6.87}$$

In particular, equation [6.86b] is derived from the *Jacobi–Anger expansion* [6.78] of the undisturbed field $p^{\text{un}} = \hat{p}_g^+ + \hat{p}_g^-$ extended to the whole space $y \in]-\infty, +\infty[$. Using equation [6.85], it leads to:

$$U_n^{(j,0,g)} = \sum_{\nu\in\mathbb{Z}} \left[\mathcal{L}_{n,\nu}^{j,+} F_{g,\nu}^+ + \mathcal{L}_{n,\nu}^{j,-} F_{g,\nu}^-\right], \tag{6.88a}$$

$$\text{with} \qquad \mathcal{L}_{n,\nu}^{j,\pm} = (\mathrm{i})^n e^{\mp \mathrm{i}n\vartheta^\nu} e^{\mathrm{i}k_x^\nu x_j \pm \mathrm{i}k_y^\nu (y_j \mp \ell_y/2)}. \tag{6.88b}$$

It is important here to note that coefficients $\mathcal{L}_{n,\nu}^{j,\pm}$ in equation [6.88b] do not depend on the index g of the grating Δ_g extracted. Finally, using the matrix formulation introduced in section 6.4.2, application of the boundary conditions at the surface of each obstacle $\Omega_{(j,0,g)}$ in the reference cluster ($q = 0$) of the grating Δ_g leads to:

$$\boldsymbol{\mathcal{A}}^g = [\boldsymbol{\mathcal{M}}^\infty]\,\boldsymbol{\mathcal{U}}^g \quad \text{with} \qquad [\boldsymbol{\mathcal{M}}^\infty] = \Big[[\boldsymbol{\mathcal{I}}] - [\boldsymbol{\mathcal{D}}]\,([\boldsymbol{\mathcal{C}}] + [\boldsymbol{\mathcal{S}}])\Big]^{-1}[\boldsymbol{\mathcal{D}}], \quad [6.89]$$

where the multiple scattering matrix $[\boldsymbol{\mathcal{M}}^\infty]$ is independent of the index g of the row Δ_g extracted, and where vectors $\boldsymbol{\mathcal{A}}^g$ and $\boldsymbol{\mathcal{U}}^g$ contain the scattering coefficients $A_n^{(j,0,g)}$ and forcing coefficients $U_n^{(j,0,g)}$ respectively. Now using the results from section 6.4.3, the field p_g^{sc} scattered from the grating Δ_g is expanded on Bloch waves as follows:

$$p_g^{\text{sc}} = \begin{cases} \displaystyle\sum_{\mu\in\mathbb{Z}} \Big[\sum_{j\in[\![1;\mathcal{N}]\!]} \sum_{m\in\mathbb{Z}} \mathcal{K}_{\mu,m}^{+,j}\, A_m^{(j,0,g)} \Big]\, e^{\mathrm{i}k_x^\mu x + \mathrm{i}k_y^\mu (y-\xi_{g+1})} & \text{if } y \geq y_g^+, \\ \displaystyle\sum_{\mu\in\mathbb{Z}} \Big[\sum_{j\in[\![1;\mathcal{N}]\!]} \sum_{m\in\mathbb{Z}} \mathcal{K}_{\mu,m}^{-,j}\, A_m^{(j,0,g)} \Big]\, e^{\mathrm{i}k_x^\mu x - \mathrm{i}k_y^\mu (y-\xi_g)} & \text{if } y \leq y_g^-, \end{cases} \quad [6.90]$$

where coefficients $\mathcal{K}_{\mu,m}^{\pm,j}$ are independent of the index g of the grating Δ_g and read:

$$\mathcal{K}_{\mu,m}^{\pm,j} = \frac{2(-\mathrm{i})^m e^{\pm \mathrm{i}m\vartheta^\mu}}{k_y^\mu \ell_x} e^{-\mathrm{i}\left(k_x^\mu x_j \pm k_y^\nu (y_j \mp \ell_y/2)\right)}. \quad [6.91]$$

Now, the total field p in both half-spaces $y > y_g^+$ and $y < y_g^-$ is recomposed as:

$$p = \begin{cases} \hat{p}_g^+ + \hat{p}_g^- + p_g^{\text{sc}} = \hat{p}_g^- + p_g^+ & \text{if } y \geq y_g^+, \\ \hat{p}_g^+ + \hat{p}_g^- + p_g^{\text{sc}} = \hat{p}_g^+ + p_g^- & \text{if } y \leq y_g^-, \end{cases} \quad [6.92]$$

which provides the expression of the fields $p_g^\pm$ in the form:

$$p_g^+ = \hat{p}_g^+(y > y_g^+) + p_g^{\text{sc}}(y > y_g^+) \quad \text{and} \quad p_g^- = \hat{p}_g^-(y < y_g^-) + p_g^{\text{sc}}(y < y_g^-). \quad [6.93]$$

Substitution of equations [6.84], [6.85] and [6.90] into [6.93] while using orthogonality of the Bloch waves (see equation [A2.15] in Appendix 2), yields:

$$\forall \mu \in \mathbb{Z}, \quad G_{g,\mu}^\pm = F_{g,\mu}^\pm e^{\mathrm{i}k_y^\mu \ell_y} + \sum_{j\in[\![1;\mathcal{N}]\!]} \sum_{m\in\mathbb{Z}} \mathcal{K}_{\mu,m}^{\pm,j}\, A_m^{(j,0,g)} \quad [6.94]$$

Vectors $\mathbb{F}_g^{\pm}$ and $\mathbb{G}_g^{\pm}$ with amplitudes $F_{g,\nu}^{\pm}$ and $G_{g,\mu}^{\pm}$ as components are defined:

$$\mathbb{F}_g^{\pm} = \{\dots F_{g,\nu-1}^{\pm},\, F_{g,\nu}^{\pm},\, F_{g,\nu+1}^{\pm},\, \}^T, \tag{6.95a}$$

$$\mathbb{G}_g^{\pm} = \{\dots G_{g,\mu-1}^{\pm},\, G_{g,\mu}^{\pm},\, G_{g,\mu+1}^{\pm},\, \}^T, \tag{6.95b}$$

and the following matrices $[\boldsymbol{\mathcal{K}}^{\pm}]$ and $[\boldsymbol{\mathcal{L}}^{\pm}]$ are formed:

$$[\boldsymbol{\mathcal{K}}^{\pm}] = \begin{bmatrix} \boldsymbol{\mathcal{K}}_{\mu-1}^{\pm,1} & \dots & \boldsymbol{\mathcal{K}}_{\mu-1}^{\pm,\mathcal{N}} \\ \boldsymbol{\mathcal{K}}_{\mu}^{\pm,1} & \boldsymbol{\mathcal{K}}_{\mu}^{\pm,j} & \boldsymbol{\mathcal{K}}_{\mu}^{\pm,\mathcal{N}} \\ \boldsymbol{\mathcal{K}}_{\mu+1}^{\pm,1} & \dots & \boldsymbol{\mathcal{K}}_{\mu+1}^{\pm,\mathcal{N}} \end{bmatrix}, \quad [\boldsymbol{\mathcal{L}}^{\pm}] = \begin{bmatrix} \boldsymbol{\mathcal{L}}_{\nu-1}^{1,\pm} & \boldsymbol{\mathcal{L}}_{\nu}^{1,\pm} & \boldsymbol{\mathcal{L}}_{\nu+1}^{1,\pm} \\ \vdots & \boldsymbol{\mathcal{L}}_{\nu}^{j,\pm} & \vdots \\ \boldsymbol{\mathcal{L}}_{\nu-1}^{\mathcal{N},\pm} & \boldsymbol{\mathcal{L}}_{\nu}^{\mathcal{N},\pm} & \boldsymbol{\mathcal{L}}_{\nu+1}^{\mathcal{N},\pm} \end{bmatrix}, \tag{6.96}$$

where line vector $\boldsymbol{\mathcal{K}}_{\mu}^{\pm,j}$ and column vector $\boldsymbol{\mathcal{L}}_{\nu}^{j,\pm}$ read:

$$\boldsymbol{\mathcal{K}}_{\mu}^{\pm,j} = \left\{\dots \mathcal{K}_{\mu,m-1}^{\pm,j},\, \mathcal{K}_{\mu,m}^{\pm,j},\, \mathcal{K}_{\mu,m+1}^{\pm,j},\, \right\}, \tag{6.97a}$$

$$\boldsymbol{\mathcal{L}}_{\nu}^{j,\pm} = \left\{\dots \mathcal{L}_{n-1,\nu}^{j,\pm},\, \mathcal{L}_{n,\nu}^{j,\pm},\, \mathcal{L}_{n+1,\nu}^{j,\pm},\, \right\}^T. \tag{6.97b}$$

Finally, the following diagonal matrix $[\boldsymbol{\varphi}]$ is defined as follows:

$$[\boldsymbol{\varphi}] = \mathrm{diag}_{\mu\in\mathbb{Z}}(e^{\mathrm{i}k_y^{\mu}\ell_y}). \tag{6.98}$$

With those notations, and recalling the structure of the vectors $\boldsymbol{\mathcal{A}}^g$ and $\boldsymbol{\mathcal{U}}^g$ in equations [6.30] and [6.27], it is possible to write equations [6.88a] and [6.94] in the form:

$$\boldsymbol{\mathcal{U}}^g = [\boldsymbol{\mathcal{L}}^{+}].\mathbb{F}_g^{+} + [\boldsymbol{\mathcal{L}}^{-}].\mathbb{F}_g^{-}, \quad \text{and} \quad \mathbb{G}_g^{\pm} = [\boldsymbol{\varphi}].\mathbb{F}_g^{\pm} + [\boldsymbol{\mathcal{K}}^{\pm}].\boldsymbol{\mathcal{A}}^g. \tag{6.99}$$

Now combining equations [6.89] and [6.99], the following relations hold:

$$\mathbb{G}_g^{+} = \left[\boldsymbol{\mathcal{T}}^{+}\right]\mathbb{F}_g^{+} + \left[\boldsymbol{\mathcal{R}}^{+}\right]\mathbb{F}_g^{-} \quad \text{and} \quad \mathbb{G}_g^{-} = \left[\boldsymbol{\mathcal{R}}^{-}\right]\mathbb{F}_g^{+} + \left[\boldsymbol{\mathcal{T}}^{-}\right]\mathbb{F}_g^{-}, \tag{6.100}$$

where the generalized matrices $[\boldsymbol{\mathcal{T}}^{\pm}]$ of transmission and $[\boldsymbol{\mathcal{R}}^{\pm}]$ of reflection read:

$$\left[\boldsymbol{\mathcal{T}}^{\pm}\right] = [\boldsymbol{\varphi}] + [\boldsymbol{\mathcal{K}}^{\pm}].[\boldsymbol{\mathcal{M}}^{\infty}].[\boldsymbol{\mathcal{L}}^{\pm}] \quad \text{and} \quad \left[\boldsymbol{\mathcal{R}}^{\pm}\right] = [\boldsymbol{\mathcal{K}}^{\pm}].[\boldsymbol{\mathcal{M}}^{\infty}][\boldsymbol{\mathcal{L}}^{\mp}]. \tag{6.101}$$

Matrices $[\boldsymbol{\mathcal{T}}^{\pm}]$ and $[\boldsymbol{\mathcal{R}}^{\pm}]$ are independent of the index g of the single grating Δ_g. Knowing the incident Bloch waves impinging the grating Δ_g, equation [6.100] makes it possible to calculate the amplitudes of the Bloch waves reflected from and transmitted through Δ_g. As shown in the next section, combinations of matrices $[\boldsymbol{\mathcal{T}}^{\pm}]$ and $[\boldsymbol{\mathcal{R}}^{\pm}]$ according to the *Transfer-Matrix Method* open the possibility of deriving the Bloch waves reflected from and transmitted through the multi-grating array.

6.5.2. *Sound scattering by the multi-grating array*

To derive the fields reflected from and transmitted through the multi-grating array, fictive boundaries Γ_g located at $y = \xi_g$ for $g \in [\![0, N_y]\!]$ are defined, where Γ_g is the interface between gratings Δ_g and Δ_{g+1} for $g \in [\![1, N_y - 1]\!]$, while Γ_0 and Γ_{N_y} are the lower and upper boundaries of the overall multi-grating array, see Figure 6.6 (b).

Below the inner boundary Γ_g where $g \in [\![1, N_y - 1]\!]$, that is, from the point of view of the grating Δ_g for $y \in]y_g^+, \xi_{g+1}]$, the actual pressure p finds the following expansion according to section 6.5.1:

$$p = \sum_{\nu \in \mathbb{Z}} \left[F_{g,\nu}^- \, e^{-\mathrm{i}k_y^\nu (y - \xi_{g+1})} + G_{g,\nu}^+ \, e^{\mathrm{i}k_y^\nu (y - \xi_{g+1})} \right] e^{\mathrm{i}k_x^\nu x}. \qquad [6.102]$$

Similarly, above the inner boundary Γ_g, that is, from the point of view of the grating Δ_{g+1} for $y \in [\xi_{g+1}, y_{g+1}^-[$, the actual pressure p finds the following expansion:

$$p = \sum_{\nu \in \mathbb{Z}} \left[F_{g+1,\nu}^+ \, e^{\mathrm{i}k_y^\nu (y - \xi_g + 1)} + G_{g+1,\nu}^- \, e^{-\mathrm{i}k_y^\nu (y - \xi_g + 1)} \right] e^{\mathrm{i}k_x^\nu x}. \qquad [6.103]$$

At the boundary Γ_g, that is, for $y = \xi_g$, both expansions in equations [6.102] and [6.103] must match. Considering the continuity of the pressure and that of the normal component of the velocity at Γ_g, while using the orthogonality of the Bloch waves, the following interface conditions are derived:

$$\mathbb{F}_g^- = \mathbb{G}_{g+1}^- \qquad \text{and} \qquad \mathbb{G}_g^+ = \mathbb{F}_{g+1}^+. \qquad [6.104]$$

In addition, using equation [6.100] and intuitive matrix notations, the following relations hold:

$$\begin{pmatrix} \mathbb{F}_g^- \\ \mathbb{G}_g^+ \end{pmatrix} = \begin{bmatrix} \mathbf{O} & \mathbf{Id} \\ [\boldsymbol{\mathcal{T}}^+] & [\boldsymbol{\mathcal{R}}^+] \end{bmatrix} \begin{pmatrix} \mathbb{F}_g^+ \\ \mathbb{F}_g^- \end{pmatrix}, \quad \begin{pmatrix} \mathbb{G}_g^- \\ \mathbb{F}_g^+ \end{pmatrix} = \begin{bmatrix} [\boldsymbol{\mathcal{R}}^-] & [\boldsymbol{\mathcal{T}}^-] \\ \mathbf{Id} & \mathbf{O} \end{bmatrix} \begin{pmatrix} \mathbb{F}_g^+ \\ \mathbb{F}_g^- \end{pmatrix}, \qquad [6.105]$$

where $\mathbf{O}$ and $\mathbf{Id}$ are null and identity matrices having the same size as $[\boldsymbol{\mathcal{T}}^\pm]$ and $[\boldsymbol{\mathcal{R}}^\pm]$. Equations [6.104] and [6.105] are combined to provide the recurrence relation:

$$\begin{pmatrix} \mathbb{G}_{g+1}^- \\ \mathbb{F}_{g+1}^+ \end{pmatrix} = [\mathbb{TM}] \begin{pmatrix} \mathbb{G}_g^- \\ \mathbb{F}_g^+ \end{pmatrix}, \qquad [6.106]$$

where the transfer matrix $\mathbb{TM}$ is given by:

$$[\mathbb{TM}] = \begin{bmatrix} \mathbf{O} & \mathbf{Id} \\ [\boldsymbol{\mathcal{T}}^+] & [\boldsymbol{\mathcal{R}}^+] \end{bmatrix} \cdot \begin{bmatrix} [\boldsymbol{\mathcal{R}}^-] & [\boldsymbol{\mathcal{T}}^-] \\ \mathbf{Id} & \mathbf{O} \end{bmatrix}^{-1}. \qquad [6.107]$$

Equation [6.106] defines a geometrical series, which leads to:

$$\forall g \in [\![0, N_y]\!], \qquad \begin{pmatrix} \mathbb{G}_g^- \\ \mathbb{F}_g^+ \end{pmatrix} = \begin{bmatrix} [\mathbb{TM}]_{\mathbb{GG}}^{(g)} & [\mathbb{TM}]_{\mathbb{GF}}^{(g)} \\ [\mathbb{TM}]_{\mathbb{FG}}^{(g)} & [\mathbb{TM}]_{\mathbb{FF}}^{(g)} \end{bmatrix} \begin{pmatrix} \mathbb{G}_0^- \\ \mathbb{F}_0^+ \end{pmatrix}, \qquad [6.108]$$

where $[\mathbb{TM}]^g$ denoting the transfer matrix $[\mathbb{TM}]$ multiplied by itself g times with the convention that $[\mathbb{TM}]^0$ is the identity matrix:

$$\begin{bmatrix} [\mathbb{TM}]_{\mathbb{GG}}^{(g)} & [\mathbb{TM}]_{\mathbb{GF}}^{(g)} \\ [\mathbb{TM}]_{\mathbb{FG}}^{(g)} & [\mathbb{TM}]_{\mathbb{FF}}^{(g)} \end{bmatrix} = [\mathbb{TM}]^g . \qquad [6.109]$$

In addition, the actual field reads as follows outside the multi-grating array:

$$p = \sum_{\nu \in \mathbb{Z}} \left[R_\nu \, e^{-\mathrm{i}k_y^\nu (y - \xi_0)} + \delta(\nu) e^{\mathrm{i}k_y^\nu (y - \xi_0)} \right] e^{\mathrm{i}k_x^\nu x} \qquad \text{for } y \leq \xi_0, \qquad [6.110a]$$

$$p = \sum_{\nu \in \mathbb{Z}} \left[T_\nu e^{\mathrm{i}k_y^\nu (y - \xi_{N_y})} \right] e^{\mathrm{i}k_x^\nu x} \qquad \text{for } y \geq \xi_{N_y}, \qquad [6.110b]$$

where R_ν and T_ν are the reflection and transmission coefficients from the multi-grating array. Identification of the coefficients leads to:

$$\mathbb{G}_0^- = \mathbb{R}, \quad \mathbb{F}_0^+ = \mathbb{I}, \quad \mathbb{G}_{N_y}^- = \mathbb{O}, \quad \mathbb{F}_{N_y}^+ = \mathbb{T}, \qquad [6.111]$$

where vectors $\mathbb{R}$, $\mathbb{I}$, $\mathbb{T}$ and $\mathbb{O}$ have the components $\mathbb{R}_\nu = R_\nu$ for the reflection coefficients, $\mathbb{I}_\nu = \delta(\nu)$ for the incident field, $\mathbb{T}_\nu = T_\nu$ for the transmission coefficients and $\mathbb{O}_\nu = 0$ since no incident field is impinging the array from above in the present example. Then, application of equation [6.109] with $g = N_y$ while using equation [6.111] provides the reflection and transmission coefficients in the form:

$$\mathbb{R} = \left[\left[[\mathbb{TM}]_{\mathbb{GG}}^{(N_y)} \right]^{-1} \left[[\mathbb{TM}]_{\mathbb{GF}}^{(N_y)} \right] \right] \mathbb{I}, \qquad [6.112a]$$

$$\mathbb{T} = \left[\left[[\mathbb{TM}]_{\mathbb{FG}}^{(N_y)} \right] \left[[\mathbb{TM}]_{\mathbb{GG}}^{(N_y)} \right]^{-1} \left[[\mathbb{TM}]_{\mathbb{GF}}^{(N_y)} \right] + \left[[\mathbb{TM}]_{\mathbb{FF}}^{(N_y)} \right] \right] \mathbb{I}. \qquad [6.112b]$$

Once the reflection and transmission coefficients are known, the vectors $\mathbb{G}_g^-$ and $\mathbb{F}_g^+$ can be derived for each row Δ_q of the array, and the scattering coefficients of each obstacle can be derived using relations presented in section 6.5.1. This last step, however, is rarely performed, since the significant data usually remains the reflection and transmission coefficients when comparing the model to experimental results.

In order to provide a more complete overview of the possibility offered by the multiple scattering method and notably through its Cartesian counterpart, it should be noted that multiple scattering method enables the calculation of the scattering coefficient of a cluster grating when excited by a line source. This requires the Wannier function [WAN 37] for which a large literature exists.

6.5.3. *Band diagram calculation*

The transfer-matrix method presented in section 6.5.2 offers the possibility of deriving the dispersion relation in a medium Ω entirely paved with the cluster Ω_{cl}, that is, when $N_y = \infty$. To do so, the wavenumber $k_x = k\cos(\theta)$ in the direction $\mathbf{e}_x$ is supposed to be prescribed by a fictitious incident wave having the fixed angle of incidence θ, and the wavenumber k_y^{eff} in the direction $\mathbf{e}_y$ is looked for, so that the following condition of quasi-periodicity in the direction $\mathbf{e}_y$ is satisfied:

$$\begin{pmatrix} \mathbb{G}^-_{g+1} \\ \mathbb{F}^+_{g+1} \end{pmatrix} = e^{\mathrm{i}k_y^{\text{eff}}\ell_y} \begin{pmatrix} \mathbb{G}^-_{g} \\ \mathbb{F}^+_{g} \end{pmatrix}. \qquad [6.113]$$

The quasi-periodicity condition [6.113] is combined with the transfer-matrix relation in equation [6.106] to provide:

$$[\mathbb{TM}] \begin{pmatrix} \mathbb{G}^-_{g} \\ \mathbb{F}^+_{g} \end{pmatrix} = \eta \begin{pmatrix} \mathbb{G}^-_{g} \\ \mathbb{F}^+_{g} \end{pmatrix}, \quad \text{with} \quad \eta = e^{\mathrm{i}k_y^{\text{eff}}\ell_y}. \qquad [6.114]$$

In other words, η is the eigenvalue of the transfer matrix $\mathbb{TM}$. The resolution of the eigenvalue problem [6.114] leads to the discrete set of solutions η_κ indexed by the positive integer κ, and the admissible wavenumbers read $k_{y,\kappa}^{\text{eff}} = -\mathrm{iLn}(\eta_\kappa)/\ell_y$. This procedure is performed at many frequencies ω so as to reconstruct the dispersion relation providing the wavenumber $k_{y,\kappa}^{\text{eff}}$ as a function of ω. The overall admissible wavenumber $k_\kappa^B = \sqrt{(k_x)^2 + (k_{y,\kappa}^{\text{eff}})^2}$ can also be calculated.

The band diagram of fully periodic arrangement can also be evaluated thanks to the scattering matrix formulation [BOT 01] or to the 2D dimensional periodic Green's function [POU 00] relying on similar features as Appendix 2, but most of these methods imply the solution of the complex roots of complex dispersion relation. When compared to the usual *plane wave expansion* method [KUS 93, VAS 02, VAS 17], which provides real frequency/real wavenumber dispersion relation via an eigenvalue problem but is restricted to media of identical type (e.g. fluid obstacles in fluid matrix), methods based on multiple scattering theory make it possible to deal with media of different types and provide complex wavenumber/real frequency dispersion relation. Moreover, these former classes of method make it possible to deal with any dissipative media, while the *extended plane*

wave expansion [HSU 05, LAU 09, ROM 10a, ROM 10b], which also provide complex wavenumber/real frequency dispersion relation is restricted to low dissipative media. Nevertheless, all methods based on multiple scattering theory provide *equifrequency surfaces* and the complex wavenumbers have to be sorted afterwards.

6.6. Application to sonic crystals

As an example of application, a 7-layer finite-depth sonic crystal composed of $a = 3.5$ cm in radii circular cylinders arranged on a $\ell = 10$ cm cubic lattice is considered when solicited at normal incidence (see Figure 6.7(a)). The surrounding material is air and no viscothermal losses are considered. Therefore, the different scatterers are considered impervious. Viscothermal losses could have been accounted for either in the form of a more advanced version of the multiple scattering theory based on linearized Navier–Stokes equations and involving the acoustic, entropic and vortex potentials or more simply using impedance boundary conditions if the viscous and thermal skin depths of two adjacent obstacles do not overlap [DUC 07].

The considered finite-depth sonic crystal is either of finite lateral extend comprising 10 rows or of infinite lateral extend. The band diagram for such a sonic crystal, when considered of infinite depth as calculated with the *plane wave expansion* method, is provided in Figure 6.7(b), while the complex wavenumber/real frequency band diagram along the ΓX direction as calculated with the method presented in section 6.5.3 is plotted against the results of the PWE calculation in Figure 6.7(c). Of particular interest is the fact that the method based on multiple scattering theory provides complex a wavenumber, therefore showing the purely imaginary nature of the wavenumber in bandgaps. The structure possesses a full bandgap around 2000 Hz, i.e. no wave can propagate in the structure in all the directions, and two bandgaps centered at 1500 Hz and above 2750 Hz along the ΓX direction in the frequency band considered. This frequency band stand is far below the Wood anomaly which arises at ≈ 3400 Hz. Therefore, only the specularly reflected and transmitted field can propagate above and below the crystal. The reflected and transmitted fields calculated in the central region at a distance ℓ above and below the finite lateral extend sonic crystal with the procedure described in section 6.3 are plotted in Figure 6.7(d) and (e). While low amplitude transmitted and large amplitude reflected fields might be noted inside the bandgaps, the diffraction by the edge of the finite lateral extend sonic crystal completely blurs the signal highlighting the use of the Pointing vector or averaging the field over a couple of periods along the lateral dimension in order to exhibit the bandgaps. The diffraction effects are also noticeable from the amplitude of these fields which are larger than 1, while the amplitude of the incident field is unitary. In the opposite, the reflected and

transmitted coefficients as calculated for the infinite lateral extend sonic crystal (Figure 6.7(f) and (g)) clearly exhibit low transmission associated with high reflection within the bandgaps. The sonic crystal being of finite depth (7-layers), six Fabry–Perot resonances can be clearly seen below the first bandgap.

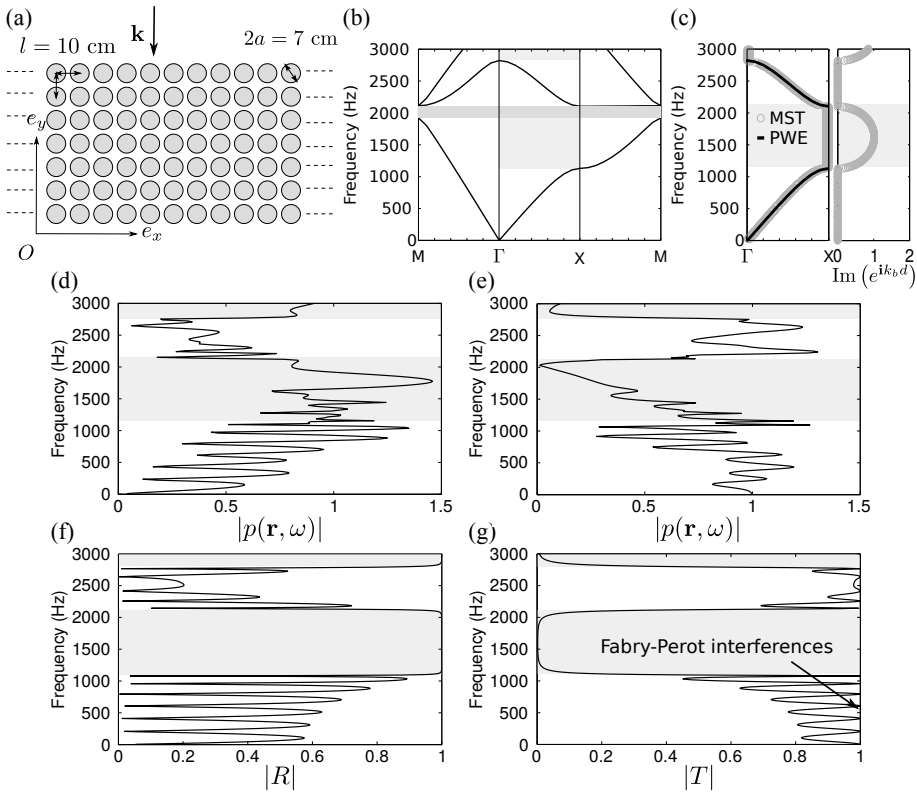

Figure 6.7. *(a) The 7-layer finite-depth sonic crystal composed of $a = 3.5\,cm$ in radius circular cylinder arranged on a $\ell = 10\,cm$ cubic lattice. (b) Band diagram of the corresponding sonic crystal when considered of infinite depth as calculated with the PWE and (c) as calculated along the ΓX direction using the method described in section 6.5.3. (d) Reflected and (e) transmitted fields calculated in the central region at a distance ℓ above and below a finte lateral extend (10 rows) sonic crystal. (f) Reflection and (g) transmission coefficients of an infinite lateral extend sonic crystal*

This example clearly highlights the efficiency of the multiple scattering theory to physically analyze the acoustic response of both finite and infinite periodic structures.

6.7. Conclusion

This chapter has presented the basic theoretical elements of multiple scattering theory in simple two-dimensional examples of increasing complexity. Emphases have been placed on the domain of validity of specific field representations and recipes have been given at each step for practical implementation. As indicated in the introduction, more complicated configurations can be modeled with multiple scattering theory, following identical procedure. This technique is now a valuable part of the toolkit for studies of photonic, phononic and sonic crystals. They provide highly accurate and efficient computational methods due to their use of rapidly convergent field expansions adapted to the particular geometry. The only remaining problem yields a highly dense arrangement of obstacles, the modeling of which requires a large number of terms for the different sums involved to converge. The next milestones for multiple scattering are its extensive use in 3D problems, problems involving elliptic obstacles, and configuration excited by a line source. While some work has already been undertaken in these area, the regular use of multiple scattering theory to solve these problems has still to be promoted. A huge challenge that multiple scattering theory has to face is its efficient application to the modeling of resonant systems as Helmholtz resonators [SCH 18], the geometry of which usually does not fit its application criteria and the modeling of which involves a non-diagonal scattering matrix in order to cope with the rapid development of metamaterials. Multiple scattering theory is a very efficient computational tool for crystals and metamaterials.

6.8. Acknowledgments

This chapter is based upon the work from COST Action DENORMS CA15125, supported by COST (European Cooperation in Science and Technology).

6.9. References

[ABR 64] ABRAMOWITZ M., STEGUN I.A., *Handbook of Mathematical Functions With Formulas, Graphs and Mathematical Tables*, National Bureau of Standards, Gaithersburg, 1964.

[ALE 16] ALEVIZAKI A., SAINIDOU R., REMBERT P. *et al.*, "Phononic crystals of poroelastic spheres", *Physical Review B*, vol. 94, p. 174306, 2016.

[ASA 03] ASATRYAN A.A., BUSCH K., MCPHEDRAN R.C. *et al.*, "Two-dimensional Green tensor and local density of states in finite-sized two-dimensional photonic crystals", *Wave Random Complex*, vol. 13, pp. 9–25, 2003.

[BAR 90] BARBER P.W., HILL S.C., *Light Scattering By Particles: Computational Methods*, World Scientific Publishing, London, 1990.

[BAT 53] BATEMAN H., *Higher Transcendental Functions*, McGraw-Hill, New York, 1953.

[BER 80] BERRYMAN J.G., "Long-wavelength propagation in composite elastic media I. Spherical inclusions", *Journal of the Acoustical Society of America*, vol. 68, pp. 1809–1819, 1980.

[BLO 28] BLOCH F., "Über die quantenmechanik der elektronen in kristallgittern", *Zeitschrift für Physik*, vol. 52, pp. 555–600, 1928.

[BOT 00] BOTTEN L.C., NICOROVICI N., ASATRYAN A.A. *et al.*, "Formulation for electromagnetic scattering and propagation through grating stacks of metallic and dielectric cylinders for photonic crystal calculations. Part I. Method", *Journal of the Optical Society of America*, vol. 17, pp. 165–2176, 2000.

[BOT 01] BOTTEN L.C., NICOROVICI N.A., MCPHEDRAN R.C. *et al.*, "Photonic band structure calculations using scattering matrices", *Physical Review E*, vol. 64, p. 046603, 2001.

[BOT 03] BOTTEN L.C., MCPHEDRAN R.C., NICOROVICI N.A. *et al.*, "Rayleigh multipole methods for photonic crystal calculations", *Progress in Electromagnetics Research*, vol. 41, pp. 21–60, 2003.

[CUT 44] CUTLER C., Electromagnetic waves guided by corrugated structures, Report no. MM 44-160-218, Bell Telephone Lab, 1944.

[DUC 07] DUCLOS A., Diffusion multiple en fluide visco-thermique, cas du cristal phononique à deux dimensions, PhD thesis, Le Mans University, 2007.

[FEL 94] FELBACQ D., TAYEB G., MAYSTRE D., "Scattering by a random set of parallel cylinders", *Journal of the Optical Society of America*, vol. 11, pp. 2526–2538, 1994.

[FLO 83] FLOQUET G., "Sur les équations différentielles linéaires à coefficients périodiques", *Ann. Sci. Éc. Norm. Supér.*, vol. 12, pp. 47–88, 1883.

[GRO 08a] GROBY J.-P., LESSELIER D., "Localization and characterization of simple defects in finite-sized photonic crystals", *Journal of the Optical Society of America*, vol. 25, pp. 146–152, 2008.

[GRO 08b] GROBY J.-P., WIRGIN A., OGAM E., "Acoustic response of a periodic distribution of macroscopic inclusions within a rigid frame porous plate", *Wave Random Complex*, vol. 18, pp. 409–433, 2008.

[GRO 11] GROBY J.-P., DAZEL O., DUCLOS A. *et al.*, "Enhancing the absorption coefficient of a backed rigid frame porous layer by embedding circular periodic inclusions", *Journal of the Acoustical Society of America*, vol. 130, pp. 3771–3780, 2011.

[HSU 05] HSUE Y.-C., FREEMAN A.J., GU B.-Y., "Extended plane-wave expansion method in three-dimensional anisotropic photonic crystals", *Physical Review B*, vol. 72, p. 195118, 2005.

[KRY 11] KRYNKIN A., UMNOVA O., CHONG A. *et al.*, "Scattering by coupled resonating elements in air", *Journal of Physics D*, vol. 44, p. 125501, 2011.

[KUS 93] KUSHWAHA M.S., HALEVI P., DOBRZYNSKI L. *et al.*, "Acoustic band structure of periodic elastic composites", *Physical Review Letters*, vol. 71, pp. 2022–2025, 1993.

[LAN 87] LANDAU L.D., LIFSHITZ E.M., *Fluid Mechanics* (2nd edition), Butterworth Heinemann, Elsevier, Oxford, 1987.

[LAU 09] LAUDE V., ACHAOUI Y., BENCHABANE S. *et al.*, "Evanescent Bloch waves and the complex band structure of phononic crystals", *Physical Review B*, vol. 80, p. 092301, 2009.

[LEV 77] LEVY T., SANCHEZ-PALENCIA E., "Equations and interface conditions for acoustic phenomena in porous media", *Journal of Mathematical Analysis and Applications*, vol. 61, pp. 813–834, 1977.

[LIN 06] LINTON C.M., "Schlömilch series that arise in diffraction theory and their efficient computation", *Journal of Physics A: Mathematical and General*, vol. 39, pp. 3325–3339, 2006.

[MAR 06] MARTIN P.A., *Multiple Scattering. Interaction of Time-Harmonic Waves With N Obstacles*, Cambridge University Press, Cambridge, 2006.

[MCP 00] MCPHEDRAN R.C., NICOROVIC N.A., "Lattice sums for gratings and arrays", *Journal of Mathematical Physics*, vol. 41, p. 7808, 2000.

[MOR 68] MORSE P.M., INGARD K.U., *Theoretical Acoustics*, McGraw-Hill, New York, 1968.

[POU 00] POULTON C.G., MOVCHAN A.B., MCPHEDRAN R.C. *et al.*, "Eigenvalue problems for doubly periodic elastic structures and phononic band gaps", *Proceedings of the Royal Society*, vol. 456, pp. 2543–2559, 2000.

[RAY 92] RAYLEIGH L., "On the influence of obstacles arranged in rectangular order upon the properties of a medium", *Philosophical Magazine*, vol. 34, pp. 481–502, 1892.

[ROM 10a] ROMERO-GARCÍA V., SÁNCHEZ-PÉREZ J., GARCIA-RAFFI L., "Evanescent modes in sonic crystals: Complex dispersion relation and supercell approximation", *Journal of Applied Physics*, vol. 108, p. 044907, 2010.

[ROM 10b] ROMERO-GARCÍA V., SÁNCHEZ-PÉREZ J., NEIRA IBÁÑEZ S.C. *et al.*, "Evidences of evanescent Bloch waves in Phononic Crystals", *Applied Physics Letters*, vol. 96, p. 124102, 2010.

[SAI 05] SAINIDOU R., STEFANOU N., PSAROBASA I.E. *et al.*, "A layer-multiple-scattering method for phononic crystals and heterostructures of such", *Computer Physics Communications*, vol. 166, pp. 197–240, 2005.

[SAN 80] SANCHEZ-PALENCIA E., *Non-Homogeneous Media and Vibration Theory*, Springer-Verlag, Berlin Heidelberg, 1980.

[SCH 18] SCHWAN L., UMNOVA O., BOUTIN C. *et al.*, "Nonlocal boundary conditions for corrugated acoustic metasurface with strong near-field interactions", *Journal of Applied Physics*, vol. 123, p. 091712, 2018.

[TOR 06] TORRENT D., HAKANSSON A., CERVERA F. *et al.*, "Homogenization of Two-dimensional clusters of rigid rods in air", *Physical Review Letters*, vol. 96, p. 204302, 2006.

[TOR 17] TORRENT D., Multiple scattering theory, COST Action DENORMS Training School "Sound Waves in Metamaterials and Porous Media", Prague. Available at: https://slideslive.com/38898499/multiple-scattering-theory?subdomain=false, 2017.

[TOU 00] TOURIN A., FINK M., DERODE A., "Multiple scattering of sound", *Waves Random Media*, vol. 10, pp. R31–R60, 2000.

[TWE 61] TWERSKY V., "Elementary function representations of Schlömilch series", *Archive for Rational Mechanics and Analysis*, vol. 8, pp. 323–332, 1961.

[VAS 02] VASSEUR J.O., DEYMIER P.A., KHELIF A. *et al.*, "Phononic crystal with low filling fraction and absolute acoustic band gap in the audible frequency range: A theoretical and experimental study", *Physical Review E*, vol. 65, p. 056608, 2002.

[VAS 17] VASSEUR J.O., "Irreducible Brillouin zone / dispersion relations (band structures) in periodic structures / Plan Wave Expansion method", *COST Action DENORMS Training School "Sound Waves in Metamaterials and Porous Media"*, Prague. Available at: https://slideslive.com/38898496/irreducible-brillouin-zonedispersion-relationship-in-periodic-structurespwe?subdomain=false, 2017.

[WAN 37] WANNIER G.H., "The structure of electronic excitation levels in insulating crystals", *Physical Review*, vol. 52, pp. 191–197, 1937.

[WEI 16] WEISSER T., GROBY J.-P., DAZEL O. *et al.*, "Acoustic behavior of a rigidly backed poroelastic layer with periodic resonant inclusions by a multiple scattering approach", *Journal of the Acoustical Society of America*, vol. 139, pp. 617–630, 2016.

[WOO 02] WOOD R.W., "On a remarkable case of uneven distribution of light in a diffraction grating spectrum", *Philosophical Magazine*, vol. 4, pp. 396–402, 1902.

[WU 08] WU Y., LAI Y., WAN Y. *et al.*, "Wave propagation in strongly scattered random elastic media: Energy equilibration and crossover from ballistic to diffusive behavior", *Physical Review B*, vol. 77, p. 125125, 2008.

PART 3

Applications of Acoustic Metamaterials

Fundamentals and Applications of Acoustic Metamaterials: From Seismic to Radio Frequency,
First Edition. Edited by Vicente Romero-García and Anne-Christine Hladky-Hennion.

7

Acoustic Metamaterials for Industrial Applications

7.1. Introduction

Noise reduction is a major societal challenge that has emerged in the last decade. Every industrial field uses some acoustic solutions, but they usually suffer from a lack of efficiency, particularly at low frequencies. This is due to various constraints that do not allow us to use the most optimal materials in terms of thickness, mass or mechanic or acoustic parameters. At the same time, metamaterials have gained increasing interest from the scientific community because of their extraordinary properties. In acoustics, these metamaterials seem to be a very promising alternative to traditional solutions, in particular for their very good subwavelength behavior. Even though research in this field is very dynamic, technology is still at the state of concept and the connection with the industry is recent. Today, there is growing demand for thin materials in industries for noise absorption or insulation, and we would like to highlight some study results that seem interesting from this point of view.

7.2. Industrial context

The scientific literature on acoustic metamaterials is very extensive and shows strong and advanced behavior. However, the laboratory configuration used in most papers is idealized and the conclusions are not necessarily transferable when they are used as such in real application. This implies that metamaterials should be developed using finite-size materials, to control low-frequency noises (between 50 and 500 Hz) with smaller thicknesses. Finding a feasible, affordable metamaterial that could satisfy all these features is a very challenging task and we would like to give some examples of works that could be developed in this way.

Chapter written by Clément LAGARRIGUE and Damien LECOQ.

This study is conducted from the perspective of industries that manufacture complex products with acoustic properties (in many cases, acoustics is just a secondary feature). In this way, two of the most common acoustic features will be discussed here, which are the acoustic correction made by absorbing materials (to reduce noises inside an enclosure), and the transmission loss case, made by insulating materials, to reduce noises outside. Other metamaterial properties such as double negative refraction, cloaking or wave-guiding will not be discussed here. In this context, metamaterials will be evaluated in the same way as classic acoustic materials in the industry, which means only on the frequency band [50 4000] Hz, usually, for a diffuse field and for finite dimensions. These constraints are widely used, and they correspond to normalized measurement protocols to qualify industrial materials. We choose to compare all solutions with only a couple of parameters on each case. For the absorption case, we will analyze only the absorption coefficient, usually obtained by:

$$\alpha = 1 - |R|^2 \qquad [7.1]$$

with R the reflection coefficient of waves at the interface between the incident field and the material. α is usually obtained in a reverberant room via the ISO standard 354:2003 [ISO 03].

For the isolation case, we analyze the transmission loss obtained by:

$$STL = 10 \log_{10} \left| \frac{W_i}{W_t} \right| \qquad [7.2]$$

with W_i the power of the incident wave coming towards the device and W_t the power of the transmitted wave through the device. This is measured by placing the material between two rooms (usually two reverberant rooms, or one reverberant and one anechoic) according to several ISO standards, for example NF EN ISO 10140-1, NF EN ISO 10140-2 and NF EN ISO 717-1 for France. These standards also allow us to calculate the insertion loss $Rw(C; C_{tr})$ widely used in the industry, which gives a weighted value in dB for the transmission loss of a material.

We also compare the working frequency band to the thickness of the material. This gives information on the efficiency of the technology in terms of subwavelength behavior. This is obtained by:

$$\Lambda = \frac{\lambda}{h} \qquad [7.3]$$

with λ the wavelength in air obtained for the low-frequency boundary and h the thickness of the material.

Engineers and researchers who develop metamaterials and carry out the transfer of technology, should keep these aspects in mind in order to use the same nomenclature as the industrial manufacturers.

7.3. Absorption case

One way to do acoustic absorption in the audible frequency range is to use open-cell porous materials. They are efficient for frequencies above the so-called quarter-wavelength resonance, where acoustic energy can be dissipated by viscous and thermal effects inside the pores. Below this frequency, they are not efficient at all and the usual way to overcome this difficulty is to use multilayers [JIN 16, CHE 16]. A good multilayered absorbing material has an impedance close to air, to minimize the reflecting waves and be lossy enough to attenuate them inside. Obtaining efficient materials at low frequencies with a good impedance mismatch is difficult. One possible solution is to combine several materials, each having one of the properties; however, this combination generally results in a drastic increase in the thickness of the material.

Finding optimal material configurations is not trivial and several studies show how to optimize them [TAN 06] with a recent special effort on periodic layered materials, which excite grating phenomena and create multi-angle broadband perfect absorption in the low frequency range [JIM 16b]. Multilayered material can also involve microperforated plates to create a mass-spring-like resonance at low frequency. This is efficient to treat low-frequency bands, but deteriorates the absorption coefficient at higher frequencies (Figure 7.1). Many studies show how to enlarge this band [WAN 11, JUN 07, SAK 10], but to our knowledge no device has shown perfect absorption over the frequency band (50–4000 Hz).

An alternative way to get closer to the perfect device has emerged with the study of heterogeneous materials, in particular with the work on double porosity material [OLN 03, BOU 98] in which the absorption coefficient is enhanced by the resonance of the microstructure, excited through the macropores. This is also close to a newly emerging material family, called metaporous materials, where the macroporosity can be replaced by inclusions (see Figure 7.2).

This takes advantage of the strong attenuation of the porous media in the high frequency range, coupled with low frequency properties linked to the grating or eventually local resonances. This study was initiated by V. Tournal *et al.* [TOU 04], considering the transmission through a rigid framed porous media with randomly arranged small-sized inclusions. They exhibit a decrease in sound transmission for some configurations (after 2 kHz for inclusion radius $R = 0.8$ mm). This leads to configurations using a periodic set of rigid inclusions embedded in a rigid porous plate and backed with a perfectly rigid wall [GRO 09, GRO 11]. A very interesting

property of these configurations is the excitation of a local mode below the quarter-wavelength resonance of the plate, which enhances the absorption coefficient and allows us to obtain a perfect absorption (see Figure 7.3).

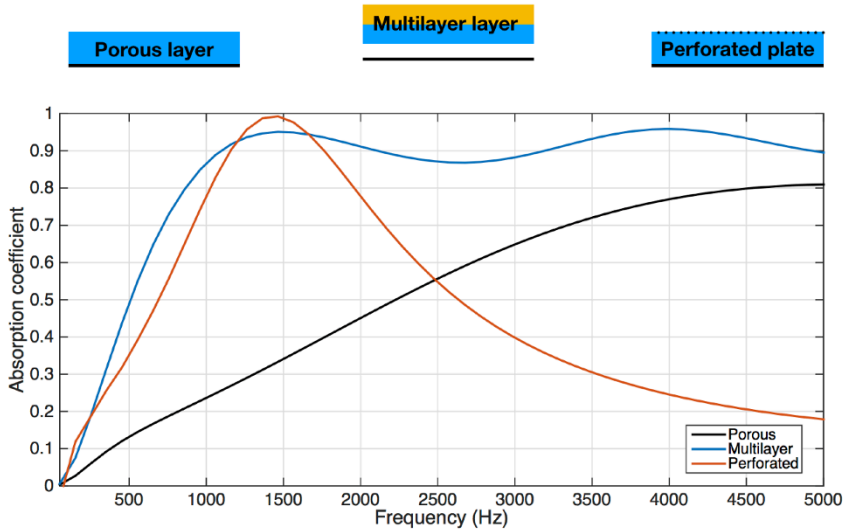

Figure 7.1. *Comparison between three classical solutions. A porous layer (melamine-like foam) of 2 cm thickness (rigidly backed) (black line), a multilayer composed of two different porous materials (melamine-like and glasswool-like foam) and an air gap (thickness $H = 2$ cm for each layer) (blue line), and a 2 cm thick porous layer with a perforated plate of thickness 1 mm and porosity $= 5\%$ (red line). For a color version of this figure, see www.iste.co.uk/romero/metamaterials.zip*

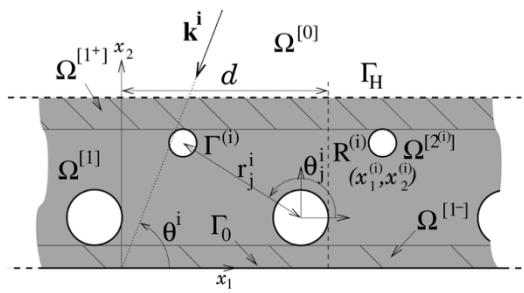

Figure 7.2. *Cross-sectional plane view of a metaporous material made of porous layers with embedded rigid scatterers [GRO 11]*

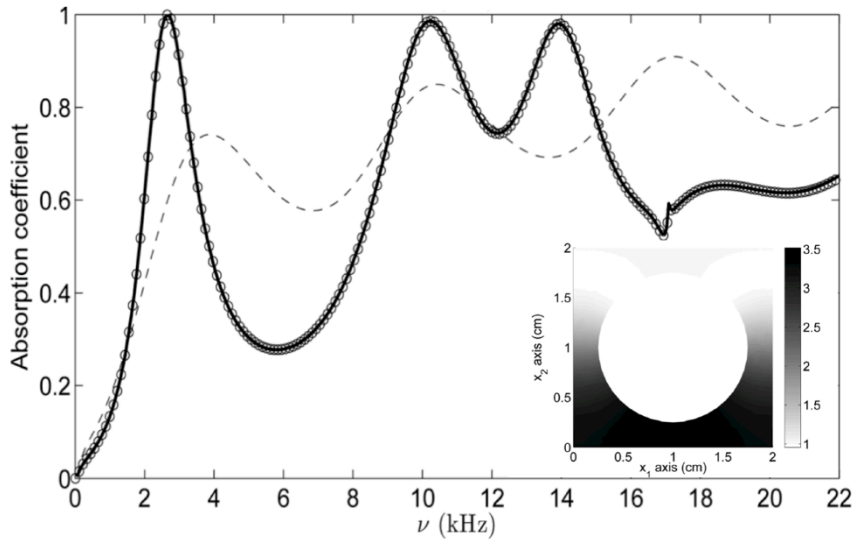

Figure 7.3. *Absorption coefficient of a $H = 2$ cm thick porous sheet of Fireflex foam backed by a rigid plate without inclusion embedded (dashed line) and with a $R = 7.5$ mm radius circular cylinder embedded per spatial period $d = 2$ cm (solid line), when the configuration is excited at normal incidence. Rigid backing at the bottom of the cell. The snapshot in the bottom-right corner is the pressure field at the first resonance (2674 Hz) [GRO 11]*

This mode, also called trapped mode, acts like a wave guide, locating the acoustic pressure inside the porous plate, between the inclusions and the rigid wall. It is dependent on the dimensions of the configuration and on the parameters of the porous media. This is interesting, because it involves only few scatterers per unit cell and can have decent performances for plate thicknesses of few centimeters at 1 kHz. The main drawback is a strong decrease at a higher frequency where the Bragg interference reflects almost all the waves. Depending on the periodicity of the inclusions, this can happen in the frequency band of interest (50–4000Hz).

Boutin *et al.* and Groby *et al.* [BOU 13, GRO 15] brought the concept even further by using locally resonant elements to add low-frequency behavior and minimize the Bragg interferences. This is the philosophy of the reference [LAG 13b], where the study starts with the case of a split-ring (SR) resonator embedded periodically in a rigid-backed porous plate. The aim is to find configurations that show high absorption over a large frequency band, only with 2 cm of porous thickness. Due to the geometry, the problem is considered 2D with the porous matrix considered as an equivalent fluid (Johnson–Champoux–Allard model

[JOH 87, CHA 91]) and the inclusions perfectly rigid. In the normal case (for example, a split-ring resonator with the opening in front of the incident wave), three types of phenomena can be noticed. The former two are similar to those observed for the rigid inclusions; the acoustic energy is still trapped between the inclusions and the rigid backing and Bragg's interferences are also noticeable at higher frequencies. The third phenomenon is the SR resonance, which enhances the absorption coefficient by trapping the sound energy inside the scatterer (Figure 7.4). In free field, the SR resonance frequency depends only on the inner radius and the opening dimensions. However, in the porous plate, the rigid backing can modify this resonance frequency. This happens when the opening is close to the rigid backing, modifying the radiation impedance of the SR and decreasing the resonance frequency. By mixing several inclusions with different resonant frequencies, it is possible to keep the absorption coefficient high between 1500 and 3500 Hz ($H = \lambda/11$) with a quite simple geometry and with only 2 cm of the porous material.

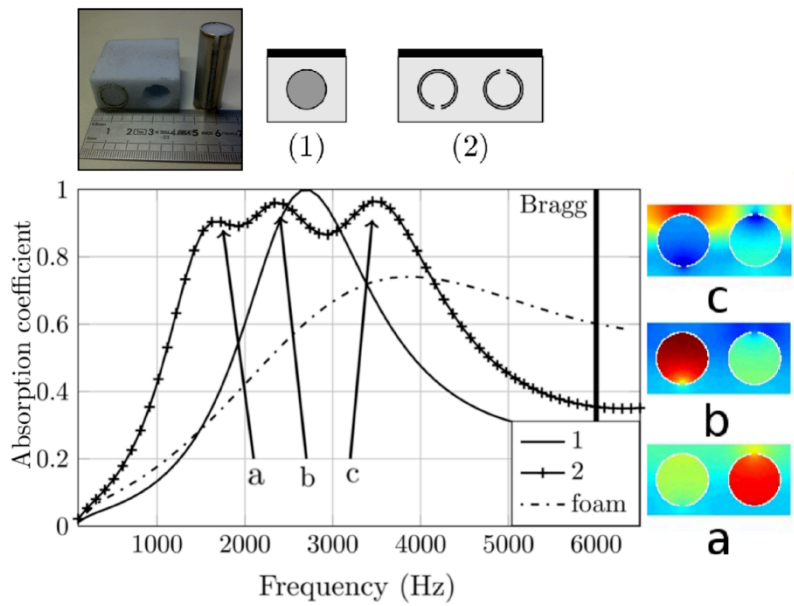

Figure 7.4. *Simulated absorption coefficient of a $H = 2$ cm thick porous sheet of melamine backed by a rigid plate without inclusion embedded ($-\times-$) and with a $R = 7.5$ mm radius split-rings (solid line), when the configuration is excited at normal incidence (incident wave coming from the bottom). Rigid backing on the top of the cell [LAG 13b]. The upper panels show the picture of the sample as well as two schematic views. The insets a, b and c show the snapshots at particular frequencies shown in the absorption spectrum. For a color version of this figure, see www.iste.co.uk/romero/metamaterials.zip*

To go further, [LAG 16] shows non-trivial configurations obtained by using optimization algorithms. The final structures still present a thickness of porous material $H = 2$ cm. The optimized unit cell is made of several resonators, composing a supercell (see the insets in Figure 7.5). In a first attempt, by only using supercells made of two split-ring resonators, optimizing for having the broadest band of absorption, the results are much better than those obtained previously. In particular, by adding more resonant element to the same supercell, for example in the rigid backing, the absorption could be enhanced, as shown in Figure 7.5. This was computed for an industrial proof of concept, where the metaporous material is glued against a corrugated plate. The corrugation can be used here as resonant back cavity in addition to the split-rings. It results in a nearly perfect absorption between 1500 and 7000 Hz.

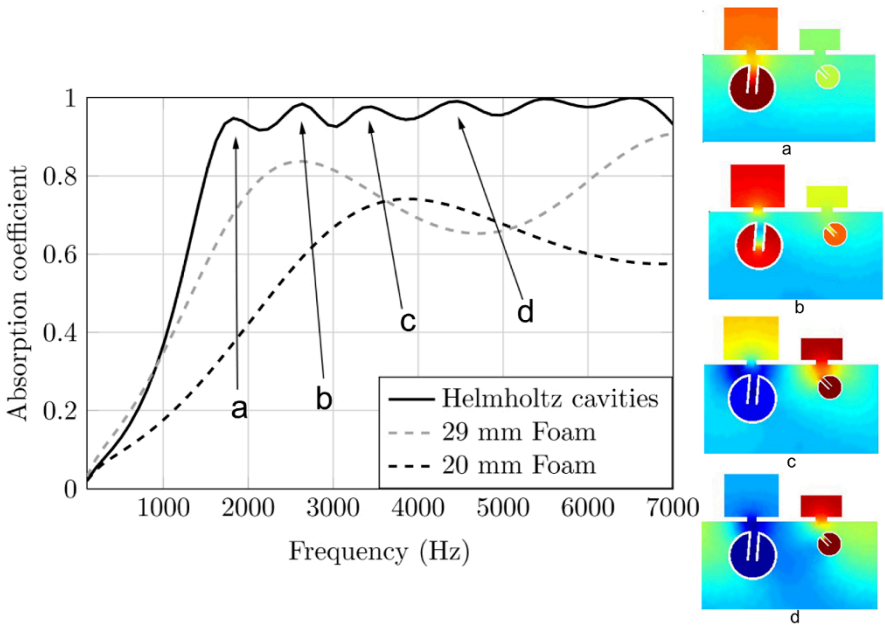

Figure 7.5. *Simulated absorption coefficient of a $H = 2$ cm thick porous sheet of melamine backed by a corrugated plate on the top of the cell without inclusion embedded (black dashed line) and with optimized geometry composed of 2D Helmholtz resonators and back cavities (solid line). The gray solid line is an equivalent homogeneous foam for an equivalent thickness including the foam plate and the back cavities [LAG 16]. The normal incident wave comes from the bottom of the insets a, b, c and d. For a color version of this figure, see www.iste.co.uk/romero/metamaterials.zip*

This concept has two limits: the first is the frequency band below 1500 Hz, where the absorption is not enhanced, and the second is the skeleton motion of the porous matrix that is not taken into account. The first issue is due to the geometry limit of the resonators. To decrease the resonance frequency, the resonators must have radii larger than the thickness plate. A way to solve this issue is to consider other geometries of resonators [YAN 15a] or to consider 3D resonators, like spheres, or more closely to this concept, perforated cylindrical tubes forming 3D Helmholtz resonators [GRO 15]. In this case, the resonance of the resonator can be lowered, but its efficiency is highly dependent on its aspect ratio and it can be difficult to obtain $\alpha = 1$ at low frequencies with a small-radius tube-shaped Helmholtz resonator (Figure 7.6).

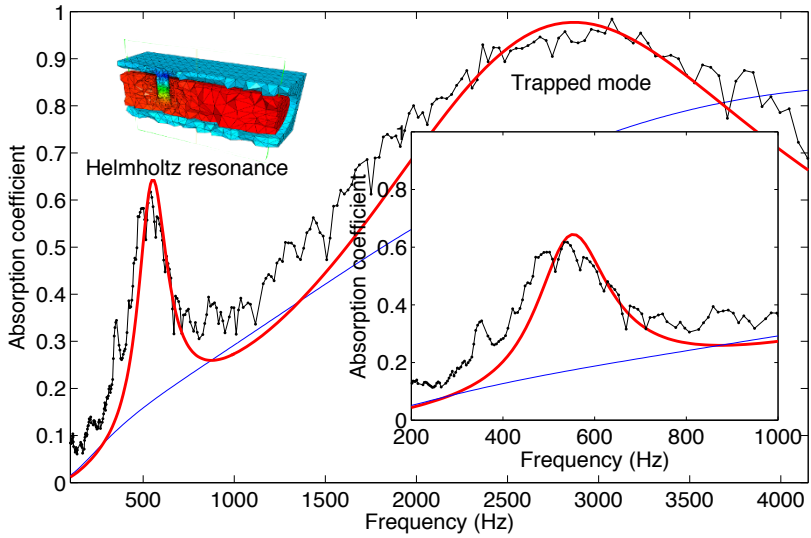

Figure 7.6. *Simulated and experimental absorption coefficient of a $H = 2$ cm thick porous sheet of melamine backed by a rigid plate, without inclusion embedded (blue line), with Helmholtz resonators measured in a square section impedance tube (black line) and with the Helmholtz resonator simulated with the finite element method (red line) [GRO 15]. For a color version of this figure, see www.iste.co.uk/romero/metamaterials.zip*

The second limit is more of an industrial consideration. In the experimental case, the motion of the skeleton could be not negligible and can change the results, in particular when the sample takes part of a complex product that is excited with both acoustics and vibrations. The large scale of the industrial sample also involves long tubes, which could be put in motion. This is why it is important to consider the porous matrix as a poroelastic material and to take into account the skeleton motion, as in [WEI 16], where the case of elastic inclusions embedded in poroelastic

melamine is studied. It shows the resonance of elastic shells of radius 8 mm at 500 Hz (see Figure 7.7) for a 2 cm thick melamine plate ($H = \lambda/34$). The same optimization study could be done with this configuration to achieve an optimized poroelastic sample, using elastic shells in addition to resonant inclusions that could show interesting enhancement below 1000 Hz.

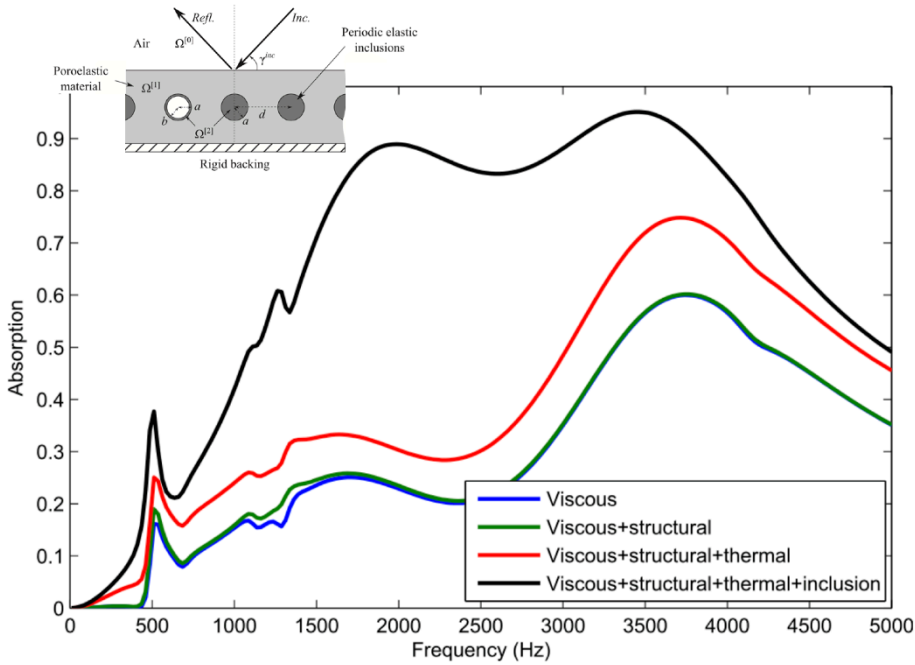

Figure 7.7. *Simulated absorption coefficient of a $H = 2$ cm thick porous sheet of melamine backed by a rigid plate with different losses taken into account without inclusion embedded and with elastic shell inclusion for radius $a = 8$ mm (black line) [WEI 16]. For a color version of this figure, see www.iste.co.uk/romero/metamaterials.zip*

Rather than tuning the local resonances and Bragg's interferences, another way to create a broadband acoustic absorber is to play with the material physical properties. This can be achieved, for example, by controlling the sound velocity inside the material. With a low sound velocity, the wavelengths are small and so it is possible to use smaller resonators to absorb low-frequency noises. An example is shown in [YAN 16], where a partitioned 3 cm thick porous plate exhibits broadband absorption. Each partition can be considered as a local resonator, as well as an effective medium with effective parameters, including an effective velocity. This velocity is very different compared to a homogeneous porous plate and allows resonances at low frequencies. The broadband absorption can be achieved not only

by partitioning the porous media with constant partitions, but also by creating a gradient of resonances where each effective layer can be efficient for a given frequency (see Figure 7.8). This results in a good absorption band between 1500 and 4000 Hz ($H = \lambda/8$) and this device shows tunable potential to achieve even lower frequency performances by optimizing the geometry. It would be interesting to see how this device behaves in an industrial experimental environment, in particular for diffuse fields.

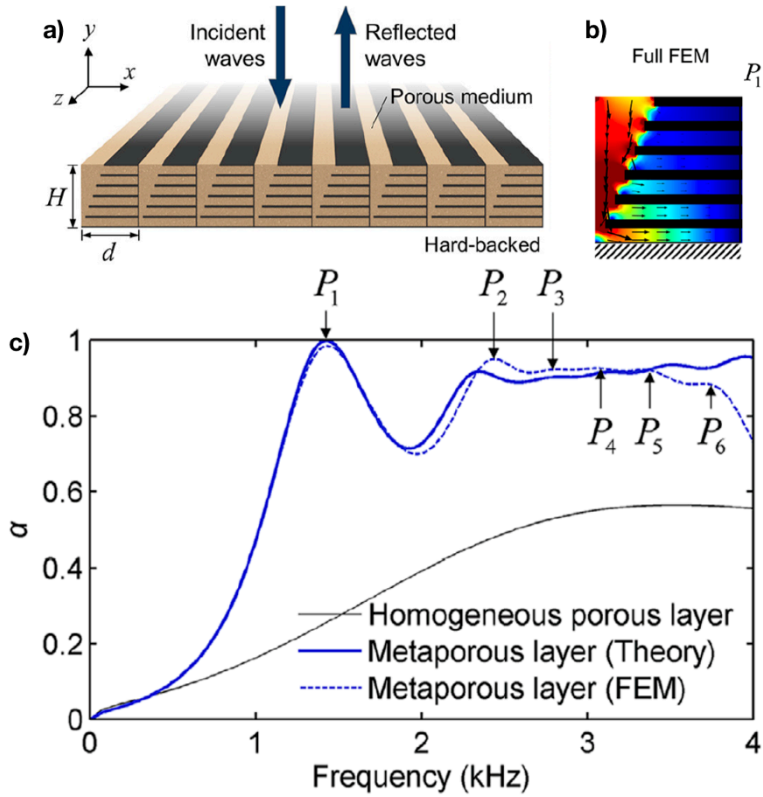

Figure 7.8. *a) Diagram of the metaporous plate. b) Snapshot of the particle velocity at $P_1 = 1430$ Hz. c) The simulated absorption coefficient of a $H = 3$ cm thick porous sheet backed by a rigid plate without inclusion embedded (black line) and with partitions (blue lines) [YAN 16]. For a color version of this figure, see www.iste.co.uk/romero/metamaterials.zip*

On the same principle, another device shows perfect absorption over the band 300–1000 Hz for 10 cm thickness ($H = \lambda/13$) [JIM 16b, JIM 17] and is efficient in diffuse fields. A remarkable fact is that this device is only made of resonators (see

Figure 7.9) and does not use porous material to add dissipation. By just tailoring the geometry of the structure, the sound velocity can be tuned and the system can be critically coupled (impedance matched), achieving resonant systems that can absorb a low frequency for extremely small sizes (2.6 cm at 300 Hz, $H = \lambda/40$) or even more [JIM 16a] with a 1.1 cm thick panel, 338 Hz ($H = \lambda/88$). Unlike other materials, this one works alone, without the need for a rigid wall to ensure zero transmission. The treated acoustic waves remain localized in the material, which makes it possible to obtain a zero reflection and transmission coefficient. In other words, this is a very good candidate for insulation applications too.

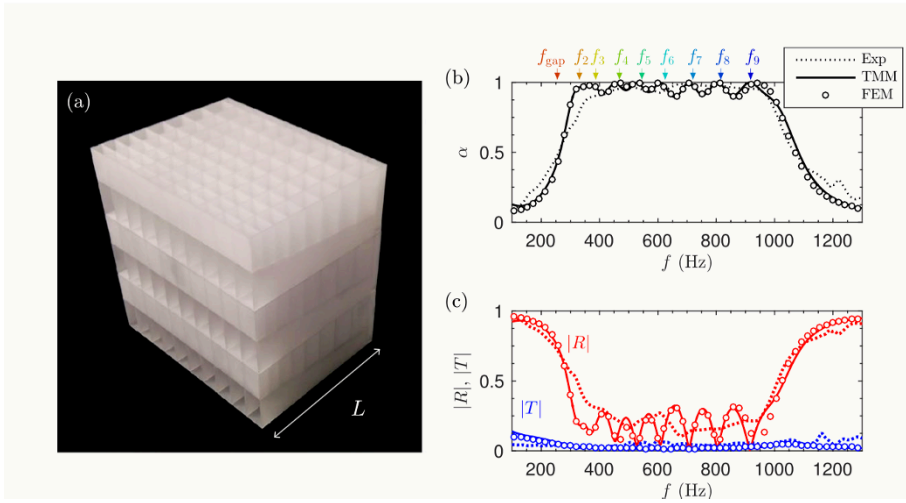

Figure 7.9. *(a) Photograph of the sample containing 10×3 unit cells. (b) Absorption obtained by using the TMM (solid line), by using FEM simulations (circles) and measured experimentally (dotted line). (c) Corresponding reflection (red curves) and transmission (blue curves) coefficients in amplitude [JIM 17]. For a color version of this figure, see www.iste.co.uk/romero/metamaterials.zip*

7.4. Transmission case

High transmission loss is usually achieved by using stiff and heavy materials. Two setups are widely used: homogeneous material panel or multilayered panels and in particular, double walls. The first one needs to have a high Young modulus and density (like concrete, for example), but this results in very heavy structures, which is not allowed in many cases. The second one exhibits bad low-frequency performances linked to the so-called mass-air-mass, or breathing frequency. This phenomenon is extremely strong and very difficult to attenuate. In this section, we will mention some

setup examples that can be used to substitute the regular walls/panels or that can be added inside the double panel to enhance the acoustic insulation.

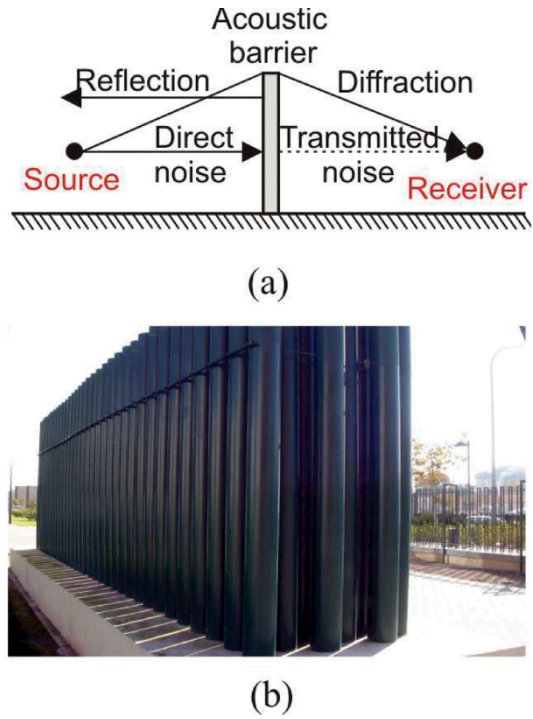

Figure 7.10. *(a) Performance of an acoustic barrier; (b) An example of a Sonic Crystal Acoustic Screen (SCAS) [SÁN 15]*

The most popular metamaterial device for transmission loss applications is the phononic crystal (see Figure 7.10), where Bragg's interferences create bandgaps. One of the most famous examples shows a bandgap in a cubic crystal made of rubber and lead spheres [LIU 00, SHE 03], showing subwavelength bandgaps compared to, for example, the sonic crystals, made of rigid cylinders in air. The frequency band of the bandgap of sonic crystals depends on the periodicity (in general $\lambda/2$) and on the filling fraction (between 0.4 and 0.6) [PHA 06]. These conditions imply (very) big scatterers and large periodicity to obtain low-frequency bandgaps. Even with a large sonic crystal, Bragg's interference bandgap does not cover all the frequency bands (50–4000 Hz), and the challenge is to create crystals with multiple bandgaps to enlarge the band of low transmission.

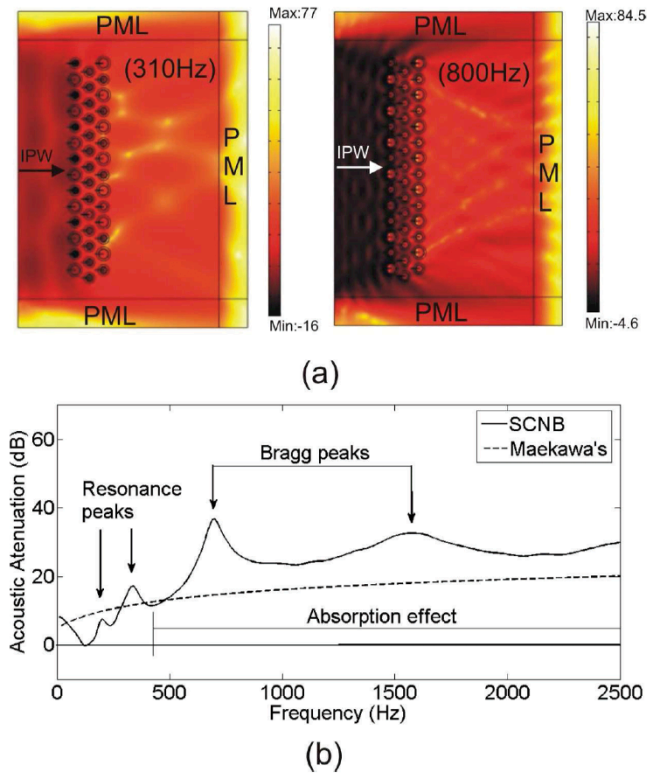

Figure 7.11. *Theoretical simulations: a) attenuation maps for 310 Hz, and 800 Hz, and b) attenuation spectrum (*$0\,\mathrm{deg}$ *incidence) measured 1 m behind the end of the SCAS [SÁN 15]. For a color version of this figure, see www.iste.co.uk/romero/metamaterials.zip*

Recent studies have shown locally multi-resonant sonic crystals [LAG 13a, KRY 11, ELF 11] with low-frequency bandgap due to resonant scatterers that cover a larger band, but the transmission outside the bandgap is still perfect. This is a real drawback when we consider industrial applications. Sonic crystal seems to only be suitable as a traffic noise barrier (too thick for an indoor application), but at the moment they act more like a bandpass filter. Psycho-acoustic studies should be interesting to see if those filtered noises can create an interesting acoustical environment or if they are unpleasant. Nevertheless, a sonic crystal barrier passed the certification for an outdoor acoustic screen [SÁN 15] and showed a significant attenuation between 500 and 2500 Hz, with an index of acoustic absorption $DL_R = 20$ dB, which corresponds to the B2 category (see Figure 7.11). This has

been made possible thanks to the use of multiphysical scatterers, composed of acoustic resonators (split-rings) coated with a combination of perforated plate and porous material [ROM 11, ROM 12]. A careful design of this kind of barriers can be achieved in order to build an efficient non-continuous barrier instead of the classical barriers for industrial application. Even though the crystal is quite thick (76 cm), it is suitable for aesthetic reasons in some town planning design.

For an indoor application, the membrane-type metamaterial seems to be very promising. The main advantage seems to be the good efficiency at a decent low frequency range for very thin membranes (usually less than 1 mm). This kind of metamaterial is usually a panel made of periodically arranged short-scale membranes that can act like resonators. It is also possible to control their resonance frequency by adding a mass at the center to create a mass-spring resonator [YAN 10, YAN 13]. The panel exhibits a maximum of transmission loss at the resonance frequency (see Figure 7.12) and by stacking multiple panels with different resonance frequencies, it is possible to obtain low transmission on all the frequency bands of interest (sound transmission loss (STL) around 40 dB from 50 to 4000 with a stack of four panels, about 1 cm thick). In comparison, a classic 10 cm thick double panel wall made of Gypsum and glass wool can have an STL between 40 and 58 dB Rw. It basically depends on the mass law and admits weaknesses at certain frequencies, as in the low frequency range with the mass-air-mass resonance [FAH 07]).

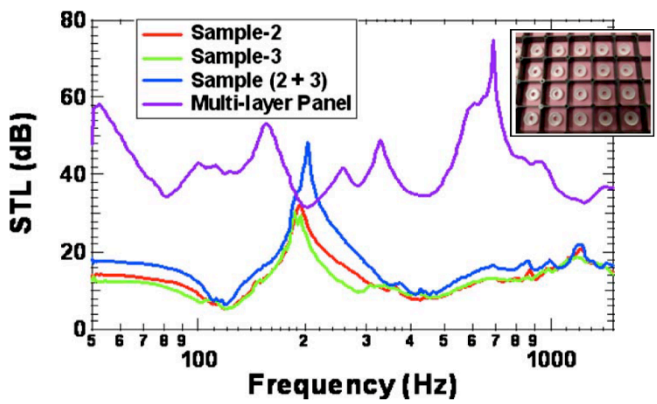

Figure 7.12. *The sound transmission loss (STL) spectra of two nominally identical single-layer samples (red and green curves), together with the STL spectrum measured from the stacking of the two samples (blue curve). The purple curve is the STL spectrum of a broadband shield consisting of four single-layer panels [YAN 10]. For a color version of this figure, see www.iste.co.uk/romero/metamaterials.zip*

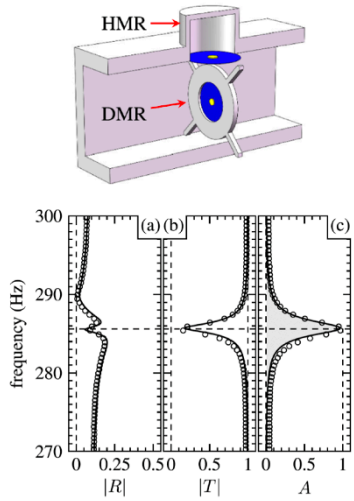

Figure 7.13. *Picture of the membranes inside an impedance tube. (a)–(c) indicate the reflexion, transmission, and absorption coefficients for the coupled membranes. Almost perfect absorption, reaching 99.2%, is seen at 285.6 Hz. The solid lines are from theory and the circles are from the experiments [YAN 15b]*

One of the main challenges of membrane-type metamaterials is obtaining a high efficiency of the membranes to overcome the mass or mass resonance and/or the mass law system. Nevertheless, it is shown that this kind of resonant device cannot reach 100% efficiency when they are used alone for transmission purposes. Pr. Ping Sheng's team are studying a method to obtain perfect absorption with membranes [YAN 15b], and 100% efficiency is only possible if two types of different resonators are coupled. As is shown in this work, a perfect absorption is obtained for a degenerate resonator, made of a simultaneous monopolar and dipolar resonator which is critically coupled (Figure 7.13). If this kind of critically coupled degenerated resonator can be developed to fit in a membrane panel, this metamaterial could be a serious substitute for a double panel.

The low-frequency behavior of the membrane seems to be an interesting feature that is visible on every study on small-scale membranes and allows the STL to be high before the first resonance frequency [YAN 13, NAI 10], whereas a mass law system begins at 0. This can be explained by a negative density induced by the membranes before the first resonance. The slope and the gain depend on both the dimensions and the characteristics of the membrane. The boundary conditions also play a crucial role in the membrane efficiency because it is important to create perfectly clamped boundary conditions on every membrane in order to obtain the exact numerical results. If the structure holding the membranes is not perfectly rigid, it can allow flexion and degrade the low-frequency behavior of the membrane metamaterial. This can cause a serious problem when the membrane metamaterial is used for large-scale application because the structure could allow low-frequency modes below the first frequency and the negative density would vanish [ANG 16]. If the holding structure is rigid enough,

the membrane metamaterial shows excellent experimental results in diffuse fields and can even be used inside a double panel structure [ANG 17] (+8 to 14 dB over several frequency bands from 200 to 800 Hz in comparison with the standard double panel). Vibro-acoustic metamaterial panels could also be a good candidate for transmission loss and can be developed for simple or double panel materials. They are based on the same resonance principle as the other metamaterials, but the resonant device uses the vibration to attenuate acoustic radiation [CLA 16]. This is possible by clamping a mass-spring-like resonator array directly on the panel to create bandgaps. This is very interesting from an industrial point of view because the wavelengths inside the panel are shorter than those in the air, which means that the resonant devices are also smaller. This principle has been tested on a real size and real condition double panel in diffuse field and shows the result of +4 dB Rw (Figure 7.14), which represents an enhancement of +4 to +10 dB over the frequency band 50 to 500 Hz [HAL 17].

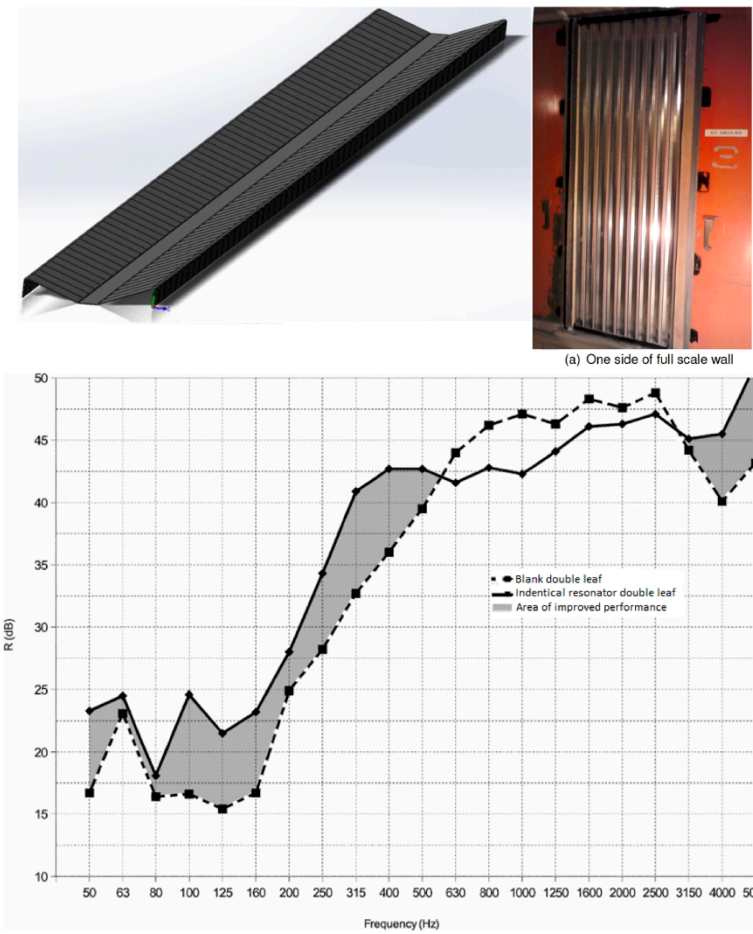

Figure 7.14. *Experimental TL in diffuse field for a vibro-acoustic metamaterial fixed against an inner face of a double panel wall [HAL 17]*

7.5. Concluding remarks

In this chapter, we wanted to highlight some studies among the existing literature. We restricted the review to audible acoustics and we discussed only a couple of different materials for the sake of clarity, but obviously, a number of other metamaterials are also very promising. Two different types of applications have been studied here, absorption and isolation metamaterials, both presenting subwavelength behavior due to the grating and local resonances. The low frequency aspect and the tunability of the whole structure are relevant for an industrial context, but technological barriers still exist. Metamaterials designers will deal with finite sample sizes and imperfect boundary conditions which will decrease their efficiency. In the case of acoustic treatment of a rigid plate (or double panel) for insulation, the plate modes play an important role in the frequency response and need to be taken into account in the simulations, but they are only visible for finite sizes. Furthermore, metamaterials have to be designed for diffuse fields for the industry, but a real diffuse field cannot be obtained with periodic simulations (one unit cell simulated with the Bloch–Floquet condition, for example) because a diffuse field is by definition a summation of the same amplitude waves with random angles and random phases uniformly distributed over the whole panel. A periodic condition will create a periodic field that does not satisfy the diffuse field condition. At the same time, finding finite-size and thin metamaterials with large absolute bandgap could be challenging, but the use of locally resonant scatterers can partially solve the problem. In general, they are not dependent on the source incidence and can admit small sizes for subwavelength behavior. This explains the renewal of study on Helmholtz resonator and on embedded resonator metamaterials. In this way, a recent trend shows new metamaterials with very smart design printed in 3D that show even better results. Even though the cost of such materials has drastically decreased over the past five years, will it one day be economically viable enough to compete with other solutions? The problem is, 3D printers cannot produce extra-large materials for now and it is very difficult to find a way to produce them with a standard industrial process. The ratio between acoustic efficiency and cost needs to be in accordance with the targeted market, and so important work has to be done to transfer the metamaterials from prototype to industrial product. This has to be done jointly between research/academic partners and the industry.

7.6. References

[ANG 16] Ang L.Y.L., Koh Y.K., Lee H.P., "Sound transmission loss of a large-scale meta-panel with membrane acoustic metamaterial", *Proceeding of ACOUSTICS*, p. 47, 2016.

[ANG 17] Ang L.Y.L., Koh Y.K., Lee H.P., "Broadband sound transmission loss of a large-scale membrane-type acoustic metamaterial for low-frequency noise control", *Applied Physics Letters*, vol. 111, no. 4, p. 041903, AIP Publishing, 2017.

[BOU 98] BOUTIN C., ROYER P., AURIAULT J., "Acoustic absorption of porous surfacing with dual porosity", *International Journal of Solids and Structures*, vol. 35, nos 34–35, pp. 4709–4737, Elsevier, 1998.

[BOU 13] BOUTIN C., "Acoustics of porous media with inner resonators", *The Journal of the Acoustical Society of America*, vol. 134, no. 6, pp. 4717–4729, ASA, 2013.

[CHA 91] CHAMPOUX Y., ALLARD J., "Dynamic tortuosity and bulk modulus in air-saturated porous media", *Journal of Applied Physics*, vol. 70, no. 4, pp. 1975–1979, AIP, 1991.

[CHE 16] CHEN W., LIU S., TONG L. *et al.*, "Design of multi-layered porous fibrous metals for optimal sound absorption in the low frequency range", *Theoretical and Applied Mechanics Letters*, vol. 6, no. 1, pp. 42–48, Elsevier, 2016.

[CLA 16] CLAEYS C., DECKERS E., PLUYMERS B. *et al.*, "A lightweight vibro-acoustic metamaterial demonstrator: Numerical and experimental investigation", *Mechanical Systems and Signal Processing*, vol. 70, pp. 853–880, Elsevier, 2016.

[ELF 11] ELFORD D.P., CHALMERS L., KUSMARTSEV F.V. *et al.*, "Matryoshka locally resonant sonic crystal", *ArXiv e-prints*, p. 1102.0399v1, February 2011.

[FAH 07] FAHY F.J., GARDONIO P., *Sound and Structural Vibration: Radiation, Transmission and Response*, 2nd edition, Academic Press, 2007.

[GRO 09] GROBY J.-P., WIRGIN A., DE RYCK L. *et al.*, "Acoustic response of a rigid-frame porous medium plate with a periodic set of inclusions", *The Journal of the Acoustical Society of America*, vol. 126, no. 2, pp. 685–693, ASA, 2009.

[GRO 11] GROBY J.-P., DAZEL O., DUCLOS A. *et al.*, "Enhancing the absorption coefficient of a backed rigid frame porous layer by embedding circular periodic inclusions", *The Journal of the Acoustical Society of America*, vol. 130, no. 6, pp. 3771–3780, ASA, 2011.

[GRO 15] GROBY J.-P., LAGARRIGUE C., BROUARD B. *et al.*, "Enhancing the absorption properties of acoustic porous plates by periodically embedding Helmholtz resonators", *The Journal of the Acoustical Society of America*, vol. 137, no. 1, pp. 273–280, ASA, 2015.

[HAL 17] HALL A., DODD G., CALIUS E., "Diffuse field measurements of locally resonant partitions", *Proceedings of ACOUSTICS*, vol. 2017, 2017.

[ISO 03] ISO, 354:2003, Acoustics – Measurement of sound absorption in a reverberation room, British Standards Institution, 2003.

[JIM 16a] JIMÉNEZ N., HUANG W., ROMERO-GARCÍA V. *et al.*, "Ultra-thin metamaterial for perfect and quasi-omnidirectional sound absorption", *Applied Physics Letters*, vol. 109, no. 12, p. 121902, AIP Publishing, 2016.

[JIM 16b] JIMÉNEZ N., ROMERO-GARCÍA V., CEBRECOS A. *et al.*, "Broadband quasi perfect absorption using chirped multi-layer porous materials", *AIP Advances*, vol. 6, no. 12, p. 121605, AIP Publishing, 2016.

[JIM 17] JIMÉNEZ N., ROMERO-GARCÍA V., PAGNEUX V. *et al.*, "Rainbow-trapping absorbers: Broadband, perfect and asymmetric sound absorption by subwavelength panels for transmission problems", *Scientific Reports*, vol. 7, no. 1, p. 13595, Nature Publishing Group, 2017.

[JIN 16] JINGFENG N., GUIPING Z., "Sound absorption characteristics of multilayer porous metal materials backed with an air gap", *Journal of Vibration and Control*, vol. 22, no. 12, pp. 2861–2872, SAGE Publication, 2016.

[JOH 87] JOHNSON D., KOPLIK J., DASHEN R., "Theory of dynamic permeability and tortuosity in fluid-saturated porous media", *Journal of Fluid Mechanics*, vol. 176, no. 1, pp. 379–402, Cambridge University Press, 1987.

[JUN 07] JUNG S.S., KIM Y.T., LEE D.H. *et al.*, "Sound absorption of micro-perforated panel", *Journal of the Korean Physical Society*, vol. 50, no. 4, pp. 1044–1051, Korean Physical Society, 2007.

[KRY 11] KRYNKIN A., UMNOVA O., CHONG A. *et al.*, "Scattering by coupled resonating elements in air", *Journal of Physics D: Applied Physics*, vol. 44, no. 12, p. 125501, IOP Publishing, 2011.

[LAG 13a] LAGARRIGUE C., GROBY J.-P., TOURNAT V., "Sustainable sonic crystal made of resonating bamboo rods", *The Journal of the Acoustical Society of America*, vol. 133, no. 1, pp. 247–254, ASA, 2013.

[LAG 13b] LAGARRIGUE C., GROBY J.-P., TOURNAT V. *et al.*, "Absorption of sound by porous layers with embedded periodic arrays of resonant inclusions", *The Journal of the Acoustical Society of America*, vol. 134, no. 6, pp. 4670–4680, ASA, 2013.

[LAG 16] LAGARRIGUE C., GROBY J.-P., DAZEL O. *et al.*, "Design of metaporous supercells by genetic algorithm for absorption optimization on a wide frequency band", *Applied Acoustics*, vol. 102, pp. 49–54, Elsevier, 2016.

[LIU 00] LIU Z., ZHANG X., MAO Y. *et al.*, "Locally resonant sonic materials", *Science*, vol. 289, no. 5485, pp. 1734–1736, American Association for the Advancement of Science, 2000.

[NAI 10] NAIFY C.J., CHANG C.-M., MCKNIGHT G. *et al.*, "Transmission loss and dynamic response of membrane-type locally resonant acoustic metamaterials", *Journal of Applied Physics*, vol. 108, no. 11, p. 114905, AIP, 2010.

[OLN 03] OLNY X., BOUTIN C., "Acoustic wave propagation in double porosity media", *The Journal of the Acoustical Society of America*, vol. 114, no. 1, pp. 73–89, ASA, 2003.

[PHA 06] PHANI A., WOODHOUSE J., FLECK N., "Wave propagation in two-dimensional periodic lattices", *The Journal of the Acoustical Society of America*, vol. 119, p. 1995, 2006.

[ROM 11] ROMERO-GARCÍA V., SÁNCHEZ-PÉREZ J.V., GARCIA-RAFFI L.M., "Tunable wideband bandstop acoustic filter based on two-dimensional multiphysical phenomena periodic systems", *Journal of Applied Physics*, vol. 110, no. 1, p. 014904, 2011. Available at: https://doi.org/10.1063/1.3599886.

[ROM 12] ROMERO-GARCÍA V., CASTINEIRA-IBANEZ S., SÁNCHEZ-PÉREZ J. *et al.*, "Design of wideband attenuation devices based on sonic crystals made of multi-phenomena scatterers", *Proceedings of the Acoustics 2012 Nantes Conference*, 2012.

[SAK 10] SAKAGAMI K., YAMASHITA I., YAIRI M. *et al.*, "Sound absorption characteristics of a honeycomb-backed microperforated panel absorber: Revised theory and experimental validation", *Noise Control Engineering Journal*, vol. 58, no. 2, pp. 157–162, Institute of Noise Control Engineering, 2010.

[SÁN 15] SÁNCHEZ-PÉREZ J.V., MICHAVILA C.R., GARCÍA-RAFFI L.M. *et al.*, "Noise certification of a sonic crystal acoustic screen designed using a triangular lattice according to the standards EN 1793 (-1;-2;-3)", *Eur EuroNoise 2015*, EuroNoise, p. 2357, 2015.

[SHE 03] SHENG P., ZHANG X., LIU Z. *et al.*, "Locally resonant sonic materials", *Physica B: Condensed Matter*, vol. 338, nos 1–4, pp. 201–205, Elsevier, 2003.

[TAN 06] TANNEAU O., CASIMIR J., LAMARY P., "Optimization of multilayered panels with poroelastic components for an acoustical transmission objective", *The Journal of the Acoustical Society of America*, vol. 120, no. 3, pp. 1227–1238, ASA, 2006.

[TOU 04] TOURNAT V., PAGNEUX V., LAFARGE D. *et al.*, "Multiple scattering of acoustic waves and porous absorbing media", *Physical Review E*, vol. 70, no. 2, p. 026609, APS, 2004.

[WAN 11] WANG C., HUANG L., "On the acoustic properties of parallel arrangement of multiple micro-perforated panel absorbers with different cavity depths", *The Journal of the Acoustical Society of America*, vol. 130, no. 1, pp. 208–218, ASA, 2011.

[WEI 16] WEISSER T., GROBY J.-P., DAZEL O. *et al.*, "Acoustic behavior of a rigidly backed poroelastic layer with periodic resonant inclusions by a multiple scattering approach", *The Journal of the Acoustical Society of America*, vol. 139, no. 2, pp. 617–629, ASA, 2016.

[YAN 10] YANG Z., DAI H., CHAN N. *et al.*, "Acoustic metamaterial panels for sound attenuation in the 50–1000 Hz regime", *Applied Physics Letters*, vol. 96, no. 4, p. 041906, AIP, 2010.

[YAN 13] YANG M., MA G., YANG Z. *et al.*, "Coupled membranes with doubly negative mass density and bulk modulus", *Physical Review Letters*, vol. 110, no. 13, p. 134301, APS, 2013.

[YAN 15a] YANG J., LEE J.S., KIM Y.Y., "Metaporous layer to overcome the thickness constraint for broadband sound absorption", *Journal of Applied Physics*, vol. 117, no. 17, p. 174903, AIP Publishing, 2015.

[YAN 15b] YANG M., MENG C., FU C. *et al.*, "Subwavelength total acoustic absorption with degenerate resonators", *Applied Physics Letters*, vol. 107, no. 10, p. 104104, AIP Publishing, 2015.

[YAN 16] YANG J., LEE J.S., KIM Y.Y., "Multiple slow waves in metaporous layers for broadband sound absorption", *Journal of Physics D: Applied Physics*, vol. 50, no. 1, p. 015301, IOP Publishing, 2016.

8

Elastic Metamaterials for Radiofrequency Applications

Micro-electromechanical components harnessing the propagation of elastic waves at frequencies in the GHz range have become ubiquitous in radio frequency (RF) systems. The most popular of these systems are mobile phones, initially developed for human-to-human communication with the first GSM phones in the late 1990s. Successive generations of communication systems have since then evolved towards an increasing amount of machine-to-machine data exchange. The fifth generation of mobile communication system (5G), whose deployment is expected in the 2020s, is heralded as the one delivering broadband Internet access to every wirelessly connected device. In such purely electrical systems, elastic wave resonant cavities have successfully established a niche in providing miniature, low loss, and fully passive resonators, which are used as frequency selection components in electronic circuits. Such elements are building blocks of low-loss band-pass filters, which in turn are key elements of the analog stages of radiofrequency transceivers, whose function is to select only the relevant portions of the radio spectrum and maintain noise levels for radio receivers to extremely low levels in order to ensure a high sensitivity.

This requirement for ever-increasing filtering capabilities over the tiniest possible fingerprint has quite naturally led the phononic crystal research community to pay some interest to a potential transposition of the concepts related to phononic crystals, or, to a lower extent, to elastic metamaterials one radio frequencies. The demonstrations in the audible or ultrasonic range of filters, waveguides or even multiplexers suggest the possibility of implementing advanced signal processing functionalities over *phononic chips*, mirroring similar developments in photonics. This process was significantly made easier by the already acute understanding of

Chapter written by Sarah BENCHABANE and Alexandre REINHARDT.

Fundamentals and Applications of Acoustic Metamaterials: From Seismic to Radio Frequency,
First Edition. Edited by Vicente Romero-García and Anne-Christine Hladky-Hennion.

dispersion engineering and Bragg band gaps in one-dimensional structures by RF filter designers. The use of periodical structures in electro-acoustic devices had a long and fruitful history already. To quote but a few examples, surface acoustic wave (SAW) transducers and reflectors rely on periodical arrays of metal electrodes fulfilling the Bragg condition and the mature solidly mounted bulk acoustic wave resonators (SMR) use a stack of alternating layers of materials with contrasting elastic constant and mass densities to confine bulk waves in a piezoelectric thin film.

The question was then to demonstrate the existence of two-dimensional and three-dimensional band gaps in the radiofrequency range, and investigate how the specific features of these *hypersonic phononic crystals* – as an increasing part of the community dubbed them – could lead to a significant conceptual and technological breakthrough that would make it possible to reach performances far beyond of the highly robust, firmly established high-frequency SAW and bulk acoustic wave (BAW) devices. Once this objective was established, works were undertaken to investigate elastic wave propagation features at a fundamental level (such as hypersonic crystals) plus proposed structures mimicking the operation of conventional radiofrequency devices used in RF electronics or in photonics, with the open goal to develop the field of *phononics*. Over time, this hype dissipated until the idea of phononic structures spread through the micro-electromechanical systems (MEMS) community, which is now proposing more practical use of the associated concepts as building blocks for their components. Following this resurgence, this field of higher-frequency phononics is re-evaluated in the numerous disciplines of physics and engineering fundamentally concerned with controlling small-wavelength elastic waves, or even phonons, in any potentially vibrating structures. This encompasses NEMS, optomechanics, microfluidics, thermal transport, or even quantum information.

This chapter proposes to go through the rather brief history of hypersonic phononic crystals, emphasizing attempts to apply the related concept to radiofrequency applications. As a starting point, section 8.1 will highlight the characteristics of elastic waves propagating at frequencies in the GHz range and account how these distinctive features have contributed to their undeniable success in wireless telecommunication applications. Then, section 8.2 will discuss the peculiarities of the fabrication of micron-sized structures and will shed light on the technological breakthroughs, which have been necessary to realize the first hypersonic phononic crystals. Elaborating on the specificities of these hypersonic crystals, section 8.3 will present early works taking inspiration from photonics or from the microwave world and will discuss why a direct transposition of these concepts to elastic wave RF components does not prove profitable. In contrast, section 8.4 will present examples of adoption of phononic crystals by the MEMS or the photonics community, where these structures bring an added value compared to

more established building blocks. Finally, a short conclusion will discuss the perspectives towards potentially interesting applications of hypersonic metamaterials.

8.1. Hypersonic elastic waves and their applications

Hypersound, sometimes also referred to as *microsound*, can be defined as elastic waves propagating at frequencies ranging from a few hundreds of MHz to a few tens of GHz, although a definite agreement on the exact frequency limits of this rather recently introduced regime has yet to be reached. In this frequency range, propagation of acoustic waves in fluids such as water, or air over significant distances (i.e. more than several micrometers) becomes difficult due to viscous losses. Hypersonic wave propagation is therefore usually restricted to solid media or to very confined microfluidic cavities. Typical wavelengths are then in the range of a few tens of micrometers down to some hundreds of nanometers. At this scale, material defects such as grain boundaries, dislocations or even interface roughness remain usually small enough to prevent the scattering or diffusion phenomena encountered for thermal phonons at THz frequencies. Hypersonic waves can thus propagate over fairly large distances, and their mathematical and physical description remains within the frame of the classical theory of elastic wave propagation in solids [CUF 12], meaning that interactions with the quasi-particles of the propagating medium can be neglected.

As shown in Figure 8.1, the frequency range for hypersound coincides with the part of the electromagnetic spectrum used for most radio transmissions. Operation of these systems in the MHz to GHz range is motivated by the fact that electromagnetic waves exhibit rather long propagation distances in free air (up to a few kilometers) at these frequencies, as the absorption by gases in the atmosphere remains relatively low. While the lower end of the spectrum, in the 100–400 MHz range, is mostly used for broadcasting signals such as frequency modulated (FM) radio or television signals, the 400 MHz–3.5 GHz range is now almost fully exploited for mobile communication systems, with some specific applications such as military, sensor systems or even microwave ovens interspersed in between the allocated frequency regions. In this range, radio signal carrier frequencies are high enough to ensure that relative bandwidths remain large enough to offer wireless communication systems satisfying data rates.

If electromagnetic (EM) waves are obviously unmatched as an information carrier, the basic law stating that the characteristic dimension of a filter is comparable to the carrier wavelength prohibits the integration of EM filters in hand-held devices. As hypersonic waves exhibit wavelengths smaller by a factor of 10^5 than electromagnetic waves with the same frequencies, it has early been suggested that a significant size reduction could be achieved for some signal processing devices by manipulating elastic waves in solids, instead of electromagnetic waves. From the

1970s to the 1990s, a large host of surface acoustic wave components such as resonators, filters, delay lines and identification tags were first demonstrated and then came into mass production to propose miniaturized analog electronic signal processing devices [MOR 07]. Nowadays, most of these components have been replaced by numerical data processing systems, due to progress in high-speed computing circuits. Yet, the sensitivity requirements of the current telecommunication standards impose being able to sample high-frequency signals with enough resolution to be able to detect a weak useful signal received from a base station positioned kilometers away from the receiver. This would not be disturbed by strong interferers and may be located in close proximity to the mobile phone. This operation can certainly be achieved by numerical signal processing, at the expense, however, of electrical power consumption. Such a trade-off is clearly not acceptable for implementation in mobile handsets and radio signals are, therefore, still processed by analog circuits that filter the RF signal before amplifying and frequency down-convert it before digitizing. Modern data transmission circuits hence remain dependent on analog band-pass filters made of miniature acoustic resonators, and their number is even increasing as the radiofrequency spectrum becomes increasingly fragmented. Options such as carrier aggregation[1] or multiple-in-multiple-out (MIMO) antennas capable of performing electromagnetic beam-forming[2], which will both be deployed in the fifth generation of mobile communications will even require a further increase in the number of acoustic components in a radiofrequency front-end [YOL 17].

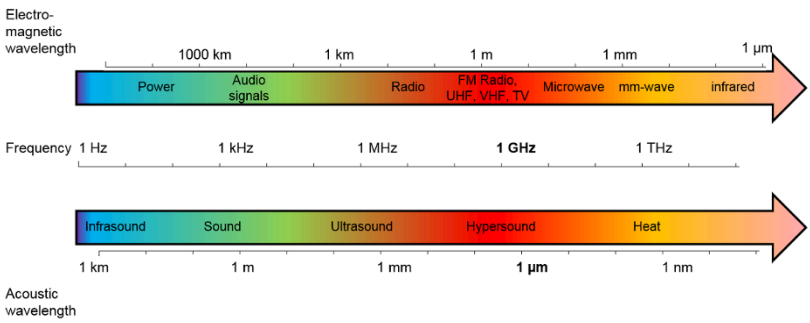

Figure 8.1. *Domains for acoustic and electromagnetic waves and comparison of their respective frequency and wavelength scales . For a color version of this figure, see www.iste.co.uk/romero/metamaterials.zip*

1 Splitting the RF signal bandwidth over several carrier frequencies for a more efficient usage of the fragmented spectrum.

2 Enabling spatial filtering and, therefore, allowing simultaneous usage of the same portion of the spectrum by multiple users at different positions with respect to the same base station.

Replacing the propagation of electromagnetic waves by elastic waves, however, requires an efficient way to transduce an electrical signal into acoustic waves and vice versa. Perhaps the most efficient and, incidentally, the first transduction mechanism historically used is piezoelectricity: a voltage carrying a signal can be transformed into strain exhibiting the same time dependence through the converse piezoelectric effect; this produces an elastic wave that propagates in the piezoelectric material and gets manipulated by the geometrical features of the device. The generated wave usually propagates up to a set of receiving electrodes where the stress fields generated by the wave cause, due to the direct piezoelectric effect, the appearance of time-varying electrical charges, that is, of a current transporting the processed signal. Electrostatic, electrostrictive or magnetostrictive transduction mechanisms are sometimes also used, but these are usually weaker effects and require bias voltages or magnetic fields to operate, while piezoelectric devices remain fully passive. The simplest application of this concept is a delay line, illustrated in Figure 8.2: two bulk acoustic wave transducers made of zinc oxide (ZnO) piezoelectric films sandwiched between two electrodes are used, respectively, to launch and detect elastic waves. In between, the propagation medium is a sapphire rod (Al_2O_3) whose function is only to allow for a propagation distance long enough to delay the transmitted signal compared to a direct transmission of an electric signal. Most delay lines used in signal processing circuits, such as early radar systems or even analog television receivers, make use of surface acoustic waves (SAWs). SAWs correspond to vibrations guided along the surface of a semi-infinite substrate with an amplitude decaying exponentially away from the surface. Depending on the considered propagating half-space, waves with different characteristics (velocities, polarizations, etc.) can be encountered. Rayleigh waves are probably the most well-known form of surface waves. These sagittally polarized, dispersion-less and theoretically loss-less waves (provided, of course that the substrate itself does not exhibit significant intrinsic losses or structural defects) have been in use since the 1960s. The main advantage of surface waves is their intrinsic sensitivity to whatever occurs at the surface of the substrate. This basically means that it is possible to access and control directly the wave propagation path using planar structures. A key element in the development of SAW devices is the invention of the so-called *interdigital transducer* (IDT) by White and Voltmer in 1965 [WHI 65] and their association with high-quality single crystal bulk substrates that allowed easily generating and using cheap lithography techniques inherited from the microelectronics industry, which will be described in further detail in section 8.2.1. Interdigital transducers consist of a periodical arrangement of metal electrodes, alternately connected to two bus bars used to convey an electrical potential. A basic surface-wave delay line is illustrated in Figure 8.2(b).

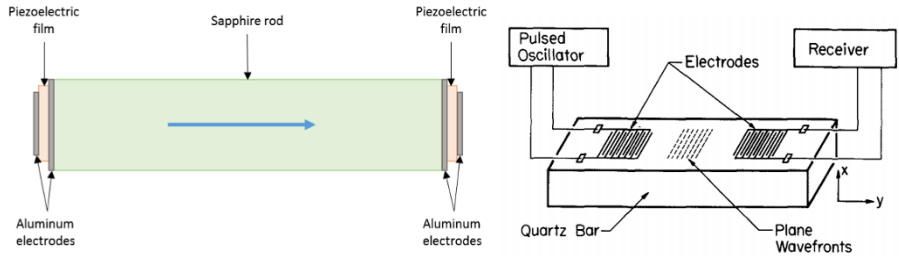

Figure 8.2. *Example of delay lines: (a) bulk acoustic wave delay line and (b) surface acoustic wave delay line. Reprinted from [WHI 65], with the permission of AIP Publishing*

For a given material, elastic wave propagation mode and structure, we define an *electromechanical coupling factor*, which corresponds to the ratio of power transferred from one domain (electrical or mechanical) to the other during one wave period. At most, this coefficient can reach 90% in high-performance piezoelectric ceramics [YAM 08]. Material losses of such ceramics are however prohibitive when operating at frequencies higher than a few MHz, hence preventing their use in RF communication devices. Single-crystal materials, such as quartz, lithium niobate or lithium tantalate, are a more well-suited alternative. In principle, electromechanical coupling factors of the order of 50% can be reached for lithium niobate or lithium tantalate, but the combination of substrate orientation and propagation mode suited for practical applications usually limits the coupling factors to below 10% [DEF 01]. This means that only a similar fraction of the signal can be efficiently processed and transformed back at the output of the signal processing component, leading to components exhibiting insertion losses in excess of 20 dB. Such a situation can not be tolerated as modern telecommunication systems require very weak signals to be processed with minimal attenuation (current filters used in the mobile phone industry require 1 dB loss only, 2 dB maximum). To overcome the limitation imposed by the relatively small electromechanical coupling factor, structures have been made resonant: since only a fraction of the power can be transduced during one wave period, power is accumulated over many periods up to the point of equilibrating the power inputs with losses within the resonant structure. In the case of surface waves, resonators can be obtained by encompassing an interdigital transducer in between two reflectors, simply built by depositing another periodical array of metal strips, usually referred to as *reflective grating*, as shown in Figure 8.3(a). Efficient reflection occurs when the pitch of the grating equals half the wavelength, that is, at the Bragg condition. The reflection coefficient per strip is, however, quite low (usually in the range of 1–4%), as reflection occurs because of the association of a strong modulation of the electrical boundary conditions with a weak perturbation of the mechanical conditions. Thus, SAW reflectors are usually made of close to 100

short-circuited electrodes. In the case of BAW resonators, relying on a thickness mode resonance, the most simple structure (although when it comes to microfabrication, things get more complex) is to form a freestanding membrane of piezoelectric material, since the air/solid interface provides a nearly perfect reflector. Hence, such a structure, shown in Figure 8.3(b), is now referred to as a *film bulk acoustic resonator* (FBAR). Due to structural strength concerns, an alternative structure relying on positioning the piezoelectric film atop an acoustic one-dimensional Bragg mirror, as sketched in Figure 8.3(c), is also industrially employed, and is referred to as *solidly mounted resonator* (SMR). Despite continuous work on more exotic structures, the industrial landscape for RF elastic wave devices is now almost fully filled with these SAW or BAW resonators only, and this situation has settled to this state since the early 2000s, with only incremental improvement since then.

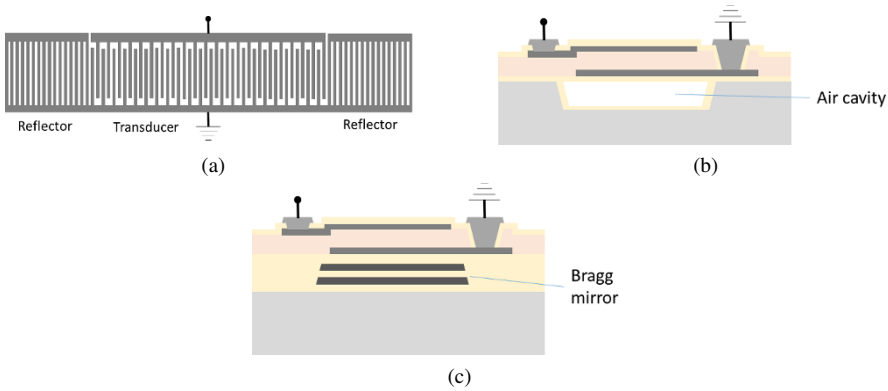

Figure 8.3. *Main resonator types used in the RF filter industry: (a) SAW resonator, (b) FBAR and (c) SMR.*

8.2. Hypersonic crystals

When the first experimental demonstrations of the occurrence of phononic band gaps were reported in the late 1990s for audible frequencies, it became quite clear that the concept could be applied to perform advanced signal processing. The first articles reported in the literature obviously dealt with structures operating in the sonic or ultrasonic regime because of their relative ease of fabrication, hence echoing the early days of photonic crystals in the microwave regime. As stated in the introduction, the so-called hypersonic regime refers to operating frequencies in the range of 100 MHz to a few GHz. In solids, this leads to characteristic dimensions of the order of the micrometer. The transposition of the phononic crystal concept to higher frequencies, where applications are potentially numerous, then has to overcome technological issues inherent to patterning at the micron scale. In addition, practical implementation

calls for compact and efficient devices, ideally based on the preferred solution for the realization of acoustic-based RF wireless devices – exploiting the piezoelectric effect observable in well-chosen substrate. A typical hypersonic crystal could therefore be:

– a micron-scale device;

– an electromechanical device, with an electrical to mechanical transduction (and conversely) ideally induced by piezoelectricity;

– a device able to perform a specific function (a resonator, a band-pass filter, etc.);

– a device that could be fabricated using large-scale processes.

In summary, an RF phononic device is a micro-electromechanical system (MEMS).

The most natural way to produce phononic crystals in this length scale is therefore to rely on classical cleanroom technologies, as is the case for conventional RF electro-acoustic devices. The difficulties that are to be faced are then similar: as a general rule, MEMS design is as strongly driven by the functions and operations it should fulfill as it is by the constraints and tolerances imposed by the manufacturing process.

In this section, we will briefly introduce some typical microfabrication techniques that have proved relevant for phononic crystal fabrication. We will then find how a hypersonic crystal design can be tied to the associated technological constraints. The last part of this section will then give practical examples reported in the literature of phononic crystals exhibiting frequency band gaps in the sub-GHz to GHz frequency range.

8.2.1. *Micron-scale fabrication*

8.2.1.1. *A short note on MEMS fabrication processes*

MEMS technology directly derives from the technological processes developed for the microelectronics industry. Yet, while integrated circuits (IC) are essentially planar devices making use of a limited number of materials, MEMS devices usually make use of whatever materials and geometries required to achieve the desired functionality. This leads to what can be considered as a major strength, as well as one of the main complications of the MEMS technology: the possibility to put together a variety of processes and materials to create very versatile devices exhibiting a potentially rich physics. This is at the expense, however, of a certain amount of predictability in the fabrication process and on the device operation. It could be said that the main key for a successful manufacturing of a MEMS device lies in an awareness of what can

be achieved in the context of a robust and repeatable process to find the better trade-off between ideal design and actual fabrication, (including the inevitable uncertainties related to some material properties).

There exists a very wide variety of microfabrication processes. This chapter does not aim at covering them in detail: specific resources will fulfill this function in a much better and more exhaustive manner. Here are no standard fabrication for MEMS devices, and this assertion is all the more true in the case of phononic crystals, as phononic devices are at a very early stage. Still, we will try here to give a rough idea of some of the technologies that may be involved.

As we mentioned earlier in this chapter, the MEMS technology finds its roots in the planar processes used in the microelectronics industry. Here as well, as for integrated circuits, the idea is to find simple, large-scale fabrication processes for devices with features that are bound to made ever smaller over time. A MEMS fabrication process can be described as the implementation of a sequence of basics steps, combined and potentially repeated many times over a substrate.

A MEMS fabrication process involves two main process families. The first relates to the so-called *front-end*, that is, to cleanroom-related process steps; the second to the *back-end*, that is, to the packaging of the fabricated device.

The substrate is ideally a commercial wafer, that is, a thin, polished slice of a specific material with a diameter of a few inches, up to 400 mm, for the currently most advanced nanoelectronics fabrication lines. The most conventional wafer dimensions are 300 mm for nanoelectronics, 200 mm for power electronics or silicon MEMS and 100 mm for more exotic substrate materials (typically the piezoelectric materials used in the SAW industry), with a recent trend for the latter to increase diameters towards 150 mm. Silicon obviously dominates the MEMS technological world, a significant number of reliable processes having been developed over the years on this semiconducting substrate in the context of microelectronics. Yet, it is not the preferred material for electro-acoustic devices that require piezoelectricity. In the surface acoustic wave industry, single-crystal piezoelectric substrates such as quartz, lithium niobate or lithium tantalate dominate the market. Single-crystal materials are usually grown from an ultrapure material source through the so-called Czochralski method, although other efficient means of artificial synthesis have been developed over the years. Quartz, for instance, is grown using hydrothermal methods proposed in 1905, that have been gradually improved over the years. This has allowed the synthesis and mass production of artificial crystals exhibiting the same properties as natural crystals as early as the 1970s. These processes lead to *boules* that are subsequently sliced along precisely defined crystal orientations and then surface-polished.

The key aspect of the front-end fabrication flow lies in the possibility to transfer a desired pattern onto this substrate at the micron scale. This pattern transfer may occur

by direct milling of the substrate, but as a much more general rule, pattern transfer is achieved indirectly by means of *surrogate layers* that can be easily shaped and subsequently removed (in other words, sacrificed) after transferring the pattern onto the wafer.

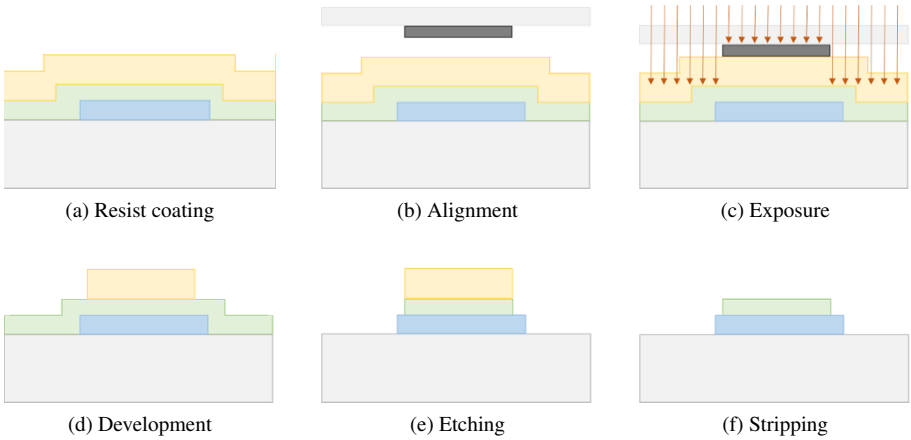

Figure 8.4. *Generic process sequence for photolithography. For a color version of this figure, see www.iste.co.uk/romero/metamaterials.zip*

Lithography is the generic process used to shape such surrogate layers. This process is a direct inheritance of the techniques used in the printing industry in the 19th century. In MEMS fabrication processes, its principle is to apply the following steps to a substrate, illustrated in Figure 8.4:

1) *Resist coating*: the substrate is coated with a polymer film, called a *resist*. This coating is made thin (100 nm–10 μm) and highly uniform by spreading it over the whole sample area by centrifugation. Variations of these techniques involve spraying a mist of photoresist over the wafer – which is particularly an efficient means to obtain a coating made of a particularly low-viscosity photoresist (known as *spray coating*); dipping the substrate in a highly viscous photoresist, therefore leaving usually a thick coating (known as *dip coating*) or laminating a solid polymer film over the substrate. This last technique is particularly useful when the wafer already contains mobile microstructures that could be destroyed by the surface tension forces brought by any liquid coming in contact with them. After coating, the photoresist is left drying for a few minutes on a hot plate to evaporate excess solvents and leave an almost solid film.

2) *Alignment*: the coated substrate is then aligned with a so-called *photomask*, which is usually a transparent [MAD 02] quartz (or some low-thermal-expansion glass) plate covered by a thin sheet of chromium, patterned in the shape of the structure

we want to transfer to the substrate (or sometimes in the shape of the inverse image of these structures). The substrate is positioned under the mask, so that mask patterns, which will be ultimately photolithographically reproduced, are aligned over already existing structures on the substrate: the first pattern transferred to a wafer usually includes a set of alignment marks that are used as a reference for subsequent process steps. The most advanced lithography tools benefit from automated alignment, which relies on machine pattern recognition and offer positioning precisions (*registrations*) typically in the 100–300 nm range.

3) *Exposure*: the substrate and the mask are then irradiated. In contact lithography, the photomask is put in direct contact with the wafer using a *contact aligner*. This is a rather inexpensive and very mature technology that allows reaching resolution below 1 μm. This is well within the requirements of most MEMS fabrication processes, but clearly below the requirements of modern SAW devices. The industrial alternative is then to use *projection lithography*, more precisely *stepper lithography* that presents the advantage of reducing mask wear by avoiding direct contact with the substrate and that allows, in the case of stepper lithography, us to reduce the projected mask pattern using a highly complex high-resolution lens system, hence allowing us to both reduce the constraints on mask fabrication and reach much higher resolution (down to 250 nm). In all cases, the chromium patterns shadow the UV irradiation, while in non-protected areas, the irradiation triggers chemical reactions in the resist that locally change its chemical properties. The simplest irradiation source is a light bulb, although ultraviolet (UV) light is preferred for its shorter wavelength and therefore smaller diffraction limit. Advanced lithography relies on deep-ultraviolet (deep-UV) light sources. As an alternative for very-high-resolution features, we can mention the possibility to use electron-beam lithography, based on electron irradiation of an appropriate resist. This last technique is mask-less, with a highly focused electron beam (down to nanometer size) being moved across the sample and alternatively switched on or off to directly draw patterns without the need to supply a mask. The drawback is the long time needed to perform a high-resolution scan over a full wafer, compared to an illumination of the whole area at once. Therefore, it is only employed for the most size-critical process steps, such as drawing nanometer-size transistor gates in advanced nanoelectronics.

4) *Development*: the substrate is then bathed in a chemical solution capable of dissolving the resist that has been chemically modified during the previous exposure step. This leaves the non-irradiated areas unaffected, causing a transfer of the chromium patterns on the photoresist film. The photoresist is then chemically stabilized by a second baking at a larger temperature than the drying step.

5) *Pattern transfer*: the pattern hosted by the photoresist is then transferred on the wafer, for example, by etching. The substrate is subjected to a chemical or physical process capable of etching the material exposed at the surface of the substrate, in the regions not protected by the photoresist patterns. This process may be a dissolution of the material by a chemical reaction occurring in liquid phase (so-called *wet etching*) or

sometimes in gaseous phase. Common techniques involve also some ion bombardment (gathered under the term *dry etching*), where the kinetic energy of accelerated ions is used to eject matter from the surface. Ion etching techniques are often assisted by some chemical reactions occurring on the surface between highly reactive ionized species formed in the plasma and the materials located on the substrate. This technique is therefore known as *reactive ion etching*. In both cases, the photoresist can act as a protection for parts of the substrate, so that patterns that were located on the mask are ultimately transferred on the substrate.

6) *Stripping*: after etching, the photoresist patterns are removed by a chemical dissolution of the polymer, leaving a substrate ready for restarting the next photolithography cycle.

The cumulation of material deposition steps, lithography and etching, makes up close to 90% of a MEMS integration process. Performing them in sequence can produce relatively complex three-dimensional structures while using mostly planar techniques. The strength of these techniques is that they are applied on a full substrate at a time, while the objects fabricated can be extremely small, so that a large number of them can be fabricated collectively. Hence, cleanroom processes are referred to as *very-large-scale integration* (VLSI). As an illustration, BAW filters typically occupy an area smaller than 1 mm^2, while fabricated on 200 mm diameter silicon substrates. A single fabrication sequence can therefore simultaneously produce more than 25,000 individual components per wafer.

8.2.1.2. *Design rules*

Despite their versatility, cleanroom fabrication processes do not allow every geometry to be produced. Therefore, the design of micron-sized structures such as phononic crystals has to always respect *design rules*, which dictate what can be fabricated and often impose limitations to the type of structures we would like to fabricate.

Design rules for micron-scale phononic structures, such as holey phononic crystals, originate from the two fabrication process conditions we covered in the previous section:

1) photolithography processes, as precise as they may have become when one considers large-scale integration of nanoelectronic circuits, always face a resolution limit. Even though the latest equipment are nowadays capable of generating nanometer-scale features using electronic beam writing or deep-UV immersion scanners, such tools cannot (yet) be considered as mainstream for phononic applications, as their cost remains prohibitive for anything else than advanced microelectronics, not to mention about academic laboratories. Therefore, it is more reasonable considering working with less expensive equipment, which offer resolutions dictated by the diffraction limit of UV or deep-UV, – that is, in the range

of 250 nm in the most favorable case. Additionally, the selectivity of the etching processes (that is, the ratio between the removal rate of the material we want to etch and the removal rate of the photoresist mask) requires that in order to form features with thicknesses or depth in the micron range, a photoresist coating of the same order of magnitude becomes necessary. Generally, the ultimate resolution that can be achieved with a photoresist mask is roughly in the same range as the photoresist thickness. This means that phononic crystal geometries have to exhibit smallest dimensions in the range of 1–2 μm: this smallest dimension has to apply to individual scatterers or to the spacing between them.

2) etching processes provide smooth and vertical sidewalls in only a few very specific cases: silicon or silicon dioxide. When considering the patterning of piezoelectric materials, such as lithium niobate or aluminum nitride, reactive ion etching usually leaves sidewalls in the range of 80 degrees, as shown in Figure 8.5(a), sometimes even less. Small-diameter holes may therefore be limited in depth, as they form a cone that would close before reaching the desired depth. This usually adds additional constraints on the depth that can be achieved.

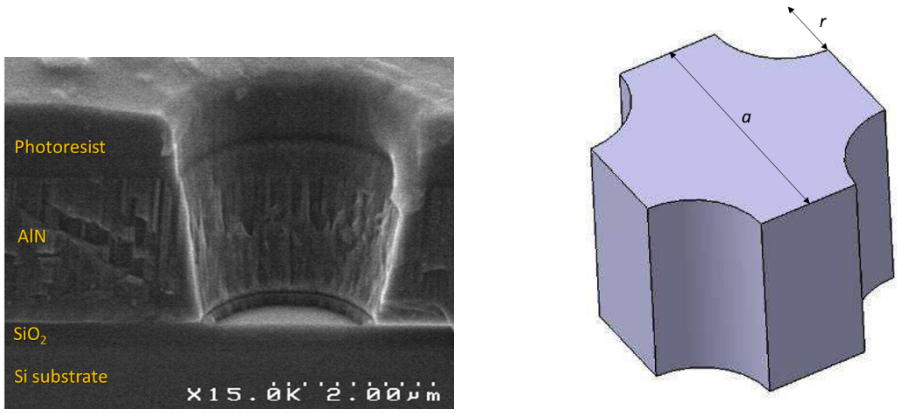

(a) (b)

Figure 8.5. *Illustration of a phononic crystal made of an array of holes embedded in a solid matrix: (a) limitation in sidewall angle revealed by a scanning electron microscope image of an actual hole obtained after etching holes in an AlN film and (b) indications of critical process dimensions*

Given the fact that the opening of phononic band gaps usually requires relatively large filling fractions [REI 11], the limiting factor is usually the spacing between two neighboring scatterers, which must remain large enough to comply with design rules. Translated in terms of dimensions for the example of a square lattice made of holes etched in a solid matrix, shown in Figure 8.5(b), photolithography processes impose

minimum values to the radius r of holes and to the spacing $a-2r$ between neighboring holes. For this reason, phononic band gaps are usually limited to frequencies below 1 GHz. Switching to higher-order band gaps may be a solution to move towards higher frequencies, but at the expense of relative width.

8.2.2. *Experimental demonstrations of hypersonic band gaps*

Despite the technological difficulty to fabricate phononic crystals exhibiting large band gaps at GHz frequencies, several demonstrations have been successfully achieved. Following some early works on the characterization of one-dimensional structures such as semiconductor superlattices or one-dimensional phononic structures [BAR 98, DHA 00, OZG 01], the true starting point for two-dimensional phononic structures is the work of Gorishnyy *et al.* in 2005 [GOR 05]. For the first time, a periodic structure made of a triangular lattice of holes with a filling ratio of up to 39% directly formed in photoresist coated on glass was fabricated and its band diagram was experimentally determined by Brillouin light spectroscopy. This was evidently seen in the 2 GHz region, as well as folding of modes at the edge of the Brillouin zone.

Subsequent to this experiment, demonstrations of phononic crystals compatible with the major types of elastic wave resonators have been proposed. In section 8.2.2.1, we will describe phononic crystals fabricated on bulk monocrystalline substrates and compatible with surface acoustic waves devices. Then, we will detail in section 8.2.2.2 crystals realized on freestanding membranes, the so-called *phononic crystal slabs*. These are compatible with many MEMS processes and especially with Lamb wave resonators, a kind of resonator that has still to find an industrial application, but which is extensively studied in the academic world. Finally, section 8.2.2.3 will focus on the few examples of phononic crystals for bulk waves and discuss the difficulty related with integrating a phononic crystal suitable for a BAW device.

8.2.2.1. *Phononic crystals for surface acoustic waves*

The combination of surface acoustic waves and piezoelectric single crystal solids such as quartz, lithium tantalate ($LiTaO_3$) or lithium niobate ($LiNbO_3$), among others, occupies a prominent position in the field of wireless telecommunications and signal processing. Single crystal substrates indeed offer piezoelectric and electromechanical coupling properties that remain unmatched by the currently available piezoelectric thin films. The theoretical demonstration by Wu *et al.* of the capability of a two-dimensional phononic crystal to open band gaps for surface acoustic waves [WU 05a] offered, therefore, particularly rich applicative prospects, while constituting a very good field for more fundamental investigations.

The very appealing properties of single-crystal substrates are, however, most of the time counter-balanced by the difficulty of processing these materials, which are

quite often complex oxides using standard micromachining technologies. Fabrication then stands as a challenge, while design is not made any easier. The strong anisotropy of acoustic wave propagation inherent to piezoelectric materials, combined with the quasi-systematic mixing of shear and longitudinal polarizations, puts tighter constraints on the geometrical parameters of the periodical structure itself [WU 04, LAU 05].

The first experimental demonstration of complete band gaps for surface acoustic waves propagating on lithium niobate substrates was performed by Benchabane *et al.* [BEN 06]. The phononic crystal consisted of a square array of 9 μm diameter air holes with a period of 10 μm. With such dimensions, the band gap extended from 203 to 226 MHz. Its existence has been characterized in transmission by using sets of interdigitated transducers (IDT) in delay line configuration. Two sets of delay lines were measured: a set of classical lines, acting as reference to calibrate the limited electric transmission of the setup, and a set of lines in which the phononic crystal was inserted, as shown in Figure 8.6. The comparison of the measured transmission (defined as the ratio between the output power measured on the receiving IDT and the incident electrical power applied to the emitting IDT) in Figure 8.6(b) for the reference (dashed) and for the delay lines with the crystal (thick continuous lines) reveals that in the low-frequency side, the crystal does not strongly perturb the transmission. Within the band gap, marked as the gray region, the transmission between the two transducers drops considerably, proving its existence. This experiment paved the way for a fully electrical characterization of high-frequency phononic crystals, and its scheme remained for long a reference set-up reused in further studies.

The most conventional fabrication technique for the etching of the array of holes in lithium niobate is reactive ion etching, using sulfur hexafluoride (SF_6) as the gas providing reactive species (F^- ions) [BEN 06]. Due to the high chemical stability of lithium niobate and the non-volatility at process temperature of some of the reaction's by-products (LiF in particular), the etching process has to operate mostly in a ballistic regime where material removal is achieved through the transfer of kinetic energy to the surface of the sample, rather than through chemical reactions. Even in such conditions, the etch rate was only 50 nm/min (as a comparison, silicon etch rates can be as high as 50 μm/min). This meant that several hours were necessary to etch holes 10 μm deep. Photoresist masks are not capable of withstanding such long exposure to a high-energy ion bombardment. Therefore, the etching process had to be made more complex, by using a 1 μm electroplated nickel mask. However, even in such conditions, the holes obtained proved conical rather than cylindrical, with a sidewall slope of about 17% for 10 μm diameter holes, as visible in the inset of Figure 8.6(a).

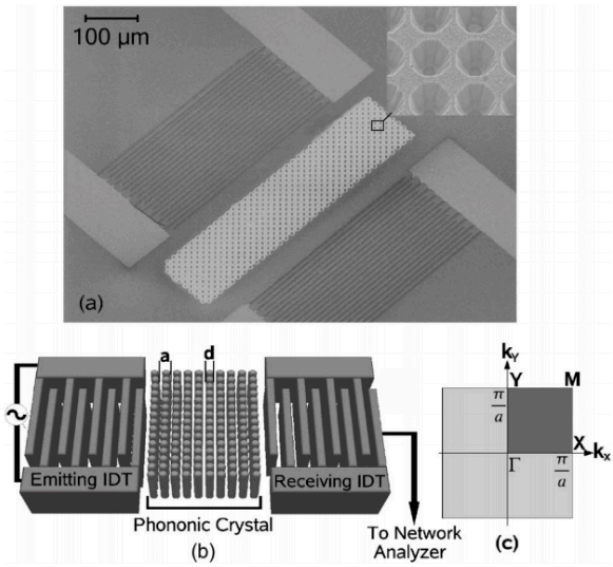

(a)

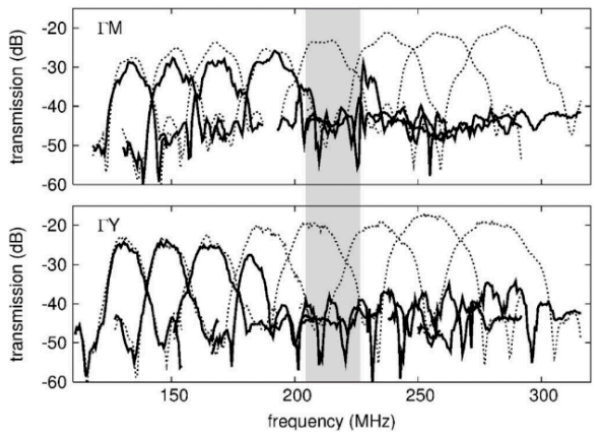

(b)

Figure 8.6. *Surface acoustic wave delay line for probing a phononic crystal made of square lattice of holes in lithium niobate: (a) scanning electron microscopy image of the fabricated device and sketch of the experimental setup and (b) electrical measurements of several delay lines (solid: including the phononic crystal; dashed: without phononic crystal) to cover the frequency range surrounding the band gap (in gray) [BEN 06]*

Several other techniques were tried to improve the etching process, especially electron irradiation [ASS 08]. The principle consists in writing patterns using an electron beam as in e-beam lithography, but this time without photoresist. Instead, the electronic charges accumulated on the surface force a local inversion of the ferroelectric domains in lithium niobate and make the material sensitive to chemical etching by pure hydrofluoric (HF) acid. The process durations proved, however, to be similar to reactive ion etching, and the holes proved also conical, with a sidewall slope of 12%. Finally, the shape of the scatterers seemed to be difficult to control, as electrostatic forces tend to spread the electrons apart from each other at the surface of the insulating lithium niobate.

Due to the difficulty to etch holes in single-crystal piezoelectric materials, work has been also devoted to form phononic crystals for surface acoustic waves on silicon substrates, in order to benefit from the easier processing of this material, which is the reference substrate for microfabrication. Wu *et al.* proposed to excite surface waves on silicon substrates using a thin film of piezoelectric zinc oxide (ZnO) deposited on top of a silicon substrate and positioned at the level of the emission and reception transducers [WU 05b]. Using a technique known as deep reactive ion etching, particularly efficient at etching high-aspect-ratio holes in silicon substrates, they managed to form a phononic crystal with holes 80 μm deep for a diameter of only 3.5 μm. This paper proposed also an improvement of the measurement set-up: in [BEN 06], eight delay lines with different IDT periods were needed in order to cover the full phononic band gap as well as frequencies in its vicinity, as shown in Figure 8.6(b). The transducers used in [WU 05b] were slanted in order to simultaneously excite several wavelengths and therefore to directly cover a wide frequency range with a single delay line, although it resulted in a decrease in the overall electrical transmission.

One particular feature of the interaction of a surface wave with a phononic crystal is visible in Figure 8.6(b): after the band gap, the transmission of acoustic waves is not necessarily recovered. For a phononic crystal made of holes periodically arranged in a piezoelectric substrate, optical heterodyne interferometry reveals a strong scattering of the surface wave as the crystal acts as a diffraction grating [KOK 07]. The strongest contribution to the attenuation, however, occurs when the surface wave dispersion crosses the so-called *sound line*, – that is, becomes faster than the slowest bulk wave and is therefore no more guided at the surface. It is also supposed that the finite depth and the conic shape of the holes enhances the coupling to bulk waves.

Aside from phononic crystals exhibiting band gaps arising from Bragg scattering, resonant metamaterials in which local resonances open hypersonic band gaps have been more recently investigated [LIU 14]. For guided waves, this idea can be seen as an extension to sub-wavelength scatterers of the well-known principle of mass loading, which consists in affecting the dispersion relation of surface elastic waves by creating corrugations or by manufacturing high-aspect-ratio structures on the surface of the substrate hosting the propagation [AUL 76, MAY 91, SOC 12], with

the aim, in particular, to slow down the propagation. It has, for example, been shown that phononic crystals made of thick metal pillars deposited on a homogeneous surface could exhibit hybridization gaps caused by local resonances of the pillars, in addition to the Bragg band gaps caused by the periodicity of the array [KHE 10a, ACH 11, YUD 16]. Interestingly, this ensures a way to open a band gap, or several, below the sound line, as shown in Figure 8.7(a). A first experimental demonstration in the GHz frequency range used aluminum pillars formed on a silicon substrate [GRA 12]. With 100 nm thick pillars having a radius of 95 nm, disposed in a square array of 500 nm period, the band structure has been determined by surface Brillouin light scattering and evidenced band gaps around 5 GHz, as shown in Figure 8.7(b).

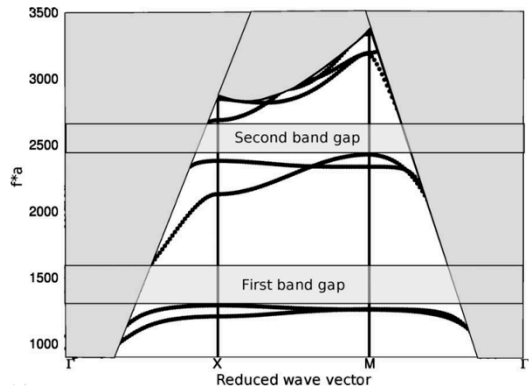

(a)

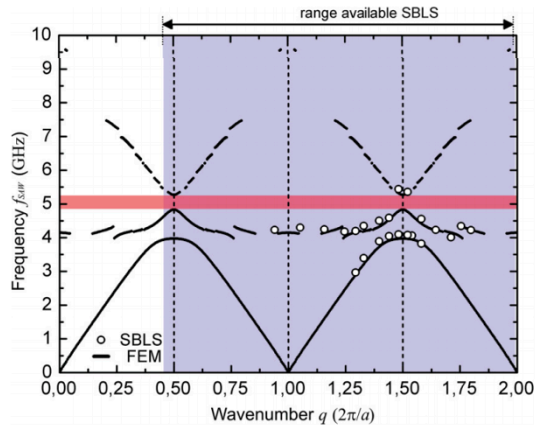

(b)

Figure 8.7. *Band gap for surface acoustic waves obtained through the coupling with local resonances of pillars: (a) theoretical calculation [KHE 10a] and (b) experimental measurement using surface Brillouin light scattering. Reprinted from [GRA 12], with the permission of the American Physical Society*

Local resonances have also been used to investigate contact resonance effects in granular materials [BOE 13, HIR 16, ELI 16], for instance, in the case of micron-sized polystyrene spheres adhered to a substrate as shown in Figure 8.8(a). These last experiments, performed through optical excitation and interferometric optical measurements, allowed the authors to determine the attenuation of surface acoustic waves propagating in a glass substrate as a function of frequency and proved the existence of an attenuation peak at the resonance frequency of the Hertzian contact, as shown in Figure 8.8(b).

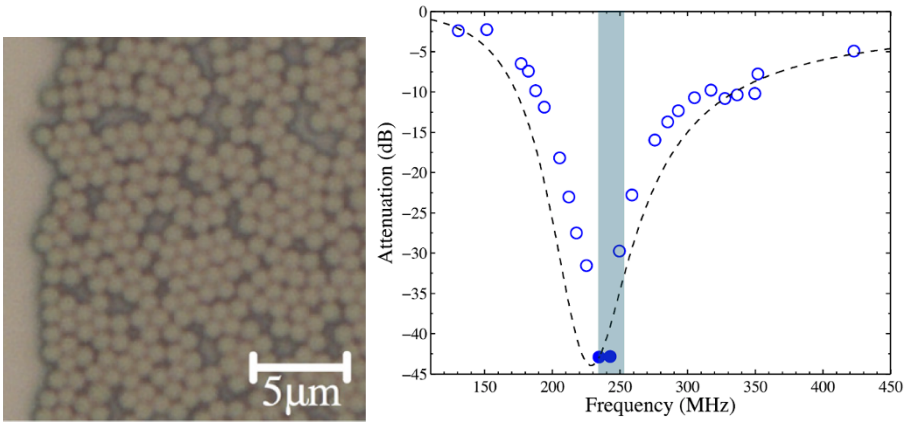

(a) (b)

Figure 8.8. *Resonant metamaterial for surface acoustic waves made of polystyrene micro-spheres adhered on a glass substrate: (a) optical micrograph and (b) measurement of the attenuation for Rayleigh waves propagating through a 170 μm strip of micro-spheres. Reprinted from [ELI 16], with the permission of AIP Publishing*

Despite the possibility of relying on resonant band gaps, of effectively designing Bragg band gaps lying below the sound line [YUD 12] or of annular patterns supporting local resonances to reduce coupling to other modes [ASH 17], some authors considered that surface acoustic wave phononic crystals lacked vertical confinement. They proposed therefore to switch to thin plates offering a vertical confinement preventing radiation in a substrate. Such crystals inserted in a vertically limited medium were soon called *phononic crystal slabs*.

8.2.2.2. *Phononic crystal slabs*

Propagation of waves in slabs calls for the study of phononic crystals for plate waves. As early as 2006, that is immediately after the theoretical demonstration of the existence of phononic crystals exhibiting stop bands for surface waves, Hsu *et al.*

calculated the dispersion curves for Lamb waves propagating in thin plates containing a periodic array of cylindrical inclusions [HSU 06, HSU 07b]. They demonstrated that the consideration of traction-free surfaces delimiting the slab significantly modifies the band structure compared to a bulk crystal, as they derive from the dispersion curves for Lamb of plate waves. Nevertheless, they demonstrated that band gaps could still be obtained, for relatively large filling fractions.

First experimental demonstrations of phononic crystal for plate waves were performed the same year by two independent groups. Hsiao *et al.* considered a slab made of epoxy encompassing steel spheres disposed in a square lattice [HSI 07]. With the spheres having 4 mm diameter, a complete phononic band gap opened around 300 kHz. Acoustic waves were excited using an emission transducer and were coupled to the slab by a prism, while an interferometric measurement scheme was employed. Closer to the hypersonic range, Olsson *et al.* [OLS 07] fabricated a micron-sized crystal made of a square lattice of cylindrical tungsten (W) scatterers (lattice parameter: 45 μm; radius, 14.4 μm) embedded in a silicon dioxide membrane (4 μm thick). This combination of materials was chosen for compatibility with the industrial fabrication of the interconnects in integrated circuits. As for SAW phononic crystals, a completely integrated measurement setup was fabricated along with the crystal: transmission of Lamb waves through the crystal was measured by a delay line made of an aluminum nitride (AlN) transducer formed on top of the silicon dioxide membrane, as shown in Figure 8.9(a). Electrical measurements, reproduced in Figure 8.9(b), reveal in this case a stop band ranging from 59 to 76 MHz.

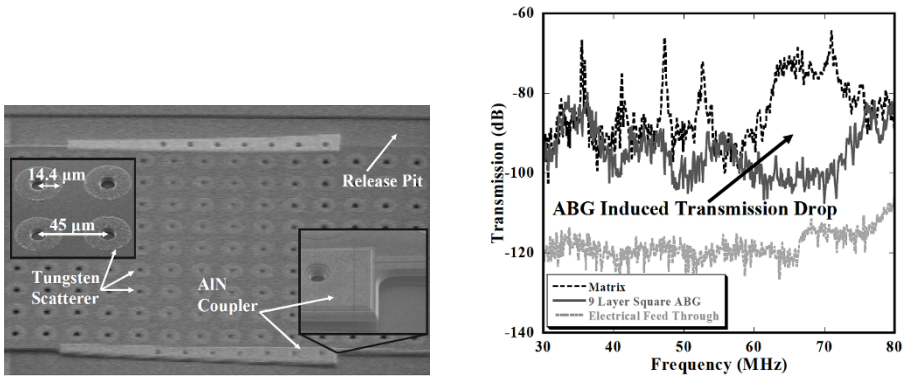

(a) (b)

Figure 8.9. *Phononic crystal for Lamb waves: (a) scanning electron microscopy (SEM) image of the crystal made of tungsten scatterers embedded in a silicon dioxide membrane inserted between two AlN transducers and (b) electrical measurements of the transmission, revealing a band gap around 70 MHz. Reprinted from [ELK 08], with the permission of AIP Publishing*

Following this first demonstration, other groups proposed different combinations of materials and crystal structures to increase the band gap center frequency and its width, the goal being ultimately to reach frequencies used for telecommunication applications (400–3,500 MHz). Mohammadi *et al.* obtained an attenuation band ranging from 119 to 150 MHz (i.e. a 23% relative bandwidth) using a crystal made of cylindrical holes disposed as an hexagonal lattice (lattice parameter, 15 μm; radius, 6.4 μm) on a 15 μm thick silicon membrane [MOH 08]. Here, the reduction in lattice parameter is responsible for the higher-frequency range, while the move to an hexagonal lattice and the increase of the filling fraction of the scatterers promote a wider stop band. Soliman *et al.* managed to obtain a significant attenuation of the acoustic transmission between 1 and 1.8 GHz by realizing a crystal with even more aggressive dimensions: 0.65 μm diameter tungsten scatterers were disposed in a square lattice with a 2.5 μm period inside a 1.15 μm thick silicon membrane [SOL 10b].

An alternative approach is to embed the phononic crystal in a material exhibiting a large sound velocity, such as aluminum nitride (AlN). This material being also piezoelectric, the phononic crystal can be integrated directly along transducers, in a way similar to earlier works on surface waves. With a phononic crystal slab realized in a silicon dioxide/aluminum nitride membrane, Gorisse *et al.* demonstrated an attenuation band for Lamb waves ranging from 600 to 950 MHz [GOR 11] using a square array of almost cylindrical holes. Simultaneously, Kuo *et al.* obtained an attenuation band for Lamb waves ranging from 850 MHz to 1.2 GHz, using a square array of "X"-shaped holes (lattice parameter, 5 μm; thickness, 1 μm; 4.2 $\times$ 0.75 μm arms) formed also in an AlN membrane [KUO 11].

As for surface acoustic waves, locally-resonant phononic crystals were also proposed, relying on pillar structures formed at the surface of a plate to open a band gap [HSU 07a]. First works considering "thin" plates (with respect to the wavelength) demonstrated that the local resonances of the pillars interact with the modes of the plate, which manifests by the opening of band gaps [PEN 08]. Thin circular plates periodically disposed within the main, thicker, plate, shown in Figure 8.10, were also proposed and exhibited a slow mode corresponding to the flexural mode of individual thin plates [SUN 10]. In both cases, this usually opens a stop band at a frequency below the Bragg band gap, although the band gap location is essentially conditioned by the resonant frequency of the scatterers. Hence, such structures are not directly suited for obtaining band gaps at frequencies compatible with RF applications.

A particularity of phononic slabs is that they are realized on elastic plate, which supports the propagation of a host of modes: symmetric and antisymmetric Lamb waves as well as shear horizontal plate waves. This produces a much more complex band structure than three-dimensional phononic crystals or than phononic crystals for surface waves. For this reason, the interaction of a phononic crystal with transducers

is more complex than in the case of phononic crystals for surface waves. This is, for example, illustrated in Figure 8.11(a), which shows the measured electrical transmission of a Lamb wave delay line used to probe a phononic crystal. A significant transmission attenuation is visible between 600 and 900 MHz, while the theoretical band gap is only expected to extend from 776 to 828 MHz [GOR 11]. Clearly, in the process of converting the Lamb waves into Bloch modes of the crystal and conversely at the output of the crystal, a large part of the acoustic power generated by the emitter transducer is lost. While this is expected inside the band gap, as only evanescent Bloch modes may transfer power through the crystal, it is fairly unexpected outside of the stop band. A first explanation for this is that the AlN or ZnO transducers used to excite or to detect waves are only capable of exciting symmetrical Lamb waves. As such, Bloch modes with shear horizontal polarization, identified in Figure 8.11(b) (left), are not expected to be excited [SOL 10b, KUO 11]. Additionally, even some Bloch modes with out-of-plane transverse or with longitudinal polarization may not be excited if their mode shape is orthogonal to the polarization of the incident or transmitted Lamb waves [GOR 11]. Such modes are then called "deaf bands" [HSI 07]. Finally, some flat bands, such as the ones labeled "b" and "c" in Figure 8.11(a), may be so localized that they do not generate strong peaks in transmission spectra. This extended attenuation range compared to the sheer phononic band gap proves highly beneficial in most applications, where phononic crystals are expected to act as reflectors. Therefore, phononic crystal slabs faced more interest than phononic crystals for surface waves and were rapidly adopted by the MEMS community as will become evident in section 8.3.2.

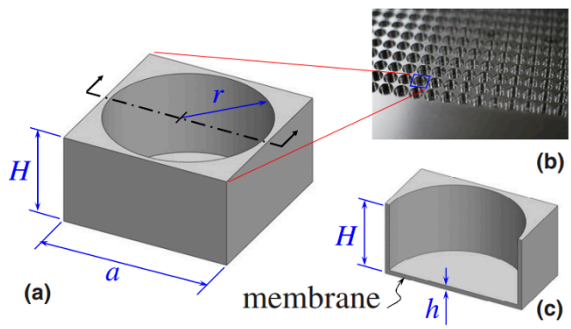

Figure 8.10. *Square lattice phononic crystal plate made of periodic membranes: (a) schematic of the unit cell, (b) photograph of the fabricated sample and (c) cross-section of the unit cell. Reprinted from [SUN 10], with the permission of AIP Publishing*

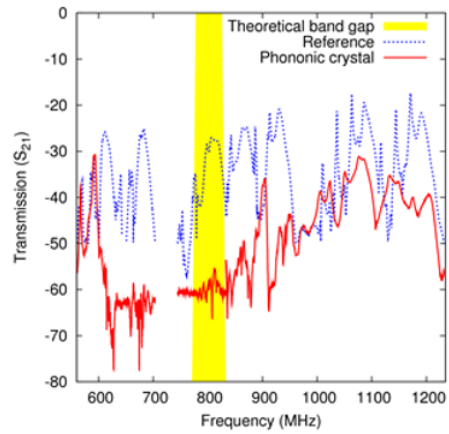

(a)

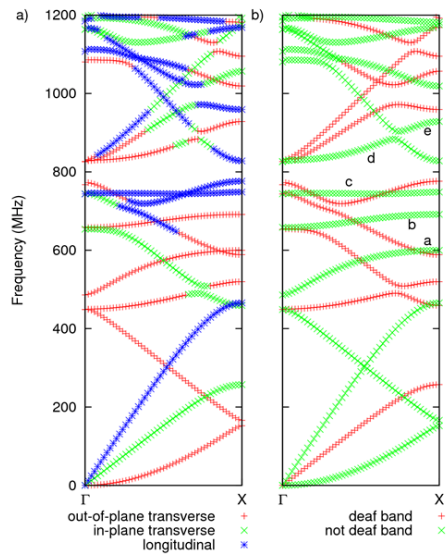

(b)

Figure 8.11. *SiO_2/AlN-based phononic crystal slab: (a) electrical transmission of a set of Lamb wave delay lines with (continuous red curve) or without (blue dashed lines) phononic crystal inserted between transducers. The theoretical band gap position is highlighted in yellow. (b) Band structure for the phononic crystal: (left) determination of the polarization of Bloch modes and (right) identification of deaf bands. Reprinted from [GOR 11], with the permission of AIP Publishing. For a color version of this figure, see www.iste.co.uk/romero/metamaterials.zip*

8.2.2.3. *Phononic crystals for bulk acoustic waves*

Despite extensive work on phononic crystals for surface acoustic wave or plate waves, no notable reports of phononic crystals that could benefit bulk acoustic wave resonators have been published, although this technology is now the second standard for elastic wave RF components behind SAW filters and is certainly more mature than the field of Lamb wave devices.

With regards to bulk acoustic wave devices, Bragg mirrors have been proposed as early as 1965 [NEW 65] to isolate a piezoelectric resonant cavity from its surroundings. With the advent of thin-film bulk acoustic resonators, this idea has been extensively developed in the solidly mounted resonator (SMR) technology. Mirrors used nowadays in this technology differ from simple quarter-wavelength stack of materials. They are usually optimized to provide a stop band for all vertically propagating wave polarizations, in order to reduce any possible leakage of acoustic power out of the resonant cavity, – even the marginal-thickness shear waves generated by mode conversions during reflection of the main thickness-extensional mode at the edges of the resonator electrodes [MAR 05]. While they are designed only for vertically propagating waves, they also prove efficient for waves propagating in the lateral direction, which usually act as parasitic modes for bulk wave resonators [TAL 06]. They have therefore even been proposed to provide a vertical confinement for waves guided in a piezoelectric film [KHE 08, KON 10, TAK 16], as will be more detailed in section 8.4.2. Such one-dimensional structures are, however, not considered as being phononic crystals or elastic metamaterials.

Phononic crystals capable of opening a band gap at the frequencies where bulk waves are exploited could hold the promise of extreme three-dimensional confinement of waves in BAW resonators and, therefore, boost quality factors beyond their actual levels. However, opening a band gap at their frequencies of operation, that is, between 1.5 and 3.5 GHz, proves difficult: as discussed in sections 8.2.1.2 and 8.2.2.2, micro-fabrication techniques allow the formation of phononic crystals with band gaps reaching frequencies up to 1 GHz. More aggressive dimensions could theoretically increase the range of frequencies achievable, by increasing the frequencies at which the Bragg condition related to the spacial periodicity of the phononic crystal, or the Mie scattering related to the dimensions of the scatterers, occurs [OLS 09]. As an example, phononic crystals made of cylindrical holes disposed in a square lattice within a silicon matrix were studied in [OSE 18]. A lattice parameter of 940 nm and a filling fraction of 76% were necessary to open a band gap extending between 2 and 3 GHz. Such a high-filling fraction is critical to decreasing the frequency of the band gap from several GHz down to 2 GHz. It leads, however, to almost unrealistic spacing between adjacent holes (15 nm) and is, therefore, impossible to implement in practical applications.

One of the only effective structures reported to date relied on an industrial process for integrated circuit manufacturing [BAR 15]: a phononic crystal was realized using the metal interconnects between transistors, made of 165 nm copper stripes separated by 85 nm, embedded in a low-permittivity solid dielectric (SiOCH) material. Due to the high miniaturization, the calculation of the band structure, shown in Figure 8.12(b), reveals the opening of a band gap extending from 2.54 to 6.35 GHz. Obtaining such fine dimensions has been, however, only made possible by the huge research and engineering efforts that the nanoelectronics industry deployed over decades to continuously keep the pace on miniaturization of integrated circuits imposed by Moore's law. Therefore, the patterning of these materials is well-established and optimized to form sub-micron features. Forming sub-micron size piezoelectric structures, which would be mandatory for collocating a high-frequency hypersonic crystal with a bulk wave resonator, still remains an extremely challenging task.

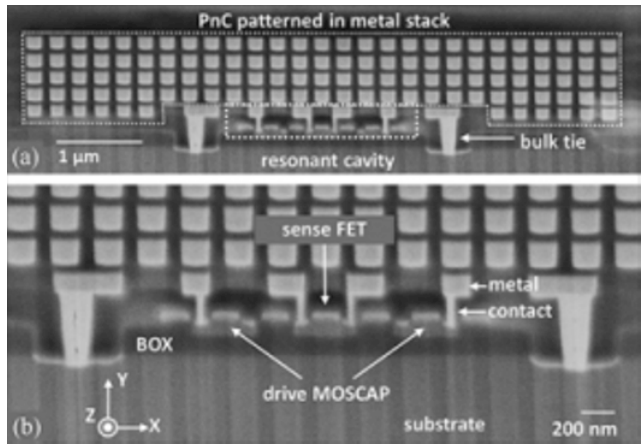

Figure 8.12. *Phononic crystal made of CMOS interconnects, realized using transistor metal interconnections (courtesy Hybrid MEMS Research Group at Purdue University: https://engineering.purdue.edu/hybridmems/). For a color version of this figure, see www.iste.co.uk/romero/metamaterials.zip*

A second issue is that the stack of materials (piezoelectric film, electrodes, passivation, Bragg mirror layers, etc.) of BAW resonators is already optimized for the main functionality of the filter. Therefore, phononic crystals have to be tailored for such a complex set of materials and have to offer wave confinement without affecting

in any other mean the stringent performances of the device. As a result, hypersonic crystals suitable for bulk wave applications is still an open investigation topic.

8.3. Phononics for RF signal processing

After early works aimed to demonstrate the ability to push phononic crystals to the hypersonic range and to overcome microfabrication challenges related to their actual implementation, at least for surface or plate waves, research groups have started focusing on applications that could benefit from this new concept.

The major characteristic of phononic crystals is their ability to open a phononic band gap, which forbids the propagation of acoustic waves regardless of their direction. This called from the very early stages of research on this topic for envisioning a tight confinement of waves in geometrically defined structures. Taking inspiration from the microwave world and from photonics, researchers proposed two different classes of functions benefiting from this confinement: waveguides in which phononic crystal constrains waves to follow a very specific path, or resonant cavities, which are regions completely surrounded by a phononic crystal and, therefore, almost fully isolated from their surrounding.

8.3.1. *Phononic waveguides*

Any defect inserted in an otherwise perfect crystal adds one or several branches to the band structure. In particular, removing a full row of scatterers in a phononic crystal has the consequence of enabling defect modes localized in the row. A slightly different view is to state that waves can be trapped in the defect row, but cannot escape if their frequency falls within the band gap of the crystal surrounding the defect. This property is at the basis of light guidance in photonic crystals. Taking this inspiration, Kafesaki *et al.* [KAF 00] theoretically proved that defect modes obtained by removing a row of scatterers in a phononic crystal, can carry acoustic power through the crystal. Interestingly, near-perfect transmission is obtained, making the defect line act as an efficient waveguide. Unlike photonic waveguides, the defect modes may be of shear or longitudinal polarizations and may interact with each other. This opens sub-band gaps, which may cause transmission drops in the waveguide at specific frequencies within the guiding band gap. Such a mechanism is not only tied to conventional phononic crystals, but has been also theoretically demonstrated in a locally-resonant phononic

plates [OUD 10]. This last case is particularly interesting as, since local resonances may open a band gap at frequencies lower than the Bragg regime, the waveguide may remain single-mode, even for relatively large waveguide width (for example, obtained by removing three lines of local resonators, as shown in Figure 8.13).

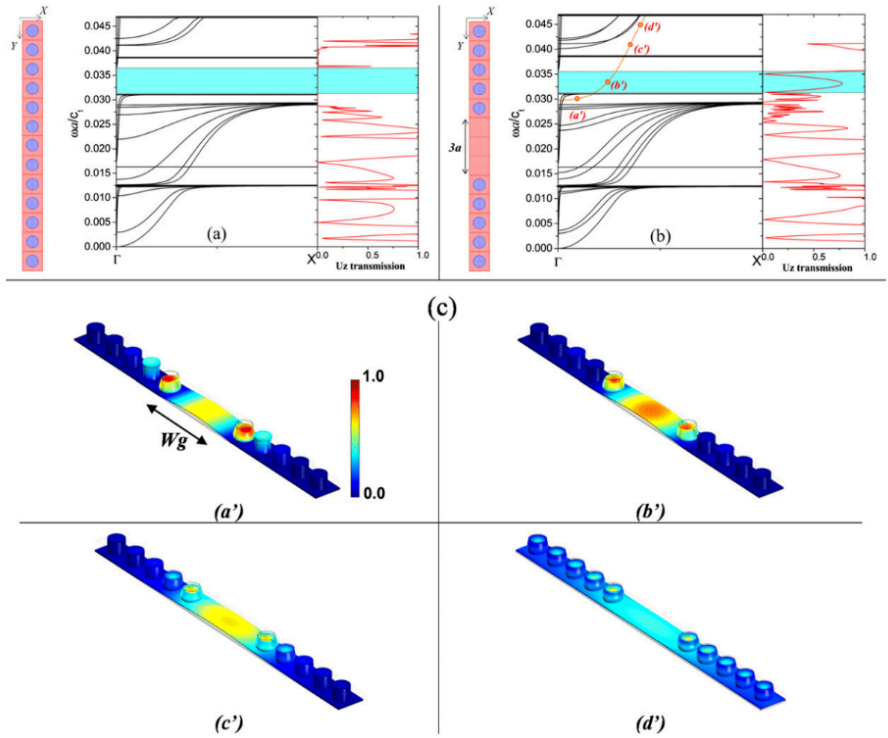

Figure 8.13. *Waveguide formed in a resonant phononic crystal slab: (a) band structure and transmission coefficient of a supercell made of 13 rubber pillars on an epoxy plate. (b) Band structure of a supercell representing the waveguide structure obtained by removing three pillars from the previous structure. (c) Displacement amplitude of the defect mode plotted for different wavenumbers, at positions indicated by red cycles in (b). Reprinted from [OUD 10], with the permission of AIP Publishing. For a color version of this figure, see www.iste.co.uk/romero/metamaterials.zip*

Slightly later, Khelif *et al.* [KHE 02] took this time analogy from microwave transmission lines. They demonstrated that the addition of lateral branches, called *stubs*, to a main transmission line causes interferences between the main wave propagating in the transmission line and the wave that has propagated into the stub, and has been reflected by the end of this usually short line. Hence, depending on the

length of the stub, this forces locally a node or an antinode, which generates features in the transmission spectrum such as transmission zeros at specific frequencies. This can be thought as the ultrasonic equivalent of a Helmholtz resonator for audible sound. A similar behavior was theoretically demonstrated in [KHE 02] for a stubbed phononic waveguide in the case of a scalar wave propagating in water with a crystal consisting of periodical solid scatterers. Figure 8.14(a) shows how an acoustic wave reflects from the end of the stub and interacts destructively with the incoming wave field. It was especially shown that the length or the width of the stub significantly affects the number and frequency of transmission zeros, as indicated in Figure 8.14(b), which shows a transmission spectrum calculated for stubs having different widths.

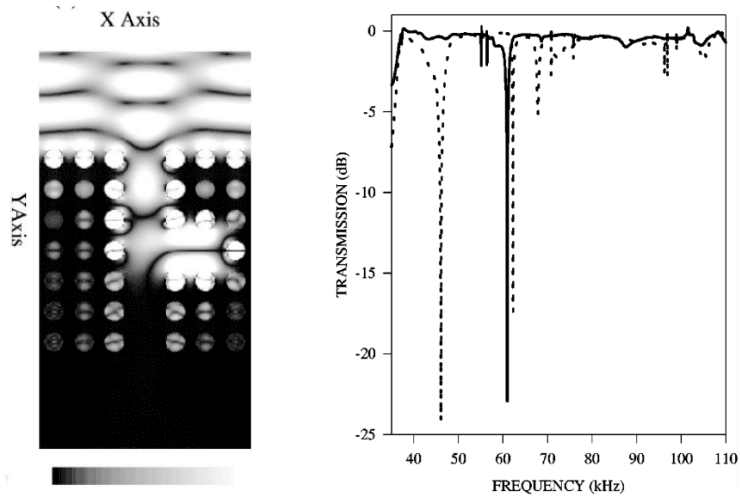

Figure 8.14. *Stubbed phononic crystal waveguide [KHE 02]: (a) calculated field amplitude at the frequency at which the stub causes a transmission zero and (b) calculated transmission coefficient as a function of frequency for a stub width of one (solid line) or two (dashed line) unit cells*

Further expansions of these concepts were investigated, this time also experimentally, to propose more complex functions. For example, Pennec *et al.* [PEN 05] used two cavities, formed by the removal of a scatterer in the phononic crystal, to couple together two waveguides, as sketched in Figure 8.15. The coupling was facilitated by stubs extending out of the waveguides towards the cavities. At the resonance of the cavity mode, waves propagating through one of the guides could be redirected towards the second waveguide, hence promoting a demultiplexing function.

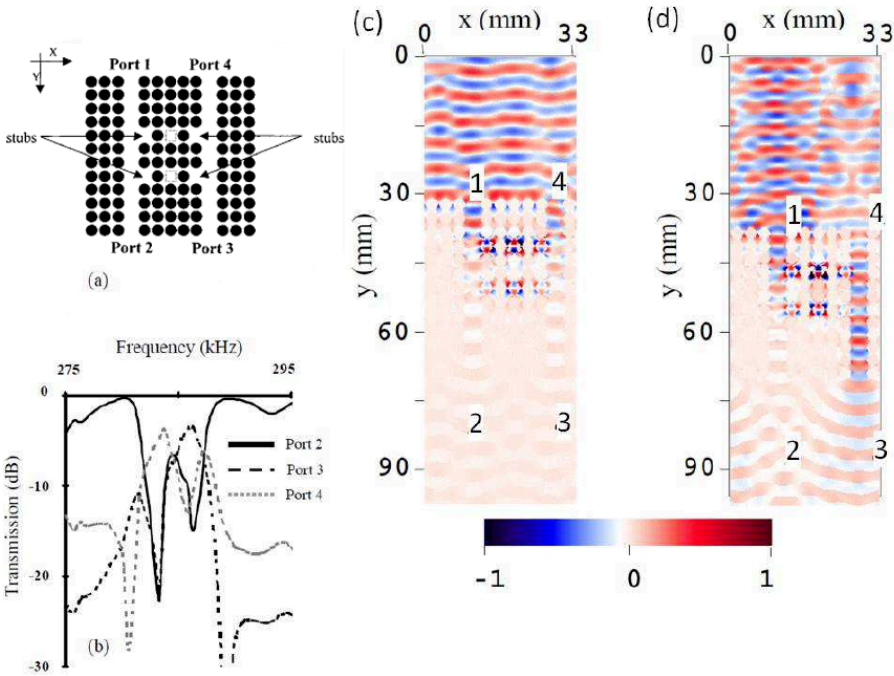

Figure 8.15. *(a) Coupling between two stubbed waveguides through resonant cavities made of two vacancies in the phononic crystal. (b) Calculated transmission spectrum at ports 2, 3 and 4 for an input excitation at port 1. (c) Calculated fields at 283 kHz, corresponding to the frequency where the transmission drops at the level of ports 2 and 3, while it is enhanced at port 4. (d) Calculated fields at 286 kHz, where the transmission drops at ports 2 and 4, and is enhanced at port 3. Reprinted from [PEN 05], with the permission of AIP Publishing. For a color version of this figure, see www.iste.co.uk/romero/metamaterials.zip*

Guidance by a line defect waveguide was experimentally demonstrated in 2004 [KHE 04], by forming a waveguide by removing rods from a periodic two-dimensional lattice of steel cylinders immersed in water. In this series of experiments, it was proved that the complete band gap is capable of forcing waves to travel across sharp bends. In 2007, Hsiao *et al.* focused on a solid phononic crystal slab [HSI 07]. They fabricated a phononic crystal structure made of steel spheres embedded in an epoxy matrix, already mentioned in section 8.2.2.2. Interferometric measurements of the wave amplitude revealed an attenuation of approximately

–45 dB for the wave transmitted through the six-period-long waveguide, which has to be compared with an attenuation of about –60 dB for the phononic crystal itself, and about –30 dB for the epoxy slab alone. These values proved to be strongly frequency-dependent and not uniform in the frequency range of the phononic band gap due to the complex band structure of the waveguide. Additionally, the additional 15 dB attenuation compared to the sole epoxy medium was too high for practical applications. As such loss rates were not observed in early experiments in water, they are likely to originate from coupling losses at the entrance or the exit of the waveguide, where mode conversions exist between the Lamb or plate waves of the slab and the modes of the crystal or conversely, as well as from intrinsic losses of the defect modes themselves.

All these demonstrations were performed in the 100–500 kHz range, therefore far below the radiofrequency range. Waveguiding of surface modes at a frequency close to 1 GHz was only demonstrated in 2015, by Benchabane *et al.* [BEN 15]. This demonstration required forming a square lattice (2.1 μm period) of holes (1.9 μm diameter, 2.5 μm deep) in a lithium niobate substrate, which opens a band gap ranging from 650 to 950 MHz. Surface waves were excited by chirped transducers capable of exciting waves from 630 to 1.3 GHz, which were fabricated by electron-beam lithography to ensure a sufficiently fine resolution of the metal electrodes. Propagation of waves was imaged by laser scanning interferometry and revealed that a single-line defect effectively guides, within the band gap, waves in a micron-size guide. As for low-frequency experiments, an attenuation of 10 dB was measured between the entrance and the exit of the waveguide, also attributed to the modal mismatch between the incident and transmitted waves and the guided mode.

Despite an effective waveguiding behavior and the possibility to implement sharp bends, propagation losses exhibited by phononic waveguides remain too large for practical applications by at least an order of magnitude. Clearly, one of the main issues pertains to the matching of defect modes to the incident waves in order to transfer nearly all the power inside the guide. A second critical point is to reduce propagation loss in the waveguide itself. While these remain still open issues, the focus of the community has shifted towards another use of localized defect modes: resonant cavities.

8.3.2. *Phononic crystal cavities*

When defects consist in the removal of a single scatterer, or a group of scatterers, in a perfect phononic crystal exhibiting a complete band gap, they give rise to a highly localized mode and, therefore, to a strong confinement of waves inside and in the close vicinity of the defect. Khelif *et al.* investigated this experimentally, with an ultrasonic phononic crystal, made of a square array of steel cylinders immersed in water [KHE 03]. They proved that the cavity formed by the removal of a single

scatterer leads to the appearance of a sharp transmission peak within the phononic band gap otherwise characterized by a low-transmission (–20 dB) region, as shown in Figure 8.16(a). When several, reasonably spaced cavities are formed, mode splitting between the coupled cavities brings up several transmission peaks.

Eventually, they demonstrated that when a sufficient number of cavities are disposed in-line, the number of split modes becomes sufficient to form a transmission band contained inside the band gap. In Figure 8.16(b), this transmission band extends roughly from 275 to 305 kHz [KHE 03]. This provides another mechanism to implement a waveguide, other than forming an extended line defect. In subsequent work, the same authors replaced cavities formed by the removal of a scatterer by inserting a line defect, that is, a spacing between two lines of unit cells of the crystal, in the direction perpendicular to the considered wave propagation direction [KHE 10b]. The band gap of the crystal ensures that waves are confined in this spacing and that the coupling between other line defects is evanescent. Such waveguides also exhibit a filtering behavior, since transmission through the set of resonators can only occur in the vicinity of the resonance frequency of individual cavities.

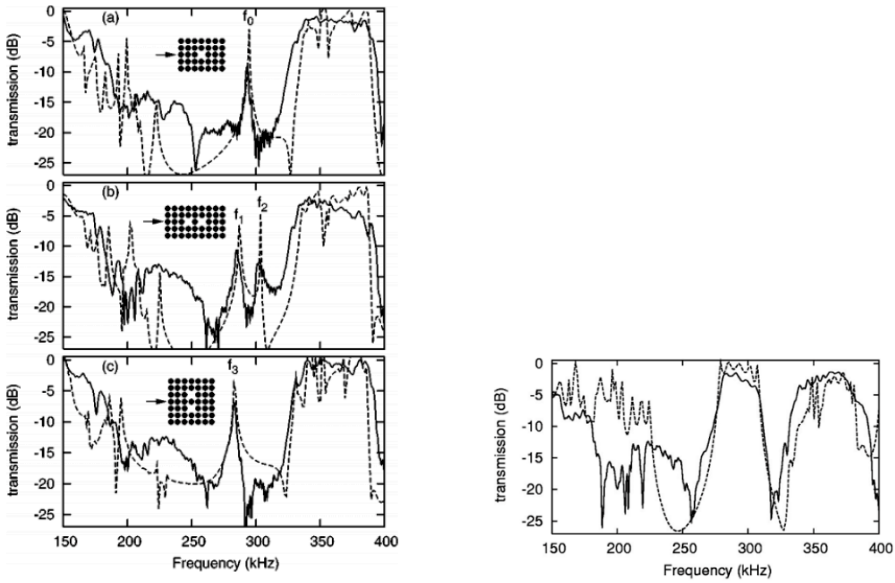

(a) (b)

Figure 8.16. *Transmission spectra for waves propagating in a steel/water phononic crystal in which several defects have been formed [KHE 03]: (a) single-defect cavities and couplings between two defects and (b) array of defects coupled to form a transmission band*

Another type of resonant cavities is Fabry–Perot-like resonators, consisting in a free propagation path inserted in between two phononic crystals. Mohammadi *et al.* [MOH 09] introduced them in phononic crystal slabs. With the set-up shown in Figure 8.17(a), they measured the transmission through the Fabry–Perot cavity and revealed the resonant modes they support. An example of such a measurement is shown in Figure 8.17(b). Sun *et al.* [SUN 09] demonstrated that the resonant modes of phononic crystal slab Fabry–Perot cavities are in fact conventional Lamb modes of the matrix slab. As they cannot couple to any mode in the phononic crystal in the frequency range of the phononic band gap, they are trapped in a resonant cavity, forming a resonance whose displacement amplitude and quality factor are only limited by the effective transmission coefficient of the phononic crystal and the quantity of power leakage out of the cavity they allow. As shown in Figure 8.17(b), Mohammadi *et al.* measured quality factors (defined as the ratio between the transmission peak center frequency and its –3 dB bandwidth) of 6,300 at a frequency of 126 MHz, with a phononic crystal extending over three periods [MOH 09]. This may not seem an outstanding figure of merit for silicon micro-resonators, but could be certainly improved with longer phononic crystals providing better insulation. Experimental data provided in [MOH 09] reveal however that, although quality factors improve with the number of crystal periods, the transmission through the Fabry–Perot resonator decreases. This is indeed expected, as better isolation from the environment makes the probing of highly confined modes more difficult from an external source.

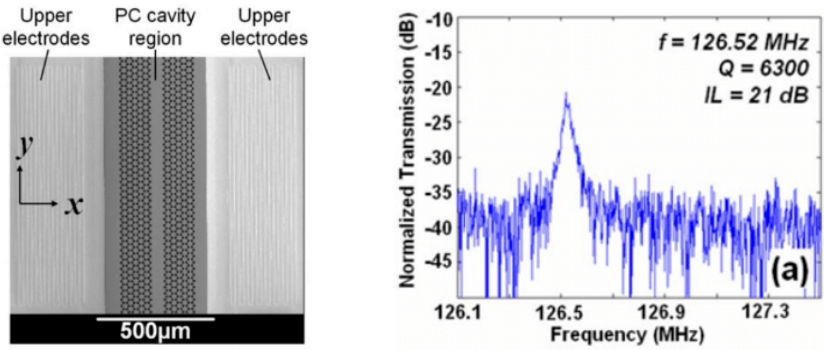

(a) (b)

Figure 8.17. *Phononic crystal slab Fabry–Perot resonators: (a) scanning electron microscopy image of a Lamb-wave delay line used to characterize the resonant cavity and (b) electrical measurement of the fundamental cavity mode falling in the phononic band gap. Reprinted from [MOH 09], with the permission of AIP Publishing*

To benefit from potentially high-quality factors while still being able to efficiently excite and detect the highly confined modes of Fabry–Perot cavities, Wu *et al.* proposed to directly insert the transducers inside the cavity. To demonstrate this idea, they inserted a ZnO/Si surface acoustic wave delay line inside a phononic Fabry–Perot cavity formed by etching a square array of cylindrical holes in the silicon substrate [WU 09], as sketched in Figure 8.18(a). In this configuration, instead of exciting propagating surface waves, the interdigitated transducer excites the low loss cavity modes, leading to a boost in the transmission coefficient of the delay lines by 7 dB, as revealed by Figure 8.18(b). Additionally, the phononic crystal provides a much more compact reflector than the conventional electrode gratings used in the surface wave filters industry. This comes, however, with the appearance parasitic dips visible in the electric transmission, caused by the multiple cavity of modes, which are also excited by the interdigitated transducers.

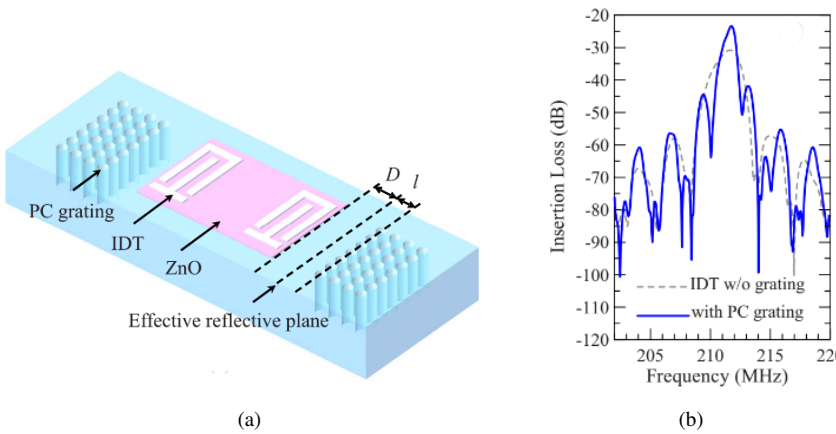

(a) (b)

Figure 8.18. *Insertion of transducers directly inside a Fabry–Perot cavity: (a) sketch of the resonator inserted in between two phononic crystals acting as reflector structures and (b) electric response of the resonator with the phononic crystal reflectors (solid line) or with conventional short-circuited electrode reflectors (dashed line). Reprinted from [WU 09], with the permission of AIP Publishing. For a color version of this figure, see www.iste.co.uk/romero/metamaterials.zip*

Taking a similar scheme, Mohammadi *et al.* [MOH 11] inserted a single transducer inside a phononic crystal slab Fabry–Perot cavity, as shown in Figure 8.19(a), and obtained similar quality factors to their earlier experiments with transducers positioned outside of the cavity [MOH 09]. In the case of phononic crystal slabs, the phononic crystal does not provide a better or more compact confinement to Lamb wave devices than the conventional membrane edges delimiting the resonant cavity employed in a majority of works, visible in Figure 8.20. It offers, however, a way of maintaining suspended membranes attached

to the substrate by a support, which prevents the leakage of waves from the membrane to the surrounding medium, hence limiting anchor losses faced when employing solid tethers. This idea received a large interest from the MEMS community and will be further developed in section 8.4.1.

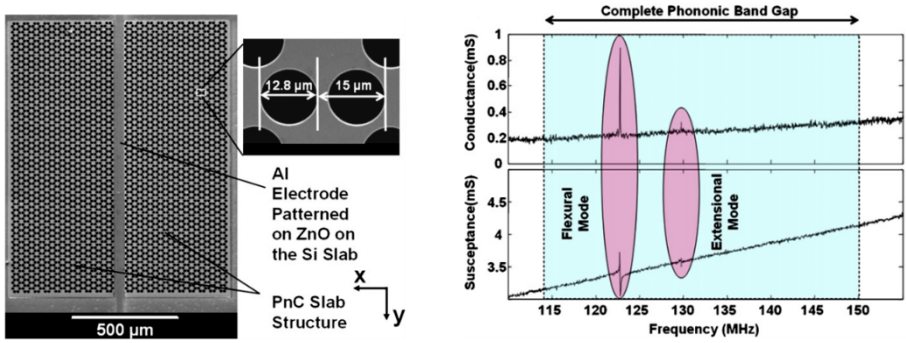

(a) (b)

Figure 8.19. *Phononic crystal employed as a reflector delimiting the resonant cavity of a Lamb wave resonator: (a) scanning electron microscopy image of the fabricated device and (b) electrical measurement of the resonator response. Reprinted from [MOH 11], Copyright 2011, with permission from Elsevier*

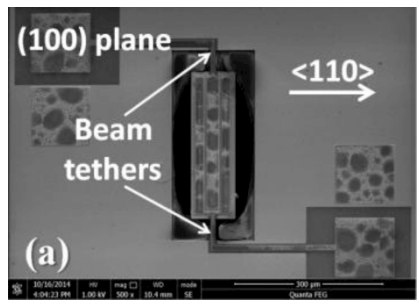

Figure 8.20. *Conventional Lamb wave resonator with a resonant cavity delimited by a straight ending of the propagation medium. Reprinted from [ZHU 19]. Copyright 2019, with permission from Elsevier*

Before that, for the sake of completeness, we briefly describe similar attempts to replace the short-circuited electrode gratings conventionally used as reflectors for surface acoustic wave resonators by phononic crystals. These were reported after the first works on Lamb wave resonators. Liu *et al.* demonstrated a phononic crystal for Love waves guided in a silica film on top of a quartz substrate and used it as a

reflector [LIU 14]. Their structure, as well as an example of electric response are shown in Figure 8.21. The experimental quality factors were however almost one order of magnitude lower than what was obtained for Lamb wave resonators using phononic crystals as reflectors. The first explanation for this was the extremely high sensitivity of the quality factor to the positioning of the crystal with respect to the electrodes, to ensure that electrodes are optimally positioned for the excitation of one specific mode of the relatively large cavity. The second point was the coupling of the Love waves with bulk waves of the substrate, due to the finite depth of the holes used as scatterers. Elaborating on this, Wang *et al.* noted that such an effect occurs primarily when waves excited by the transducer impinge the phononic crystal: mode conversion between the Love wave (in their case, guided in a GaN layer on a sapphire substrate) and Bloch modes causes a significant excitation of bulk waves radiating in the substrate [WAN 15]. To overcome this fact, they implemented a smooth transition between the free propagation medium and the phononic crystal, taking the form of a crystal starting with a gradient of scatterers diameter in the propagation direction. This way, they managed to obtain a quality factor of 880 for a resonator surrounded by a graded phononic crystal, compared to a quality factor of 248 for a sharp crystal. The drawback is, however, a loss in electromechanical coupling factor with the practical extension of the resonant cavity out of the transducer. This is due to the fact that transduction does not take place in the whole cavity, thus decreasing its efficiency. Additionally, even though this gradual matching of the crystal to the cavity improves quality factors, they still remain lower that what can be conventionally obtained using conventional short-circuited electrode reflectors. As for Lamb wave resonators, the benefit lies, however, in the reduced footprint offered by the very compact phononic crystal.

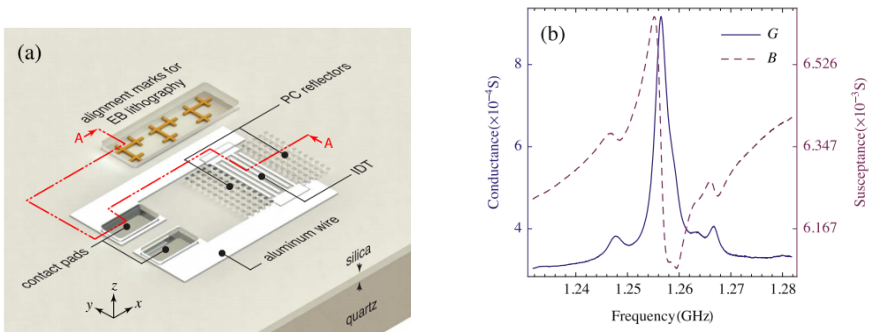

Figure 8.21. *Love wave resonator using a phononic crystal as a reflector: (a) sketch of the resonator structure and (b) electrical response close to the resonance. Reprinted from [LIU 14]. Copyright 2014, The Authors. Published under Creative Commons(CC BY 4.0) license (https://creativecommons.org/licenses/by/4.0/). For a color version of this figure, see www.iste.co.uk/romero/metamaterials.zip*

8.4. Practical applications of phononic crystals

Clearly, the initial expectations for phononic crystals in the 2000s, driven by the possibility to guide waves along phononic channels and to manipulate them using resonant cavities or stubs, are not living up to the expectations of the RF telecommunication systems community. Potentially practical implementation are mostly limited to their use as building blocks of resonator structures: mostly as very compact reflectors. Even so, their added value may be questioned, as well-established, simpler and at least effective reflector structures are already employed by the resonator community. Niche applications for phononic crystals however remain, notably in the field of MEMS resonators, SAW devices and in relation with photonics, which we detail in this section.

8.4.1. *Phononics for MEMS resonators*

As highlighted in section 8.3.2, phononic crystals do not perform more effectively than conventional reflector structures for acoustic resonators. This is especially true for Lamb wave (also referred to as contour mode) resonators that rely on ending abruptly the resonant cavity with a solid/air interface to implement a perfect reflector. Such resonators, implemented as suspended membranes, need mechanical supports to remain attached to the substrate. These anchors may provide a path for acoustic leakage out of the resonators. This is where Sorenson *et al.* proposed to replace the usually straight tethers supporting the resonator body, an example of which is depicted in Figure 8.20, by a phononic crystal whose band gap falls around the resonance frequency of the resonator in order to confine acoustic waves in the resonant cavity. A first version of such a crystal is a line of ring-shaped resonant structures, an example of which is shown in Figure 8.22(a) [SOR 11]. With such anchors, the quality factor of the resonator considered in [QIN 16] increases from 2,660, in the case where straight tethers are employed, to 6,250. This comes, however, at the expense of adding small parasitic resonances at the edges of the phononic band gap. Using instead a gourd-shaped periodic structure, shown in Figure 8.23(a), which geometrically differs less from a conventional straight tether, Wu *et al.* obtained a reduced quality factor improvement (from 1,304 for a straight tether to 1,893 for the gourd-shaped phononic crystal tethered resonator, as visible in Figure 8.23(b)). They managed, to even remove some parasitic resonances that could be noted on measurements of resonators with straight tethers [WU 16].

For appropriate designs, the achievable quality factor increase can therefore be significant and proves the effectiveness of phononic crystal tethers to suppress anchor losses. Yet, more conventional methods have already demonstrated a similar efficiency. The easiest and most straightforward method is to design straight tethers

with a length corresponding to a quarter wavelength. Considering electrostatically actuated length extensional resonators, Jansen *et al.* have thoroughly investigated the dependence of the quality factor of the resonator on the length of the support tethers [JAN 11]. They demonstrated that the quality factor of a suspended MEMS resonator can increase from 3,000 to 19,000 with a proper design of straight tethers, hence showing that there is no absolute need to involve more fragile and complex designs as phononic tethers.

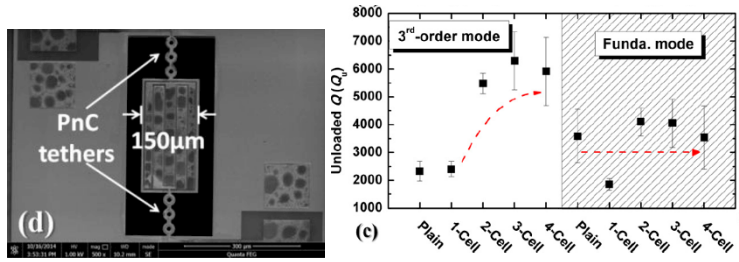

(a) (b)

Figure 8.22. *Lamb wave resonator with a phononic crystal tether based on a line of ring resonators (a) and implact of the type of tether on the measured quality factor(b). Reprinted from [ZHU 19]. Copyright 2019, with permission from Elsevier. For a color version of this figure, see www.iste.co.uk/romero/metamaterials.zip*

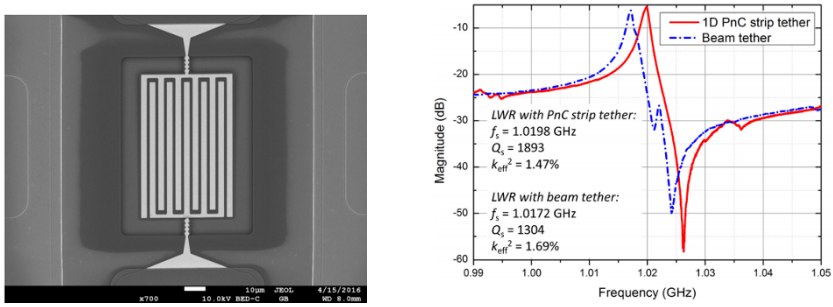

(a) (b)

Figure 8.23. *Lamb wave resonator with gourd-shape phononic crystal tethers: (a) optical microscope picture; (b) measurement of a resonator (red continuous line) and comparison with a reference structure with a conventional tether (blue dashed line). Reprinted from [WU 16], with the permission of AIP Publishing. For a color version of this figure, see www.iste.co.uk/romero/metamaterials.zip*

Tu *et al.* have in addition demonstrated that periodic arrays of holes and while they efficiently decrease anchor losses, they may also increase the amount of thermoelastic damping by one order of magnitude [TU 12]. This is probably do to with an increase in the coupling of shear deformations to compression of the matrix material. In the case of a Lamé mode resonator, this increased thermoelastic damping manages to replace anchor losses as the dominant loss mechanism.

There is, however, one point for which phononic crystal anchors provide a clear added-value: heat dissipation. Campanella *et al.* have investigated the behavior of Lamb wave resonators whose resonant cavity is limited by a phononic crystal and compared it to that of a conventional resonator delimited by a solid/air interface. When applying relatively high electrical input power, the resonators delimited by a phononic crystal revealed lower temperature increase than conventional ones. Assuming that the phononic crystal does not impact the dependence of the resonance frequency on temperature (which is caused by thermal expansion of the whole structure, as well as by the dependence of the elastic constants on temperature) the results in reduced frequency shifts due to temperature dependence of the resonance frequency [CAM 14] and, therefore, in a better frequency stability. This is very likely caused by the fact that the crystal, although filled with many holes, provides an additional path for heat dissipation compared to the abrupt ending of the resonator structure. The drawback is, however, reduced linearity, possibly attributed to the increased thermoelastic damping mentioned earlier.

As a conclusion, using phononic crystals as reflectors or as tethers for MEMS resonators is clearly not more effective than well-designed conventional tethers or air/solid interface reflectors. On the contrary, it may even increase the amount of thermoelastic damping compared to a fully solid structure. However, in some specific cases, it may provide a path for heat dissipation, which may find some interest if thermal stability is the major criterion sought.

8.4.2. *Phononics for surface acoustic wave resonators*

As we have seen in section 8.3.2, the initial attempts to replace the shorted electrode reflectors commonly employed in SAW resonators did not reveal a major gain in quality factors or in electromechanical coupling factors. Given also the fact, as discussed in section 8.2.2.1, that fabricating these crystals in piezoelectric substrates drastically complicates the otherwise simple fabrication process for SAW devices, it seems very unlikely that this approach finds application in the SAW filter industry unless phononic crystals manage bringing about a genuine technological or conceptual breakthrough.

It cannot, however, be denied that the SAW industry nowadays faces technological challenges linked to the inevitable increase in the required operation

frequency of filters. The major limitation in the operation frequency of SAW devices is the resolution of the interdigitated electrodes required to excite these waves, as the electrodes already exhibit submicron dimensions at frequencies higher than 1 GHz. This is a direct consequence from the relatively low propagation velocities of surface waves. Current standards at 2.45 GHz already call for finger dimensions lying straight at the limit of steppers used up to at least a few years back in the SAW industry, that is, 350 nm. The new resolution limit of 250 nm, – set by more recent lower-cost projection lithography affordable by others than the IC industry, – is about to be reached. Such dimensions raise considerable reliability concerns as the electric fields developing across sub-micron gaps reach rapidly extremely large values, which limits the power-handling capabilities of SAW devices. Therefore, the SAW filter community has been actively investigating other types of waves with higher phase velocities in the last four decades [HAG 72, TAN 07, CHI 10]. A solution is to deposit a thin piezoelectric film on top of a high-velocity substrate such as silicon, sapphire or diamond. In such structures, surface modes benefit from an increase in phase velocity due to the large stiffness of the substrate, seen through the evanescent tail of the mode. Truly guided modes, – confined mostly in the piezoelectric film through total internal reflection and exhibiting considerably large phase velocities, – are often overlooked, as they usually suffer from lower electromechanical coupling factors.

Elaborating on this, Khelif *et al.* [KHE 08] proposed to completely guide waves in the piezoelectric film by relying on the confinement brought by an acoustic Bragg mirror. Taking the example of a tungsten/aluminum multilayer, they theoretically demonstrated that such a 1D phononic crystal can open an omnidirectional band gap and can therefore prohibit any radiation of waves towards the substrate in the frequency band of interest. Adding a piezoelectric film on top of the superlattice produces defect modes localized in the film, which acts as an effective waveguide. In such conditions, they proved that resonances can be obtained at 5.5 GHz for interdigitated electrode periods of 1.2 μm. Such a structure is reasonably achievable both in terms of electrodes dimensions and in the fabrication of the superlattice, which only requires the deposition of six films on a substrate, a technological process that remains simpler than the processes in use by the RF BAW industry.

A similar idea was further considered by Koné *et al.* [KON 10], although their Bragg mirror did not necessarily open an omnidirectional band gap. Provided that the transmission of waves from the piezoelectric film to the substrate remains low enough (typically below –25 dB, as seen in Figure 8.24(a)) for waves mixing longitudinal and shear polarization at a wavelength compatible with the period of the interdigitated transducer, the mirror fulfills its role and can efficiently trap waves in the piezoelectric film, as seen on the displacement distribution shown in Figure 8.24(b). In such conditions, the guided waves operate very close to Lamb waves and can, therefore, exhibit very large phase velocities. In [KON 10], a

resonance frequency of 1.83 GHz was reached using a mode similar to the S_1 Lamb mode in a piezoelectric plate, for an electrode period of 8.4 μm.

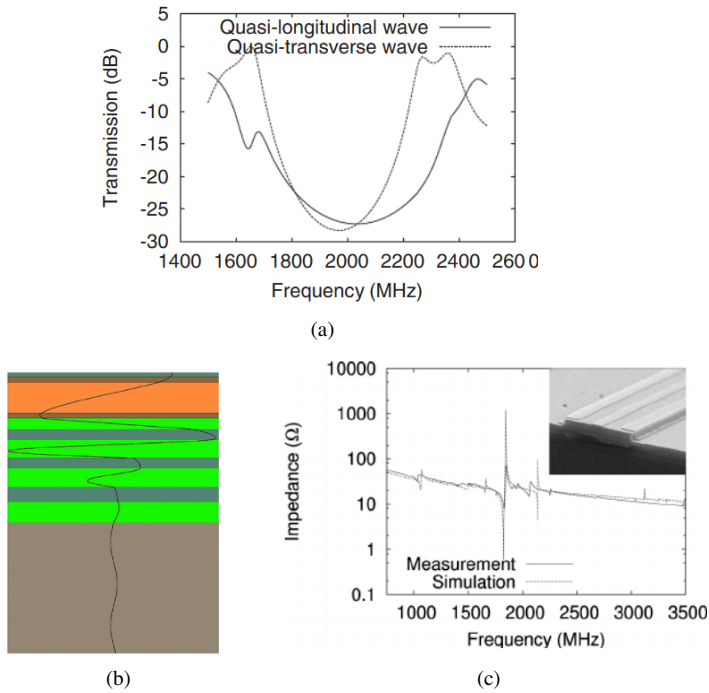

Figure 8.24. *Resonators exploiting waves guided in an aluminum nitride film on top of an SiN/SiOC Bragg mirror: (a) transmission coefficient for longitudinal and shear waves of the Bragg reflector, (b) sketch of the layer stack and of the vertical displacement field versus depth of the mode of interest and (c) electric response (inset, a scanning electron microscopy image of the resonator) of the resonator (solid) along with the simulated response (dashed). Reprinted from [KON 10], with the permission of AIP Publishing*

Despite reaching high frequencies, the resonators obtained in these initial works suffered from relatively low electromechanical coupling factors (respectively 0.75% and 2%). This made them inappropriate for the synthesis of front-end filters. The reason for such low electromechanical coupling factors originated from the fact that Lamb waves in aluminum nitride, which was considered as the piezoelectric film in these two works, exhibit naturally relatively weak electromechanical coupling factor. This material performs better for bulk wave resonators. For this reason, Takai *et al.* [TAK 16] investigated the use of lithium tantalate as the piezoelectric material, since it benefits from increased piezoelectric properties compared to aluminum nitride.

This material cannot be readily deposited, but a thin single-crystal film of $LiTaO_3$ can be transferred on a supporting substrate as an alternative. Takai *et al.* used this technology to transfer such a film on top of a Bragg mirror made of silicon dioxide and aluminum nitride or silicon nitride, to fabricate resonators and filters operating at 1.9 GHz. The low intrinsic losses of lithium tantalate, added to the high confinement of waves brought by the acoustic reflector, provided quality factors close to 4,000, that is, three times larger than conventional SAW devices fabricated on a bulk lithium tantalate substrate. Moreover, inserting silicon dioxide in the resonator, – a material that, unlike nearly any other, – has the extremely interesting property of having a stiffness increasing with temperature, offers some significant compensation of the frequency drifts with temperature. The cumulation of these three important parameters for the synthesis of high-performance filters has caused this solution to be dubbed "incredibly high-performance SAW" (IHP-SAW) and made it currently a hot topic in the filter community.

Still, one-dimensional superlattices, or Bragg mirrors, cannot be fully related to phononics. The literature, however, features some higher-dimensional examples of particularly well-suited applications of phononic crystals to SAW resonators. One elegant approach has been proposed by Solal *et al.* [SOL 10a] to solve the issue related to parasitic resonances appearing in SAW resonators due to diffraction effects in the electrode gratings and causing lateral standing waves, which perturb the electric response of resonators. These phenomena degrade the quality factor of these components, which translates into additional transmission losses for a filter. To prevent their formation, the authors propose to add a second periodicity to the initial one inherited from the periodic electrode strips. This takes the form of tungsten plugs added periodically on top of the interdigitated electrodes of resonators, as sketched in Figure 8.25(a). This two-dimensional periodic structure opens a band gap, which then prevents the propagation of waves in the direction perpendicular to the expected surface waves, and as such improves the quality factor of SAW resonators. With a very close approach, Yantchev and Plessky [YAN 13] considered acoustic diffraction, not only inside the electrode gratings as a source of loss in SAW resonators, but also towards the outside of the resonators. These sources of leakage arise from the natural diffraction occurring due to the finite length of the electrodes, as well as because at their ends the electrodes face the opposite bus bar, so that the local electric field perpendicular to the expected propagation direction causes the excitation of laterally propagating waves. To prevent these losses, they also propose to add plugs over the bus bars of the SAW resonators. Their work has so far only remained theoretical, and for the moment, industrial SAW filters do not seem to embed phononic structures for parasitic resonances suppression.

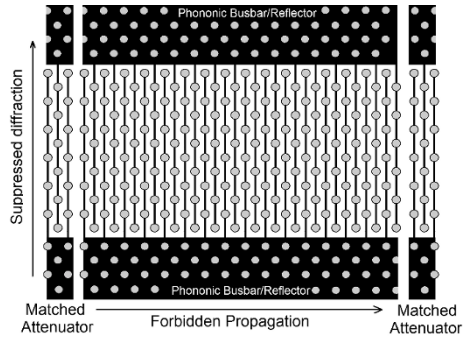

Figure 8.25. *Phononic crystal made of W plugs positioned on top of the electrodes of a SAW resonator for the suppression of lateral wave diffraction in interdigitated transducers. Reprinted from [YAN 13], with the permission of AIP Publishing*

8.4.3. *Phononics for photonics*

As a last field of application, a striking feature of Figure 8.1 is that hypersonic waves exhibit the same wavelengths as optical waves. Optical communications are another way to transmit data in addition to air propagation. The fact that radiofrequency acoustic waves share the same wavelengths as optical waves, and can therefore interact at the wavelength level, offers one way of manipulating optical waves with radiofrequency signals.

Interaction of light with elastic waves, however, occurs irrespective of the commensurability of their respective wavelength. The most widespread component illustrating this is the acousto-optical modulator: the strain produced by an elastic wave causes periodic variations of the refractive index of the medium that affects the propagation of optical waves, usually by acting like a time-dependent diffraction grating. Because these perturbations occur at regular intervals they cause a modulation of the optical signal and are widely used in acousto-optic modulators. Commercial acousto-optical modulators are based on interactions occurring in a bulk substrate, with a transduction piezoelectric layer usually separated from the propagation medium [XU 92]. Attempts to transpose the concept of these devices to integrated optical systems have been reported in the literature. The proposed integrated modulators rely on surface acoustic waves to provide the necessary strain, due to their ease of fabrication and the natural confinement of strain close to the surface of the substrates where optical waveguides can be easily implemented. If diffraction efficiencies close to one could be reached [TSA 13], efficiency of the acousto-optical coupling is, however, relatively low and requires very long

interaction length and high input acoustic power to achieve satisfying performances. The concepts and capabilities offered by the advent of photonic and phononic crystals appeared as potential ways to circumvent these limitations. Tailoring the dispersion properties of optical waves with photonic crystals has, for instance, led to the concept of *slow light*, when the group velocity of optical waves can be strongly decreased by the bending of dispersion curves close to the edges of the photonic band gap. This calls for largely increased interaction times with the perturbation source, either electro-optic [ROU 06, BRO 08] or acousto-optic [RUS 03, LIM 05, COU 10]. Even stronger interaction is expected when the interaction between elastic strains and electromagnetic fields is exacerbated by a simultaneous confinement of the acoustic and optical waves in a phononic/photonic waveguide or cavity. This fact was first observed in one-dimensional superlattices [TRI 02], and then doserved in specifically designed photonic crystal fibers [KAN 09] or cavities [FUH 11]. It has then motivated the research for crystals simultaneously exhibiting band gaps for optical and elastic waves, also dubbed *phoxonic crystals*.

Maldolvan and Thomas theoretically demonstrated that complete photonic and phononic band gaps can open in infinite two-dimensional square or hexagonal lattices of holes [MAL 06a]. They also showed that such crystals could be used to provide simultaneous confinement of elastic and optical waves in cavities [MAL 06b]. Later, Pennec *et al.* [PEN 10] and Mohammadi *et al.* [MOH 10] demonstrated that this is also possible in silicon slabs drilled with circular air holes forming a honeycomb lattice for high filling fractions. They demonstrated that other arrangements lead to gaps only valid for some specific polarizations of light. El Hassouani *et al.* demonstrated that arrays of silicon pillars formed on top of a silicon dioxide slab, and on their side, can exhibit complete phoxonic band gaps for any type of lattice [ELH 10].

The field enhancement expected by a joint confinement of light and sound also opens appealing perspectives in the fast expanding field of *optomechanics*. Optomechanics is based on the use and enhancement of the interaction between optical radiation-pressure forces and mechanical motion. This interaction was initially exploited to achieve ground-state cooling for ions in ultracold atom experiments and has since then shown its potential for coherent control of the mechanical motion of micro- or nanoscale objects with relatively large masses, hence setting an exciting playground for, among others, the realization of table top quantum experiments [ASP 14]. In some cases, radiation-pressure forces can be seen as a relevant way to replace the conventional piezoelectric or electrostatic transduction for nanostructures, since these schemes do not scale favorably when dimensions become smaller, while optical forces become significant for low-mass objects. This, – associated with the intrinsic contactless nature of this transduction scheme, in the sense that no electrodes are required at the level of the resonator, – makes it particularly suited to ultrasensitive mechanical sensing [KRA 12]. As a now fairly

standard scheme for such an experiment, Li *et al.* excited the vibration of a freestanding clamped–clamped silicon beam using the electromagnetic radiation forces generated by its proximity with an optical waveguide and probed the displacement of this resonator through an evanescent coupling between the optical waveguide and the nano-beam [LI 08]. One of the first applications of this readout scheme is optical modulation: the displacements of the resonator induced by the optical forces induces a time-varying geometrical configuration, which in turn translates in tuning the photonic circuits [ROS 09]. Conversely through the interplay of the mechanical nonlinearities, – which are naturally strong in nanoscale mechanical structures, – the optical forces can oppose in some configuration the motion of the mechanical structure and quench it. This allows us to counteract the natural motion of a nano-mechanical structure caused by the thermal phonon bath, and is therefore called *optical cooling* [ARC 06].

All these applications require high-quality factor, mechanical and optical structures to convert the relatively weak forces into large displacements, or to benefit from a naturally weak coupling to the thermal phonon bath [FON 10]. Such high-quality factors are achieved by a proper choice of material with low damping (silicon, or strained silicon nitride [FON 10]), as well as with a beam structure capable of offering a strong localization for the optical and mechanical modes. This is where phoxonic crystals come into play. In [EIC 09], the crystal takes the form of a one-dimensional crystal with a ladder shape, obtained by etching almost rectangular holes along the length of a silicon nano-beam. Several designs combining phononic crystal-based acoustic shielding and one- and two-dimensional optomechanical cavities were then proposed and implemented [SAF 10, CHA 12]. More recent structures rely now on a combination of strain engineering and mechanical decoupling from the surroundings of the resonator [GHA 18, FED 19]. Engineering strain consists in tapering the nano-beam to concentrate stress up to the material yield strength in the region where waves will be localized. When in high tension, the material is made stiffer, which strongly decreases its mechanical damping. Mechanical decoupling is achieved by adding a phononic crystal to suppress anchor losses, as was proposed for MEMS resonators. To accommodate for the dispersion induced by the tapering of the beam, the phoxonic crystal, – taking the form of stubs added to the edges of the beam, – is also tapered, as shown in Figure 8.26. Such an exquisite arrangement manages to provide elastic modes with quality factor times frequency products in the range of 10^{15} Hz at room temperature, which is an order of magnitude higher than the best electromechanical resonators reported to date. The perspectives opened by such high-quality factors are resonators with extremely long phonon coherence time. Also a sufficiently low number of thermal phonons reveal quantum elastic effects in relatively large mechanical objects without the need to go towards cryogenic temperatures.

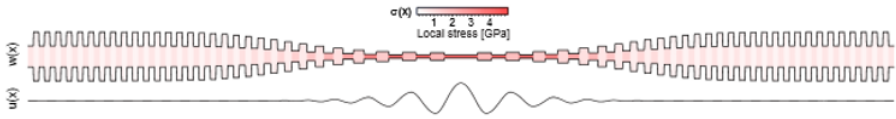

Figure 8.26. *Nano-mechanical beam resonator benefiting from strain engineering and from a phononic crystal to increase the phonon coherence time. Reprinted from [FED 19]. Copyright 2019, with the permission of the American Physical Society*

From a shorter-term perspective, optomechanical systems have proved relevant for the realization of radiofrequency signal processing devices, given the intrinsic information transfer occurring between the optical and the RF or microwave domains in such physical systems. A practical implementation to the field of information and communication technologies however requires a higher level of integration that can be reached by integrating an electrical or piezoelectrical actuation scheme to the opto-mechanical system in order to drive the mechanical motion through external, stronger, coherent RF driving fields. These optomechanical on-chip devices have received growing interest over the past few years, and tend to integrate a rising number of functionalities and degrees of freedom for both the RF and the optical regimes [WIN 11, BOC 13, XIO 13]. If a complete integration of simultaneous photonic and phononic crystals or cavities in such systems is still to be unambiguously demonstrated, then strategies based on the association of a photonic nanobeam with a phononic waveguide have been used to show that both optical and mechanical excitation and readout of the RF signal could be achieved [BAL 16]. Interestingly, the proposed architecture integrates interdigitated transducers operating at 2.4 GHz, a configuration that brings the proposed device closer to more classical piezoelectric RF components and paves the way to an integrated circuitry supporting traveling elastic waves. This broadens the already wide avenues opened by recent developments in nano-opto-electromechanical systems [MID 18]. Whether elastic metamaterials will be considered as presenting enough added-value to be integrated in already complex systems is still an open discussion.

8.5. Perspectives

The applications of phononic crystals, or more generally of elastic metamaterials, to radiofrequency applications is a perfect example of adoption of a new technology following the *hype cycle* developed by the research and advisory firm Gartner [GAR 16].

Starting with early works on phononic crystals as a *technology trigger*, initial expectations were the possibility of introducing phononic chips built upon phononic

waveguide circuits. The ambition was to achieve complex functions devoted to wave manipulations, which would outperform RF electronics with a tremendous level of miniaturization. Early developments led in the early 2000s demonstrated the possibility of implementing phononic crystals operating in the hypersonic regime and compatible with already existing acoustic resonator structures such as SAW or BAW devices. The confidence grew when waveguides, stubbed structures and resonant cavities were demonstrated, until reaching a *peak of inflated expectations* in the early 2010s. It however soon became evident that the specifications that could be expected from phononic structures were far behind the needs of RF communications systems, which were already pushing mature technologies such as SAW or BAW devices to extremes. Waveguides suffered from utterly large losses; reflectors, although compact, did not provide a better confinement than existing solutions and even induced more complexity and caused additional design concerns. Even the adoption of phononic crystals as replacement for resonator anchors by the MEMS community did, generally speaking, not fulfill expectations. The *trough of disillusionment* was reached.

There are some clues that the *slope of enlightenment* may be the current state for radiofrequency elastic metamaterials, although one can only look backwards to evaluate a position on a hype cycle *a posteriori*. As discussed in section 8.4.2, some applications are still under investigation for SAW devices: the current interest in incredibly high-performance SAW filters may be a sign, although these devices have not yet entered in mass production as promised in the end of 2016 [TAK 16].

We can also briefly mention some ongoing works for integration of mechanical resonators within integrated circuits [BAR 15], with the goal of delivering miniaturized timing functions directly at the core of circuits, or to provide mechanical signal processing, which could lower power consumption compared to the same functions achieved using transistors. Such mechanical devices, being solidly embedded inside the interconnection structures of transistors, would have to rely on hypersonic crystals such as the ones described in Figure 8.12(a). More generally, the field of *acoustoelectronics*, – that is the manipulation of electrons by acoustic waves propagating in semiconductor materials, or the perturbation of transistors (e.g. the modulation of their gate voltage) by a radiofrequency wave – is also currently a growing field of interest.

The fields of phoxonics or optomechanics described in section 8.4.3 are also full of promises. Such structures could benefit optical telecommunications, as well as high-sensitivity sensors and quantum information processing. Mechanical confinement has proved to be a necessary ingredient of these optomechanical systems and may provide an application field for elastic metamaterials. In addition to actuation through radiation-pressure forces, the recent reports of optomechanical

platforms involving coherent elastic wave source in the GHz range have triggered some interest in the community of quantum electromechanics. Inspired by the use of surface acoustic wave devices in semiconductor physics as charge and spin carriers [HER 11, MCN 11], the field of circuit quantum electrodynamics (CQED), defined as the solid-state equivalent of QED, has started adopting SAW [GUS 14] and BAW [CHU 17] devices as the source of the mechanical motion to be coupled with superconducting qubits. In this context, operating at GHz frequencies and with mechanical cavities with high quality factors is key, which may revive interest for hypersonic phononic cavities.

8.6. References

[ACH 11] ACHAOUI Y., KHELIF A., BENCHABANE S. *et al.*, "Experimental observation of locally-resonant and Bragg band gaps for surface guided waves in a phononic crystal of pillars", *Physical Review B*, vol. 83, p. 104201, American Physical Society, March 2011. Available at: https://doi.org/10.1103/PhysRevB.83.104201.

[ARC 06] ARCIZET O., COHADON P.-F., BRIANT T. *et al.*, "Radiation-pressure cooling and optomechanical instability of a micro-mirror", *Nature*, vol. 444, p. 71, 2006. Available at: https://doi.org/10.1038/nature05244.

[ASH 17] ASH B.J., WORSFOLD S.R., VUKUSIC P. *et al.*, "A highly attenuating and frequency tailorable annular hole phononic crystal for surface acoustic waves", *Nature Communications*, vol. 8, p. 174, 2017. Available at: https://doi.org/10.1038/s41467-017-00278-0.

[ASP 14] ASPELMEYER M., KIPPENBERG T.J., MARQUARDT F., "Cavity optomechanics", *Reviews of Modern Physics*, vol. 86, pp. 1391–1452, American Physical Society, December 2014. Available at: https://doi.org/10.1103/RevModPhys.86.1391.

[ASS 08] ASSOUAR B.M., VINCENT B. MOUBCHIR H., "Phononic crystals based on $LiNbO_3$ realised using domain inversion by electron-beam irradiation", *IEEE Transactions on Ultrasonics, Ferroelectrics, and Frequency Control*, vol. 55, no. 2, pp. 273–278, 2008. Available at: https://doi.org/10.1109/TUFFC.2008.645.

[AUL 76] AULD B., GAGNEPAIN J., "Horizontal shear surface 432waves on corrugated surfaces", *Electronics Letters*, vol. 12, pp. 650–433, 1976.

[BAL 16] BALRAM K.C., DAVANCO M.I., SONG J.D. *et al.*, "Coherent coupling between radiofrequency, optical and acoustic waves in piezo-optomechanical circuits", *Nature Photonics*, vol. 10, pp. 346–352, 2016. Available at: https://doi.org/10.1038/nphoton.2016.46.

[BAR 98] BARTELS A., DEKORSY T., KURZ H. *et al.*, "Coherent control of acoustic phonons in semiconductor superlattices", *Applied Physics Letters*, vol. 72, p. 2844, 1998. Available at: https://doi.org/10.1063/1.121476.

[BAR 15] BAR B., MARATHE R., WEINSTEIN D., "Theory and design of phononic crystals for unreleased CMOS-MEMS resonant body transistors", *Journal of Microelectromechanical systems*, vol. 24, pp. 1520–1533, 2015. Available at: https://doi.org/10.1109/JMEMS.2015.2418789.

[BEN 06] BENCHABANE S., KHELIF A., RAUCH J. *et al.*, "Evidence for complete surface wave band gap in a piezoelectric phononic crystal", *Physical Review E*, vol. 73, p. 065601, 2006. Available at: https://doi.org/10.1103/PhysRevE.73.065601.

[BEN 15] BENCHABANE S., GAIFFE O., SALUT R. *et al.*, "Guidance of surface waves in a micron-scale phononic crystal line-defect waveguide", *Applied Physics Letters*, vol. 106, p. 081903, 2015. Available at: https://doi.org/10.1063/1.4913532.

[BOC 13] BOCHMANN J., VAINSENCHER A., AWSCHALOM D.D. *et al.*, "Nanomechanical coupling between microwave and optical photons", *Nature Physics*, vol. 9, pp. 712–716, 2013. Available at: https://doi.org/10.1038/nphys2748.

[BOE 13] BOECHLER N., ELIASON J.K., KUMAR A. *et al.*, "Interaction of a contact resonance of microspheres with surface acoustic waves", *Physical Review Letters*, vol. 111, p. 036103, American Physical Society, July 2013. Available at: https://doi.org/10.1103/PhysRevLett.111.036103.

[BRO 08] BROSI J.-M., KOOS C., ANDREANI L.C. *et al.*, "High-speed low-voltage electro-optic modulator with a polymer-infiltrated silicon photonic crystal waveguide", *Optics Express*, vol. 16, no. 6, pp. 4177–4191, OSA, 2008. Available at: https://doi.org/10.1364/OE.16.004177.

[CAM 14] CAMPANELLA H., WANG N., NARDUCCI M. *et al.*, "Integration of RF MEMS resonators and phononic crystals for high frequency applications with frequency-selective heat management and efficient power handling", *2014 International Electron Device Meeting*, pp. 566–569, 2014. Available at: https://doi.org/ 10.1109/IEDM.2014.7047102.

[CHA 12] CHAN J., SAFAVI-NAEINI A.H., HILL J.T. *et al.*, "Optimized optomechanical crystal cavity with acoustic radiation shield", *Applied Physics Letters*, vol. 101, no. 8, p. 081115, 2012. Available at: https://doi.org/10.1063/1.4747726.

[CHI 10] CHIANG Y.-F., SUNG C.-C., RO R., "Effects of metal buffer layer on characteristics of surface acoustic waves in ZnO/metal/diamond structures", *Applied Physics Letters*, vol. 96, p. 154104, 2010. Available at: https://doi.org/10.1063/1.3400219.

[CHU 17] CHU Y., KHAREL P., RENNINGER W.H. *et al.*, "Quantum acoustics with superconducting qubits", *Science*, vol. 358, pp. 199–202, 2017. Available at: https://doi.org/10.1126/science.aao1511.

[COU 10] COURJAL N., BENCHABANE S., DAHDAH J. *et al.*, "Acousto-optically tunable lithium niobate photonic crystal", *Applied Physics Letters*, vol. 96, p. 131103, 2010. Available at: https://doi.org/10.1063/1.3374886.

[CUF 12] CUFFE J., CHAVEZ E., SHCHEPETOV A. *et al.*, "Phonons in slow motion: Dispersion relations in ultrathin Si membranes", *Nano Letters*, vol. 12, pp. 3569–3573, 2012. Available at: https://doi.org/10.1021/nl301204u.

[DEF 01] DEFRANOULD P., WRIGHT P., "Filtres à ondes de surface", *Techniques de l'Ingénieur*, Editions TI, 2001.

[DHA 00] DHAR L., ROGERS J.A., "High frequency one-dimensional phononic crystal characterized with a picosecond transient grating photoacoustique technique", *Applied Physics Letters*, vol. 77, p. 1402, 2000. Available at: https://doi.org/10.1063/1.1290388.

[DIE 01] DIEULESAINT E., ROYER D., "Dispositifs acousto-électroniques", *Techniques de l'Ingénieur*, Editions TI, 2001.

[EIC 09] EICHENFIELD M., CHAN J., COMACHO R.M. *et al.*, "Optomechanical crystals", *Nature*, vol. 462, p. 78, 2009. Available at: https://doi.org/10.1038/nature08524.

[ELH 10] EL HASSOUANI Y., LI C., PENNEC Y. *et al.*, "Dual phononic and photonic band gaps in a periodic array of pillars deposited on a thin plate", *Physical Review B*, vol. 82, p. 155405, 2010. Available at: https://doi.org/10.1103/PhysRevB.82.155405.

[ELI 16] ELIASON J., VEGA-FLICK A., HIRAIWA M. *et al.*, "Resonant attenuation of surface acoustic waves by a disordered monolayer of microspheres", *Applied Physics Letters*, vol. 108, p. 061907, 2016. Available at: https://doi.org/10.1063/1.4941808.

[FED 19] FEDOROV S.A., ENGELSEN N.J., GHADIMI A.H. *et al.*, *Physical Review B*, vol. 99, p. 054107, 2019. Available at: https://doi.org/10.1103/PhysRevB.99.054107.

[FON 10] FONG K.Y., PERNICE H.P., LI M. *et al.*, "High Q optomechanical resonators in silicon nitride nanophotonic circuits", *Applied Physics Letters*, vol. 97, p. 073112, 2010. Available at: https://doi.org/10.1063/1.3480411.

[FUH 11] FUHRMANN D.A., THON S.M., KIM H. *et al.*, "Dynamic modulation of photonic crystal nanocavities using gigahertz acoustic phonons", *Nature Photonics*, vol. 5, pp. 605–609, 2011. Available at: https://doi.org/10.1038/nphoton.2011.208.

[GAR 16] GARTNER, Available at: https://www.gartner.com/en/research/methodologies/gartner-hype-cycle, 2016.

[GHA 18] GHADIMI A.H., FEDOROV S.A., ENGELSEN N.J. *et al.*, "Elastic strain engineering for ultralow mechanical dissipation", *Science*, vol. 360, pp. 764–768, 2018. Available at: https://doi.org/10.1126/science.aar6939.

[GOR 05] GORISHNYY T., ULLAL C., MALDOVAN M. *et al.*, "Hypersonic phononic crystals", *Physical Review Letters*, vol. 94, p. 115501, March 2005. Available at: https://doi.org/10.1103/PhysRevLett.94.115501.

[GOR 11] GORISSE M., BENCHABANE S., TEISSIER G. *et al.*, "Observation of band gaps in the GHz range and deaf bands in a hypersonic aluminium nitride phononic crystal slab", *Applied Physics Letters*, vol. 98, p. 234103, 2011. Available at: https://doi.org/10.1063/1.3598425.

[GRA 12] GRACZYKOWSKI B., MIELCAREK S., TRZASKOWSKA A. *et al.*, "Tuning of a hypersonic surface phononic band gap using a nanoscale two-dimensional lattice of pillars", *Physical Review B*, vol. 86, p. 085426, 2012. Available at: https://doi.org/10.1103/PhysRevB.86.085426.

[GUS 14] GUSTAFSSON M.V., AREF T., KOCKUM A.F. *et al.*, "Propagating phonons coupled to an artificial atom", *Science*, vol. 346, no. 6206, pp. 207–211, American Association for the Advancement of Science, 2014. Available at: https://doi.org/10.1126/science.1257219.

[HAG 72] HAGON P.J., DYAL L., LAKIN K.M., "Wide band UHF compression filters using aluminum nitride on sapphire", *Proceedings of the 1972 IEEE Ultrasonics Symposium*, pp. 274–275, 1972. Available at: https://doi.org/10.1109/ULTSYM.1972.196078.

[HER 11] HERMELIN S., TAKADA S., YAMAMOTO M. *et al.*, "Electrons surfing on sound wave as a plateform for quantum optics with flying electrons", *Nature*, vol. 477, pp. 435–438, 2011. Available at: https://doi.org/10.1038/nature10416.

[HIR 16] HIRAIWA M., ABI GHANEM M., WALLEN S.P. *et al.*, "Complex contact-based dynamics of microsphere monolayers revealed by resonant attenuation of surface acoustic waves", *Physical Review Letters*, vol. 116, p. 198001, American Physical Society, May 2016. Available at: https://doi.org/10.1103/PhysRevLett.116.198001.

[HSI 07] HSIAO F.-L., KHELIF A., MOUBCHIR H. *et al.*, "Complete band gaps and deaf bands of triangular and honeycomb water-steel phononic crystals", *Journal of Applied Physics*, vol. 101, p. 044903, 2007. Available at: https://doi.org/10.1063/1.2472650.

[HSU 06] HSU J.-C., WU T.-T., "Efficient formulation for band-structure calculations of two-dimensional phononic crystal plates", *Physical Review B*, vol. 74, p. 144303, 2006. Available at: https://doi.org/10.1103/physrevb.74.144303.

[HSU 07a] HSU J.-C., WU T.-T., "Lamb waves in binary locally resonant phononic plates with two-dimensional lattices", *Applied Physics Letters*, vol. 90, p. 201904, 2007. Available at: https://doi.org/10.1063/1.2739369.

[HSU 07b] HSU J.-C., WU T.-T., "Analysis of Lamb-wave dispersion and band gaps of two-dimensional piezoelectric phononic-crystal plates", *Proceedings of the 2007 IEEE Ultrasonics Symposium*, pp. 624–627, 2007. Available at: https://doi.org/10.1109/ultsym.2007.162.

[JAN 11] JANSEN R., STOFFELS S., ROTTENBERG X. *et al.*, "Optimal T-support anchoring for BAR-type BAW resonators", *MEMS 2011*, pp. 609–612, 2011. Available at: https://doi.org/10.1109/memsys.2011.5734498.

[KAF 00] KAFESAKI M., SIGALAS M., GARCIA N., "Frequency modulation in the transmittivity of wave guides in elastic-wave band-gap materials", *Physical Review Letters*, vol. 85, pp. 4044–4047, 2000. Available at: https://doi.org/10.1103/physrevlett.85.4044.

[KAN 09] KANG M.S., NAZARKIN A., BRENN A. *et al.*, "Tightly trapped acoustic phonons in photonic crystal fibres as highly nonlinear artificial Raman oscillators", *Nature Physical*, vol. 5, pp. 276–280, 2009. Available at: https://doi.org/10.1038/nphys1217.

[KHE 02] KHELIF A., DJAFARI-ROUHANI B., VASSEUR J. *et al.*, "Transmittivity through straight and stublike waveguides in a two-dimensional phononic crystal", *Physical Review B*, vol. 65, p. 174308, 2002. Available at: https://doi.org/10.1103/physrevb.65.174308.

[KHE 03] KHELIF A., CHOUJAA A., DJAFARI-ROUHANI B. *et al.*, "Trapping and guiding of acoustic waves by defect modes in a full-band-gap ultrasonic crystal", *Physical Review B*, vol. 68, p. 214301, 2003. Available at: https://doi.org/10.1103/physrevb.68.214301.

[KHE 04] KHELIF A., CHOUJAA A., BENCHABANE S. *et al.*, "Guiding and bending of acoustic waves in highly confined phononic crystal waveguides", *Applied Physics Letters*, vol. 84, p. 4400, 2004. Available at: https://doi.org/10.1063/1.1757642.

[KHE 08] KHELIF A., CHOUJAA A., RAUCH J.-Y. *et al.*, "The OmniSAW device concept", *IEEE Ultrasonics Symposium*, 2008. Available at: https://doi.org/10.1109/ultsym.2008.0075.

[KHE 10a] KHELIF A., ACHAOUI Y., BENCHABANE S. *et al.*, "Locally resonant surface acoustic wave band gaps in a two-dimensional phononic crystal of pillars on a surface", *Physical Review B*, vol. 81, p. 214303, 2010. Available at: https://doi.org/10.1103/physrevb.81.214303.

[KHE 10b] KHELIF A., MOHAMMADI S., EFTEKHAR A.A. *et al.*, "Acoustic confinement and waveguiding with a line-defect structure in phononic crystal slabs", *Journal of Applied Physics*, vol. 108, p. 084515, 2010. Available at: https://doi.org/10.1063/1.3500226.

[KOK 07] KOKKONEN K., KAIVOLA M., BENCHABANE S. *et al.*, "Scattering of surface acoustic waves by a phononic crystal revealed by heterodyne interferometry", *Applied Physics Letters*, vol. 91, p. 083517, 2007. Available at: https://doi.org/10.1063/1.2768910.

[KON 10] KONÉ I., DOMINGUE F., REINHARDT A. *et al.*, "Guided acoustic wave resonators using an acoustic Bragg mirror", *Applied Physics Letters*, vol. 96, p. 223504, 2010. Available at: https://doi.org/10.1063/1.3440370.

[KRA 12] KRAUSE A.G., WINGER M., BLASIUS T.D. *et al.*, "A high-resolution microchip optomechanical accelerometer", *Nature Photonics*, vol. 6, pp. 768–772, 2012. Available at: https://doi.org/10.1038/nphoton.2012.245.

[KUO 11] KUO N.-K., PIAZZA G., "1 GHz phononic band gap structure in air/aluminum nitride for symmetric Lamb waves", *MEMS 2011*, pp. 740–743, 2011. Available at: https://doi.org/10.1109/memsys.2011.5734531.

[LAU 05] LAUDE V., WILM M., KHELIF A. *et al.*, "Full band gap for surface acoustic waves in a piezoelectric phononic crystal", *Physical Review E*, vol. 71, p. 036607, 2005. Available at: https://doi.org/10.1103/physreve.71.036607.

[LI 08] LI M., PERNICE W.H.P., XIONG C. *et al.*, "Harnessing optical forces in integrated photonic circuits", *Nature*, vol. 456, pp. 480–484, 2008. Available at: https://doi.org/10.1038/nature07545.

[LIM 05] DE LIMA JR M.M., SANTOS P.V., "Modulation of photonic structures by surface acoustic waves", *Reports on Progress in Physics*, vol. 68, no. 7, p. 1639, 2005.

[LIU 14] LIU T.-W., TSAI Y.-C., LIN Y.-C. *et al.*, "Design and fabrication of a phononic-crystal-based Love wave resonator in GHz range", *AIP Advances*, vol. 4, p. 124201, 2014. Available at: https://doi.org/10.1063/1.4902018.

[MAD 02] MADOU, MARC J., *Fundamentals of Microfabrication: The Science of Miniaturization*, CRC Press, Boca Raton, 2002.

[MAL 06a] MALDOLVAN M., THOMAS E.L., "Simultaneous complete elastic and electromagnetic band gaps in periodic structures", *Applied Physics B*, vol. 83, p. 595, 2006. Available at: https://doi.org/10.1007/s00340-006-2241-y.

[MAL 06b] MALDOLVAN M., THOMAS E.L., "Simultaneous localization of photons and phonons in two-dimensional periodic structures", *Applied Physics Letters*, vol. 88, p. 251907, 2006. Available at: https://doi.org/10.1063/1.2216885.

[MAR 05] MARKSTEINER S., KAITILA J., FATTINGER G.G. *et al.*, "Optimization of acoustic mirrors for solidly mounted BAW resonators", *Proceedings of the IEEE Ultrasonics Symposium*, pp. 329–332, 2005. Available at: https://doi.org/10.1109/ULTSYM.2005.1602861.

[MAY 91] MAYER P.A., ZIERAU W., MARADUDIN A., "Surface acoustic waves propagating along the grooves of a periodic grating", *Journal of Applied Physics*, vol. 69, no. 4, pp. 1942–1947, 1991. Available at: https://doi.org/10.1063/1.348969.

[MCN 11] MCNEIL R.P.G., KATAOKA M., FORD C.J.B. *et al.*, "On-demand single-electron transfer between distant quantum dots", *Nature*, vol. 477, pp. 439–442, 2011. Available at: https://doi.org/10.1038/nature10444.

[MID 18] MIDOLO L., SCHLIESSER A., FIORE A., "Nano-opto-electro-mechanical systems", *Nature Nanotechnology*, vol. 13, pp. 11–18, 2018. Available at: https://doi.org/10.1038/s41565-017-0039-1.

[MOH 08] MOHAMMADI S., EFTEKHAR A.A., KHELIF A. *et al.*, "Evidence of large high frequency complete phononic band gaps in silicon phononic crystal plates", *Applied Physics Letters*, vol. 92, p. 221905, 2008. Available at: https://doi.org/10.1063/1.2939097.

[MOH 09] MOHAMMADI S., EFTEKHAR A.A., HUNT W.D. *et al.*, "High-Q micromechanical resonators in a two-dimensional phononic crystal slab", *Applied Physics Letters*, vol. 94, p. 051906, 2009. Available at: https://doi.org/10.1063/1.3078284.

[MOH 10] MOHAMMADI S., EFTEKHAR A.A., KHELIF A. *et al.*, "Simultaneous two-dimensional phononic and photonic band gaps in opto-mechanical crystal slabs", *Optics Express*, vol. 18, p. 9164, 2010. Available at: https://doi.org/10.1364/oe.18.009164.

[MOH 11] MOHAMMADI S., EFTEKHAR A.A., POURABOLGHASEM R. *et al.*, "Simultaneous high-Q confinement and selective direct piezoelectric excitation of flexural and extensional lateral vibrations in a silicon phononic crystal slab resonator", *Sensors and Actuators A: Physical*, vol. 167, 2011. Available at: https://doi.org/10.1016/j.sna.2011.03.014.

[MOR 07] MORGAN D., *Surface Acoustic Wave Filters - With Applications to Electronic Communications and Signal Processing*, 2nd edition, Academic Press, 2007.

[NEW 65] NEWELL W., "Face-mounted piezoelectric resonators", *Proceedings of the IEEE*, vol. 53, pp. 575–581, 1965. Available at: https://doi.org/10.1109/proc.1965.3925.

[OLS 07] OLSSON R.H., FLEMING J.G., EL-KADY I.F. *et al.*, "Micromachined bulk wave acoustic bandgap devices", *Transducers and Eurosensors '07*, pp. 317–321, 2007. Available at: https://doi.org/10.1109/sensor.2007.4300132.

[OLS 09] OLSSON R.H., EL-KADY I., "Microfabricated phononic crystal devices and applications", *Measurement Science and Technology*, vol. 20, p. 012002, 2009. Available at: https://doi.org/10.1088/0957-0233/20/1/012002.

[OSE 18] OSEEV A., MUKHIN N.V., LUCKLUM R. *et al.*, "Towards macroporous phononic crystal based structures for FBAR applications. Theoretical investigation of technologically competitive solutions", *Microsystem Technologies*, vol. 24, pp. 2389–2399, 2018. Available at: https://doi.org/10.1007/s00542-017-3616-1.

[OUD 10] OUDICH M., ASSOUAR M.B., HOU Z., "Propagation of acoustic waves and waveguiding in a locally resonant phononic crystal plate", *Applied Physics Letters*, vol. 97, p. 193503, 2010. Available at: https://doi.org/10.1063/1.3513218.

[OZG 01] OZGUR U., LEE C.-W., EVERITT H.O., "Control of coherent acoustic phonons in semiconductor quantum wells", *Physical Review Letters*, vol. 86, p. 5604, 2001. Available at: https://doi.org/10.1103/physrevlett.86.5604.

[PEN 05] PENNEC Y., DJAFARI-ROUHANI B., VASSEUR J. *et al.*, "Acoustic channel drop tunneling in a phononic crystal", *Applied Physics Letters*, vol. 87, p. 261912, 2005. Available at: https://doi.org/10.1063/1.2158019.

[PEN 08] PENNEC Y., DJAFARI-ROUHANI B., LARABI H. *et al.*, "Low-frequency gaps in a phononic crystal constituted of cylindrical dots deposited on a thin homogeneous plate", *Physical Review B*, vol. 78, p. 104105, 2008. Available at: https://doi.org/10.1103/physrevb.78.104105.

[PEN 10] PENNEC Y., DJAFARI-ROUHANI B., EL BOUDOUTI E.H. *et al.*, "Simultaneous existence of phononic and photonic band gaps in periodic crystal slabs", *Optics Express*, vol. 18, p. 14301, 2010. Available at: https://doi.org/10.1364/oe.18.014301.

[QIN 16] QIN P., ZHU H., LEE J. E.-Y. *et al.*, "Phase noise reduction in a VHF MEMS-CMOS oscillator using phononic crystals", *Journal of the Electron Devices Society*, vol. 4, p. 149, 2016. Available at: https://doi.org/10.1109/jeds.2016.2527045.

[REI 11] REINKE C.M., SU M.F., OLSSON III R.H. *et al.*, "Realization of optimal bandgaps in solid-solid, solid-air, and hybrid solid-air-solid phononic crystal slabs", *Applied Physics Letters*, vol. 98, p. 061912, 2011.

[ROS 09] ROSENBERG J., LIN Q., PAINTER O., "Static and dynamic wavelength routing via the gradient optical force", *Nature Photonics*, vol. 3, pp. 478–483, 2009. Available at: https://doi.org/10.1038/nphoton.2009.137.

[ROU 06] ROUSSEY M., BERNAL M.-P., COURJAL N. *et al.*, "Electro-optic effect exaltation on lithium niobate photonic crystals due to slow photons", *Applied Physics Letters*, vol. 89, p. 241110, 2006. Available at: https://doi.org/10.1063/1.2402946.

[RUS 03] RUSSELL P.S.J., MARIN E., DÍEZ A. *et al.*, "Sonic band gaps in PCF preforms: Enhancing the interaction of sound and light", *Optics Express*, vol. 11, no. 20, pp. 2555–2560, OSA, October 2003. Available at: https://doi.org/10.1364/oe.11.002555.

[SAF 10] SAFAVI-NAEINI A.H., PAINTER O., "Design of optomechanical cavities and waveguides on a simultaneous bandgap phononic-photonic crystal slab", *Optics Express*, vol. 18, no. 14, pp. 14926–14943, OSA, July 2010. Available at: https://doi.org/10.1364/oe.18.014926.

[SOC 12] SOCIÉ L., BENCHABANE S., ROBERT L. *et al.*, "Surface acoustic wave guiding in a diffractionless high aspect ratio transducer", *Applied Physics Letters*, vol. 102, p. 113508. 2013. Available at: https://doi.org/10.1063/1.4795939.

[SOL 10a] SOLAL M., GRATIER J., KOOK T., "A SAW resonator with two-dimensional reflectors", *IEEE Transactions on Ultrasonics, Ferroelectrics, and Frequency Control*, vol. 57, pp. 30–37, 2010. Available at: https://doi.org/10.1109/freq.2009.5168174.

[SOL 10b] SOLIMAN Y., SU M., LESEMAN Z. *et al.*, "Phononic crystals operating in the gigahertz range with extremely wide band gaps", *Applied Physics Letters*, vol. 97, p. 193502, 2010. Available at: https://doi.org/10.1063/1.3504701.

[SOR 11] SORENSON L., FU J.L., AYAZI F., "One-dimensional linear acoustic bandgap structures for performance enhancement of AlN-on-Silicon micromechanical resonators", *2011 16th International Solid-State Sensors, Actuators and Microsystems Conference*, pp. 918–921, 2011. Available at: https://doi.org/10.1109/transducers.2011.5969685.

[SUN 09] SUN J.-H., WU T.-T., "Lamb wave source based on the resonant cavity of phononic crystal plates", *IEEE Transactions on Ultrasonics, Ferroelectrics, and Frequency Control*, vol. 56, p. 121, 2009. Available at: https://doi.org/10.1109/tuffc.2009.1011.

[SUN 10] SUN C.-Y., HSU J.-C., WU T.-T., "Resonant slow modes in phononic crystal plates with periodic membranes", *Applied Physics Letters*, vol. 97, p. 031902, 2010. Available at: https://doi.org/10.1063/1.3464955.

[TAK 16] TAKAI T., IWAMOTO H., TAKAMINE Y. *et al.*, "Incredible high performance SAW resonator on novel multi-latered substrate", *Proceedings of IEEE Ultrasonics Symposium*, pp. 456–459, 2016. Available at: https://doi.org/10.1109/ultsym.2016.7728455.

[TAL 06] TALHAMMER R., "Spurious mode suppression in BAW resonators", *Proceedings of IEEE Ultrasonics Symposium*, pp. 456–459, 2006. Available at: https://doi.org/10.1109/ultsym.2006.122.

[TAN 07] TANAKA A., YANAGITANI T., MATSUKAWA M. *et al.*, "Propagation characteristics of SH-SAW in (11–20) ZnO layer/silica glass substrate structure", *Proceedings of 2007 IEEE Ultrasonics Symposium*, pp. 280–283, 2007. Available at: https://doi.org/10.1109/ultsym.2007.81.

[TRI 02] TRIGO M., BRUCHHAUSEN A., FAINSTEIN A. *et al.*, "Confinement of acoustical vibrations in a semiconductor planar phonon cavity", *Physical Review Letters*, vol. 89, p. 227402, 2002. Available at: https://doi.org/10.1103/physrevlett.89.227402.

[TSA 13] TSAI C., *Guided-Wave Acousto-Optics: Interactions, Devices, and Applications*, Springer Series in Electronics and Photonics, Springer Berlin Heidelberg, 2013. Available at: https://doi.org/10.1117/1.oe.30.6.bkrvw1.

[TU 12] TU C., LEE J. E.-Y., "Increased dissipation from distributed etch holes in a lateral breathing mode silicon micromechanical resonator", *Applied Physics Letters*, vol. 101, p. 023504, 2012. Available at: https://doi.org/10.1063/1.4733728.

[WAN 15] WANG S., POPA L.C., WEINSTEIN D., "Tapered phononic crystal SAW resonator in GaN", *Proceedings of 2015 IEEE MEMS Conference*, pp. 1028–1031, 2015. Available at: https://doi.org/10.1109/memsys.2015.7051137.

[WHI 65] WHITE R., WOLTMER F., "Direct piezoelectric coupling to surface elastic waves", *Applied Physics Letters*, vol. 7, p. 314, 1965. Available at: https://doi.org/10.1063/1.1754276.

[WIN 11] WINGER M., BLASIUS T.D., ALEGRE T.P.M. *et al.*, "A chip-scale integrated cavity-electro-optomechanics platform", *Optics Express*, vol. 19, no. 25, pp. 24905–24921, OSA, December 2011. Available at: https://doi.org/10.1364/oe.19.024905.

[WU 04] WU T.-T., HUANG Z.-G., LIN S., "Surface and bulk acoustic waves in two-dimensional phononic crystal consisting of materials with general anisotropy", *Physical Review B*, vol. 69, p. 094301, 2004. Available at: https://doi.org/10.1103/physrevb.69.094301.

[WU 05a] WU T.-T., HSU Z.-C., HUANG Z.-G., "Band gaps and the electromechanical coupling coefficient of a surface acoustic wave in a two-dimensional piezoelectric phononic crystal", *Physical Review B*, vol. 71, p. 064303, 2005. Available at: https://doi.org/10.1103/physrevb.71.064303.

[WU 05b] WU T.-T., WU L.-C., HUANG Z.-G., "Frequency band-gap measurement of two-dimensional air/silicon phononic crystals using layered slanted finger interdigital transducers", *Journal of Applied Physics*, vol. 97, p. 094916, 2005. Available at: https://doi.org/10.1063/1.1893209.

[WU 09] WU T.-T., WANG W.-S., SUN J.-H. *et al.*, "Utilization of phononic crystal reflective gratings in a layered surface acoustic wave device", *Applied Physics Letters*, vol. 94, p. 101913, 2009. Available at: https://doi.org/10.1063/1.3100775.

[WU 16] WU G., ZHU Y., MERUGU S. *et al.*, "GHz spurious mode free AlN Lamb wave resonator with high figure of merit using one dimensional phononic crystal tethers", *Applied Physics Letters*, vol. 109, p. 013506, 2016. Available at: https://doi.org/10.1063/1.4955410.

[XIO 13] XIONG C., FAN L., SUN X. *et al.*, "Cavity piezootomechanics: Piezoelectrically excited, optically transduced optomechanical resonators", *Applied Physics Letters*, vol. 102, p. 021110, 2013. Available at: https://doi.org/10.1063/1.4788724.

[XU 92] XU J., STROUD R., *Acousto-Optic Devices: Principles, Design, and Applications*, New York, Wiley, 1992.

[YAM 08] YAMASHITA Y., HOSONO Y., "High effective lead perovskite ceramics and single crystals for ultrasonic imaging", in HEYWANG W., LUBITZ K., WERSING W. (eds), *Piezoelectricity: Evolution and Future of a Technology*, Chapter 9, pp. 223–244, Springer, Berlin, 2008. Available at: https://doi.org/10.1007/978-3-540-68683-5_9.

[YAN 13] YANTCHEV V., PLESSKY V., "Analysis of two dimensional composite surface grating structures with applications to low loss microacoustic resonators", *Journal of Applied Physics*, vol. 114, p. 074902, 2013. Available at: https://doi.org/10.1063/1.4818476.

[YOL 17] Yole Développement, RF Front-End modules and components for cellphones, 2017.

[YUD 12] YUDISTIRA D., PENNEC Y., DJAFARI ROUHANI B. *et al.*, "Non-radiative complete surface acoustic wave bandgap for finite-depth holey phononic crystal in lithium niobate", *Applied Physics Letters*, vol. 100, p. 061912, 2012. Available at: https://doi.org/10.1063/1.3684839.

[YUD 16] YUDISTIRA D., BOES A., GRACZYKOWSKI B. *et al.*, "Nanoscale pillar hypersonic surface phononic crystals", *Physical Review B*, vol. 94, p. 094304, American Physical Society, September 2016. Available at: https://doi.org/10.1103/physrevb.94.094304.

[ZHU 19] ZHU H., LEE J.E.-Y., "Design of phononic crystal tethers for frequency-selective quality factor enhancement in AlN piezoelectric-on-silicon resonator", *Procedia Engineering*, vol. 120, pp. 516–519, 2019.

9

Acoustic Metamaterials and Underwater Acoustics Applications

9.1. Materials for underwater acoustics: what applications?

Electromagnetic waves propagate poorly underwater, unlike acoustic waves which can be observed at long distance from the emitter, depending on source level and frequency. The development of the first sonar systems together with submarines about one century ago has initiated an extensive use of underwater sound by navies mainly in relation to underwater warfare. More recently, the increasing worldwide demand of energy and natural resources and the globalization of the economy have led to a steady increase of maritime traffic and industrial anthropogenic activity at sea. The growing concern of the scientific community regarding the impact of underwater sound on marine life incites policy makers and stakeholders of the maritime domain to mitigate their impact through appropriate measures. In that context, acoustic materials for different applications are presented below:

– reduction of noise radiated from underwater vehicles;

– reduction of acoustic target strength of underwater vehicles;

– integration of acoustic detection systems;

– underwater acoustics environmental issues

9.1.1. *Reduction of noise radiated from underwater vehicles*

Most underwater vehicles or submarines are equipped with machinery items and with propellers, which produce noise and vibration, radiating underwater sound

Chapter written by Christian AUDOLY.

Fundamentals and Applications of Acoustic Metamaterials: From Seismic to Radio Frequency,
First Edition. Edited by Vicente Romero-García and Anne-Christine Hladky-Hennion.

waves throughout the hull or directly if the noisy equipment is outside the hull. The sound emission, which is continuous through time, is higher at low frequencies and can propagate underwater at long distances, producing a sound field that can be detected by an adverse passive sonar, as shown in Figure 9.2. The noise emission is characterized by the radiated noise level, a quantity expressed in dB re 1 μPa^2 as a function of frequency, back-propagated at 1 meter.

In order to reduce the risk to be detected by an adverse passive sonar system, a requirement of importance for naval submarines is that the radiated noise level must not exceed a limit value agreed between the supplier and the customer, generally expressed in the form of a curve dependent on frequency. With the objective to fulfill the requirements, measures are taken at design by using intrinsically silent machinery equipment items, by reducing the transfer functions to the hull, thanks to elastic devices and mounts, and by designing silent propellers. An additional possibility is the use of external acoustic decoupling coatings, which allow significantly reducing the radiation efficiency of the radiated hull. The coating, generally a few centimeters thick with a low acoustic impedance, is schematically presented in Figure 9.1, affecting the transfer path numbers 1 (vibratory) and 3 (airborne). The frequency range of interest is from a very low frequency up to a few tens of kHz.

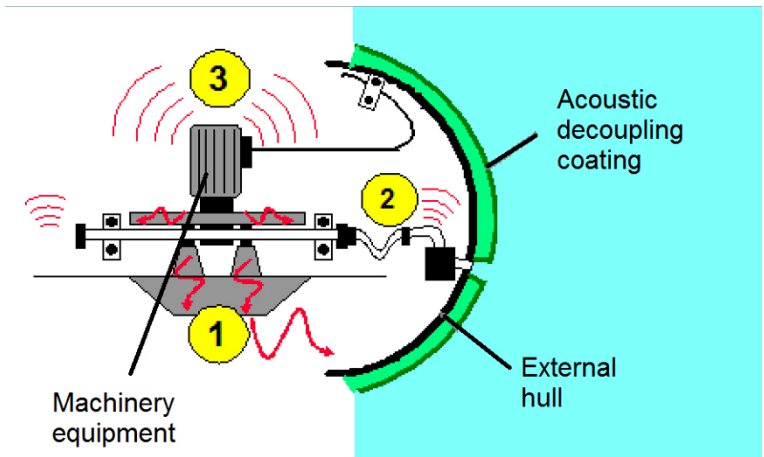

Figure 9.1. *Reduction of hull-radiated noise using an acoustic decoupling coating*

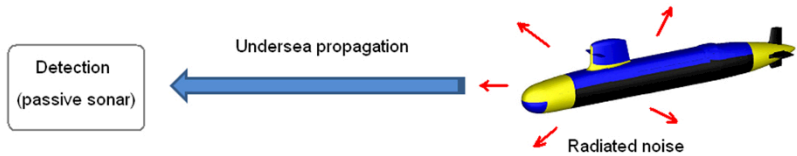

Figure 9.2. *Detection of an underwater vehicle by a passive sonar system*

9.1.2. *Reduction of acoustic target strength of underwater vehicles*

Another threat for underwater vehicles is low-frequency active sonars. The sonar emits powerful sound waves, in the form of short pulses, which propagate undersea. A sufficiently large submerged structure will generate an echo, characterized by the acoustic target strength (ratio of the backscattered energy and the incident energy), likely to be detected by the receiving antenna and processor of the sonar system (Figure 9.3). The target can also be an underwater object such as a mine. The frequencies of interest are generally from a few kHz up to 100 kHz, but new systems tend to use lower frequencies in order to increase their detection range.

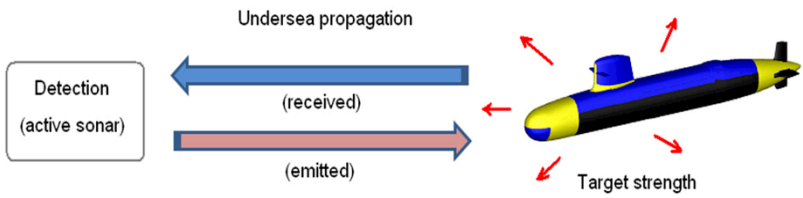

Figure 9.3. *Detection of an underwater vehicle by an active sonar system*

Target strength mainly depends on the size, shape and acoustic reflectivity of external surfaces, as well as on the direction of incoming waves. A first type of solution aiming to reduce target strength is the adaptation of the external shape, in conjunction with acoustic deflectors or screens, but this is not always feasible. Therefore, another possibility is the use of anechoic coatings, allowing the reduction of the outer hull by absorbing the incoming wave, as shown in Figure 9.4.

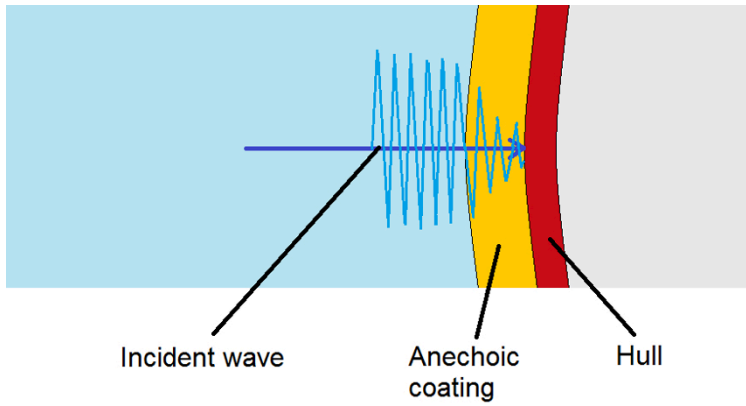

Figure 9.4. *Absorption of an incident wave using an anechoic coating*

9.1.3. *Integration of acoustic detection systems*

Ships and submarines are often fitted with acoustic systems for sensing the environment, detecting other underwater objects or for navigation aid. Acoustic materials or coatings are involved in the systems' integration in order to improve the acoustic response of the hydrophones (underwater acoustic sensors) or to protect the acoustic arrays from noise emitted by the ship (called self-noise). Some examples are illustrated in Figure 9.5:

– (left) for civilian applications, the hull of research vessels is equipped with different acoustic sensors requiring careful integration, possibly involving acoustic materials;

– (right) anechoic coatings are installed in order to eliminate reflected waves that could disturb the array response.

9.1.4. *Underwater acoustics environmental issues*

A growing matter of concern in the scientific community is the underwater noise pollution related to anthropogenic activity and its adverse impact on marine life. The European Community adopted in 2008 the MSFD (Marine Strategy Framework Directive), requiring the Member States to take appropriate measures in order to achieve a good environmental status by 2020 [EUR 08]. Among different forms of pollution, the introduction of energy, including underwater noise, has been taken into

account. In fact, most marine animals use sound for their biological functioning, such as finding prey or underwater communication. Two main cases must be considered:

– high level impulsive sound emissions that may lead to injuries or auditory troubles. This is the case in particular for active sonar pulses, underwater air guns used for oil and gas prospection at sea and marine pile driving (e.g. during the installation of offshore wind farms);

– lower level, but continuous, noise emissions. Except if the marine animals are very close to the sound source, these will not produce injuries. However, the inadequate soundscape leads to auditory masking or behavior changes, leading in the long term to negative effects. This is the case for noise footprints related to commercial ship traffic and marine renewable energy systems in operation.

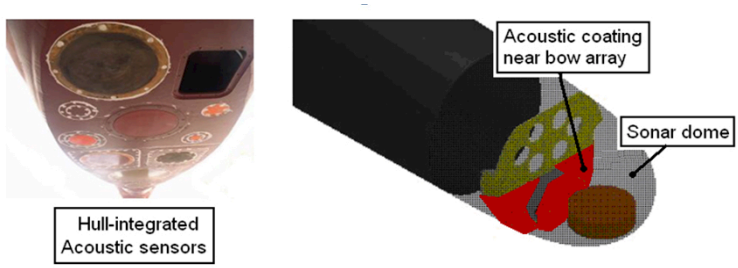

Figure 9.5. *Materials for the integration of acoustic sensors (left: research vessel; right: submarine bow section). For a color version of this figure, see www.iste.co.uk/romero/metamaterials.zip*

The frequency range of interest can be large, but the major concern is for low frequencies, typically lower than a few kHz. Some research or technology developments have addressed the mitigation of underwater noise. For example, regarding pile driving noise, the classical mitigation solution being the use of bubble curtains, alternative solutions using networks of rubber foam spheres or underwater resonators have been considered. An example of such a solution is presented in Figure 9.6.

Another important source of underwater noise is commercial shipping. Noise footprint mitigation solutions and strategies have been studied in the scope of a recent collaborative project [AUD 17]. A possible option is the installation of decoupling coatings on the ship hull.

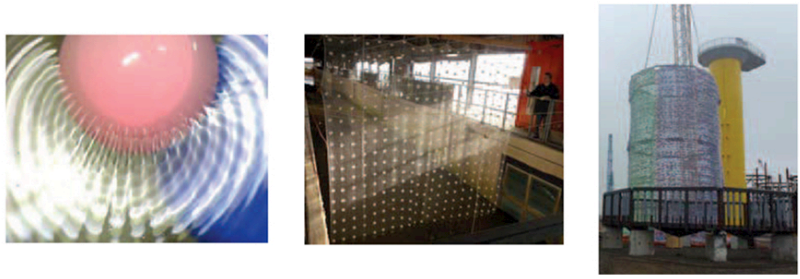

Figure 9.6. *Reduction of underwater noise emissions from pile driving using networks of rubber foam spheres (left: interaction of an acoustic wave with a sphere; middle: presentation in a workshop; right: preparation of deployment at sea). From Kuhn et al. [KUH 13])*

9.2. Definitions and characterization

9.2.1. *General*

Acoustic materials can have one or several of the following features:

– homogeneous: physical properties are the same within the material. On the contrary, layered or composite materials are heterogeneous;

– isotropic: the acoustical properties are independent from the direction. Again, composite layered materials are anisotropic;

– linear: the properties are independent of the intensity or level of excitation;

– dissipative: when a sound wave propagates inside the material, there is energy loss and the amplitude of the wave decays along the path;

– dispersive: the wave speed of sound is frequency-dependent.

An isotropic homogeneous material is characterized by the volumetric mass and two sound speeds (longitudinal and transverse). If the material is dissipative, in the case of harmonic excitation, then the sound speed is represented by a complex-valued quantity. A phononic crystal is an inhomogeneous medium formed by a periodic arrangement of inclusions in a host medium (fluid or solid). When varying frequency, a dispersive behavior appears, represented by the dispersion curve. Stop-bands, related to Bragg wave interference effects, correspond to frequencies where there is no long-range coherent propagation in the periodic material.

Metamaterials are artificial composites whose acoustic properties are uncommon in comparison to natural materials or their components. For example, they exhibit negative volumetric mass and/or sound speed or very high losses in some frequency ranges. There are two main differences with phononic crystals:

– the effects can occur at low frequencies (i.e. the thickness of the material or coating can be small in comparison to the wavelength);

– the distribution of inclusions can be either random or periodic, whereas phononic crystals are necessarily periodic.

9.2.2. *The acoustic cloak concept*

The concept of an "acoustic cloak", which has been reported many times in the literature, should not be confused with the concept of a metamaterial. As shown in Figure 9.7, the objective of the acoustic cloak concept is to achieve perfect stealth by diverting the scattered acoustic field from the target. The incoming wave does not penetrate the target, but its path is modified in such a way that it is trapped inside the cloak and reconstituted at the back. Two theories can be used to design such a coating: transformational acoustics and scattering cancellation.

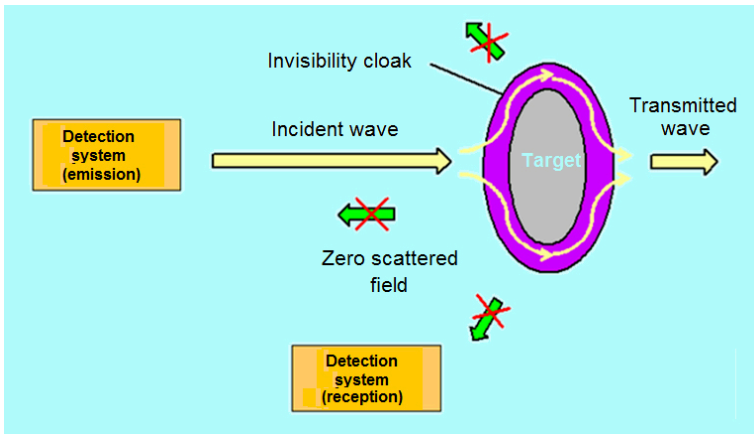

Figure 9.7. *Illustration of the acoustic cloak concept*

Transformation acoustics is based on a theory where the geometrical coordinates are modified in a domain surrounding the object in order to force the waves to split on it instead of interacting. The acoustics properties of the invisibility cloak domain

(density, speed of sound) are selected in order to allow the penetration of the incoming waves and the deviation of the wave path along their propagation. As shown in Figure 9.8, in the original theory, the density and sound speeds inside the cloak correspond to non-dissipative heterogeneous and anisotropic materials, with increasing values when the distance to the surface of the object decreases [CUM 07].

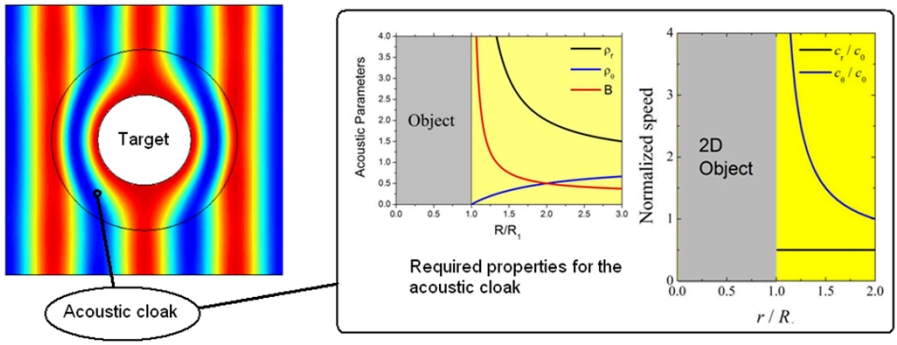

Figure 9.8. *Acoustic cloaking using transformation acoustics. From [CUM 07]. For a color version of this figure, see www.iste.co.uk/romero/metamaterials.zip*

The second approach is acoustic cloaking based on scattering cancellation. The target is surrounded by small secondary objects or structures whose acoustic fields, combined with the target echo of the main body, produce an overall null scattered far field. An example of application [SÁN 14] with simulations and laboratory experiments is shown in Figure 9.9.

In summary, to obtain the desired cloaking effect, the physical properties of the coating must be uncommon, thus requiring the use of special materials. In principle, acoustic metamaterials represent a technological solution to realize the constitutive materials in the cloak. However, our industry viewpoint is that the perfect cloak concept is not mature enough to be considered for practical applications in underwater acoustics. To date, although some authors claim otherwise, the theoretical and experimental works have led to thick coatings and/or narrowband efficiency. For that reason, in this chapter, we will focus on metamaterials themselves and not on the cloak concept.

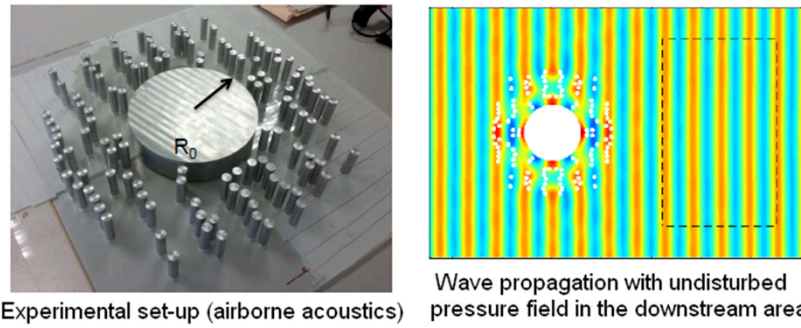

Figure 9.9. *Acoustic cloaking using scattering cancellation. From García-Chocano et al. [GAR 11]. For a color version of this figure, see www.iste.co.uk/romero/metamaterials.zip*

9.2.3. *Determination of performances of underwater acoustic materials and coatings*

Let us consider here the case of a submarine, which is the most demanding regarding performance and integration issues. First, as illustrated in Figure 9.10, depending on the needs, acoustic coatings can be installed on different parts of the hull: rigid pressure hull, bridge fin, bridge casing, aft and bow frameworks [AUD 11].

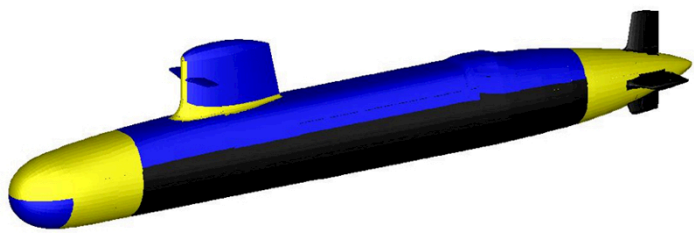

Figure 9.10. *Illustration of a submarine external hull with different areas*

Note that the supporting structure is not necessarily the pressure hull. For example, the skin of the bridge fin is often made with composite material such as GRP (glass-reinforced plastic), which is acoustically semi-transparent and not rigid.

Second, there are many non-acoustic requirements from the naval architects and the shipyards in order to practically integrate the coatings on a hull:

– limited thickness, generally no more than a few centimeters;

– limited density;

– sufficient thermal conductivity;

– limited static compressibility when submarine is diving;

– fire resistance;

– resistance to seawater environment;

– compatibility with gluing process.

Depending on the type of coating (anechoic, decoupling) and its zone of integrations, the relevant parameters for acoustic performance will be one of the following (Figure 9.11):

– decoupling efficiency or attenuation;

– reflection and/or transmission coefficient;

– anechoic coefficient (rigid backing).

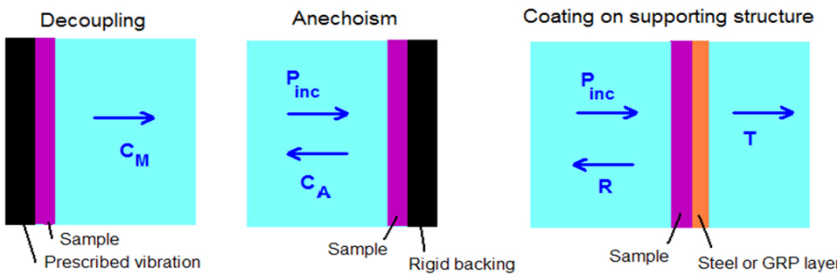

Figure 9.11. *Determination of acoustic performance of hull coatings. For a color version of this figure, see www.iste.co.uk/romero/metamaterials.zip*

The coefficients depend on frequency and incidence angle. They are non-dimensional and generally expressed in decibels. Characterization is usually done in acoustic tanks with measurement on test panels of size 1 m $\times$ 1 m (Figure 9.12).

Some recent work was done to improve the measurement techniques. Also, because it is not possible to directly obtain the decoupling and anechoic coefficients,

the measurement can be done with only the immersed coating, and a post-processing technique is used to obtain the information of interest [AUD 12].

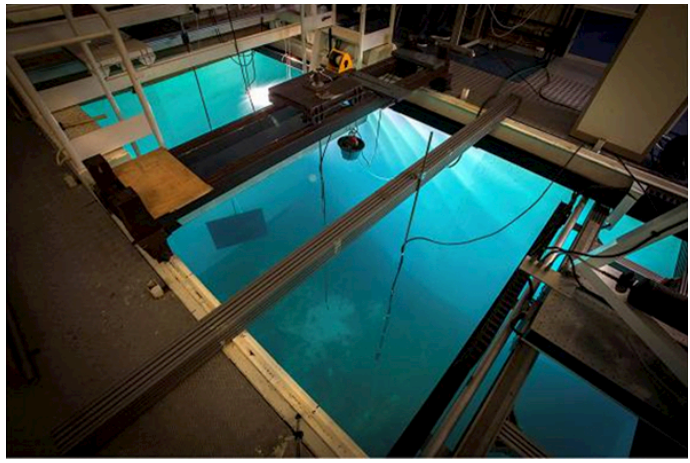

Figure 9.12. *Measurement of test panels of acoustic materials in a water tank. Example of the facility at ISEN, Lille*

9.3. Overview of current technology

The following is an overview of different media and materials in relation to underwater acoustics:

– fluids (water, seawater, some types of oil) are isotropic and have little dissipation and dispersion;

– gas (air or other gases) can be present in seawater in the form of bubbles, or encapsulated in other materials such as elastomers. In both cases, they have a strong acoustical effect. For example, a bubble curtain can produce large attenuation of the underwater acoustic propagation;

– metals (e.g. the hull of a ship) are isotropic and have little dissipation and dispersion;

– structural composite materials such as GRP (glass-reinforced plastics) are anisotropic and present a relatively small dispersion and dissipation;

– elastomers, which are often used for waterproofing or encapsulating transducers, are generally homogeneous (or considered as such) and isotropic. They are strongly dispersive and dissipative for transversal (or shear waves) but not for longitudinal waves. In fact, the longitudinal speed of elastomers' sound is close to that of water, and as a consequence, they behave as a transparent medium for the interaction

with underwater sound waves. Also, they do not have any significant attenuation or absorption performance if not combined with other materials or inclusions. Consequently, the availability of anechoic and decoupling materials for underwater acoustics requires a special design. Two classical concepts are introduced below: the micro-inclusion technology and the alberich-type coatings.

9.3.1. *Micro-inclusion-type acoustic coatings*

The principle of micro-inclusion technology consists of introducing some air or gas content in an elastomer matrix in the form of micro-cavities or micro-balloons with soft walls (size typically a few tens of μm). Also, other inclusions such as carbon black or minerals can be added to adjust density or to comply with some non-acoustic requirements. Although other elastomers can be used, polyurethanes are commonly used thanks to their versatility and the possibility to mold pieces without needing special thermal or high-pressure treatments. The volume ratio of air or gas is generally a few percent for anechoic coatings and 10% or more for decoupling ones. Once finished, the coating takes the form of tiles that can be installed on ship hulls following a gluing process. When needed, it is possible to design coatings with several layers of micro-inclusion materials (see Figure 9.13). Each layer is a heterogeneous, isotropic, dispersive and dissipative medium. However, for the frequency ranges of interest here, the material can be modeled as an equivalent homogeneous material, because the inclusions are very small compared to the wavelength and below resonance [KUS 74]. Therefore, this type of material cannot be considered as part of the category of metamaterials. In particular, there is a low-frequency limit related to thickness/wavenumber. Also, it should be noted that when submitted to hydrostatic pressure, the apparent volume ratio of air or gas diminishes, and consequently the composite's acoustic properties will evolve [BER 10].

Figure 9.13. *Acoustic coating technology using micro-inclusion materials*

The acoustic performances of a coating using that technology depend mainly on:

– the number of layers and their thickness;

– the acoustic characteristics of each layer, more particularly the density and the complex celerity of longitudinal waves (which depend on frequency and temperature).

Prediction of performance and design can be done using analytical models:

– evaluation of the effective parameters of the micro-inclusion materials using quasi-static homogenization models mentioned previously;

– propagation of plane waves in a multilayer medium with planar interfaces.

The modeling principle and an example of simulation results are shown in Figure 9.14.

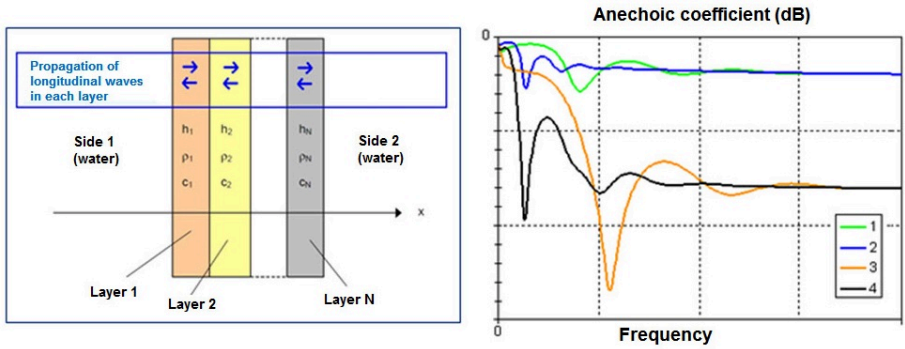

Figure 9.14. *Prediction of acoustic properties of a single-layer or multilayer micro-inclusion coating (right, numbers 1–4 correspond to different designs, with designs 3 and 4 having anechoic performances). For a color version of this figure, see www.iste.co.uk/romero/metamaterials.zip*

9.3.2. *Alberich-type acoustic coatings*

As micro-inclusion materials behave like homogeneous materials, their acoustic performances are directly linked to the reduced frequency, which is proportional to the ratio of thickness to the speed of sound in the material. Thus, it is, for example, difficult to design efficient anechoic materials at low frequencies. An alternative concept is the Alberich-type acoustic coating. The name comes from the historical rubber coating installed on a German submarine during World War II (Figure 9.15 (left)), which was designed with lattices of resonant cavities of appropriate diameters

corresponding to frequencies to be absorbed. This type of coating generally consists of a periodic arrangement of air cavities molded in an elastomer or rubber matrix. With that concept, it is possible to design both decoupling and anechoic coatings, with possibly improved performances, exploiting resonant phenomena. However, due to the resonant behavior, some limitations may appear regarding the frequency bandwidth of efficiency. In addition, similarly to the micro-inclusion technology, the performances are dependent on hydrostatic pressure because of the presence of voids or air inclusions.

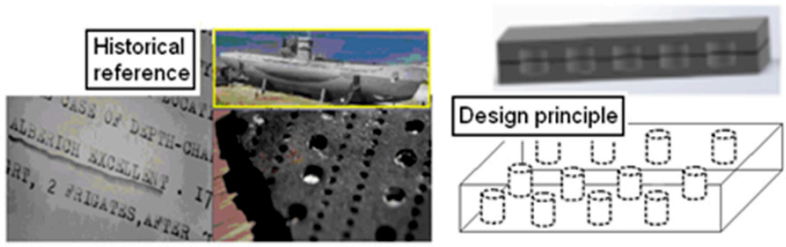

Figure 9.15. *Alberich-type acoustic coating technology*

Prediction of the acoustic performances of this type of coating can be done using the finite element method, by modeling a unit cell of the periodic structure. The first development of the numerical method was done in the framework of the ATILA code [HLA 91].

9.4. Examples of research in underwater acoustics metamaterials

A lot of research is currently being done worldwide, and as it is not possible to give a complete overview, we will focus here on some work done in France, including early research back in the 1990s.

9.4.1. *Compliant tube gratings*

The concept was introduced in the United States (and also studied in the Soviet Union) as a solution for submarine flank array acoustic barriers, in order to reduce noise coming from the hull to the array. It consists of a periodic array of resonant flat empty tubes made with metal or composite material. If properly designed, the tubes can withstand hydrostatic pressure up to a certain limit, without significant change in the acoustic performances. Theoretical models were developed using a semi-analytical approach: the partial domain method [RAD 82]. During my PhD thesis, I developed predictive models using both the previous method and the multiple-scattering theories

[AUD 89]. Note that the multiple-scattering theories can also deal with non-periodic arrangements. Results, checked for comparison with experimental results, show that there is a low transmission coefficient around some resonant frequencies of the tubes' cross-section (Figure 9.16).

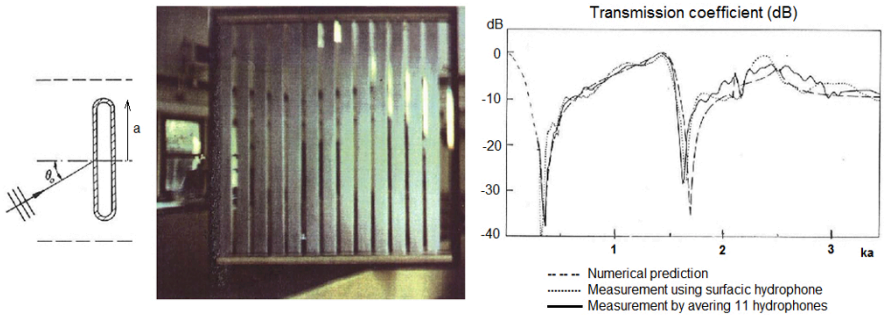

Figure 9.16. *Compliant tube grating – theory and experiment*

In order to improve the bandwidth associated with low transmission coefficients, it is possible to use several layers of tubes with different cross-sections. Figure 9.17 shows the result obtained using a bi-layer compliant tube grating, the tubes in the second layer being homothetic by a factor of 2 [AUD 91]. Also, regarding integration issues, the tube gratings can be embedded as a whole in a viscoelastic layer.

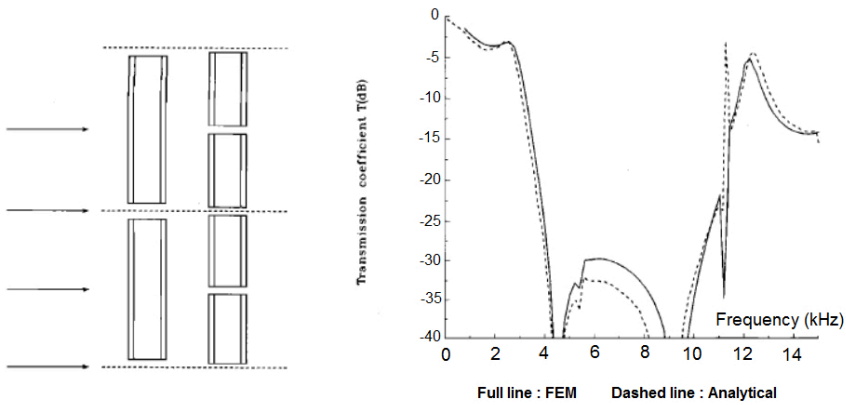

Figure 9.17. *Bi-layer compliant tube grating*

9.4.2. *Metamaterials formed with a periodic arrangement of inclusions in a viscoelastic matrix*

A first type that can considered to belong to the acoustic metamaterials category is the Alberich coating, already introduced in the previous section. In the scope of the development of the ATILA code for the modeling of periodic materials, different studies were carried out to optimize their performances or to compare with experimental results. As an example, Figure 9.18 presents the case of a coating formed with air cavities (in the form of short cylinders) in a layer of polyurethane, arranged periodically in two directions [HLA 91]. A strong attenuation is obtained in a certain frequency band, which is relatively narrow because of the resonant behavior. We observe as well a good comparison between experiment and prediction using the numerical model, provided we have a good knowledge of the characteristics of the matrix.

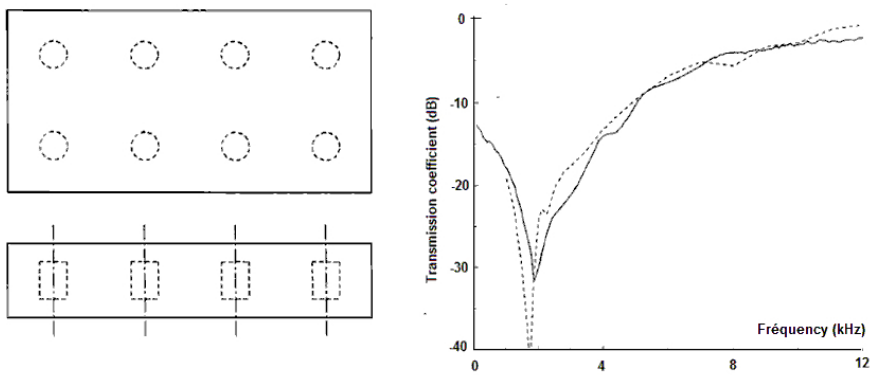

Figure 9.18. *Alberich material – test case and comparison with finite element method model. From [HLA 91]*

Recently, a thesis has revisited the concept of resonant inclusions in a viscoelastic matrix, considering multilayer structures including periodic arrangements of inclusions [MÉR 15]. A first objective was to develop a method allowing the determination of dispersion curves in a periodic material modeled by finite elements, taking into account losses in the matrix. Two methods were developed, giving consistent results, with an example in Figure 9.19:

– the “Bianco–Parodi” method, using the comparison of two fictive samples with different numbers of layers;

– the “transfer function” method, which uses a single elementary cell; it is more computationally time-consuming but provides more information (all solutions, including transverse equivalent wave speed).

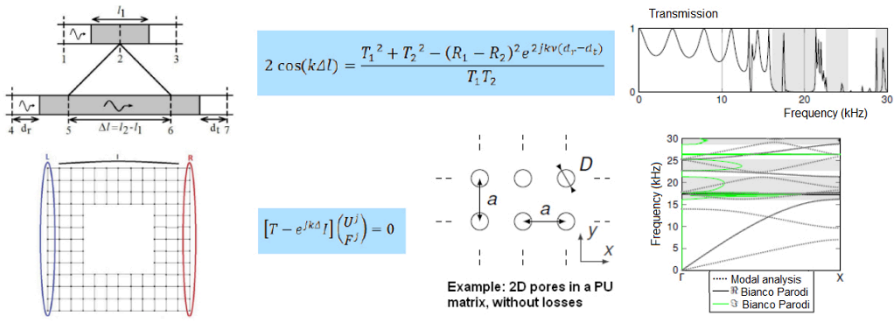

Figure 9.19. *Determination of effective speed of sound in periodic acoustic metamaterials modeled by the finite elements (left: principle of the two methods; right: transmission coefficient and dispersion curve). From [MÉR 15].For a color version of this figure, see www.iste.co.uk/romero/metamaterials.zip*

Parametric studies were carried out by varying the number of layers and the losses in the matrix for two cases: pores and steel rods (Figure 9.20, left). When the damping coefficient increases, it is more difficult to relate the stop bands and pass bands with the curves of reflection and the transmission coefficient according to the frequency, especially in the case of pores. One sample with one layer of steel rods embedded in a polyurethane matrix was tested in a water tank under the form of a test panel (Figure 9.20, right) and a good agreement was obtained with numerical prediction.

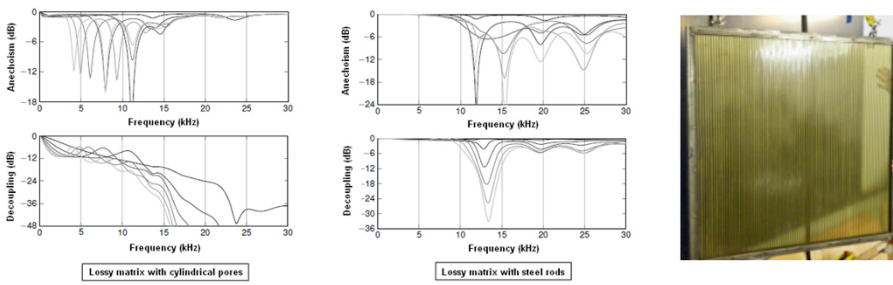

Figure 9.20. *Periodic gratings of cylindrical pores or steel rods embedded in a viscoelastic layer (left: influence of matrix losses on the acoustic performance; right: test sample). From [MÉR 15]*

Furthermore, parametric studies with a larger number of layers showed that it was possible to obtain a low transmission coefficient in a wide frequency with rigid scatterers, which is a configuration insensitive to hydrostatic pressure.

The performance could be enhanced using an "edge effect", i.e. by using rods of greater diameter for the two extreme layers. Other results were obtained by using "core-shell" inclusions (in such cases the inclusion is formed by the rod surrounded by a layer of material with stiffness smaller than that of the matrix). See Figure 9.21.

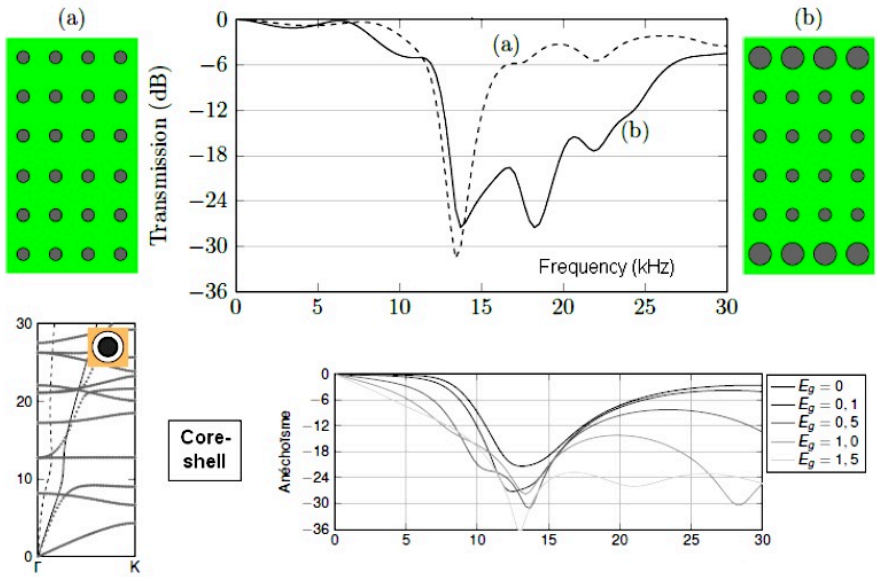

Figure 9.21. *Parametric study on metamaterials made with periodic arrangements of inclusions (top: concept with rigid inclusions and edge effect; bottom: core–shell inclusions). From [MÉR 15]*

9.4.3. *Metamaterials formed with a random distribution of inclusions in a viscoelastic matrix*

Another possibility to alter the wave propagation in a material and to obtain metamaterial effects is to incorporate a random distribution of inclusions in a viscoelastic matrix. Different authors have developed predictive models using the multiple scattering theory, assuming that the inclusions are spherical. The first step is to determine the effective parameters (speed of sound and density) as a function of frequency. Then, the reflection and transmission coefficients of a finite thickness layer of the composite material immersed in water can be computed using an analytical model.

A first attempt was made in the 1990s, where air inclusions were actually molded into viscoelastic layers [AUD 94]. An inversion technique was used to estimate the

effective speed of sound from the experimental results, and compared to models such as Waterman's [WAT 61]. The results, shown in Figure 9.22, confirmed the large variation of speed of sound in relation to the local resonances of the inclusions. However, a significant deviation was found between theory and experiment for a periodic configuration, and indeed, in that case, a finite element model is more suitable.

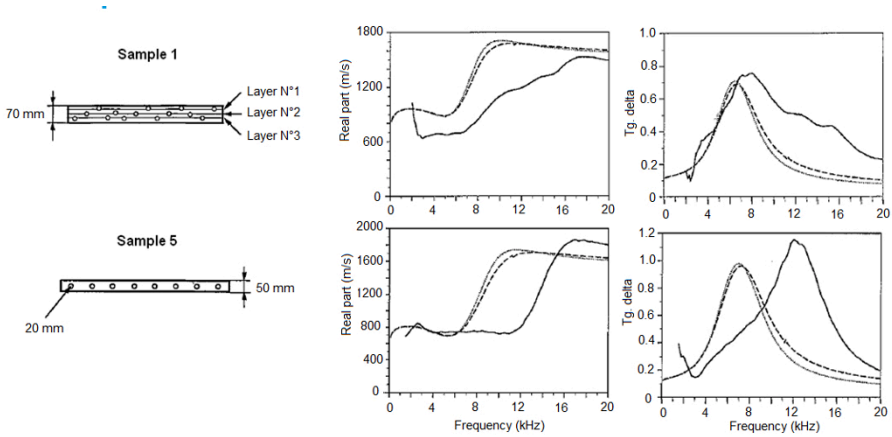

Figure 9.22. *Estimation of effective speed of sound of a viscoelastic layer containing distributions of spherical air inclusions. From [AUD 94]*

The subject was also theoretically and experimentally treated in a thesis [LEP 13a], considering both acoustically soft and hard spherical inclusions (polystyrene foam and lead, respectively) incorporated into different polymer matrices. The samples and inclusions were small, but as the experiments are done at ultrasonic frequencies, it was possible to observe the local resonances. An example of theoretical results for the effective speed of sound and density of the composites is shown in Figure 9.23. An interpretation of the phenomena observed is:

– in the case of soft inclusions: a dominant effect of monopole resonances leading to strong variations in the effective speed of sound and small variations in density;

– in the case of heavy inclusions: dominant effect of dipole resonances (or inertia behavior) leading to a significant variation in effective density and a small variation in speed of sound.

Of course, the importance of the phenomena is greater when the concentration of inclusions in the matrix is greater.

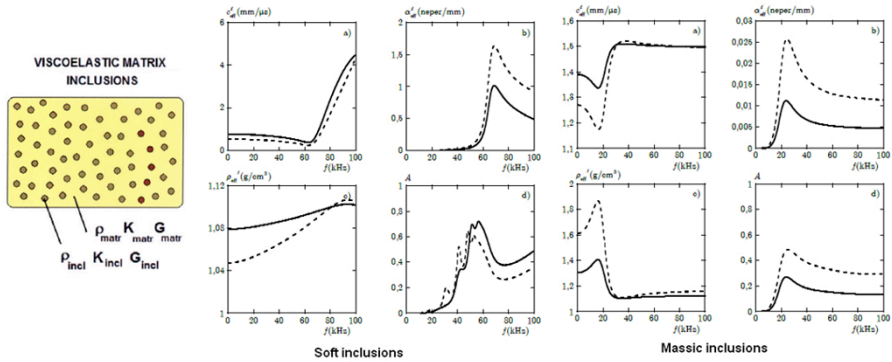

Figure 9.23. *Theoretical effective speed of sound in composites formed by resonant spherical inclusions randomly distributed in a polymer matrix (left: soft inclusions; right: massic inclusions); the dashed lines correspond to a greater concentration. From [LEP 13a]*

In Figure 9.24, it is shown that the use of core-shell inclusions (i.e. an inclusion formed of a high density core in a layer of soft material), can also give interesting acoustical effects, for example, a negative effective density [LEP 13b]. Here, the results are only theoretical (no samples were made for experiments), in contrast to the previous case.

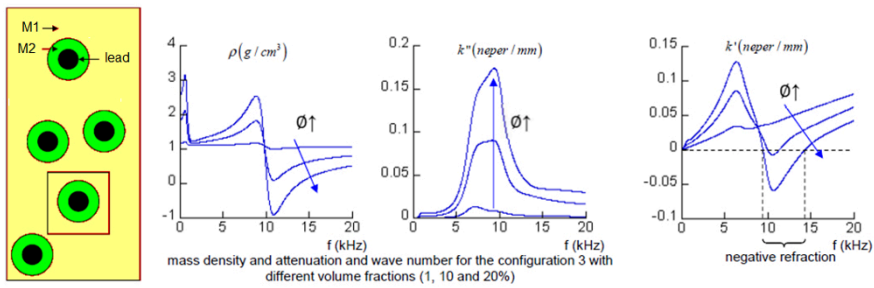

Figure 9.24. *Theoretical effective acoustic properties of a composite material with random distribution of core–shell inclusions in a polymer matrix, for increasing values of the concentration* Φ

From a technological point of view, a key aspect is the availability of inclusions with adequate and well-controlled characteristics. For that purpose, recent work has

focused on the use of a special process to realize porous silicon material with the possibility of tuning the acoustic properties [BA 16].

9.5. Challenges and perspectives

Despite the fact that hull acoustic coatings have already been used for some decades, there are still needs to be addressed, depending on the application:

– coatings for ship acoustic discretion and stealth:

- anechoism at low and very low frequencies,

- decoupling at low and very low frequencies,

- trade-off between acoustic performances and resistance/stability to hydrostatic pressure;

– underwater detection systems: multipurpose materials optimized for sonar array integration;

– civilian applications:

- commercial ships and marine renewable energy systems: low-cost decoupling coatings,

- acoustic materials for very deep waters.

Note also that the marine environment induces technological constraints, therefore:

– the choice of base materials must be done carefully;

– the transposition of solutions from airborne acoustics is not relevant or at least not straightforward.

Metamaterial-like concepts have been studied for a long time, but have recently gained a “hot topic” status. The emergence of new concepts of metamaterials, with new types of inclusions and arrangements in a matrix, allows us to open perspectives for solutions of applications in underwater acoustics with better performances:

– efficiency with low thickness-to-wavelength ratio;

– exploitation of stop-bands, super-resonant effects, negative dynamic density and/or wavenumber;

– new types of inclusions and/or optimum repartition in one or several layers.

However, together with the optimization of design, the practical realization of these new concepts, in compliance with the environmental constraints of underwater acoustics, and the experimental verification of the performances require more research and development effort.

9.6. References

[AUD 89] AUDOLY C., Etude de barrières acoustiques formées de réseaux d'obstacles résonnants, PhD thesis, University of Toulon, 1989.

[AUD 91] AUDOLY C., "Acoustic wave scattering from periodic gratings: Application to underwater acoustic baffles", *Undersea Defence Technology Conference*, Paris, France, 1991.

[AUD 94] AUDOLY C., "Acoustic analysis of panels made with viscoelastic materials containing resonant cavities", *Acta Acustica*, vol. 2, no. 5, 1994.

[AUD 11] AUDOLY C., "Acoustic characterisation of anechoic or decoupling coatings taking into account the supporting hull", *RINA Warship Conference. Naval Submarines and UUV*, Bath, UK, 29–30 June, 2011.

[AUD 12] AUDOLY C., "Determination of efficiency of anechoic or decoupling hull coatings using water tank acoustic measurements", *Congrès Français d'Acoustique*, Nantes, France, 2012.

[AUD 17] AUDOLY C., GAGGERO T., BAUDIN E. *et al.*, "Mitigation of underwater radiated noise related to shipping and its impact on marine life: A practical approach developed in the scope of AQUO project", *IEEE Journal of Oceanic Engineering*, vol. 42, no. 2, pp. 373–387, 2017.

[BA 16] BA A.S., Etude de la transmission acoustique de métaplaques localement résonantes, PhD thesis, University of Bordeaux, 2016.

[BER 10] BERETTI S., "Réponse acoustique d'élastomères micro-inclusionnaires soumis à la pression d'immersion", *Congrès Français d'Acoustique*, Lyon, France, 2010.

[CUM 07] CUMMER S., SCHURIG D., "One path to acoustic cloaking", *New Journal of Physics*, vol. 9, p. 45, 2007.

[EUR 08] EUROPEAN PARLIAMENT, Maritime Strategy Framework Directive 2008/56/EC, Council of the European Union, 2008.

[GAR 11] GARCÍA-CHOCANO V.M., SANCHIS L., DÍAZ-RUBIO A. *et al.*, "Acoustic cloak for airborne sound by inverse design", *Applied Physics Letters*, vol. 99, no. 7, p. 074102, 2011.

[HLA 91] HLADKY-HENNION A.-C., DECARPIGNY J., "Analysis of the scattering of a plane acoustic wave by a doubly periodic structure using the finite element method: Application to Alberich anechoic coatings", *Journal of the Acoustical Society of America*, vol. 90, no. 6, p. 3356, 1991.

[KUH 13] KUHN C., "Hydro sound dampers (HSD) – A new offshore piling noise mitigation system", *1st Conference on Underwater Acoustics*, Corfu, June 2013.

[KUS 74] KUSTER G.T., TOKSÖZ M.N., "Velocity and attenuation of seismic waves in two-phase media: Part I. Theoretical formulations", *Geophysics*, vol. 39, p. 587, 1974.

[LEP 13a] LEPERT G., Etude des interactions élasto-acoustiques dans des métamatériaux formés d'inclusions résonnantes réparties aléatoirement, PhD thesis, University of Bordeaux, 2013.

[LEP 13b] LEPERT G., ARISTÉGUI C., PONCELET O. *et al.*, "Study of the acoustic behavior of materials with core-shell inclusions", *12th Anglo-French Physical Acoustics Conference*, Fréjus, France, 2013.

[MÉR 15] MÉRESSE P., Matériaux absorbants à structure périodique et inclusions résonantes pour l'acoustique sous-marine, PhD thesis, Lille 1 University of Science and Technologies, 2015.

[RAD 82] RADLINSKI R., SIMON M., "Scattering by multiple grating of compliant tubes", *Journal of the Acoustical Society of America*, vol. 72, no. 607, 1982.

[SÁN 14] SÁNCHEZ-DEHESA J., "Advances in acoustics metamaterials and acoustic cloaks", *ARIADNA Workshop*, 2014.

[WAT 61] WATERMAN P., TRUELL R., "Multiple scattering of waves", *Journal of Mathematical Physics*, vol. 2, no. 4, p. 512, 1961.

Appendices

Fundamentals and Applications of Acoustic Metamaterials: From Seismic to Radio Frequency,
First Edition. Edited by Vicente Romero-García and Anne-Christine Hladky-Hennion.

Appendix 1

Homogenization of Thin 3D Periodic Structures in the Time Domain – Effective Boundary and Jump Conditions

A1.1. Properties of the effective coefficients $(A_{\alpha\beta}, C_{\alpha\beta})$ and $(B_\alpha, C_{1\alpha})$

We will see some relations between the effective coefficients. The demonstration of these relations is given for a structured film (the case of a structure on or in the vicinity of a rigid layer simply follows).

A1.1.1. $A_{23} = A_{32}$ *and* $A_{\alpha\alpha} \geq 0$ *(the same for* $C_{\alpha\beta}$*)*

Below, we will prove that:

$$A_{\alpha\beta} = A_{\beta\alpha} = \int_{\mathcal{Y}} \nabla Q_\alpha \cdot \nabla Q_\beta \mathrm{d}\mathbf{y}. \qquad [A1.1]$$

To do so, it is sufficient to evaluate

$$\begin{aligned} 0 &= \int_{\mathcal{Y}} Q_\alpha \Delta (Q_\beta + y_\beta) \\ &= -\int_{\mathcal{Y}} \nabla Q_\alpha \cdot \nabla Q_\beta \mathrm{d}\mathbf{y} - \int_{\mathcal{Y}} \frac{\partial Q_\alpha}{\partial y_\beta} \mathrm{d}\mathbf{y} + \int_{\partial\mathcal{Y}} Q_\alpha \nabla (Q_\beta + y_\beta) \cdot \mathbf{n} \, \mathrm{d}s. \end{aligned}$$

The last integral over $\partial\mathcal{Y}$ vanishes on Γ and on the rigid wall, on the periodic boundaries along y_2 and y_3 by periodicity, and also on $\mathsf{Y}(+y_1^m)$ when $y_1^m \to +\infty$

Chapter written by Agnès MAUREL, Kim PHAM and Jean-Jacques MARIGO.

since $n = \mathbf{e}_1$ and $\nabla Q_\beta \to 0$. This makes it possible to conclude that $A_{23} = A_{32}$ and that for $\alpha = \beta$, A_{22} and A_{33} are positive.

The same applies for $C_{\alpha\beta}$ where the last integral on $\partial\mathcal{Y}$ vanishes for the same reasons as in the case of a wall, but now we use that $\nabla(Q_\beta + y_\beta) \cdot \mathbf{n}$ vanishes on both $\mathsf{Y}(\pm y_1^m)$ when $y_1^m \to +\infty$ since $n = \pm\mathbf{e}_1$ and $\nabla Q_\beta \to 0$.

A1.1.2. $B_\alpha = -C_{1\alpha}$, $\alpha = 2, 3$

We will establish that:

$$B_\alpha = -C_{1\alpha} = \int_{\mathcal{Y}} \nabla Q_1 \cdot \nabla Q_\alpha \mathrm{d}\mathbf{y}. \qquad \text{[A1.2]}$$

To do so, it is sufficient to evaluate the above integral using

$$0 = \int_{\mathcal{Y}} Q_\alpha \Delta Q_1 = -\int_{\mathcal{Y}} \nabla Q_1 \cdot \nabla Q_\alpha \mathrm{d}\mathbf{y} + \int_{\partial\mathcal{Y}} Q_\alpha \, \nabla Q_1 \cdot \mathbf{n} \, \mathrm{d}s.$$

The last integral vanishes on Γ and on the lateral boundaries in the y_2 and y_3 directions by periodicity. We remain with the two integrals over $\mathsf{Y}(y_1^m)$ (where $\nabla Q_1 \cdot \mathbf{n} = 1$ in the limit of large $|y_1^m|$) and over $\mathsf{Y}(-y_1^m)$ (where $\nabla Q_1 \cdot \mathbf{n} = -1$). It follows that the last integral reduces precisely to B_α, which proves the first equality in [A1.2]. Next, we consider the integral

$$0 = \int_{\mathcal{Y}} Q_1 \Delta(Q_\alpha + y_\alpha) = -\int_{\mathcal{Y}} \nabla Q_1 \cdot \nabla Q_\alpha \mathrm{d}\mathbf{y} - \int_{\mathcal{Y}} \frac{\partial Q_1}{\partial y_\alpha} + \int_{\partial\mathcal{Y}} Q_1 \, \nabla(Q_\alpha + y_\alpha) \cdot \mathbf{n} \, \mathrm{d}s.$$

The last integral vanishes on Γ and on the periodic boundaries, and also on $\mathsf{Y}(\pm y_1^m)$, where $\mathbf{n} = \pm\mathbf{e}_1$ with $\nabla Q_\alpha \to 0$. This proves the second equality in [A1.2].

Appendix 2

Introduction to the Multiple Scattering Theory: Green-Kirchhoff Integral and Bloch Wave Amplitudes

Here, the *2-D ℓ-periodic Green function* $\mathcal{G}^{\ell}_{\mathbf{x}_s}(\mathbf{x})$ is defined. It consists of the wavefield created at the point $\mathbf{x}$ by the ℓ-periodic arrangement of line sources located at the points $\mathbf{x}_{s,q} = \mathbf{x}_s + q\ell\mathbf{e}_x$ in the plane $\mathcal{P}$, with $q \in \mathbb{Z}$. The point $\mathbf{x}_s = x_s\mathbf{e}_x + y_s\mathbf{e}_y$ is supposed to be above or below the reference cluster $\Omega^0_{\rm cl}$, i.e. $x_s \in [-\ell/2; \ell/2]$ and $y_s > y^+$ or $y_s < y^-$. Two consecutive sources are supposed to display the phase shift $e^{-{\rm i}k_x\ell}$, so that the field $\mathcal{G}^{\ell}_{\mathbf{x}_s}(\mathbf{x})$ satisfies:

$$\text{div}(\mathbf{grad}(\mathcal{G}^{\ell}_{\mathbf{x}_s})) + k^2\mathcal{G}^{\ell}_{x_s}(\mathbf{x}) = \sum_{q\in\mathbb{Z}} \delta(\mathbf{x} - \mathbf{x}_{s,q})e^{-{\rm i}k_x q\ell}, \qquad [A2.1]$$

where $\delta(\mathbf{x} - \mathbf{x}_{s,q}) = 1$ if $\mathbf{x} = \mathbf{x}_{s,q}$ but $\delta(\mathbf{x} - \mathbf{x}_{s,q}) = 0$ otherwise. On the contrary, the scattered field $p^{\rm sc}$ satisfies the Helmholtz equation:

$$\text{div}(\mathbf{grad}(p^{\rm sc})) + k^2 p^{\rm sc} = 0. \qquad [A2.2]$$

Multiplying equation [A2.2] by $\mathcal{G}^{\ell}_{\mathbf{x}_s}$ and equation [A2.1] by $p^{\rm sc}$ provides the two equations:

$$\mathcal{G}^{\ell}_{\mathbf{x}_s}\text{div}(\mathbf{grad}(p^{\rm sc})) + k^2 p^{\rm sc}\mathcal{G}^{\ell}_{\mathbf{x}_s} = 0, \qquad [A2.3a]$$

$$p^{\rm sc}\text{div}(\mathbf{grad}(\mathcal{G}^{\ell}_{\mathbf{x}_s})) + k^2 p^{\rm sc}\mathcal{G}^{\ell}_{x_s} = p^{\rm sc}\sum_{q\in\mathbb{Z}} \delta(\mathbf{x} - \mathbf{x}_{s,q})e^{-{\rm i}k_x q\ell}. \qquad [A2.3b]$$

Chapter written by Logan SCHWAN and Jean-Philippe GROBY.

Fundamentals and Applications of Acoustic Metamaterials: From Seismic to Radio Frequency,
First Edition. Edited by Vicente Romero-García and Anne-Christine Hladky-Hennion.

Subtracting equation [A2.3a] from [A2.3b] yields:

$$\mathcal{L}(p^{\text{sc}}, \mathcal{G}^{\ell}_{\mathbf{x}_s}) = p^{\text{sc}} \sum_{q\in\mathbb{Z}} \delta(\mathbf{x} - \mathbf{x}_{s,q}) e^{-\mathrm{i}k_x q\ell}, \qquad \text{[A2.4a]}$$

$$\text{with} \qquad \mathcal{L}(p^{\text{sc}}, \mathcal{G}^{\ell}_{\mathbf{x}_s}) = p^{\text{sc}} \text{div}(\mathbf{grad}(\mathcal{G}^{\ell}_{\mathbf{x}_s})) - \mathcal{G}^{\ell}_{\mathbf{x}_s} \text{div}(\mathbf{grad}(p^{\text{sc}})). \qquad \text{[A2.4b]}$$

Using the differential identity $u\text{div}(\mathbf{g}) = \text{div}(u\mathbf{g}) - \mathbf{grad}(u)\cdot\mathbf{g}$ where u is a scalar field and $\mathbf{g}$ is a vector field, equation [A2.4b] becomes:

$$\mathcal{L}(p^{\text{sc}}, \mathcal{G}^{\ell}_{\mathbf{x}_s}) = \text{div}\left[p^{\text{sc}}\mathbf{grad}(\mathcal{G}^{\ell}_{\mathbf{x}_s})) - \mathcal{G}^{\ell}_{\mathbf{x}_s}\mathbf{grad}(p^{\text{sc}})\right]. \qquad \text{[A2.5]}$$

Equation [A2.4a] is integrated over the volume $\mathcal{V} = [-\ell/2; \ell/2] \times [-h; h]$, where $h > \max\{|y^+|, |y^-|, |y_s|\}$; see Figure 6.4. It leads to:

$$\int_{\mathcal{V}} \mathcal{L}(p^{\text{sc}}, \mathcal{G}^{\ell}_{\mathbf{x}_s})\, \mathrm{d}\mathcal{V} = \int_{\mathcal{V}} p^{\text{sc}}(\mathbf{x}) \sum_{q\in\mathbb{Z}} \delta(\mathbf{x} - \mathbf{x}_{s,q}) e^{-\mathrm{i}k_x q\ell}\, \mathrm{d}\mathcal{V}. \qquad \text{[A2.6]}$$

Since only the source $\mathbf{x}_s = \mathbf{x}_{s,0}$ belongs to $\mathcal{V}$, the following relation holds:

$$\int_{\mathcal{V}} p^{\text{sc}}(\mathbf{x}) \sum_{q\in\mathbb{Z}} \delta(\mathbf{x} - \mathbf{x}_s - q\ell\mathbf{e}_x) e^{-\mathrm{i}k_x q\ell}\, \mathrm{d}\mathcal{V} = p^{\text{sc}}(\mathbf{x}_s). \qquad \text{[A2.7]}$$

Substituting equations [A2.5] and [A2.7] into [A2.6] and applying the divergence theorem, the following relation, called the *Green–Kirchhoff Integral Theorem*, is derived:

$$p^{\text{sc}}(\mathbf{x}_s) = \int_{\partial\mathcal{V}} \left[p^{\text{sc}}\mathbf{grad}(\mathcal{G}^{\ell}_{\mathbf{x}_s})) - \mathcal{G}^{\ell}_{\mathbf{x}_s}\mathbf{grad}(p^{\text{sc}})\right] \cdot \mathbf{n}_{\mathcal{V}}\, \mathrm{d}\mathcal{V}, \qquad \text{[A2.8]}$$

where $\partial\mathcal{V}$ is the boundary of $\mathcal{V}$ while $\mathbf{n}_{\mathcal{V}}$ is its outward normal vector. Since the integrand in equation [A2.8] is ℓ-periodic, it takes identical values at the boundaries $x = \pm\ell/2$ of the volume $\mathcal{V}$, while $\mathbf{n}_{\mathcal{V}} = \pm\mathbf{e}_x$ changes sign. Then, integrals over the boundaries $x = \pm\ell/2$ of $\mathcal{V}$ cancel one another out in equation [A2.8], which becomes:

$$p^{\text{sc}}(\mathbf{x}_s) = \Pi_h^+ + \Pi_h^- + \sum_{j\in[\![1;\mathcal{N}]\!]} \Pi_j, \qquad \text{[A2.9a]}$$

$$\text{with} \qquad \Pi_h^{\pm} = \pm \int_{\Gamma_h^{\pm}} \left[p^{\text{sc}}\mathbf{grad}(\mathcal{G}^{\ell}_{\mathbf{x}_s})) - \mathcal{G}^{\ell}_{\mathbf{x}_s}\mathbf{grad}(p^{\text{sc}})\right] \cdot \mathbf{e}_y\, \mathrm{d}\mathbf{x} \qquad \text{[A2.9b]}$$

$$\text{and} \qquad \Pi_j = -\int_{\Gamma_j} \left[p^{\text{sc}}\mathbf{grad}(\mathcal{G}^{\ell}_{\mathbf{x}_s})) - \mathcal{G}^{\ell}_{\mathbf{x}_s}\mathbf{grad}(p^{\text{sc}})\right] \cdot \mathbf{n}_j\, \mathrm{d}\mathbf{x}, \qquad \text{[A2.9c]}$$

where $\Gamma_h^{\pm}$ are the boundaries of $\mathcal{V}$ at $y = \pm h$ and Γ_j is the boundary of obstacle Ω_j with outward normal vector $\mathbf{n}_j$. To calculate these integrals, the analytical expression of the Green function $\mathcal{G}^{\ell}_{\mathbf{x}_s}$ is now required. To determine the value of $\Pi_h^{\pm}$, the Green function $\mathcal{G}^{\ell}_{\mathbf{x}_s}$ is written in the Cartesian coordinate system $(O, \mathbf{e}_x, \mathbf{e}_y)$ by expanding the *Dirac comb* on the right-hand side of equation [A2.1] in its Fourier series:

$$\sum_{q\in\mathbb{Z}} \delta(\mathbf{x} - \mathbf{x}_s - q\ell\mathbf{e}_x) e^{-\mathrm{i}k_x q\ell} = \frac{\delta(y - y_s)}{\ell} \sum_{\mu\in\mathbb{Z}} e^{-\mathrm{i}k_x^{\mu}(x-x_s)}, \qquad [A2.10]$$

where $k_x^{\mu} = k_x + 2\pi\mu/\ell$. The periodic Green function is sought in the form:

$$\mathcal{G}^{\ell}_{\mathbf{x}_s}(x, y) = \sum_{\mu\in\mathbb{Z}} \hat{\mathcal{G}}_{\mu}(y) e^{-\mathrm{i}k_x^{\mu}(x-x_s)} \qquad [A2.11]$$

and the substitution of [A2.10] and [A2.11] into [A2.1] provides:

$$\frac{\partial^2 \hat{\mathcal{G}}_{\mu}}{\partial y^2} + (k_y^{\mu})^2 \hat{\mathcal{G}}_{\mu} = \frac{\delta(y - y_s)}{\ell} \quad \Rightarrow \quad \hat{\mathcal{G}}_{\mu}(y) = \frac{e^{\mathrm{i}k_y^{\mu}|y-y_s|}}{2\mathrm{i}k_y^{\mu}\ell} \text{ for } k_y^{\mu} \neq 0, \qquad [A2.12]$$

where $(k_y^{\mu})^2 = k^2 - (k_x^{\mu})^2$. Equation [A2.12] is substituted into [A2.11] to provide the Green function $\mathcal{G}^{\ell}_{\mathbf{x}_s}$ in the Cartesian coordinate system $(O, \mathbf{x})$ in the form of plane waves radiated from the line $y = y_s$, along which the sources are arranged periodically:

$$\mathcal{G}^{\ell}_{\mathbf{x}_s}(x, y) = \sum_{\mu\in\mathbb{Z}} \frac{1}{2\mathrm{i}k_y^{\mu}\ell} e^{-\mathrm{i}k_x^{\mu}(x-x_s)+\mathrm{i}k_y^{\mu}|y-y_s|}. \qquad [A2.13]$$

The calculation of $\Pi_h^{\pm}$ in equation [A2.9b] with $\mathcal{G}^{\ell}_{\mathbf{x}_s}$ and p^{sc} in equations [A2.13] and [6.69] yields:

$$\Pi_h^{+} = 0 \qquad \text{and} \qquad \Pi_h^{-} = 0, \qquad [A2.14]$$

where the following orthogonality relation has been used:

$$\int_{x=-\ell/2}^{x=\ell/2} e^{\mathrm{i}(k_x^{\nu} - k_x^{\mu})x} \,\mathrm{d}x = \int_{x=-\ell/2}^{x=\ell/2} e^{\mathrm{i}\frac{2\pi(\nu-\mu)}{\ell}x} \,\mathrm{d}x = \ell\delta(\nu - \mu). \qquad [A2.15]$$

Equation [A2.14] means that the scattered field p^{sc} in equation [A2.9a] stems only from integrals Π_j over the surface Γ_j of the obstacles, and not from integrals $\Pi_h^{\pm}$ over

the fictive and arbitrary boundaries at $y = \pm h$. To calculate Π_j, the Green function $\mathcal{G}^{\ell}_{\mathbf{x}_s}$ is expressed as the superposition of the cylindrical waves emitted from each source:

$$\mathcal{G}^{\ell}_{\mathbf{x}_s} = \sum_{q\in\mathbb{Z}} \frac{1}{4\mathrm{i}} \psi_0(\mathbf{r}_{s,q}) e^{-\mathrm{i}k_x q\ell} \quad \text{with} \quad \mathbf{r}_{s,q} = \mathbf{x} - \mathbf{x}_{s,q}. \tag{A2.16}$$

Graf's addition theorem [6.16] is applied to provide:

$$\psi_0(\mathbf{r}_{s,q}) = \psi_0(\mathbf{r}^{j,0}_{s,q} + \mathbf{r}_j) = \sum_{m\in\mathbb{Z}} \psi_{0-m}(\mathbf{r}^{j,0}_{s,q}) \zeta_m(\mathbf{r}_j) \text{ for } |\mathbf{r}_j| < |\mathbf{r}^{j,0}_{s,q}|, \tag{A2.17}$$

where $\mathbf{r}^{j,0}_{s,q} = \mathbf{x}_{j,0} - \mathbf{x}_{s,q}$ and $\mathbf{r}_j = \mathbf{x} - \mathbf{x}_{j,0}$. The condition $|\mathbf{r}_j| < |\mathbf{r}^{j,0}_{s,q}|$ is satisfied here, since the integration point $\mathbf{x}$ belongs to Γ_j when calculating Π_j, while sources at $\mathbf{x}_{s,q}$ are further away from O_j. Substitution of equation [A2.17] into [A2.16] provides:

$$\mathcal{G}^{\ell}_{\mathbf{x}_s}(\mathbf{r}_j) = \frac{1}{4\mathrm{i}} \sum_{q\in\mathbb{Z}} \sum_{m\in\mathbb{Z}} \psi_{-m}(\mathbf{r}^{j,0}_{s,q})\, \zeta_m(\mathbf{r}_j)\, e^{-\mathrm{i}k_x q\ell}. \tag{A2.18}$$

In addition, section 6.4.2 provided the scattered field in the vicinity of Ω_j in the form:

$$p^{\mathrm{sc}}(\mathbf{r}_j) = \sum_{n\in\mathbb{Z}} A^j_n \psi_n(\mathbf{r}_j) + (\mathcal{E}^j_n - U^j_n)\zeta_n(\mathbf{r}_j). \tag{A2.19}$$

The calculation of Π_j in equation [A2.9c] with $\mathcal{G}^{\ell}_{\mathbf{x}_s}$ and p^{sc} in equations [A2.18] and [A2.19] yields:

$$\Pi_j = \sum_{q\in\mathbb{Z}} \sum_{n\in\mathbb{Z}} (-1)^n A^j_n\, \psi_n(\mathbf{r}^{j,0}_{s,q})\, e^{-\mathrm{i}k_x q\ell} = \sum_{q\in\mathbb{Z}} \sum_{n\in\mathbb{Z}} A^j_n\, \psi_n(\mathbf{r}^{s,0}_{j,q})\, e^{\mathrm{i}k_x q\ell}, \tag{A2.20}$$

with $\mathbf{r}^{s,0}_{j,q} = \mathbf{x}_{s,0} - \mathbf{x}_{j,q}$, and where the orthogonality relation [6.14] has been used, as well as the following properties[1] of the Bessel and Hankel functions:

$$\mathrm{J}_{-n}(ka_j)\mathrm{J}'_n(ka_j) - \mathrm{J}'_{-n}(ka_j)\mathrm{J}_n(ka_j) = 0 \text{ since } \mathrm{J}_{-n} = (-1)^n \mathrm{J}_n, \tag{A2.21a}$$

$$\mathrm{J}_{-n}(ka_j)\mathrm{H}'_n(ka_j) - \mathrm{J}'_{-n}(ka_j)\mathrm{H}_n(ka_j) = 2\mathrm{i}(-1)^n/(\pi ka_j). \tag{A2.21b}$$

Equation [A2.20] shows that Π_j is the field scattered by all the obstacles $\Omega_{j,q\in\mathbb{Z}}$.

The Green function $\mathcal{G}^{\ell}_{\mathbf{x}_s}$ is now written in yet another form, which hybridizes Cartesian coordinates for the field point $\mathbf{x}_s$ and polar coordinates for the integration

1 Equation [A2.21b] is the Wronskian between Bessel and Hankel functions.

point $\mathbf{x}$. Following the same procedure as in section 6.3.5, the plane waves $e^{-\mathrm{i}k_x^\mu x \pm \mathrm{i}k_y^\mu y}$ in equation [A2.13] are written as:

$$e^{-\mathrm{i}k_x^\mu x \pm \mathrm{i}k_y^\mu y} = e^{-\mathrm{i}k_x^\mu x_j \pm \mathrm{i}k_y^\mu y_j}\ e^{-\mathrm{i}kr_j\cos(\theta_j - \vartheta^\mu)}, \qquad [A2.22]$$

where (r_j, θ_j) are polar coordinates of $\mathbf{x}$ in the coordinate system $(O_j, \mathbf{r}_j)$ while ϑ^μ is such that $k_x^\mu = k\cos(\vartheta^\mu)$ and $k_y^\mu = k\sin(\vartheta^\mu)$. Then, the Jacobi–Anger expansion [6.38] is used to provide the following expansion on regular wavefunctions:

$$e^{-\mathrm{i}k_x^\mu x \pm \mathrm{i}k_y^\mu y} = e^{-\mathrm{i}k_x^\mu x_j \pm \mathrm{i}k_y^\mu y_j} \sum_{m\in\mathbb{Z}} (-\mathrm{i})^m e^{\pm \mathrm{i}m\vartheta^\mu} \zeta_m(\mathbf{r}_j). \qquad [A2.23]$$

Substitution of equation [A2.23] into [A2.13] yields:

$$\mathcal{G}^\ell_{\mathbf{x}_s}(\mathbf{r}_j) = \sum_{\mu\in\mathbb{Z}} \frac{e^{\mathrm{i}k_x^\mu(x_s - x_j) - \varepsilon \mathrm{i}k_y^\mu(y_s - y_j)}}{2\mathrm{i}k_y^\mu \ell} \sum_{m\in\mathbb{Z}} (-\mathrm{i})^m e^{\varepsilon \mathrm{i}m\vartheta^\mu} \zeta_m(\mathbf{r}_j), \qquad [A2.24]$$

where $\varepsilon = +1$ if $y > y_s$, i.e. if $r_j\sin(\theta_j) > (y_s - y_j)$, while $\varepsilon = -1$ if $y < y_s$, i.e. if $r_j\sin(\theta_j) < (y_s - y_j)$. The calculation of Π_j in equation [A2.9c] with $\mathcal{G}^\ell_{\mathbf{x}_s}$ and p^{sc} in equations [A2.24] and [A2.19] yields the following relation when using the orthogonality relation [6.14] and the properties in equation [A2.21]:

$$\Pi_j = \begin{cases} \displaystyle\sum_{\mu\in\mathbb{Z}} \left(\sum_{m\in\mathbb{Z}} K^+_{\mu,m} A^j_m \right) e^{\mathrm{i}k_x^\mu(x_s - x_j) + \mathrm{i}k_y^\mu(y_s - y_j)} & \text{if } y_s > y_j + a_j, \\ \displaystyle\sum_{\mu\in\mathbb{Z}} \left(\sum_{m\in\mathbb{Z}} K^-_{\mu,m} A^j_m \right) e^{\mathrm{i}k_x^\mu(x_s - x_j) - \mathrm{i}k_y^\mu(y_s - y_j)} & \text{if } y_s < y_j - a_j, \end{cases} \qquad [A2.25]$$

where

$$K^\pm_{\mu,m} = 2(-\mathrm{i})^m e^{\pm \mathrm{i}m\vartheta^\mu}/(k_y^\mu \ell). \qquad [A2.26]$$

Comparison of both expressions [A2.20] and [A2.25] found for the integral Π_j shows that the field scattered by all the obstacles $\Omega_{j,q\in\mathbb{Z}}$ can be expanded for $|y_s - y_j| > a_j$ on outgoing Bloch waves which seem to be radiated from the line $y = y_j$ along which the center $O_{j,q}$ of the obstacles $\Omega_{j,q\in\mathbb{Z}}$ are aligned.

List of Authors

Christian AUDOLY
Naval Group Research
Technopole de la Mer
Ollioules
France

Sarah BENCHABANE
CNRS, UMR 6174
Institut FEMTO-ST
University of Burgundy – Franche-Comté
Besançon
France

Vicente CUTANDA HENRÍQUEZ
Center for Acoustic-Mechanical Micro Systems
Technical University of Denmark
Kongens Lyngby
Denmark

Jean-Philippe GROBY
CNRS, UMR 6613 – LAUM
Le Mans
France

Anne-Christine HLADKY-HENNION
CNRS, UMR 8520 – IEMN
Lille
France

Noé JIMÉNEZ
Instituto de Instrumentación para Imagen Molecular
Spanish National Research Council
Valencia
Spain

Clément LAGARRIGUE
MetAcoustic
Le Mans
France

Damien LECOQ
MetAcoustic
Le Mans
France

Martin LOTT
CNRS, UMR 5275 – ISTerre
University of Grenoble Alpes
France

Fundamentals and Applications of Acoustic Metamaterials: From Seismic to Radio Frequency,
First Edition. Edited by Vicente Romero-García and Anne-Christine Hladky-Hennion.

Jean-Jacques MARIGO
CNRS, UMR 7649 – LMS
Ecole Polytechnique
Palaiseau
France

Agnès MAUREL
CNRS, UMR 7587
Institut Langevin
ESPCI ParisTech
Paris
France

Kim PHAM
CNRS, UMR 9219 – IMSIA
ENSTA ParisTech
and
EDF, CEA
University of Paris-Saclay
Palaiseau
France

Alexandre REINHARDT
University of Grenoble Alpes
CEA, LETI
Grenoble
France

Vicente ROMERO-GARCÍA
CNRS, UMR 6613 – LAUM
Le Mans
France

Philippe ROUX
CNRS, UMR 5275 – ISTerre
University of Grenoble Alpes
France

José SÁNCHEZ-DEHESA
Wave Phenomena Group
Electronic Engineering Department
Polytechnic University of Valencia
Spain

Logan SCHWAN
CNRS, UMR 6613 – LAUM
Le Mans
France

Jérôme VASSEUR
CNRS, UMR 8520 – IEMN
Cité Scientifique
Villeneuve d'Ascq
France

Index

Fundamentals and Applications of Acoustic Metamaterials: From Seismic to Radio Frequency,
First Edition. Edited by Vicente Romero-García and Anne-Christine Hladky-Hennion.

S, U, V, W

Other titles from

in

Waves

2019

DAHOO Pierre-Richard, LAKHLIFI Azzedine
Infrared Spectroscopy of Triatomics for Space Observation (Infrared Spectroscopy Set – Volume 2)

RÉVEILLAC Jean-Michel
Electronic Music Machines: The New Musical Instruments

2018

SAKHO Ibrahima
Screening Constant by Unit Nuclear Charge Method: Description and Application to the Photoionization of Atomic Systems

2017

DAHOO Pierre-Richard, LAKHLIFI Azzedine
Infrared Spectroscopy of Diatomics for Space Observation (Infrared Spectroscopy Set – Volume 1)

PARET Dominique, HUON Jean-Paul
Secure Connected Objects

PARET Dominque, SIBONY Serge
Musical Techniques: Frequencies and Harmony

RÉVEILLAC Jean-Michel
Analog and Digital Sound Processing

STAEBLER Patrick
Human Exposure to Electromagnetic Fields

2016

ANSELMET Fabien, MATTEI Pierre-Olivier
Acoustics, Aeroacoustics and Vibrations

BAUDRAND Henri, TITAOUINE Mohammed, RAVEU Nathalie
The Wave Concept in Electromagnetism and Circuits: Theory and Applications

PARET Dominique
Antennas Designs for NFC Devices

PARET Dominique
Design Constraints for NFC Devices

WIART Joe
Radio-Frequency Human Exposure Assessment

2015

PICART Pascal
New Techniques in Digital Holography

2014

APPRIOU Alain
Uncertainty Theories and Multisensor Data Fusion

JARRY Pierre, BENEAT Jacques N.
RF and Microwave Electromagnetism

LAHEURTE Jean-Marc
UHF RFID Technologies for Identification and Traceability

SAVAUX Vincent, LOUËT Yves
MMSE-based Algorithm for Joint Signal Detection, Channel and Noise Variance Estimation for OFDM Systems

THOMAS Jean-Hugh, YAAKOUBI Nourdin
New Sensors and Processing Chain

TING Michael
Molecular Imaging in Nano MRI

VALIÈRE Jean-Christophe
Acoustic Particle Velocity Measurements using Laser: Principles, Signal Processing and Applications

VANBÉSIEN Olivier, CENTENO Emmanuel
Dispersion Engineering for Integrated Nanophotonics

2013

BENMAMMAR Badr, AMRAOUI Asma
Radio Resource Allocation and Dynamic Spectrum Access

BOURLIER Christophe, PINEL Nicolas, KUBICKÉ Gildas
Method of Moments for 2D Scattering Problems: Basic Concepts and Applications

GOURE Jean-Pierre
Optics in Instruments: Applications in Biology and Medicine

LAZAROV Andon, KOSTADINOV Todor Pavlov
Bistatic SAR/GISAR/FISAR Theory Algorithms and Program Implementation

LHEURETTE Eric
Metamaterials and Wave Control

PINEL Nicolas, BOURLIER Christophe
Electromagnetic Wave Scattering from Random Rough Surfaces: Asymptotic Models

SHINOHARA Naoki
Wireless Power Transfer via Radiowaves

TERRE Michel, PISCHELLA Mylène, VIVIER Emmanuelle
Wireless Telecommunication Systems

2012

LALAUZE René
Chemical Sensors and Biosensors

LE MENN Marc
Instrumentation and Metrology in Oceanography

LI Jun-chang, PICART Pascal
Digital Holography

2011

BECHERRAWY Tamer
Mechanical and Electromagnetic Vibrations and Waves

BESNIER Philippe, DÉMOULIN Bernard
Electromagnetic Reverberation Chambers

GOURE Jean-Pierre
Optics in Instruments

GROUS Ammar
Applied Metrology for Manufacturing Engineering

LE CHEVALIER François, LESSELIER Dominique, STARAJ Robert
Non-standard Antennas

2010

BEGAUD Xavier
Ultra Wide Band Antennas

MARAGE Jean-Paul, MORI Yvon
Sonar and Underwater Acoustics

2009

BOUDRIOUA Azzedine
Photonic Waveguides

BRUNEAU Michel, POTEL Catherine
Materials and Acoustics Handbook

DE FORNEL Frédérique, FAVENNEC Pierre-Noël
Measurements using Optic and RF Waves

FRENCH COLLEGE OF METROLOGY
Transverse Disciplines in Metrology

2008

FILIPPI Paul J.T.
Vibrations and Acoustic Radiation of Thin Structures

LALAUZE René
Physical Chemistry of Solid-Gas Interfaces

2007

KUNDU Tribikram
Advanced Ultrasonic Methods for Material and Structure Inspection

PLACKO Dominique
Fundamentals of Instrumentation and Measurement

RIPKA Pavel, TIPEK Alois
Modern Sensors Handbook

2006

BALAGEAS Daniel *et al.*
Structural Health Monitoring

BOUCHET Olivier *et al.*
Free-Space Optics

BRUNEAU Michel, SCELO Thomas
Fundamentals of Acoustics

FRENCH COLLEGE OF METROLOGY
Metrology in Industry

GUILLAUME Philippe
Music and Acoustics

GUYADER Jean-Louis
Vibration in Continuous Media

WILEY END USER LICENSE AGREEMENT

Go to www.wiley.com/go/eula to access Wiley’s ebook EULA.

METAMATERIALS APPLIED TO WAVES SET

Coordinated by Frédérique de Fornel and Sébastien Guenneau

In the last few decades, metamaterials have revolutionized the ways in which waves are controlled, and applied in physics and practical situations. The extraordinary properties of metamaterials, such as their locally resonant structure with deep subwavelength band gaps and their ranges of frequency where propagation is impossible, have opened the way to a host of applications that were previously unavailable. Acoustic metamaterials have been able to replace traditional treatments in several sectors, due to their better performance in targeted and tunable frequency ranges with strongly reduced dimensions.

This is a training book composed of nine chapters written by experts in the field, giving a broad overview of acoustic metamaterials and their uses. The book is divided into three parts, covering the state-of-the-art, the fundamentals and the real-life applications of acoustic metamaterials.

Vicente Romero-García is a CNRS researcher at Laboratoire d'Acoustique de l'Université du Mans (LAUM), France. He is the leader of the research axis "Metamaterials" at LAUM and "Metamaterials for audible sound" at the GdR META.

Anne-Christine Hladky-Hennion is a principal scientist at the CNRS and at the Institute of Electronics, Microelectronics and Nanotechnology (IEMN), France. Her main research interests are phononic structures and acoustic metamaterials. She was the director of the GdR META.

www.iste.co.uk

WILEY

9 781786 303363